

# **Supramolecular Structure in Confined Geometries**

September 7, 2012 | <http://pubs.acs.org>  
Publication Date: August 20, 1999 | doi: 10.1021/bk-1999-0736.fw001

# Supramolecular Structure in Confined Geometries

**Srinivas Manne**, EDITOR  
*University of Arizona*

**Gregory G. Warr**, EDITOR  
*University of Sydney*



American Chemical Society, Washington, DC

**American Chemical Society  
Library**

**1155 16th St., N.W.  
Washington, D.C. 20036**

In *Supramolecular Structure in Confined Geometries*; Manne, S., et al.; ACS Symposium Series; American Chemical Society: Washington, DC, 1999.



**Supramolecular structure in  
confined geometries**

**Library of Congress Cataloging-in-Publication Data**

Supramolecular structure in confined geometries / Srinivas Manne, editor. Gregory G. Warr, editor.

p. cm.—(ACS symposium series ; 736)

Includes bibliographical references and index.

ISBN 0-8412-3615-1

1. Macromolecules—Congresses. 2. Chemistry, Physical and Theoretical.

I. Manne, Srinivas. II. Warr, Gregory G. III. Series

QD380.S879 1999  
547'.7—dc21

99-23650  
CIP

The paper used in this publication meets the minimum requirements of American National Standard for Information Sciences—Permanence of Paper for Printed Library Materials, ANSI Z39.48-1984.

Copyright © 1999 American Chemical Society

Distributed by Oxford University Press

All Rights Reserved. Reprographic copying beyond that permitted by Sections 107 or 108 of the U.S. Copyright Act is allowed for internal use only, provided that a per-chapter fee of \$20.00 plus \$0.50 per page is paid to the Copyright Clearance Center, Inc., 222 Rosewood Drive, Danvers, MA 01923, USA. Republication or reproduction for sale of pages in this book is permitted only under license from ACS. Direct these and other permission requests to ACS Copyright Office, Publications Division, 1155 16th St., N.W., Washington, DC 20036.

The citation of trade names and/or names of manufacturers in this publication is not to be construed as an endorsement or as approval by ACS of the commercial products or services referenced herein; nor should the mere reference herein to any drawing, specification, chemical process, or other data be regarded as a license or as a conveyance of any right or permission to the holder, reader, or any other person or corporation, to manufacture, reproduce, use, or sell any patented invention or copyrighted work that may in any way be related thereto. Registered names, trademarks, etc., used in this publication, even without specific indication thereof, are not to be considered unprotected by law.

PRINTED IN THE UNITED STATES OF AMERICA

**American Chemical Society  
Library  
1155 16th St., N.W.  
Washington, D.C. 20036**

In *Supramolecular Structure in Confined Geometries*; Manne, S., et al.; ACS Symposium Series; American Chemical Society: Washington, DC, 1999.

# Advisory Board

## ACS Symposium Series

Mary E. Castellion  
ChemEdit Company

Arthur B. Ellis  
University of Wisconsin at Madison

Jeffrey S. Gaffney  
Argonne National Laboratory

Gunda I. Georg  
University of Kansas

Lawrence P. Klemann  
Nabisco Foods Group

Richard N. Loepky  
University of Missouri

Cynthia A. Maryanoff  
R. W. Johnson Pharmaceutical  
Research Institute

Roger A. Minear  
University of Illinois  
at Urbana-Champaign

Omkaram Nalamasu  
AT&T Bell Laboratories

Kinam Park  
Purdue University

Katherine R. Porter  
Duke University

Douglas A. Smith  
The DAS Group, Inc.

Martin R. Tant  
Eastman Chemical Co.

Michael D. Taylor  
Parke-Davis Pharmaceutical  
Research

Leroy B. Townsend  
University of Michigan

William C. Walker  
DuPont Company

September 7, 2012 | <http://pubs.acs.org>  
Publication Date: August 20, 1999 | doi: 10.1021/bk-1999-0736.fw001

# Foreword

THE ACS SYMPOSIUM SERIES was first published in 1974 to provide a mechanism for publishing symposia quickly in book form. The purpose of the series is to publish timely, comprehensive books developed from ACS sponsored symposia based on current scientific research. Occasionally, books are developed from symposia sponsored by other organizations when the topic is of keen interest to the chemistry audience.

Before agreeing to publish a book, the proposed table of contents is reviewed for appropriate and comprehensive coverage and for interest to the audience. Some papers may be excluded in order to better focus the book; others may be added to provide comprehensiveness. When appropriate, overview or introductory chapters are added. Drafts of chapters are peer-reviewed prior to final acceptance or rejection, and manuscripts are prepared in camera-ready format.

As a rule, only original research papers and original review papers are included in the volumes. Verbatim reproductions of previously published papers are not accepted.

ACS BOOKS DEPARTMENT

# Preface

The behavior of supramolecular structures and assemblies under spatially confined conditions is a central problem in the physics and chemistry of “soft matter.” As the degree of confinement approaches a relevant supramolecular length scale, significant deviations from bulk behavior are generally observed. These deviations often play a central role in both technological and biological processes, in applications as diverse as lubrication, liquid spreading, filtration, mesoscopic materials synthesis, and biological pattern formation.

The objective of this symposium, and this volume, is to bring together a group of researchers from a broad range of academic disciplines and industry to explore the common features of a confining field on supramolecular structure and behavior. Recent advances in experimental techniques (such as neutron reflectometry, atomic force microscopy, and surface force measurements) have opened this field to experimental investigations that were previously impossible. This volume centers around the confinement of polymers, biomolecules, and surfactants by interfaces, particles, and porous media. Although most of the chapters are based on research presentations given by the authors at the symposium itself, a few select chapters were also solicited after the symposium to complement the overall program and fill in some gaps in the subject matter.

This volume is divided broadly into three sections, among which there is considerable overlap. Surfactant Confinement explores the confinement of surfactants and the resulting changes in their aggregation properties; confinement is effected by a single interface (Chapters 1 and 2), between two interfaces (Chapters 3 and 4), by a combination of interfacial effects and fluid flow (Chapter 5), or by bulk electrostatic interactions and finite-volume effects (Chapter 6). Polymer Confinement considers the confinement of polymer melts and solutions; these include boundary layer lubrication between solid surfaces (Chapter 7), glass transitions in free-standing films (Chapter 8), interfacial confinement effects in adsorbed block copolymers and homopolymers (Chapters 9, 10, and 12), and confinement by lyotropic liquid crystalline phases (Chapter 11). Finally, Confinement of Biomolecules considers confinement effects in biomolecules; these can be due to bulk solvent flow (Chapter 13), tethering and confinement between solid surfaces (Chapters 14 and 15), filtration through porous media (Chapter 16), or organic synthesis inside porous media (Chapter 17).

Although the choice of subjects included in this volume is not intended to be comprehensive, it is intended to be representative of the multidisciplinary breadth of research areas that have supramolecular confinement as a common feature.



It is our hope that this symposium and volume will serve as a point of departure for further systematic study of this fertile common ground between chemistry, physics, chemical engineering, and materials science.

We acknowledge financial assistance from Rhodia, Inc. (Cranbury, NJ), and from the American Chemical Society Petroleum Research Fund. Their generous support enabled us to bring together a large group of researchers, including many internationally recognized leaders in fields where spatial confinement is important, and thus contributed significantly to the success of the symposium. We also thank John Texter for his advice and assistance with both the symposium and its proceedings.

SRINIVAS MANNE  
Department of Physics  
University of Arizona  
1118 East 4th Street  
Tucson, AZ 85721

GREGORY G. WARR  
School of Chemistry  
University of Sydney  
Sydney, New South Wales 2006  
Australia

## Chapter 1

# Supramolecular Structure of Surfactants Confined to Interfaces

Srinivas Manne<sup>1</sup> and Gregory G. Warr<sup>2</sup>

<sup>1</sup>Department of Physics, University of Arizona, 1118 East 4th Street,  
Tucson, AZ 85721

<sup>2</sup>School of Chemistry, University of Sydney,  
Sydney, New South Wales 2006, Australia

The mounting evidence for the existence of surfactant aggregates at solid/solution interfaces prompts a re-examination of common experimental techniques for studying surfactant adsorption. The simple models of a surfactant monolayer or bilayer, while reasonable in the face of older experimental data, are now seen to be inadequate to describe the rich range of order seen by atomic force microscopy and other techniques. In this manuscript we review the results of atomic force microscopy which demonstrate the existence of surface micelles, look again at the experimental results which pointed towards surface aggregates, and also look ahead at how the existence of surface micelles requires us to revise the interpretation of other experimental studies and our entire picture of adsorbed films.

### Introduction

Adsorption of a simple solute at an interface is nothing more than an accumulation over and above what would normally be present based on bulk solution concentration. The adsorption of such solutes can easily be modeled by a Langmuir-type mechanism involving an interaction between a solute and a (not necessarily well-defined) surface site. This leads to the well-known Langmuir isotherm, which describes adsorption behavior up to surface coverage of a filled monolayer.

The behavior of surfactants and polymers is much more rich. Interactions between these compounds give rise to self-assembly in bulk solution and, for polymers, in the melt. The supramolecular structures thus formed are labile, and may be easily influenced by external fields. This is perhaps best known from the range of rheological behaviors of polymer melts and solutions,<sup>1</sup> of surfactant systems,<sup>2</sup> and in biopolymer solutions (see Chapter 13).

A shear or elongational flow field is, in many ways, the top end of the hierarchy of confinement, where the motion of the material itself is the confining field. Often flow is present in other situations and must be considered in addition to wall effects in pore or slit geometries (see e.g. Chapters 5, 7, 9 & 16). A pore or slit is confinement expressed most conventionally; A slit may be formed from two solid surfaces (Chapters 4 & 15), by liquid droplets or air bubbles (Chapters 3 & 8), or by the bilayers of a surfactant lamellar phase (Chapter 11).

A useful starting point for building up this hierarchy of confinement geometries and supramolecular structures is to consider small surfactants confined in two dimensions; that is, confined at a single interface. Specifically we consider here adsorbed surfactant films where the adsorbed structures are in equilibrium with a bulk solution.

Recent atomic force microscopy (AFM) studies have demonstrated the close connection between bulk and interfacial (adsorbed) self-assembly structures of both polymers and surfactants. In the case of surfactants on a range of substrates, AFM has revealed the existence of lateral structure in adsorbed surfactant films consistent with adsorbed hemicylindrical, cylindrical and spherical micelles. These are discussed in detail below.

The first evidence that surfactant films contained aggregates arose from adsorption studies. In their landmark 1955 papers, Gaudin and Fuerstenau<sup>3</sup> noted co-operativity in the adsorption mechanisms of cationic and anionic surfactants on quartz; at low concentrations the adsorption was weak and increased only slightly as bulk concentration increased. However above a critical concentration the amount adsorbed increased suddenly and rapidly. Hydrophobic aggregates on the surface were postulated and these were dubbed *hemi-micelles*. This appellation stuck, and an abrupt upward turn in an adsorption isotherm has come to be regarded as diagnostic for the presence of hemi-micelles.

Although there is strong evidence for aggregates at low surface coverage, the conventional interpretation of adsorbed films has favored eventual saturation of the substrate by a laterally unstructured coating. In this chapter we review recent and not-so-recent evidence for self-assembly of surfactants at a range of solid/solution interfaces and discuss evidence for the proposal that adsorbed films consist of arrays of surface micelles (Figure 1(a)) rather than a laterally structureless film (Figure 1(b)), even when the surface is fully covered.

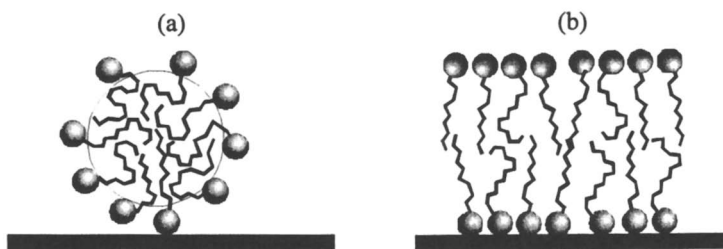


**Figure 1.** (a) adsorbed micelles (spherical or cylindrical) versus (b) classical bilayer pictures of surfactant adsorption. The thickness in both cases is approximately twice the surfactant length.

## Adsorption Isotherms - Solution Depletion Methods

Solution depletion methods<sup>4</sup> were the earliest techniques used to investigate surfactant adsorption, and over the decades a large database of surfactant-solvent-surface combinations has been collected in this way. They probe the interfacial adsorption of surfactants by measuring the drop in surfactant concentration in the free solution caused by the exposure of this solution to a solid of known surface area. This is typically measured as a function of the initial surfactant concentration, resulting in a plot of the adsorbed density of surfactant molecules vs. the solution concentration—the adsorption isotherm. These plots generally show a rapid increase in adsorption density near the cmc, followed by a plateau thereafter. An example is shown in Figure 2.<sup>5</sup> The post-cmc plateau coverage is often consistent with a vertical monolayer for hydrophobic substrates and a vertical bilayer for hydrophilic substrates, and these morphologies have served as the “standard models” for interpreting adsorption data.<sup>6,7,8,9</sup> However, some investigations have shown evidence in support of surface saturation by interfacial micelles (discussed below).

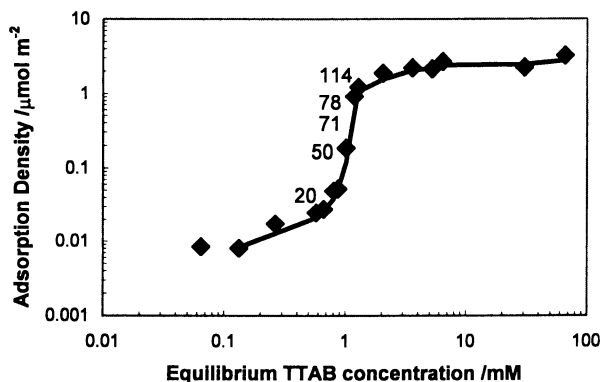


**Figure 2.** Adsorption isotherm of tetradecyltrimethylammonium (TTAB) bromide onto  $\text{Al}_2\text{O}_3$ , also showing aggregation numbers of surface micelles from pyrene fluorescence quenching.

In principle it should be possible to distinguish between distinct interfacial aggregates and a flat layer by measuring the adsorption density, since, for example, close-packed spheres and parallel cylinders would give rise to densities that are, respectively, 0.605 and 0.785 times that of a bilayer. However this identification is made difficult by uncertainties in the determination of solid surface area.

For a typical surfactant headgroup, it takes of order  $10 \text{ m}^2$  of surface area to deplete the solution of  $1 \mu\text{mol}$  of surfactant. It is therefore impractical to use interfaces whose areas can be measured directly, and suspensions of fine powders are used instead to create a detectable depletion. Unfortunately, no completely reliable ways exist to measure interfacial areas of powder suspensions. For example, gas adsorption

isotherms on dry powders may have limited relevance for the wet state, where incomplete wetting may reduce the effective interfacial area, or solution-induced delamination (in the case of layered solids) may increase it. One comparison of surface area measurement by gas adsorption vs. electron microscopy characterization showed a 20% discrepancy even for dry, monodisperse, spherical latex particles.<sup>10</sup> For layered solids such as graphon and clays, where adsorption on a particular crystal face (the basal plane) is typically of interest, another serious problem is the proportional increase in chemical heterogeneities (step and edge sites) with decreasing particle size. This is of particular concern for hydrophobic surfaces, on which step sites are typically polar and hydrophilic. Uncertainties in the measurement of changes in surfactant concentration, and in the proper analysis of adsorption isotherms, are discussed in a thorough review by Hough and Rendall.<sup>4</sup>

The most compelling evidence for interfacial micelles from adsorption isotherms comes from *comparative* adsorption measurements, among different surfactants and with varying degrees of surface modification. Rupprecht *et al.* have shown that the saturation adsorption density on silica of an amphiphilic cation (tetradecylpyridinium) depends strongly on the counterion, showing a sixfold increase in adsorption when the counterion is changed from chloride (weakly binding) to salicylate (strongly binding).<sup>11</sup> Such a dramatic enhancement of adsorption is difficult to reconcile with a bilayer model, where surfactant ion-surface interactions and steric packing should dominate. However, it is completely consistent with interfacial aggregate growth around an electrostatically adsorbed “anchor” molecule, since similar increases in aggregation number are observed in free micelles when the counterion binding affinity is increased. This model is further confirmed by adsorption measurements on silica surfaces modified by a low density of covalently tethered alkyl groups.<sup>12</sup> Even anionic surfactants are shown to adsorb to these surfaces, with the adsorption density increasing with the degree of surface alkylation. The widely spaced alkyl groups are interpreted as “nucleation sites” for surfactant aggregation, leading to a saturated layer of interfacial micelles around the cmc.

Given the general agreement of this interpretation with AFM observations (see below), it is safe to predict that future work in adsorption isotherms will consider multiple models of interfacial structure (e.g., close-packed spheres, parallel cylinders etc.) as theoretical starting points for the interpretation of adsorption data on single-chain surfactants.<sup>13</sup>

## Calorimetry

Calorimetry<sup>14</sup> is primarily used to probe the energetics of surfactant adsorption and not the structure as such; however, these measurements are often used to deduce plausible adsorption mechanisms and hence infer interfacial structure. One commonly used technique is *flow calorimetry*.<sup>15</sup> Here the solution is flowed through a column containing the adsorbent powder. This column is kept at constant temperature inside the microcalorimeter chamber; temperature regulation is accomplished by a feedback loop that controls current through a heating coil. After the column equilibrates to a given temperature in a constant flow of pure solvent, a known quantity of surfactant is released into the flow, and the net heat input (or output) required to maintain the

constant temperature is monitored. Typically this is read off as the area under the curve of heat flow,  $(dQ/dt)$  vs.  $t$ . Since this process is isothermal, the net heat transfer is simply the enthalpy of adsorption. The quantity of interest is usually the heat transfer per molecule, or the molar enthalpy of adsorption, which is the measured enthalpy divided by the molar adsorption density. For this reason, calorimetry is often performed in close conjunction with solution depletion measurements (see Chapter 2).

Surfactant adsorption mechanisms and structure are often intuited by comparing adsorption calorimetry results with those of micellization in free solution. Experiments on both hydrophilic (silica)<sup>16,17,18</sup> and hydrophobic (graphite)<sup>15,19</sup> surfaces show that the adsorption is strongly exothermic at very low surface coverages but becomes weakly exothermic or even endothermic at coverages exceeding ~10% of saturation. The former step is therefore energy-driven and should be dominated by surfactant-surface interactions (since the coverage is very low), whereas the latter step is more entropy-driven and should be dominated by intermolecular interactions. For most surfactants, bulk micellization is also an endothermic or weakly exothermic process;<sup>20</sup> the primary driving force is the entropy gained by expelling initially ordered water molecules around the tailgroups into the bulk solvent. This similarity has been used to argue in favor of interfacial aggregate formation beginning at moderate surface coverage. Moreover, the experimental value of molar adsorption enthalpy for moderate to high surface coverage has been found to match the known value of micellization enthalpy in certain cases.<sup>18</sup> The temperature variation in the adsorption enthalpy at high coverages also closely follows the temperature variation of micellization enthalpy, providing further evidence for this mechanism.<sup>19</sup>

While these studies show strong evidence for aggregative adsorption as the *mechanism*, they do not by themselves definitively exclude the possibility of uniform monolayers and bilayers as the final *equilibrium* structure once surface saturation has been reached. Findenegg *et al.* have taken a step in this direction by comparing the theoretical enthalpy of half-cylindrical aggregation on graphite (the AFM result) to the enthalpy associated with horizontal-to-vertical reorientation of surfactants (the “standard model”);<sup>19</sup> only the former is found to be consistent with their calorimetry data.

## Reflectance Techniques

A powerful and increasingly common suite of techniques for investigating thin adsorbed films are based on the angular dependence of the reflection of an incident beam from a bulk surface in contact with a surfactant solution and, therefore, coated with an equilibrium adsorbed film. Optical reflectometry is most useful for thick films, such as those formed by particles deposited on a surface. However neutrons and x-rays have much shorter wavelengths and can be used to examine adsorbed films in greater detail. Neutron reflectometry has recently become a widespread tool for investigating adsorbed surfactant layers at air/liquid, liquid/liquid and solid/liquid interfaces. X-ray reflectometry has yet to gain widespread use except in air/liquid films, although increasing intensities available in synchrotron sources may bring this into play for other interfaces. A recent and promising development of both neutron and x-ray reflectometry exploits off-specular reflections and scattering from solution near the

surface to determine structural details. Aspects of these techniques are discussed further in Chapters 2 and 5.

As discussed extensively by Zemb and others<sup>21</sup> with respect to *scattering*, reflectivity is essentially the same whether light, neutrons or x-rays are employed as the source of radiation. Whereas refraction and reflection of light is sensitive to refractive index, x-ray optics are sensitive to electron densities (atomic number), and neutrons are sensitive to nuclear properties as expressed in the scattering length density. It is this property of neutrons which leads to *contrast variation* by isotopic substitution experiments in both neutron reflectometry and small-angle neutron scattering. The other significant difference between visible light and x-ray or neutron optics is one of resolution; The smallest length scale is determined by the maximum achievable wave vector,  $Q$ , defined by:-

$$Q = \frac{4\pi}{\lambda} \sin \theta$$

where  $\lambda$  is the wavelength of the radiation, and  $\theta$  the angle of incidence. The maximum resolution achievable depends on wavelength, and the shorter wavelengths of neutrons and x-rays give much improved spatial resolution.

Ellipsometry is an optical technique which exploits the particular sensitivity of the polarization of a reflected beam to the presence of an adsorbed layer at an interface. Although more sensitive than optical reflectometry, the resolution is such that it is not possible to obtain detailed information on adsorbed layer structure from ellipsometry.

### *Neutron Reflectometry (NR)*

The conventional interpretation of NR experiments treats the adsorbed layer as a laterally unstructured film.<sup>22</sup> The combination of reflections from the solid/film and film/solution interfaces give rise to an interference fringe which may be characterised to first order by a thickness and average scattering length density,  $\beta$ . In reality the adsorbed film is not usually homogeneous. Its composition and hence scattering length density may vary as a function of position normal to the bulk interface. The film is then notionally divided into layers of different scattering length density corresponding to e.g. head group and alkyl tails of surfactant. It is common to add onto this description a surface roughness, often as a simple Gaussian. The picture of adsorbed films emerging from NR studies is the commonly-accepted one consisting of a monolayer on a hydrophobic substrate, or bilayer on a hydrophilic solid. The spatial resolution of NR even permits the separate identification of head-group and alkyl tail regions. This is facilitated by experiments in which surfactants are selectively isotopically substituted to create regions of different scattering length density.<sup>23</sup> And yet, this picture is clearly at odds with the evidence for the existence of adsorbed micellar aggregates, particularly on hydrophilic substrates.

Another incongruity is the observation that adsorbed layers on hydrophilic surfaces virtually never form a coherent film with 100% surface coverage, according to NR studies. A patchy film is usually invoked to explain the derived surface coverages, consisting of islands of bilayer. This too is inconsistent with AFM images.

However a laterally unstructured film is not the only possible interpretation of neutron reflectometry data.<sup>24</sup> A model based on adsorbed cylindrical or spherical micelles has recently been developed which yields comparable quality fits to an adsorbed bilayer in simulated films<sup>25</sup> and experiments.<sup>26</sup> The reflectivity of an adsorbed film of TTAB on sapphire at pH=11, fitted to a bilayer and to adsorbed cylindrical and spherical micelles is shown in Figure 3. The fitted surface coverages and film thicknesses for this system are listed in Table 1. The quality of each of the fits is comparable, however the low thickness and incomplete surface coverage mitigate against a coherent bilayer. The TTAB alkyl tail is approximately 18Å long, so we expect the surface layer to be about twice this in thickness, whether in the form of aggregates or not.

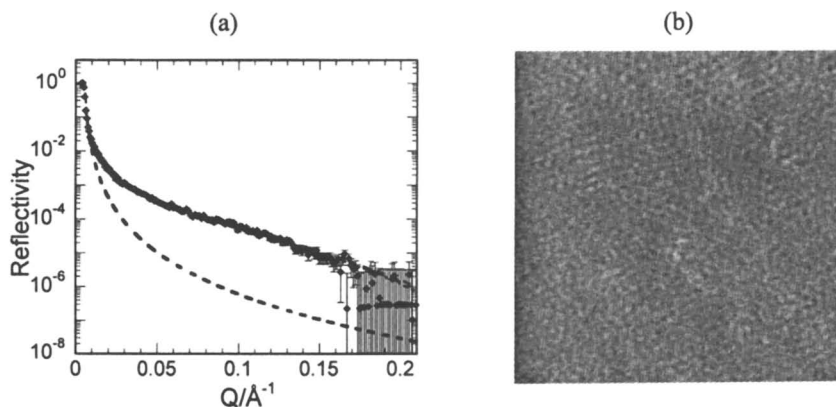


**Figure 3.** (a) Neutron reflectometry data for TTAB adsorbed onto a sapphire crystal. Solid lines show (indistinguishable) fits to adsorbed cylinders, spheres, and a bilayer. Dashed line shows reflectivity from the sapphire/D<sub>2</sub>O interface. (b) 250×250 nm AFM image of spherical micelles adsorbed onto sapphire crystal. In both data sets the equilibrium TTAB concentration is 0.025M.

**Table 1.** Best fit parameters to neutron reflectometry data shown in Figure 3.

	Fractional coverage	Thickness /Å
Bilayer	0.53	25±1
Cylinder	0.45	30±2
Sphere	0.41	34±2

A pleasing feature of the adsorbed aggregates model is that surface coverages less than 100% emerge naturally from the packing of spheres or cylinders on a surface; Closest-packing for cylinders leads to a maximum surface coverage of 79%, and 61% for spheres. Both surface aggregate fits shown are physically reasonable on the basis of fractional coverage (Table 1). Considering the derived parameters, particularly layer



thickness, spheres seem to be the most likely structure, but there is little by which to choose between spheres and cylinders using neutron reflectometry alone.

AFM reveals that this surfactant film does in fact consist of spheres, as shown in Figure 3(b).

### Ellipsometry

Ellipsometry has long been used to investigate adsorbed films of surfactants, and recently attention has turned to the existence of aggregates at the solid/solution interface. Because ellipsometry yields two parameters, both the average refractive index and thickness of an adsorbed film may be deduced. More detailed models of adsorbed surfactant films, similar in character to those used to model neutron reflectometry, have also been constructed.

The work on surface aggregates, largely due to Tiberg, has concentrated on nonionic surfactants adsorbed onto bare and hydrophobically-modified silica. On silica, surface coverages at the plateau adsorption are found to decrease as ethoxy chain length increases.<sup>27</sup> From this it is inferred that, as in solution, longer chain lengths correspond to smaller aggregates (see Table 2).

**Table 2.** Ellipsometry<sup>27</sup> and fluorescence quenching<sup>33</sup> data for adsorbed nonionic surfactants on silica. Ellipsometry of poly(oxyethylene) dodecyl ethers yields an absolute fractional surface coverage. Fluorescence quenching of poly(oxyethylene) octyl phenyl ethers yields the aggregation numbers directly. Bulk aggregation numbers are shown for comparison.

surfactant	$\Gamma_{\max}$	surfactant	$N_{\text{agg}}$ (bulk)	$N_{\text{agg}}$ (adsorbed)
C <sub>12</sub> E <sub>5</sub>	0.54	OPE-9.5	132	210
C <sub>12</sub> E <sub>6</sub>	0.44	OPE-12.5	107	97
C <sub>12</sub> E <sub>8</sub>	0.25	OPE-30	40	42

Similar conclusions were drawn for polydisperse (Triton) nonionics adsorbed on silica and their sulfonated derivatives on titania.<sup>28</sup>

On hydrophobic (dimethyloctylsilylated silica) surfaces, ellipsometric studies are consistent with a laterally coherent monolayer. This differs from AFM observations for both ionic<sup>29,30</sup> and nonionic<sup>31</sup> surfactants on graphite. As discussed below however, evidence for the uniqueness of graphite as a substrate for adsorption is mounting.

The picture developed for nonionic surfactants adsorbed on hydrophilic silica is similar to that due to AFM images of adsorbed ionic surfactants. The adsorbed surfactants are aggregated into small micelles.

### Fluorescence Probe Studies

The fluorescence quenching studies of Levitz<sup>32,33</sup> and Somasundaran<sup>5</sup> provided some of the first direct evidence for surface aggregates. Adapted from earlier work by Turro<sup>34</sup>

and others<sup>35</sup> on micellar solutions, this technique involves observing the quenching of the emission of a micelle-bound fluorophore by an added quencher.

The technique is essentially statistical. The aggregates under study are notionally divided into four classes; micelles with quencher and fluorophore, micelles with fluorophore only, micelles with quencher only, and micelles with neither fluorophore nor quencher. Only fluorophore-containing micelles are probed. Assuming a random (Poisson) distribution of both additives, the fraction of micelles containing a certain number of quenchers,  $x$ , is known to be

$$P_x = \frac{\langle x \rangle^x \exp(-\langle x \rangle)}{x!} \quad ; \quad P_0 = \exp(-\langle x \rangle)$$

where  $\langle x \rangle$  is the *average* number of quenchers per micelle in the system.

The aggregation number of the surface micelles is then obtained from the relative fluorescence intensities in the presence and absence of quencher. The aggregation number,  $N$ , may be obtained from time-resolved fluorescence<sup>36</sup> or from static emission intensities using<sup>34</sup>

$$N = \frac{[S]_{surf}}{[Q]_{surf}} \ln \left( \frac{I(0)}{I(Q)} \right)$$

Here,  $[S]$  and  $[Q]$  are the concentrations of surfactant and quencher on the surface.

In the time-resolved quenching experiment a delta-pulse excitation is used and the decay of fluorescence intensity with time is determined.  $I(0)$  and  $I(Q)$  are the intensities from all micelles and from micelles with fluorophores only measured at time zero after excitation. This is usually obtained by fitting the decay to a known function of time,  $t$ :-

$$I(t) = I(0) \exp(-k_0 t - \langle x \rangle (1 - \exp(-k_Q t)))$$

where  $k_0$  is the rate constant for unquenched fluorescence emission,  $k_Q$  is the rate constant for intramicellar quenching (bimolecular collision of fluorophore and quencher), giving rise to a fast decay component followed by a slow, unquenched decay. In this method the micelle aggregation number is obtained either from the fitted curve, using  $\langle x \rangle = [Q]_{surf}/N[S]_{surf}$ , or by noting that the long-time tail of the fluorescence is an exponential described by

$$I(t) = I(0) \exp(-\langle x \rangle) \exp(-k_0 t)$$

Extrapolating the long-time tail back to  $t=0$ , gives  $I(Q) = I(0) \exp(-\langle x \rangle)$ , and aggregation number is determined as above.

In the static emission method,  $I$  is simply the static fluorescence intensity measured at quencher concentration  $[Q]$ , and  $N$  is determined from the ratio of intensities with and without quencher.

This technique relies on several key assumptions.

- A. Fluorophore and quencher are both fully micelle bound, with no exchange between aggregates. The presence of additives is assumed not to alter micelle structure.
- B. The concentration of surfactant *in aggregates* must be known. In bulk solution this is usually equated to the critical micelle concentration. On a substrate the adsorbed

amount may be measured separately and all adsorbed surfactant is presumed to be in aggregates.

- C. Quenching must be rapid. This is particularly important in static fluorescence studies, where the approximation is made that there is *no emission* from micelles with quencher added (fast decay). Any emission from aggregates containing quenchers may change the apparent aggregation number. This effect is particularly significant at larger aggregation numbers where quenching is slowed by the long diffusion time before quencher and probe can encounter one another.<sup>37</sup>

Almgren has shown that quenching in long, cylindrical micelles does not obey the equation for small micelles.<sup>38,39</sup> The quenching law is derived from a one-dimensional diffusion-reaction equation and is independent of micelle length. The time-resolved fluorescence decay in such cases becomes nonexponential at long times.

AFM studies of surfactants adsorbed onto mica frequently show long, flexible cylinders separated by a few Ångströms. This is precisely the situation in which fluorescence quenching studies will fail to yield a meaningful aggregation number, even in bulk solution. AFM imaging of such aggregates has only been carried out above the critical micelle concentration, where the surface is saturated. At lower concentrations smaller surface aggregates may be observed.

Highly concentrated micelle solutions also deviate from the expected behavior due to intermicellar exchange of fluorophores and quenchers.<sup>40</sup> In highly concentrated systems this permits quenchers and probes in different micelles to interact, falsely reducing  $I(Q)$  and increasing the apparent aggregation number. This applies to adsorbed films at full coverage, independent of aggregate morphology. Previous work has postulated that adsorbed hemi-micelles transform to a coherent bilayer at saturation, in conflict with AFM observations. However comparison with bulk solution studies suggest instead that the model used to interpret fluorescence quenching studies may break down at high surface coverage due either to the formation of cylindrical aggregates or close-packed spheres. Once the cmc is exceeded, fluorescence necessarily probes both bulk and surface micelles. In any case the technique cannot be used to unequivocally infer adsorbed film structure at high coverage.

At lower concentrations where attempts at AFM imaging have been unsuccessful, fluorescence quenching provides a useful window into the formation of aggregates. Its use in a wide range of bulk solution systems has demonstrated it to be a versatile probe of many adsorbed aggregates.

Levitz' pioneering fluorescence probe studies of nonionic surfactant adsorbed films on silica first established that these techniques could be used to study interfacial structure. This demonstrated that fluorescence emission kinetics followed that of a bulk micellar solution, and therefore that small surface micelles were present in octyl phenol ethoxylates like Triton X-100 (OPE-9.5). Aggregation numbers on silica closely track those observed in bulk solution (see Table 2), and are consistent with the results of ellipsometric studies.

This work was extended to ionic surfactants by Somasundaran *et al.*, showing that they, too, form micelle-like aggregates on hydrophilic surfaces. Aggregation numbers are consistent with small, spherical micelles below the adsorption plateau (full surface coverages), but seem to grow with increasing concentration. An illustrative example of

fluorescence quenching results for TTAB adsorbed onto  $\text{Al}_2\text{O}_3$  is shown on the adsorption isotherm in Figure 2.<sup>5</sup> This system corresponds to the AFM image and neutron reflectometry results for TTAB above the cmc shown in Figure 3.

Other fluorescence probe studies have been employed to investigate the structure of adsorbed surfactant films less directly. A measure of polarity or effective dielectric constant for surfactant aggregates, as well as measurements of microviscosity,<sup>41</sup> are both consistent with adsorbed aggregates, although it is difficult to be persuaded of the discrimination afforded by such techniques.

## Atomic Force Microscopy (AFM)

The AFM<sup>42</sup> images a sample surface by positioning a force sensor—usually a small pyramidal tip attached to a sensitive cantilever spring—very close to a sample surface and detecting variations in tip-sample force as the sample is raster-scanned. A typical cantilever size is  $100 \times 30 \times 0.5 \mu\text{m}$ , with a spring constant of order  $0.1 \text{ N/m}$ ; tips are typically  $4 \mu\text{m}$  in size and square pyramidal in shape, with an end radius in the range  $5$  to  $50 \text{ nm}$ . The cantilever deflection (in response to the force exerted on the tip) is detected by an optical lever with a magnification factor of order  $1000$ . The use of surface forces as a contrast mechanism, combined with optical lever detection, makes it simple to adapt AFM imaging to solid-liquid interfaces;<sup>43</sup> the fluid cell need only be transparent (usually glass) and incorporate a fluid inlet and outlet.

The dc force resolution of the AFM is limited primarily by the thermal background. From the thermal oscillations of the cantilever, given by

$$\frac{1}{2} k_B T = \frac{1}{2} k_{\text{spring}} z_{\text{max}}^2$$

the calculated background force  $F_{\text{max}} = k_{\text{spring}} z_{\text{max}}$  is of order  $10 \text{ pN}$ . However the minimum detectable force *variation* during imaging can actually be much less than this value, for two reasons. First, signal-to-noise ratios of far less than unity can be detected, especially (as is often the case) for surface structures having well-defined symmetries and periodicities; such structures effectively convert a dc detection scheme into an ac measurement, where the dominant spatial periodicities can be identified by eye and quantified by fast Fourier transforms. Second, the presence of a repulsive force gradient between tip and sample (such as the exponential force gradient observed in electric double layer forces) increases the effective spring constant by the quantity  $\partial F / \partial z$ , thereby reducing the thermal noise background. For these reasons, local force variations approaching  $1 \text{ pN}$  can often be detected.

Imaging of adsorbed surfactant films is accomplished by mapping the colloidal stabilization forces between the tip and sample when they are immersed in surfactant solution above the cmc (Fig. 4(a)).<sup>29</sup> Force curves show an exponential repulsion consistent with electric double layer forces at long range (the measured Debye length usually agrees to within 15% of the predicted value), followed by a much steeper short range interaction, followed by irreversible rupture of the outer surfactant layers on tip and sample (hemifusion). Force-contrast imaging is performed by setting the operating force in the precontact repulsive part of the curve before the rupture. Image contrast

(Fig. 4(b)) is usually best in the steeper short-range part of the force curve, although images have also been obtained further out in the double layer.

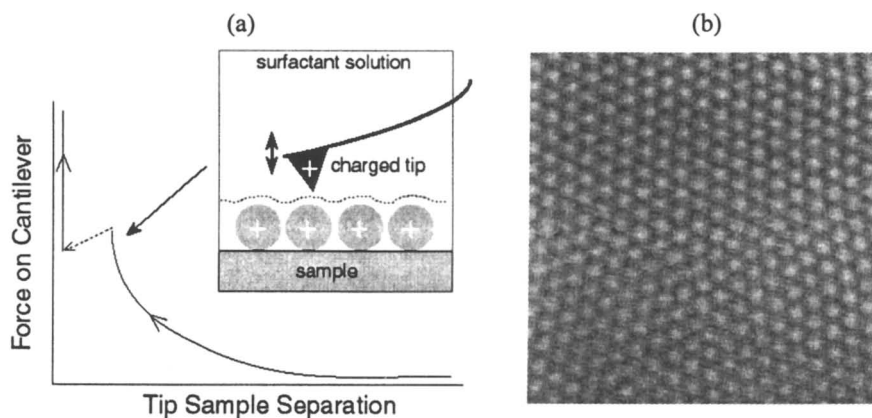


**Figure 4.** (a) Schematic of AFM imaging mechanism for interfacial surfactant aggregates. The adsorption of surfactant on both tip and sample creates repulsive stabilization forces (in this case electric double layer forces) that can extend 1-100 nm beyond the plane of contact. These repulsive interactions are mapped by setting the imaging force in the pre-contact region as shown. (b) 150 x 150 nm image of spherical micelles in a hexagonal pattern at the mica-solution interface. The surfactant is a divalent cationic surfactant with a  $C_{18}$  tail.<sup>47</sup>

Typical imaging forces are of order 0.1 to 1 nN, and typical “fly heights” are of order 1 nm above the surface aggregates. At these small separations, the tip-sample repulsion can arise from a number of contributions; in addition to electric double layer interactions between ionic surfactant headgroups, or steric overlap interactions between nonionic surfactant headgroups, other contributions include solution confinement effects related to the finite sizes of solvent molecules and/or counterions, and mechanical/elastic response of surfactant aggregates caused by steric overlap of interior tailgroups. During imaging, a number of these interactions probably act simultaneously, and the relative contribution of each remains a subject for further research. Whereas the background imaging force is of order 100 to 1000 pN, the measured lateral *variations* in this force—i.e., the force modulation caused by the periodic aggregates—is typically much smaller, of order 1 to 10 pN (roughly 1% of the background). This is consistent with theoretical expectations; even for long-ranged Coulomb interactions, calculations show that the modulation of electrostatic potential above a lattice of discrete charges decays to ~1% of the overall background when the test plane is only a single lattice spacing above the grid.<sup>44</sup>

AFM results, when coupled with those from other techniques, show that the shape, size and arrangement of interfacial surfactant aggregates depend on both intermolecular and molecule-surface interactions.<sup>45</sup> The aggregate shape can be understood as a

compromise between free curvature as defined by the dimensionless packing parameter<sup>46</sup> and the specific constraints imposed by molecule-surface interactions. The interaggregate arrangement can be interpreted as a two-dimensional surfactant mesophase which is somewhat related to the bulk phase behavior at higher concentrations.<sup>47</sup> Specific results are summarized below. All structures reported are at room temperature for surfactant concentrations above the cmc.

### *Ionic Surfactants on Oppositely Charged Hydrophilic Surfaces*

In these systems, surfactant headgroups interact electrostatically with the surface, leading to aggregates of thickness roughly twice the surfactant length, with headgroups facing the surface as well as the solution. A variety of aggregate morphologies has been observed, from spherical aggregates<sup>45,47,48</sup> (both randomly arranged and hexagonally close packed), to cylindrical aggregates<sup>45,47,48</sup> (short and long parallel rods and curved wormlike aggregates), to flat bilayers.<sup>45,47</sup> On the anionic surface of silica, single-chain cationic surfactants give rise to spherical aggregates resembling bulk micelles.<sup>45</sup> These aggregates have a well-defined nearest-neighbor spacing but no long-range order. They have been interpreted as arising from the electrostatic binding of individual surfactant molecules to the charge sites on the surface, which then serve as nucleation sites for micellar aggregation above the cmc. This interpretation has been corroborated by changes in nearest-neighbor spacing with pH, with higher pH solutions resulting in greater surface charge density and a corresponding reduction in interaggregate spacing. Accordingly, interfacial aggregates are expected to resemble bulk micelles whenever the surface charge density (or adsorption site density) of the substrate falls short of (or at most equals) the charge density on the surface of a micelle. Since surface potentials are typically rather high (of order 100 mV) for spherical micelles,<sup>49</sup> most charged surfaces satisfy the above requirement, and globular interfacial aggregates are expected for most single-chain ionic surfactants. Preliminary results on quartz and alumina confirm this view.<sup>26</sup>

A notable exception to this is the cleavage plane of mica, wherein exchangeable surface cations result in a much higher adsorption site density than on silica. Here the observed surface aggregates often have a lower degree of curvature than the corresponding aggregates in free solution.<sup>45,47,48</sup> The mica surface has been interpreted as acting like a highly charged “planar counterion” (or “countersurface”),<sup>47</sup> acting to bring interfacial headgroups closer together than their equilibrium separation in bulk solution, thereby increasing the effective packing parameter at the interface. This is analogous to the induction of a sphere-to-rod transformation in bulk solution by multivalent counterions. Thus some surfactants that form spherical micelles in solution have been observed to form cylindrical aggregates on mica, and likewise some surfactants that form cylindrical micelles in solution have been observed to form bilayers on mica.<sup>47</sup> However, other surfactants that have dimensional packing parameters far from transition values have been found to have aggregate curvatures on mica unchanged from those in free solution. Work is in progress to quantify the effective change in interfacial packing parameter caused by a countersurface of known potential.

While it is tempting to regard the aggregate morphology on mica as a two-dimensional lyotropic mesophase caused simply by a surface-induced zone of high concentration, there does not appear to be a simple correlation between observed interfacial

morphologies on mica and three-dimensional lyotropic phases. For example, of those surfactants which form close-packed spheres on mica,<sup>47,48</sup> some (e.g., divalent surfactants) express a micellar cubic phase in bulk solution,<sup>50</sup> whereas others such as alkyl triethylammonium surfactants do not.<sup>51</sup> However, it is true that all surfactants (so far) that have formed cylindrical aggregates on mica express, as expected, a hexagonal phase as their first liquid crystalline phase. Moreover, univalent double-chained surfactants form flat bilayers on mica,<sup>45</sup> also as expected from the predominance of lamellar phases in bulk.<sup>52</sup>

The mica lattice appears to exert a weak orienting influence on the axial directions of cylindrical aggregates and on the symmetry axes of hexagonally packed spherical aggregates. However the evidence has been conflicting,<sup>45,47,48</sup> probably because local AFM images of small areas do not always reflect overall surface trends; this is especially true when the degree of epitaxial orientation is small, as is expected when a flat surface interacts with a small and symmetric headgroup. This is in marked contrast to the graphite case discussed below.

#### *Nonionic and Zwitterionic Surfactants on Hydrophilic Surfaces*

In these cases the adsorption and surface aggregation are expected to be driven not by charge-charge interactions but by weaker charge-dipole and hydrogen-bonding interactions between surface sites and the surfactant headgroup. The only zwitterionic surfactant studied so far has been dodecyl dimethylammonio-propanesulfonate (DDAPS),<sup>53</sup> which has a cationic group adjacent to the chain followed by a terminal anionic group. This surfactant has been shown to form randomly packed spherical aggregates on the anionic surfaces of both mica and silicon nitride, in agreement with the aggregate morphology in free solution.<sup>54</sup>

A strictly nonionic system that has been widely studied in the past is the adsorption of polyethyleneoxide (PEO)-based surfactants on silica. A recent AFM study<sup>55</sup> has shown that many of these surfactants make globular (roughly spherical) aggregates on the silica surface, with the spheres randomly arranged on the silica surface at nearest-neighbor distances somewhat greater than twice the surfactant length. As with ionic surfactants on silica, these interfacial aggregates reflect bulk micelle morphology.<sup>56</sup> PEO-based surfactants with relatively longer tailgroups or shorter headgroups, which have a tendency towards bilayer structures in solution, showed similar tendencies on silica.<sup>55</sup>

#### *Surfactants on Anisotropic Hydrophobic Surfaces*

The first AFM study of interfacial aggregation was on the cleavage plane of graphite,<sup>29</sup> motivated by the frequent use of graphite crystals as AFM substrates and by long-standing use of graphon as a hydrophobic adsorbent for surfactants. Initial investigations revealed that the crystal lattice, and the resulting anisotropy of its interactions with linear alkyl chains, is *the* defining feature in determining the aggregate morphology. This central role of the lattice has since been confirmed for a variety of surfactants with wide differences in headgroup chemistry and molecular geometry.<sup>30,31,45,47,53,55,57,58</sup>

Unlike hydrophilic surfaces, graphite interacts primarily with surfactant tailgroups via hydrophobic and van der Waals interactions. It has long been known that the graphite surface adsorbs and orients alkyl chains along its three equivalent symmetry axes, with the alkyl chain following the zigzag line connecting nearest-neighbor carbon atoms on graphite.<sup>59,60</sup> A similar orientational constraint should apply to surfactants, and AFM results bear out this view. Images show *linear, parallel* aggregates oriented *perpendicular* to an underlying symmetry axis and spaced apart by a little over *twice* the surfactant length. These are consistent with *half-cylindrical* aggregates, wherein molecules adjacent to the surface are arranged tail-to-tail along parallel strips, with tailgroups oriented *parallel* to a graphite symmetry axis.<sup>29</sup>

The degree of control exerted by the graphite surface is illustrated by the remarkable universality of the above morphology: For surfactants with 12 or more carbon atoms in the tailgroup, *those that are capable of cylindrical curvature—i.e., those that show a hexagonal phase anywhere in the bulk phase diagram—reveal half-cylindrical aggregates on graphite.* These include surfactants that are ionic,<sup>29,30,45,47,57</sup> nonionic<sup>31,55,58</sup> and zwitterionic,<sup>53</sup> and those that form spherical, cylindrical, or even flat bilayer aggregates on mica.<sup>45,47,53</sup> Several of these molecules (e.g., C<sub>12</sub>TAC and the asymmetric gemini surfactants) even have a pronounced micellar cubic phase (spherical curvature) that suppresses the hexagonal phase (cylindrical curvature) until relatively high concentrations. For one surfactant (the nonionic C<sub>12</sub>E<sub>5</sub>), the hexagonal phase is only expressed at temperatures somewhat lower than room temperature (18.5°C),<sup>56</sup> even though half-cylinders on graphite are clearly observed at room temperature. Even polymeric surfactants adopt structures based principally on anisotropic interactions between the alkyl chain and substrate (Chapter 12).

Surfactants that do not self-assemble into half-cylindrical aggregates include (i) univalent double-tailed surfactants that express only lamellar and bicontinuous bulk phases, for which cylindrical curvature is not favored; and (ii) surfactants with 10 or fewer carbon atoms in the tailgroup, which form flat vertical monolayers on graphite, evidently because the tail falls short of a critical length required for orientation by the graphite surface.<sup>55</sup>

Preliminary results with another crystalline hydrophobic surface, the cleavage plane of MoS<sub>2</sub>, shows similar half-cylindrical aggregates running perpendicular to surface symmetry axes,<sup>45</sup> despite the marked differences in lattice symmetry, spacing, and surface chemistry between this surface and graphite. This indicates that strong tailgroup orientations leading to half-cylindrical aggregates may be a feature common to all crystalline hydrophobic adsorbents. The degree of surface control is much greater than for hydrophilic surfaces because hydrophobic surfaces interact with the entire length of the tailgroup, which makes up most of the surface area of the molecule. The anisotropy of this interaction apparently gives rise to the half-cylindrical shape as well as to the specific orientation of this aggregate relative to substrate symmetry axes.

### *Surfactants on Isotropic Hydrophobic Surfaces*

Given the evidently crucial role of surface anisotropy above, an important test case is a flat hydrophobic surface that is amorphous and isotropic, such as silanated silica. Unfortunately, very little is known about aggregate morphologies for this case, partly



because of difficulties in achieving hydrophobicity while keeping the overall surface roughness small on the length scale of surfactant molecules. Initial results on a somewhat rough silanated surface show flat, continuous monolayers of nonionic surfactants.<sup>55</sup> However experimentation is still needed on substrates that reproduce the hydrophobicity and atomic smoothness of graphite without its anisotropy.

### *Shape Changes and Kinetics in Interfacial Aggregates*

A number of induced shape changes in interfacial aggregates have recently been reported. Spherical aggregates on mica have been converted to parallel cylinders, both by displacement of the initially adsorbed surfactant by another (in this case DDAPS displaced by C<sub>12</sub>TAB),<sup>61</sup> and by binding specific counterions directly to the aggregates themselves (in this case salicylates to divalent cationic surfactants).<sup>47</sup> The former results in slow exchange kinetics over a period of hours, whereas the latter results in fast binding kinetics over a period of seconds to minutes. In addition, cylindrical aggregates of C<sub>16</sub>TAB on mica have been converted to spheres by the addition of surface-binding co-ions (in this case Cs<sup>+</sup>) that take up some of the adsorption sites, resulting in a lower-density aggregate structure.<sup>62</sup> The addition of dodecanol to SDS solutions has been observed to give rise to swollen half-cylindrical micelles coexisting with flat featureless aggregates on graphite.<sup>63</sup> Even in the absence of additives, there have been reports of very slow shape changes (over many hours) of some cationic surfactant aggregates on mica.<sup>62</sup>

### *Limitations of AFM Imaging and Interpretation*

Data from probe microscopy can be at risk from imaging artifacts, since the technique is somewhat invasive. A number of standard controls have evolved over the years to counteract these concerns, and they have been successfully applied to images of interfacial aggregates. Aggregate morphologies are observed to be repeatable from scan to scan and are generally independent of scan parameters (size, speed and direction) and cantilever properties (spring constant, tip radius, and constituent material). The strongest lines of evidence that the observed morphologies are not somehow being created by solution confinement are (i) the consistency between AFM images and previous adsorption measurements for isolated surfaces; (ii) the observed registry between aggregate morphology and surface symmetry axes; and (iii) the expected variation of aggregate shape with molecular geometry and with specifically binding counterions on mica.<sup>47</sup> In addition, interfacial aggregates have also been used as templates for the synthesis of mesoscopic silicate films, which have faithfully reproduced and confirmed the interfacial morphology observed at the solid-solution interface.<sup>47, 64</sup>

Nevertheless, some concern about disruption of the native aggregate structure is justified. The image resolution typically improves as the imaging force is increased towards the tip breakthrough point (where the surfactant layer is ruptured); however, these high forces sometimes perturb the aggregate structure, as evidenced by irreproducible images between successive scans. An effect of scan direction has also been reported, with half-cylindrical aggregates registering larger spacings when oriented perpendicular to the fast scan direction relative to those oriented parallel to this

direction.<sup>30</sup> The pressure exerted by the AFM tip may cause some local spreading and flattening of surfactant aggregates below the tip, and this distortion may be prevented from relaxing back to equilibrium along the fast scan direction. As a general rule, it is prudent to confirm observed structures and spacings at the lowest forces at which imaging is still possible, and to check these spacings at more than one scan direction for greater accuracy.

Caution should also be exercised in interpreting AFM images of surfactant aggregates. Since the tip traverses a kind of equipotential surface, the height information in the adsorbate film is largely suppressed (see inset, Figure 4(a)). A sectional profile across an AFM image therefore reveals only local force variations and not the true adsorbate topography as such. (The two plots would coincide only in the event of a true hard-wall interaction between a “point probe” and the adsorbate layer; this is far from the case here, since finite tip sizes and Debye lengths on the order of nanometers both act to broaden the effective area of tip-adsorbate interaction to well past a single micelle.) In particular, the identification of some linear aggregates as “half-cylinders” and others as “full cylinders” is based not on measured height differences, but on (i) comparison to effective occupational areas as measured by adsorption isotherms or to thicknesses as measured by surface force apparatus; and (ii) knowledge of the particular surface chemistry;<sup>47</sup> hydrophilic surfaces interact with headgroups and lead to “full” aggregate structures, whereas hydrophobic surfaces interact with tailgroups and lead to “half” structures. However, not all surfaces can be so unambiguously classified (e.g. gold),<sup>65</sup> and the identification of full vs. half aggregates is not always straightforward.

An additional consequence of the lack of true height information is that it is difficult to judge *based on AFM images alone* how much (if any) substrate is exposed between adjacent aggregates. Only the *periodicity* of the aggregate arrangement can be quantified, and the lateral *size* of the aggregates must be inferred from a knowledge of the molecular dimensions of the surfactant. From these data the spacings between adjacent aggregates can be deduced, and it is typically small in comparison to the aggregate size. Spherical aggregates tend to be spaced further apart than cylindrical aggregates, consistent with the greater degree of surface charge expected for spheres.<sup>47</sup> The aggregate spacing has been shown to be a function of concentration, although it quickly approaches an asymptotic value (close to the physical size of the micelles) around the cmc.<sup>30</sup>

## Surface Force Measurements

While the AFM excels at detecting local force *variations*, it is, in its unmodified form, less practical for making quantitative force measurements that can be compared to theoretical predictions. Its drawbacks are twofold: for a given force measurement, the corresponding tip-sample separation cannot be measured independently; and the shape and surface chemistry of the imaging tip are ill-defined. The latter challenge was elegantly met by the advent of the colloid probe technique,<sup>66</sup> wherein a colloidal particle of known radius and composition is glued to the end of the AFM tip and serves as a well-defined interaction probe. To date, the problem of independent measurement of tip-sample separation has not been solved.

Although usage of the colloid probe technique is on the rise, the surface force apparatus (SFA)<sup>67,68</sup> is still the mainstay of surface force measurements. The SFA measures forces between two curved mica sheets, thus combining well-defined radii of curvature with atomically flat surfaces of known surface chemistry. The separation between mica surfaces is measured independently by interferometry, allowing comparison of force vs. distance measurements to theoretical interaction potentials via the Derjaguin approximation.

There have been several SFA investigations of surface forces in surfactant solutions,<sup>69</sup> motivated both by the need to quantify and model colloidal stabilization forces caused by surfactant adsorption, and by the desire to understand interfacial surfactant behavior in general. SFA was the first technique<sup>70</sup> to directly measure thicknesses of adsorbed surfactant layers by quantifying the “hard wall” separation in surfactant solutions relative to that in pure water; consistent with adsorption isotherms, cationic surfactant layers on mica and silica above the cmc were found to have thicknesses comparable to twice the surfactant length. The SFA has also been used to quantify the onset of colloidal *destabilization* due to charge neutralization in dilute surfactant solutions, as well as colloidal *restabilization* due to interfacial aggregation just below the cmc. Force measurements have also been used to deduce surface potentials and charge densities of ionic surfactant layers by fitting solutions of the Poisson-Boltzmann equation to the force data.<sup>70, 71, 72</sup>

While force measurements by SFA and the colloid probe technique have provided valuable insight into colloidal stabilization forces as such, theoretical comparisons hinge on the assumed model for lateral structure of the surfactant film, which cannot be directly probed by force measurements alone. In the absence of contrary evidence, cationic surfactants have generally been assumed to adsorb as flat bilayers on mica above the cmc,<sup>70,71,72</sup> and this simple model has been used as the basis for theoretical comparisons involving electric double layer forces,<sup>73</sup> depletion and structural forces,<sup>74</sup> and membrane fusion.<sup>75</sup> As discussed above, recent AFM results indicate that the flat bilayer assumption is justified only for lipid-like surfactants, whereas single-chain surfactants typically self-assemble as an array of spherical or cylindrical aggregates above the cmc. It is therefore worth exploring how aggregate curvature and lateral structure in the adsorbate layer affects theoretical interpretations of surface force measurements.

First, the assumption of a flat bilayer causes simple counting errors, leading to an overestimate of the number of interfacial surfactant molecules and consequently an underestimate of the dissociation constant for a given fitted value of the adsorbate charge density. For the case of close-packed spheres, wherein the surface occupation ratio is 0.605, the dissociation constant is underestimated by ~40%. The agreement is better for close-packed cylindrical aggregates, but can be considerably worse for any morphologies incorporating nonzero spacings between aggregates.

Second, the presence of textured or heterogeneously charged adsorbate layers may significantly affect theoretical predictions of electric double layer interactions, giving rise to different best-fit values of surface potential, charge density and so on, than would be the case for the bilayer assumption. A recent theoretical treatment<sup>76</sup> of double layer forces between periodically heterogeneous surfaces—undertaken with surfactant adsorption in mind—concludes that the *additional* interaction due to the charge

heterogeneity (i) can be attractive or repulsive depending on the registry between the fixed charge distributions, and (ii) is *always* attractive if lateral self-adjustment of charges is allowed. It is an open question whether the aggregate arrangements on the two mica surfaces are laterally fixed or, over the time scale of a measurement, mutually adjust to a minimum energy conformation as the surfaces approach each other.

Third, theoretical models for structural forces in micellar solutions have assumed that micelles are confined between flat featureless walls.<sup>74</sup> At least for micellar solutions between solid surfaces, a more appropriate model would be confinement between *textured* walls (patterned either with lines or dots), wherein the surface corrugation and periodicity have a length scale similar to the size of the confined species.

Despite these caveats, it is worth emphasizing that surface forces measured in double-chain surfactant solutions *can* be compared to simple theory, since these surfactants do adsorb as flat bilayers.

## Conclusion

This chapter is primarily concerned with the determination of supramolecular *structures* formed by surfactant molecules at interfaces. Structure is, however, just one part of the problem. A complete understanding would also involve descriptions of the kinetics and energetics of interfacial self-assembly, along with a mathematical model that explains these data and predicts the behavior for general surfactant-solvent-surface combinations. One approach might be to impose an interfacial “boundary condition” to geometric packing arguments, in order to arrive at an effective packing parameter which is dependent on surface properties.

The development of a unifying model has been hindered in the past by a lack of direct and independent knowledge of structure, which is essential to the proper interpretation of other measured properties such as energetics and colloidal forces. Lateral mapping of colloidal stabilization forces by AFM, when combined with other quantitative measurements (by SFA, adsorption isotherms etc.), has provided a direct window into interfacial aggregation. An experimental “database” of interfacial structures is now well underway. In the future, this knowledge should prove useful for more refined interpretations of interfacial properties as well as more accurate models of interfacial self-assembly.

## Acknowledgments

This work was supported by the Australian Research Council (G.G.W.) and by funding from the University of Arizona (S.M.). We would like to thank H.N. Patrick & J.C. Schulz for allowing us to use their unpublished results, and for helpful discussions.

## References

- <sup>1</sup> J.D. Ferry, *Viscoelastic Properties of Polymers*, 3<sup>rd</sup> Ed, John Wiley & Sons, 1980.
- <sup>2</sup> H.Hoffmann in *Structure and Flow in Surfactant Solutions*, ACS Symposium Series No. 578, C.A. Herb & R.K. Prud'homme, Eds., American Chemical Society 1994.
- <sup>3</sup> A.M. Gaudin and D.W. Fuerstenau, *Trans AIME*, 1955, 1; *Trans AIME*, 1955, 958.
- <sup>4</sup> Reviewed in D.B. Hough and H.M. Rendall, "Adsorption of Ionic Surfactants," in G.D. Parfitt and C.H. Rochester, Eds., *Adsorption from Solutions at the Solid/Liquid Interface*. Academic Press, London, 1983. Pp. 247-319.
- <sup>5</sup> D.Fan, P. Somasundaran, N.J.Turro, *Langmuir*, 1997, 13, 506-510
- <sup>6</sup> A.C. Zettlemoyer, *J. Colloid Interface Sci.* 1962, 28, 343-369.
- <sup>7</sup> F.Z. Saleeb and J.A. Kitchener, *J. Chem. Soc.* 1965, 911-917.
- <sup>8</sup> M.A. Yeskie and J.H. Harwell, *J. Phys. Chem.* 1988, 92, 2346-2352.
- <sup>9</sup> W.N. Rowlands, and R.J. Hunter, *Clays and Clay Minerals*, 1992, 40, 287.
- <sup>10</sup> H.J. van den Hun and J.W. Vanderhoff, in R.M. Fitch, Ed., *Polymer Colloids*. Plenum Press, New York, 1971.
- <sup>11</sup> J. Leimbach, J. Sigg and H. Rupprecht, *Colloids Surf.* 1995, 94, 1-11.
- <sup>12</sup> J. Leimbach and H. Rupprecht, *Colloid Polym. Sci.* 1993, 271, 307-309.
- <sup>13</sup> B.-Y. Zhu, T. Gu, *J. Chem. Soc., Faraday Trans. 1*, 1989, 85, 3813, 3819.
- <sup>14</sup> Reviewed in J. Seidel, *Thermochim. Acta* 1993, 229, 257-270.
- <sup>15</sup> G.H. Findenegg, B. Pasucha and H. Strunk, *Colloids Surf.* 1989, 37, 223-233.
- <sup>16</sup> M. Lindheimer, E. Keh, S. Zaini and S. Partyka, *J. Colloid Interface Sci.* 1990, 138, 83-91.
- <sup>17</sup> S. Partyka, M. Lindheimer and B. Faucompre, *Colloids Surf. A* 1993, 76, 267-281.
- <sup>18</sup> Z. Kiraly, R.H.K. Börner and G.H. Findenegg, *Langmuir* 1997, 13, 3308-3315.
- <sup>19</sup> Z. Kiraly and G.H. Findenegg, *J. Phys. Chem.* 1998, 102, 1203-1211.
- <sup>20</sup> For a table of thermodynamic parameters of micellization, see M.J. Rosen, *Surfactants and Interfacial Phenomena*, pp. 116-117. Wiley, New York, 1978.
- <sup>21</sup> Y.Chevalier, T.N. Zemb, *Phys. Rep.* 1990, 53, 279-371
- <sup>22</sup> X.-L. Zhou, S.-H. Chen, *Phys. Rep.* 1995, 257, 223-348.
- <sup>23</sup> E.A. Simister, E.M. Lee, R.K. Thomas, J. Penfold, *J. Phys. Chem.*, 1992, 96, 1373-1382
- <sup>24</sup> P.D.Butler, W.A. Hamilton, L.J.Magid, J.B.Hayter, T.M. Slawewcki, B. Hammouda *Faraday Discuss Chem. Soc.* 1996, 104, 65-78, 88-91
- <sup>25</sup> J.C. Schulz, G.G. Warr, W.A. Hamilton, P.D. Butler, submitted to *J. Phys. Chem. B*.
- <sup>26</sup> J.C. Schulz, G.G. Warr, W.A. Hamilton, P.D. Butler, unpublished results.
- <sup>27</sup> F.Tiberg, *J. Chem. Soc., Faraday Trans.*, 1996, 92, 531-538

- <sup>28</sup> L.Luciani, R.Denoyel, *J. Colloid Interface Sci.*, **1997**, *188*, 75-80
- <sup>29</sup> S.Manne, J.P. Cleveland, H.E. Gaub, G.D. Stucky, P.K. Hansma, *Langmuir*, **1994**, *10*, 4409-4413
- <sup>30</sup> E.J.Wanless, W.A. Ducker, *J. Phys. Chem.*, **1996**, *100*, 3207-3214
- <sup>31</sup> H.N. Patrick, G.G. Warr, S. Manne, I.A. Aksay, *Langmuir* **1997**, *13*, 4349-4356
- <sup>32</sup> P. Levitz, H. Van Damme, D.Keravis *J. Phys. Chem.*, **1984**, *88*, 2228.
- <sup>33</sup> P. Levitz, H. Van Damme, *J. Phys. Chem.*, **1986**, *90*, 1302.
- <sup>34</sup> N.J.Turro, A. Yekta *J. Amer. Chem. Soc.*, **1978**, *100*, 5951
- <sup>35</sup> J.Lang in *The Structure, Dynamics and Equilibrium Properties of Colloidal Systems*, 1-38; D.M. Bloor & E. Wyn-Jones (Eds), Kluwer, 1990
- <sup>36</sup> S.S. Atik, M. Nam, L.A. Singer, *Chem. Phys. Lett.* **1979**, *67*, 75-80; J.-E. Löfroth, *Ph. D. Thesis*, University of Göteborg, **1982**
- <sup>37</sup> G.G. Warr and F. Grieser, *J. Chem. Soc., Faraday Trans. 1*, **1986**, *82*, 1813
- <sup>38</sup> M.Almgren, J.Alsins, E.Mukhtar, J. van Stam, *J. Phys. Chem.*, **1988**, *92*, 4479-4483
- <sup>39</sup> M.Almgren, J.Alsins, J. van Stam, E.Mukhtar, *Prog. Colloid Polym Sci.*, **1988**, *76*, 68-74
- <sup>40</sup> P.P. Infelta, M. Grätzel, J.K. Thomas *J. Phys. Chem.*, **1974**, *78*, 190; M.Tachiya, *J. Chem. Phys.* **1982**, *76*, 340-348
- <sup>41</sup> P.Somasundaran, J.T.Kunjappu, *Coll. Surf.*, **1989**, *37*, 245-268
- <sup>42</sup> G. Binnig, C.F. Quate and Ch. Gerber, *Phys. Rev. Lett.* **1986**, *12*, 930-933.
- <sup>43</sup> B. Drake *et al.*, *Science* **1989**, *243*, 1586-1590.
- <sup>44</sup> J.E. Lennard-Jones and B.M. Dent, *Trans. Faraday Soc.* **1928**, *24*, 92-108.
- <sup>45</sup> S. Manne and H.E. Gaub, *Science* **1995**, *270*, 1480-1482.
- <sup>46</sup> J.N. Israelachvili, D.J. Mitchell, B.W. Ninham, *J. Chem. Soc. Faraday Trans. 2*, **1976**, *72*, 1525
- <sup>47</sup> S. Manne, T.E. Schäffer, Q. Huo, P.K. Hansma, D.E. Morse, G.D. Stucky and I.A. Aksay, *Langmuir* **1997**, *13*, 6382-6387.
- <sup>48</sup> H.N. Patrick, G.G. Warr, S. Manne and I.A. Aksay, *Langmuir*, **1999**, *15*, 1685-1692.
- <sup>49</sup> M.S. Fernandez and P.P. Fromherz, *J. Phys. Chem.*, **1977**, *81*, 1755.
- <sup>50</sup> H. Hagslätt, O. Söderman and B. Jönsson, *Langmuir* **1994**, *10*, 2177-2187.
- <sup>51</sup> E.S. Blackmore and G.J.T. Tiddy, *J. Chem. Soc., Faraday Trans. 2*, **1988**, *84*, 1115.
- <sup>52</sup> G.G. Warr, R. Sen, D.F. Evans and J.E. Trend, *J. Phys. Chem.* **1988**, *92*, 774-783.
- <sup>53</sup> W.A. Ducker and L.M. Grant, *J. Phys. Chem.* **1996**, *100*, 11507-11511.
- <sup>54</sup> P-G. Nilsson, B. Lindman and R.G. Laughlin, *J. Phys. Chem.* **1984**, *88*, 6357-6362.

September 7, 2012 | <http://pubs.acs.org>  
Publication Date: August 20, 1999 | doi: 10.1021/bk-1999-0736.ch001

- <sup>55</sup> L.M. Grant, F. Tiberg and W.A. Ducker, *J. Phys. Chem.* **1998**, *102*, 4288-4294.
- <sup>56</sup> D.J. Mitchell, G.J.T. Tiddy, L. Waring, T. Bostock and M.P. McDonald, *J. Chem. Soc. Faraday Trans. 1* **1983**, *79*, 975-1000.
- <sup>57</sup> E.J. Wanless and W.A. Ducker, *Langmuir* **1997**, *13*, 1463-1474.
- <sup>58</sup> N.B. Holland, M. Ruegsegger and R.E. Marchant, *Langmuir* **1998**, *14*, 2790-2795.
- <sup>59</sup> A.J. Groszek, *Proc. Royal Soc. London A* **1970**, *314*, 473-498.
- <sup>60</sup> J.P. Rabe and S. Buchholz, *Science* **1991**, *253*, 424-427.
- <sup>61</sup> W.A. Ducker and E.J. Wanless, *Langmuir* **1996**, *12*, 5915-5920.
- <sup>62</sup> R.E. Lamont and W.A. Ducker, *J. Amer. Chem. Soc.* **1998**, *120*, 7602-7607.
- <sup>63</sup> E.J. Wanless, T.W. Davey and W.A. Ducker, *Langmuir* **1997**, *13*, 4223-4228.
- <sup>64</sup> I.A. Aksay, M. Trau, S. Manne, I. Honma, N. Yao, L. Zhou, P. Fenter, P.M. Eisenberger and S.M. Gruner, *Science* **1996**, *273*, 892-898.
- <sup>65</sup> M. Jaschke, H.-J. Butt, H.E. Gaub and S. Manne, *Langmuir*, **1997**, *13*, 1381.
- <sup>66</sup> W.A. Ducker, T.J. Senden and R.M. Pashley, *Nature* **1991**, *353*, 239-241.
- <sup>67</sup> D. Tabor and R.H.S. Winterton, *Proc. Royal Soc. London A* **1969**, *312*, 435-450.
- <sup>68</sup> J.N. Israelachvili and D. Tabor, *Proc. Royal Soc. London A* **1972**, *331*, 19-38.
- <sup>69</sup> Reviewed in J.L. Parker, *Prog. Surf. Sci.* **1994**, *4*, 205-271.
- <sup>70</sup> R.M. Pashley and J.N. Israelachvili, *Colloids Surf.* **1981**, *2*, 169-187.
- <sup>71</sup> R.M. Pashley, P.M. McGuiggan, R.G. Horn and B.W. Ninham, *J. Colloid Interface Sci.* **1988**, *126*, 569-578.
- <sup>72</sup> P. Kekicheff, H.K. Christenson and B.W. Ninham, *Colloids Surf.* **1989**, *40*, 31-41.
- <sup>73</sup> R.M. Pashley and B.W. Ninham, *J. Phys. Chem.* **1987**, *91*, 2902-2905.
- <sup>74</sup> P. Richetti and P. Kekicheff, *Phys. Rev. Lett.* **1992**, *68*, 1951-1954.
- <sup>75</sup> C.A. Helm, J.N. Israelachvili and P.M. McGuiggan, *Science* **1989**, *246*, 919-922.
- <sup>76</sup> S.J. Miklavic, D.Y.C. Chan, L.R. White and T.W. Healy, *J. Phys. Chem.* **1994**, *98*, 9022-9032.

## Chapter 2

# Interfacial Effects of Dilute Solutions and Lyotropic Liquid Crystalline Phases of Nonionic Surfactants

Gerhard H. Findenegg, Christian Braun, Peter Lang, and Roland Steitz

Iwan-N.-Stranski-Institut für Physikalische und Theoretische Chemie,  
Technische Universität Berlin, 10623 Berlin, Germany

### 1. Introduction

Interfaces represent regions in which the symmetry of the intermolecular force field is severely perturbed. The reduced spatial dimensionality imposed by a flat surface represents the simplest case of confinement of a system. Minimization of the surface free energy may cause a spontaneous reconstruction of the structure in the outermost layers of a crystal. Confinement has also a strong influence on the relative stability of different phases of a substance, and gives rise to a wealth of surface effects on phase transitions[1,2]. If the surface particles are less tightly bound than those in the interior of a crystal, one may expect that melting will start at the surface and propagate into the interior of the crystal. Such a behavior is called *surface melting* and has been observed for various metals and molecular crystals including ice[1]. The opposite effect, i.e. when an ordered surface layer coexists with a bulk liquid at temperatures above the melting point of the bulk phase, is called *surface freezing* and has been observed so far for mesogenic substances forming thermotropic liquid crystals[3] and for long-chain n-alkanes and alkanols[4]. It has been conjectured that surface freezing can occur only for molecules having an elongated (rod-like) shape, for which the surface can induce an alignment of their long axis parallel to each other, which in turn causes a tight binding of the molecules in such an ordered surface layer. Recently, evidence of such surface-induced shifts of first-order phase transitions has also been obtained for lyotropic systems of amphiphilic compounds[5]. In these systems the building units of ordered structures are not individual molecules but supramolecular (micellar) aggregates of molecules, which may be of spherical, rod-like or disk-like shape.

In this article we review recent studies of surface effects of dilute aqueous solutions and lyotropic liquid crystalline phases formed by amphiphilic chain molecules. Compounds of the oligo-oxyethylene mono-n-alkyl ether family, abbreviated as  $C_mE_n$ , are commonly used as model amphiphiles in physicochemical studies, since their properties can be tuned by varying the chain lengths of the hydrophobic alkyl chain ( $C_m$ ) and the hydrophilic oligo-oxyethylene chain ( $E_n$ ). Like other surfactants,  $C_mE_n$  amphiphiles assemble to loosely packed adsorbed monolayers at the air/water interface and they aggregate to micelles, bilayer membranes or vesicles



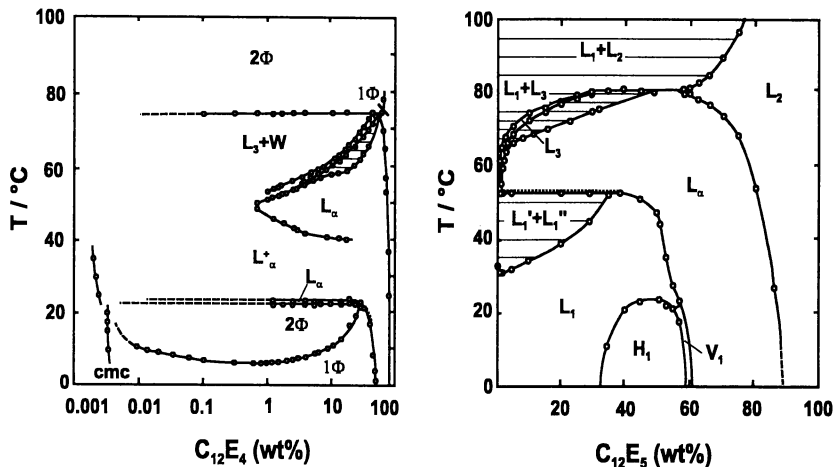


Figure 1. Phase diagram of the system  $C_{12}E_4$  + water (left)[6] and  $C_{12}E_5$  + water. (right)[7]. Note that in the diagram of the  $C_{12}E_4$  system the composition (wt-percent surfactant) is plotted on a logarithmic scale. The meaning of the symbols is explained in the text. The phase diagrams were redrawn with permission from reference 6 and 7.

in the aqueous solution, strongly dependent on their concentration in the aqueous phase. Regular packings of spherical or cylindrical micelles and bilayer membranes then form lyotropic liquid crystalline phases of cubic ( $V_1$ ), hexagonal ( $H_1$ ) and lamellar ( $L_\alpha$ ) structure for surfactants with alkyl chain length  $m \geq 10$ . Figure 1 shows the phase diagrams for  $C_{12}E_4$  and  $C_{12}E_5$ , two typical representatives of this family[6,7]. For the former system the composition is plotted on a logarithmic scale to show details of the diagram at low amphiphile concentration, viz. the temperature dependence of the critical micelle concentration (cmc) and the lower boundary of the liquid-liquid coexistence region. Note that the lyotropic phases generally extend over a rather wide range of surfactant concentrations due to the fact that different amounts of water can be incorporated between the micellar aggregates[8].

This article is organized as follows: In Section 2 we discuss aspects of the adsorption of surfactants from dilute aqueous solutions onto hydrophilic solid surfaces, with an emphasis on surface aggregation phenomena below the cmc. We shall see that this surface aggregation is closely related to micelle formation in the bulk solution and may be considered as a surface-induced pre-transition below the bulk cmc. In Sections 3 and 4 recent results on surface ordering of lyotropic phases at a solid/fluid interface, and at the free surface of the lyotropic phase, will be outlined. Surface-sensitive methods like neutron reflectometry and X-ray reflection Bragg diffraction have been employed in these studies to obtain structural information about the interfacial region of these lyotropic systems.

## 2. Surface aggregation of amphiphiles from dilute solutions

Adsorption of nonionic surfactants from aqueous solutions onto well-defined solid surfaces commonly occurs in two distinct steps. The first step involves the

displacement of water molecules which had been in contact with the surface by the amphiphilic molecules; accordingly, this step depends on the relative strength of interaction of the amphiphile and water molecules with the solid substrate. Hydrophilic surfaces (silica or metal oxides) with surface hydroxyl groups or other polar sites are strongly hydrated, just as the hydrophilic heads of the surfactant molecules, and thus the adsorption affinity of the surfactant molecules is weak in this initial region (low-affinity regime)[9]. On a hydrophobic surface, on the other hand, strong adsorption of the hydrophobic tails of the surfactant molecules will occur even from highly dilute solutions, until the entire surface is covered by a surfactant monolayer (high-affinity adsorption)[10,11]. In either case, the molecules adsorbed in the first step can act as a *template* for a subsequent surface aggregation process of the surfactant[12]. Below we shall consider the surface aggregation on hydrophilic surfaces in more detail. Figure 2 (a and b) shows an isotherm of the adsorbed amount per unit surface area ( $\Gamma_1$ ) and the respective integral enthalpy of adsorption ( $\Delta_{21}H$ ) of the short-chain surfactant  $C_8E_4$  from aqueous solutions onto a hydrophilic silica surface. The solid substrate used in this study[9] is a mesoporous silica glass with mean pore size of ca. 24 nm. Since the pore diameter is significantly greater than the length of a fully extended surfactant molecule (ca. 2 nm), it is believed that the adsorption behavior is similar to that on a flat surface, i.e. confinement effects caused by the limited pore space will have no pronounced influence on the adsorption isotherm in this case. The initial low-affinity region of the isotherm exhibits a weakly convex shape and reaches a value of no more than  $0.06 \mu\text{mol m}^{-2}$  (corresponding to a mean area of ca.  $28 \text{ nm}^2$  per adsorbed molecule) at a concentration corresponding to ca. 60 percent of the cmc. However, as the surfactant concentration is increased further, the adsorbed amount increases steeply until one reaches the cmc at which  $\Gamma_1$  levels off to a plateau value of  $6 \mu\text{mol m}^{-2}$  ( $0.28 \text{ nm}^2$  per molecule) at the given temperature. The sharp increase in  $\Gamma_1$  is attributed to a surface aggregation process in which the few physically anchored surfactant molecules are believed to play a decisive role as nucleation sites for surface micelles. The concentration at which this process commences is called *critical surface aggregation concentration* (csac). Above the cmc the chemical potential of the surfactant remains nearly constant and thus no further adsorption occurs.

The *shape* of the adsorption isotherm ( $\Gamma_1$  vs.  $c_1$ ) exhibited in Figure 2a is fairly general for nonionic surfactants on hydrophilic surfaces, and it can be characterized by four parameters, viz., the csac and cmc, and the extent of adsorption at the csac and at the plateau of the isotherm. On the other hand, this plateau value of the isotherm appears to depend strongly on the nature of the surfactant and on temperature, which implies that the size and/or shape of the surface aggregates is variable.

For  $C_8E_4$ , the amount adsorbed at this plateau corresponds to an apparent cross-sectional area per molecule of  $0.28 \text{ nm}^2$  in a hypothetical monolayer arrangement (which is not plausible), or an area of  $0.56 \text{ nm}^2$  per molecule if a bilayer is formed. In such a bilayer arrangement one anticipates that the oxyethylene chains in the first layer are attached to the surface while those of the molecules in the second layer will face the aqueous phase. On the assumption that the tetraethylene glycol block ( $E_4$ ) occupies an area of ca.  $0.36 \text{ nm}^2$ , the present results for the isotherm of  $C_8E_4$  suggest that the adsorbed layer represents a fragmented (patchy) bilayer which covers ca. 60 percent of the surface at the given temperature ( $25^\circ\text{C}$ ). This finding illustrates that the pronounced plateau of the adsorption isotherms does not imply surface saturation but

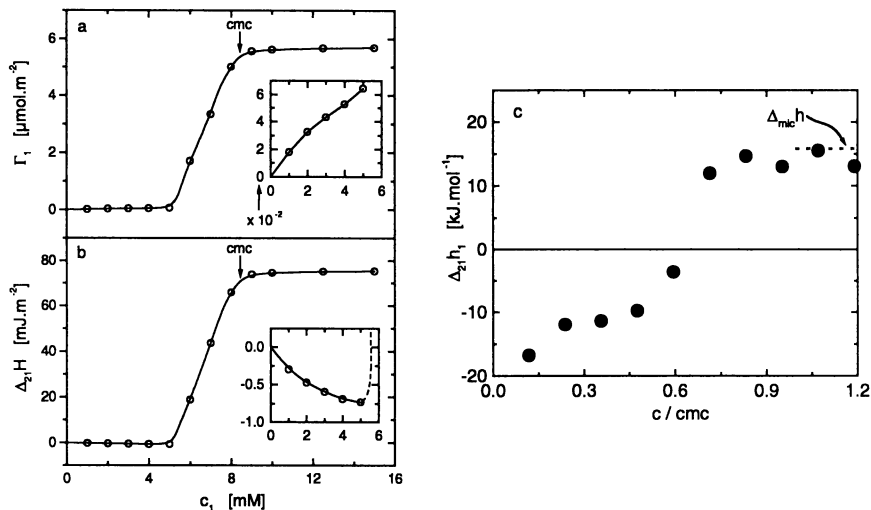


Figure 2. Adsorption of  $\text{C}_8\text{E}_4$  from aqueous solution on CPG (24 nm) porous silica glass at  $25^\circ\text{C}$ : (a and b) Adsorbed amount  $\Gamma_1$  and integral enthalpy of adsorption  $\Delta_{21}H$  vs. bulk concentration  $c_1$ . (c) Differential molar enthalpy of adsorption  $\Delta_{21}h$  vs. relative concentration  $c/\text{cmc}$ ; the dotted line indicates the molar enthalpy of micellization  $\Delta_{\text{mic}}h$  at  $25^\circ\text{C}$  (reproduced from ref. 9).

is due to the fact that the chemical potential of the surfactant remains nearly constant after reaching the cmc.

More information about the nature of the surface aggregation process can be obtained from the enthalpy of adsorption. The isotherm of  $\Delta_{21}H$  vs.  $c_1$  for  $\text{C}_8\text{E}_4$  on the hydrophilic silica glass is slightly exothermic in the low-affinity region up to the csac, but strongly endothermic in the surface aggregation regime above the csac. Figure 2c shows the differential molar enthalpies of adsorption from solution,  $\Delta_{21}h = d(\Delta_{21}H)/d\Gamma_1$  as a function of the reduced bulk concentration  $c/\text{cmc}$ . In the low-affinity region (isolated anchor molecules)  $\Delta_{21}h$  is exothermic, with an initial value of ca. -15 kJ/mol, indicating that the adsorption of the anchor molecules from aqueous solution onto the (hydrated) surface hydroxyl groups is energetically favorable. The differential enthalpy of surface aggregation above the csac is endothermic and the value of  $\Delta_{21}h$  is in close agreement with the molar enthalpy of micelle formation in the bulk solution ( $\Delta_{\text{mic}}h$ ). These findings support the conjecture that the process of surface aggregation and micelle formation in the bulk are similar phenomena.

A remarkable feature of the surface aggregation of  $\text{C}_m\text{E}_n$  amphiphiles is the pronounced inverse temperature dependence of the adsorbed amount  $\Gamma_1$  in the plateau region of the isotherms. As an example Figure 3 shows the adsorption isotherms for  $\text{C}_8\text{E}_4$  on CPG (17 nm) silica glass in the temperature range from 5 to  $45^\circ\text{C}$ . A positive temperature derivative  $d\Gamma_1/dT > 0$  is consistent with the positive (endothermic) enthalpy of adsorption in the aggregative adsorption regime at  $c > \text{csac}$ , which in turn correlates with the endothermic enthalpy of micellization  $\Delta_{\text{mic}}h > 0$  and the negative temperature dependence of the cmc (see Fig. 1a). An inverse (positive) temperature dependence of

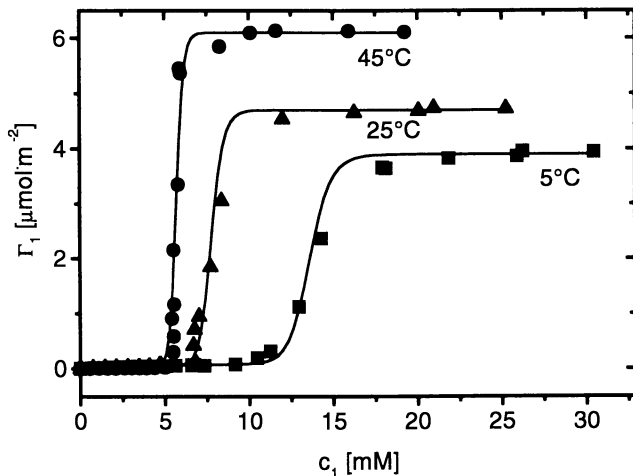


Figure 3. Adsorption isotherms of  $C_8E_4$  on CPG (17 nm) silica glass at three temperatures. The curves represent a fit by the Gu[13] model (Reproduced with permission from reference 27. Copyright 1999 O. Dietsch.)

$\Gamma_1$  is also observed in the aggregative adsorption regime of  $C_mE_n$  amphiphiles on hydrophobic surfaces[9]. It is attributed to a dehydration of the hydrophilic head groups, which renders the amphiphiles to become less hydrophilic as the temperature is increased. This dehydration effect is also causing the phase separation of the  $L_1$  phase at elevated temperatures (see Fig. 1).

Finally, we note that the critical surface aggregation concentration is strongly correlated with the cmc of the surfactant[9]. In this sense we may consider surface aggregation as a surface-induced pre-micellization process which, like other pre-transitional phenomena at interfaces, exhibits some universal features. Several details of the surface aggregation of surfactants at hydrophilic surfaces are not yet understood (e.g., the nature of the binding of the anchor molecules, or the factors dominating the size and shape of the surface aggregates at the onset of bulk micellization). It will also be of interest to study the universal aspects of surface aggregation in greater depth.

### 3. Lyotropic phases against solid surfaces. - Neutron reflectivity studies

**3.1. Technique of neutron reflectivity.** In recent years neutron reflectivity has proved to be a powerful tool for the investigation of solid/liquid interfaces with respect to structure and composition of adsorbed material at the interface[14-17]. The technique probes the variation in scattering length density  $Nb$  (i. e. the product of the number density  $N$  of the material and its neutron scattering length  $b$ ) as a function of depth  $z$ , with excellent spatial resolution down to the sub-nanometer scale and penetration depths of hundreds of nanometers. In addition, neutron reflectometry is a non-destructive method and thus, repetitive measurements on one specimen can be performed. The experimental setup of a typical neutron reflectivity experiment at the solid/liquid interface is depicted in Figure 4. The liquid sandwiched between a PTFE trough and the silicon substrate. Monochromatic neutrons pass through the

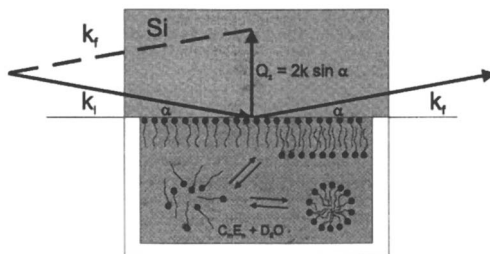


Figure 4. Sketch of the scattering geometry in a neutron reflectivity experiment at the solid/liquid interface. The scattering vector  $\mathbf{Q}_z$ , defined by the difference of the wave vectors of the incident and the scattered beam,  $\mathbf{Q}_z = \mathbf{k}_f - \mathbf{k}_i$ , is perpendicular to the interface.

silicon block and are reflected off the silicon/liquid interface and are subsequently counted with a position sensitive detector (PSD,  $^3\text{He}$ ) as a function of the angles of incidence and exit,  $\alpha_i$  and  $\alpha_f$ . The reflected intensity,  $I(\alpha_f)$ , normalized to incident intensity,  $I_0$ , for specular condition  $\alpha_i = \alpha_f$  may then be rewritten as the reflectivity  $R(Q_z)$  as a function of the wave vector difference  $Q_z = 2k \cdot \sin \alpha$  of the scattered and incident beam with wave vector modulus  $k_i = k_f = k = 2\pi/\lambda$ . Experimentally specular conditions are achieved, by tilting the sample cell by  $\alpha$  and setting the detector angle to  $2\alpha$  with respect to the direction of the incident beam. Since the direction of the scattering vector  $\mathbf{Q}_z$  is perpendicular to the interface,  $R(Q_z)$  is related to the density gradient across the interface by [18,19]

$$R(Q_z) = R_F(Q_z) \cdot \left| \frac{1}{Nb_\infty} \int \frac{dNb(z)}{dz} \exp(iQ_z z) dz \right|^2 \quad (1)$$

where  $R_F(Q_z)$  refers to the Fresnel reflectivity [19] of the interface and  $Nb_\infty$  denotes the scattering length density of the bulk material. Due to the phase problem involved in the inverse Fourier transformation there is no unique solution to the determination of the density profiles  $Nb(z)$  from reflectivity measurements. The most common way of data analysis is the comparison between the measured spectrum and simulated reflectivity spectra from model profiles which in turn may then be optimized by fitting routines. An alternative approach is the model-free analysis of reflectivity data with the so-called simulated annealing technique [20].

**3.2. Surface effects accompanying the  $L_\alpha$ -to- $L_\alpha^+$  transition.** The interface of a solution of the amphiphile  $\text{C}_{12}\text{E}_4$  in  $\text{D}_2\text{O}$  at a weight fraction of the surfactant  $w_s=0.29$  against a silicon wafer with a hydrophobic coating has been studied in a temperature range from 20 to 44 °C by neutron reflectometry. In this temperature range a sample with the given composition is expected to transform from the micellar phase  $L_1$  to three lamellar states (see Figure 1a) in which water layers are separated by double layers of the surfactant. In our experiments  $\text{D}_2\text{O}$  was used instead of  $\text{H}_2\text{O}$  to enhance neutron contrast between the surfactant and the solvent.

Figure 5 shows a typical set of specular neutron reflectivity spectra of the boundary layer of a 29 wt-% solution of  $\text{C}_{12}\text{E}_4$  in  $\text{D}_2\text{O}$  against the silicon wafer with

hydrophobic coating, as a function of sample temperature, starting in the isotropic micellar phase  $L_1$  at 20.5 °C. The corresponding reflectivity curve exhibits a broad shoulder with a saddle point. This shoulder is mainly due to small angle scattering of the micellar aggregates in the bulk which is superimposed on the reflectivity spectrum of the solid/liquid interface[21]. On increasing the temperature by 0.3 K a Bragg peak develops in the scattering curve. This Bragg peak originates from well ordered lamellae of surfactant bilayers and hence is evidence of the phase transition of the sample from the isotropic micellar phase,  $L_1$ , into the lamellar state,  $L_\alpha$ . Further heating induces additional changes in the ordered state of the complex fluid. In the temperature range from 20.9 °C to 22.4 °C the Bragg peak position is not stable but shifts to smaller scattering vectors with temperature and time. This shift corresponds to an increase of the repeat distance  $d$  of the lamellae from 74 Å to 90 Å. Above 22.4 °C and up to 44.2 °C the  $d$ -spacing is almost temperature independent. However, in this temperature region the sample still undergoes changes in its molecular organization. This is evident from the pronounced increase of the width of the Bragg peak, the loss of the second order peak and also the increase of reflected intensity in the low  $Q$  region just above the total external reflection edge (see Fig. 5).

From the detailed investigation of the temperature and time dependence of the neutron reflectivity experiments three different stable states of the complex fluid have been identified:  $L_1$  for  $T < 19.4$  °C,  $L_\alpha$  for  $20.6$  °C  $< T < 20.9$  °C and a state termed  $L_\alpha^+$  by Strey[6,22] for  $T > 22.4$  °C, and transition zones between these stable states[23] (Note that transition temperatures are about 2 K lower than indicated in Figure 1a, due to the substitution of  $H_2O$  by  $D_2O$ ). The structure of the  $L_\alpha^+$  state has not been finally clarified. It was claimed that it represents a lamellar structure destroyed by stirring[6] which cannot reform due to an energy barrier. However, our data show that the  $L_\alpha^+$  state occurs as well with samples at rest. Furthermore, we did not observe the reformation of the  $L_\alpha$  phase at high temperatures, in contradiction to the phase diagram in Figure 1a.

In the  $L_\alpha$  state the correlation length of adjacent lamellae - estimated from the full width at half maximum (fwhm) of the corresponding Bragg peak - is of the order of 30 lattice constants. This situation changes on the transition into the  $L_\alpha^+$  state: here, the correlation length of adjacent lamellae reduces to 5 lattice planes at 44 °C. The structural difference between the  $L_\alpha$  and the  $L_\alpha^+$  state becomes most evident from so called transverse rocking scans which are displayed for both states in Figure 6. During such a scan the detector is fixed to the angle at which the Bragg-peak has its maximum,  $2\alpha_{\text{Bragg}}$ , and the sample is rocked by the angle  $\delta$  in a way that  $\delta=0$  corresponds to  $\alpha=\alpha_{\text{Bragg}}$ , for the angle between the interface and the incident beam. For a perfect layer structure with all layers oriented parallelly to the interface a sharp reflex at  $\delta=0$  is expected. In the opposite limit, when the layers are oriented at random with respect to the surface, a constant background with a small peak originating from the specularly reflected beam should be observed. Accordingly, we interpret the rocking curve from the  $L_\alpha$  phase as being generated by a highly ordered lamellar structure with a strong coupling of the bilayers to the solid/liquid interface. On the other hand, the data from the  $L_\alpha^+$  state indicate a broad orientational distribution of the surfactant bilayers possibly originating from a multilayered vesicular type structure without strong coupling to the interface. Thus it is evident that the coupling of lyotropic phases to a solid substrate depends in a delicate way on the organization of the phase on a mesoscopic scale.

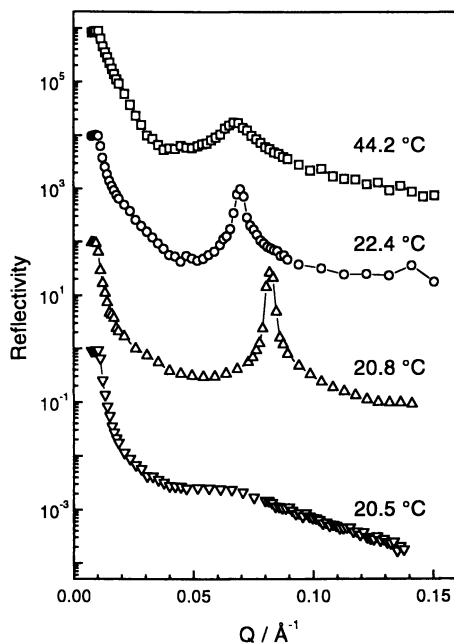


Figure 5. Specular neutron reflectivity from the interface of a solution of  $C_{12}E_4$  in  $D_2O$  (29 wt-% surfactant) against a silicon wafer with hydrophobic coating as a function of sample temperature. The individual spectra are displaced relative to each other by factors of  $10^2$ ,  $10^4$  and  $10^6$ , respectively, from bottom to top. (Reproduced with permission from reference 23.)

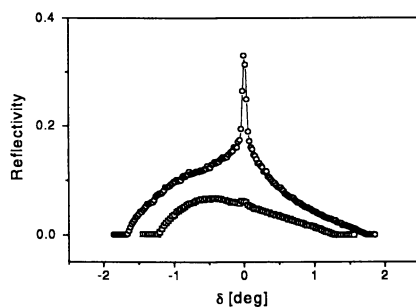


Figure 6. Transverse rocking scans of the two lamellar states of  $C_{12}E_4$  in  $D_2O$  against a silicon substrate with hydrophobic coating at fixed  $2\alpha$  position around the Bragg peak positions:  $L_\alpha$  phase ( $\alpha_{Bragg} = 1.86^\circ$ , i.e.  $0.088 \text{ \AA}^{-1}$  at  $20.6^\circ\text{C}$ , open circles) and the  $L_\alpha^+$  phase ( $\alpha_{Bragg} = 1.46^\circ$ , i.e.  $0.069 \text{ \AA}^{-1}$  at  $25.3^\circ\text{C}$ , open squares);  $\delta = \alpha - \alpha_{Bragg}$ . (Reproduced with permission from reference 23)

**3.3 Surface effects accompanying the  $L_1$ -to- $H_1$  transition.** As a further example for investigating interfacial effects of phase transitions in lyotropic surfactant systems we have studied the isotropic-to-hexagonal ( $L_1 \rightarrow H_1$ ) transition in the system  $C_{12}E_5 + D_2O$ .

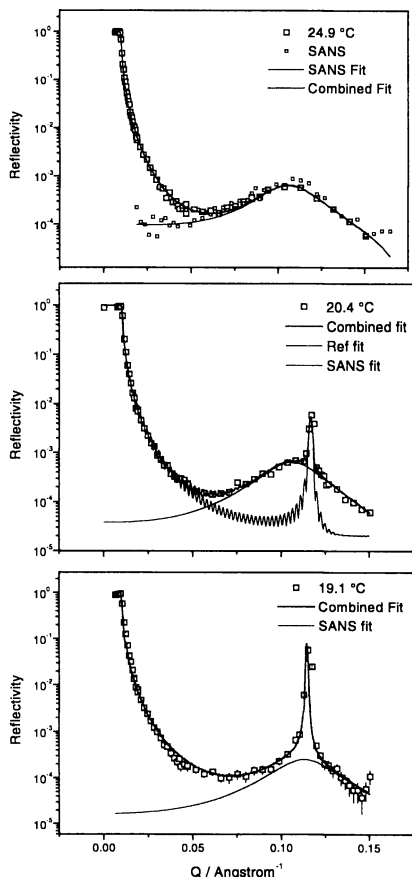


Figure 7. Neutron reflectivity of the boundary layer of a solution of 39 wt-%  $C_{12}E_5$  in  $D_2O$  against a silicon wafer with hydrophobic coating:  $L_1$  phase at 24.9 °C (top);  $H_1$  phase at the  $L_1 \rightarrow H_1$  phase transition temperature at 20.4 °C (middle); and at 19.1 °C, i.e. - 1.3K below the phase transition (bottom). In the graph of the  $L_1$  phase the measured SANS contribution for a fixed angle of incidence of  $1^\circ$  is also shown, together with the best fit of a Lorentzian on a linear background to these SANS data. In the graphs of the  $H_1$  phase simulated Lorentzian profiles are also shown (SANS fit) which account for the SANS

contribution in the  $H_1$  phase necessary to fit the measured reflectivity spectrum. The combined fit to the reflectivity spectrum at 24.9 °C is the incoherent superposition of the best fit to the SANS data and the simulated reflectivity of a single surfactant depleted liquid layer ( $Nb_{depl} = 4.03 \cdot 10^{-6} \text{ \AA}^{-2}$ ,  $d_{depl} = 2000 \text{ \AA}$  with a rms-roughness at the liquid site of 125 Å) between the silicon substrate and the bulk fluid ( $Nb_{bulk} = 3.76 \cdot 10^{-6} \text{ \AA}^{-2}$ ). The combined fit to the reflectivity spectrum at 20.4 °C is the incoherent superposition of the best fit to the SANS data and the best simulated reflectivity (Ref fit) of a multilayer model (50 repeating units) of surfactant depleted ( $Nb_{depl} = 4.55 \cdot 10^{-6} \text{ \AA}^{-2}$ ,  $d_{depl} = 30 \text{ \AA}$ ) and surfactant enriched slabs ( $Nb_{enr} = 3.59 \cdot 10^{-6} \text{ \AA}^{-2}$ ,  $d_{enr} = 24 \text{ \AA}$ ). The slabs are oriented parallel to the solid surface and simulate the density variation in  $z$  of the hexagonal arrangement of the cylindrical aggregates. The combined fit to the data at 19.1 °C is the superposition of the Ref fit (not shown) based on a multilayer model (99 repeating units) of surfactant depleted ( $Nb_{depl} = 4.97 \cdot 10^{-6} \text{ \AA}^{-2}$ ,  $d_{depl} = 31 \text{ \AA}$ ) and surfactant enriched slabs ( $Nb_{enr} = 2.87 \cdot 10^{-6} \text{ \AA}^{-2}$ ,  $d_{enr} = 24 \text{ \AA}$ ) parallel to the solid surface and the SANS fit. Note that the SANS contribution decreases markedly in the  $H_1$  phase with increasing distance from the transition temperature. Note also that the difference in scattering length density between surfactant depleted and surfactant enriched slabs in the  $H_1$  phase increases with increasing distance from the phase transition temperature.



This transition was again studied by neutron reflectivity at the interface of a silicon wafer with hydrophobic coating. For a mixture of 40 wt-%  $C_{12}E_5$  in  $D_2O$  (cf. Fig. 1b) reflectivity curves recorded at different temperatures are presented in Figure 7. The isotropic micellar solution  $L_1$  transforms spontaneously to the  $H_1$  ordered state at 20.4 °C upon cooling as indicated by the appearance of the 01 Bragg peak at that temperature in the reflectivity spectrum of the silicon/liquid interface. Again this phase transition temperature is about 3K lower than in the phase diagram of Figure 1b, due to the isotope effect of substituting  $H_2O$  by  $D_2O$ . In contrast to the ordering transition  $L_1$ -to- $L_\alpha$  of the system  $C_{12}E_4 + D_2O$ , there is no variation of the d-spacing of the ordered state with temperature down to the lowest experimental temperature of 19.1 °C. From the 01 Bragg peak the d-spacing of the cylindrical surfactant aggregates is found to be 53.4 Å, in good agreement with the value found for the  $H_1$  phase of 39 wt-%  $C_{12}E_5$  in  $H_2O$  at the air/water interface by X-ray reflectivity[5].

The broad shoulder in the reflectivity spectrum of the solid/liquid interface in the isotropic state of the fluid at 24.9 °C (Figure 7) is due to small angle scattering from micelles in the bulk, as can be seen from the superimposed normalized SANS spectrum obtained from the sample at a fixed angle of incidence of 1° by moving solely the detector. The SANS contribution matches the reflectivity spectrum for  $Q > 0.06 \text{ \AA}^{-1}$  and the SANS spectrum is of Lorentzian shape with a center position of the small angle scattering peak at  $0.106 \text{ \AA}^{-1}$  corresponding to a correlation length of 59 Å in the isotropic bulk state of the fluid. The SANS contribution decreases markedly on entering the  $H_1$  phase, while the intensity of the 01 Bragg peak increases with increasing distance from the transition temperature  $T_{L_1 \rightarrow H_1}$  (see Figure 7). The simulations also shown in Figure 7 suggest that this increase in the Bragg scattered intensity is mainly due to the evolution of neutron contrast between surfactant depleted and surfactant enriched zones on the supramolecular self-assembly of cylindrical aggregates in the  $H_1$  phase (see figure caption 7 for details).

The  $H_1$  phase of the complex fluid is macroscopically aligned with respect to the silicon/liquid interface with its (01) lattice planes parallel to the surface of the substrate. This is evident from the transverse rocking scan of the sample performed at the Bragg peak position (see Figure. 8). From the peak width (fwhm) of the rocking peak the maximum inclination of the (01) lattice planes with respect to the substrate surface was estimated to 0.15°.

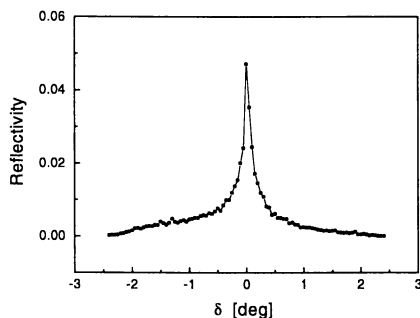


Figure 8. Transverse rocking scan of the  $H_1$  phase of  $C_{12}E_0 + D_2O$  against a Si-wafer with hydrophobic coating at fixed  $2\alpha$  position around the 01 Bragg peak position ( $\alpha_{\text{Bragg}} = 2.47^\circ$ , i.e.  $0.116 \text{ \AA}^{-1}$  at  $19.7^\circ\text{C}$ );  $\delta = \alpha - \alpha_{\text{Bragg}}$ .

#### 4. Lyotropic phases against the free interface

**4.1. X-ray total-external-reflection diffraction (XTERD).** As discussed in the preceding section, a liquid/solid interface may influence the structure of a complex fluid on a mesoscopic scale. In this section we will describe structural and thermodynamic effects of the free surface of liquid crystalline phases. Specifically we shall deal with the hexagonal  $H_1$ -phase of  $C_{12}E_5$  in water. An adequate tool for the investigation of surface-related effects is the x-ray total-external-reflection-Bragg diffraction technique developed by Marra and Eisenberger[24] (abbreviated XTERD).

In a conventional small angle x-ray scattering (SAXS) experiment, the diffraction pattern is observed in transmission, whereas in an XTERD experiment the angular distribution of the scattered intensity is recorded in reflection geometry. A schematic set-up for this kind of experiment is sketched in Figure 9. Like in the specular reflectivity experiments discussed above, the scattering vector is given by the wave vector difference of scattered and incident beam. However, in an XTERD-experiment the scattering vector is no longer perpendicular to the interface but there are also components in the surface ( $xy$ ) plane. According to Figure 9 the modulus of the scattering vector in this plane is  $Q_{xy} = 4\pi \sin \theta / \lambda$ , where  $\theta$  is half the angle between the projections onto the surface plane of the incident and the diffracted beam.

XTERD-experiments are superior to transmission scattering experiments in the respect that they allow to distinguish between structural information from the sample surface region and from the bulk simply by variation of the angle of incidence. If  $\alpha_i$  is smaller than  $\alpha_c$ , the critical angle of total external reflection, the refracted beam degenerates to an evanescent wave which propagates parallel to the surface with an amplitude decaying exponentially in the  $z$ -direction. Thus, x-rays penetrate the sample only to a limited depth  $\Lambda_0$  which is approximately 5 nm for aqueous systems[25]. In the opposite limit ( $\alpha_i \gg \alpha_c$ ) the effective penetration depth extends to a macroscopic scale. Consequently, as one varies  $\alpha_i$ , structural properties of the bulk and the surface region will contribute with different weights to the reflected diffraction pattern.

**4.2. Binding of the hexagonal phase to the surface and surface relaxation** As displayed in Figure 1b the stability region of the hexagonal phase of  $C_{12}E_5$  in water spans a composition range of  $0.27 < w_s < 0.58$  at  $0^\circ\text{C}$ , where  $w_s$  represents the weight fraction of the surfactant. The congruent melting point of this phase is found at about  $24^\circ\text{C}$  and at a surfactant content of about 45 weight percent[7].

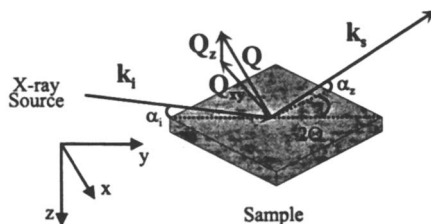


Figure 9: Sketch of the scattering geometry in an XTERD-experiment. The primary beam forward direction is denoted the  $y$ -direction while the  $z$ -direction is defined perpendicular to the surface. The scattering vector is defined as  $\mathbf{Q} = \mathbf{k}_s - \mathbf{k}_i$

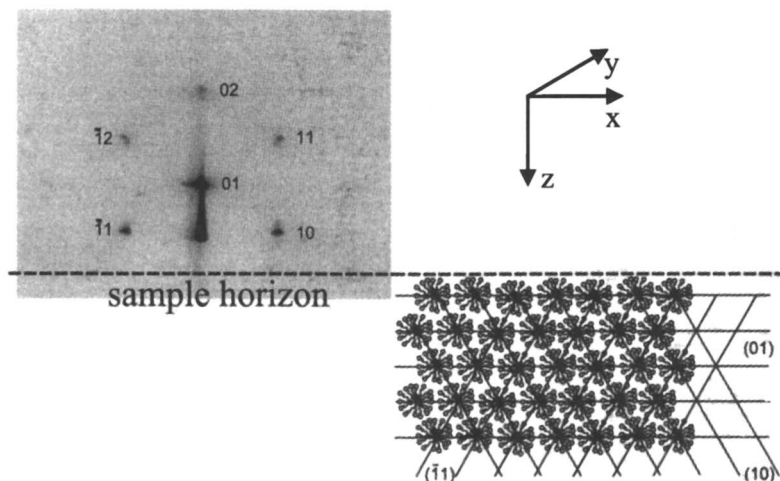


Figure 10: Image plate of the diffraction pattern from the  $H_1$ -phase of  $C_{12}E_5$  in water at  $w_s=0.39$  observed in reflection geometry with  $\alpha_i = 0.8\alpha_c$ . On the right the hexagonal arrangement of cylindrical aggregates is sketched, where the long axes are disposed parallel in the  $y$ -direction (adapted from reference 26).

It is common understanding that this phase consists of cylindrical micelles which are regularly packed in a two-dimensional array without any periodicity in the direction of the cylinder long axis. Two-dimensional diffraction patterns obtained from the  $H_1$  phase in a transmission SAXS experiment consist of Debye-Scherrer rings which is typical for powder samples. On the other hand, the two-dimensional diffraction patterns observed in reflection geometry look completely different[26]. Figure 10 shows an image plate pattern obtained from a sample with  $w_s=0.39$ ; this pattern consists of a distinct set of hexagonally arranged Bragg-peaks.

Hexagonal diffraction patterns are generated by a regular hexagonal arrangement of scatterers as sketched on the right of Figure 10. Threadlike surfactant aggregates oriented with their long axes parallel to the surface form hexagonally packed bundles in the plane perpendicular to the sample horizon. If the (01) set of nearest-neighbor lattice planes is aligned parallel to the liquid/air interface, the corresponding 01 and 02 Bragg spots are located in the beam-forward direction as a function of momentum transfer  $Q_z$  only. Any inclination of the lattice planes, i.e. any rotation of the hexagonal arrays around the  $y$ -axis would rotate the corresponding diffraction pattern by the same angle. In the limiting case that all orientations of the lattice planes were equally distributed, diffraction rings would occur. Consequently, a diffraction pattern consisting of discrete spots proves that the (01) planes are indeed parallel to the surface and no other orientation of the hexagonal arrays with respect to the liquid/air interface is realized. Similar two dimensional diffraction patterns are observed at angles of incidence larger than  $\alpha_c$ , i.e. up to  $\alpha_i = 3\alpha_c$  which shows that the close binding of the lattice planes to the liquid/air interface persists several micrometers into the sample bulk.

Closer inspection of the diffraction pattern displayed in Figure 10 reveals that the Bragg spots consist of doublets of peaks, one of which disappears if the angle of

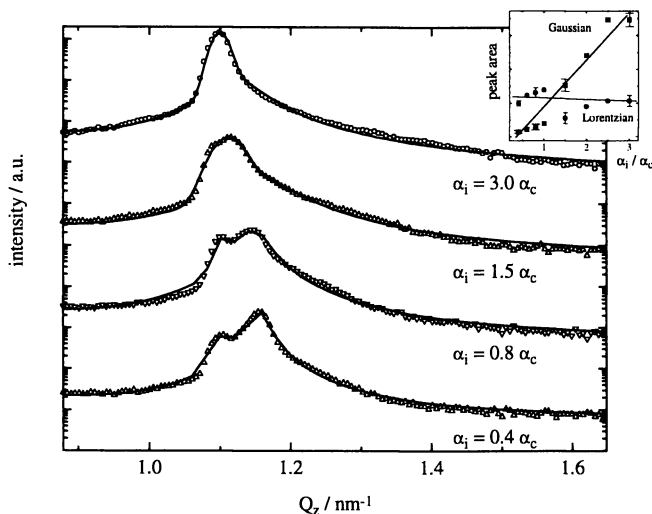


Figure 11: PSD-spectra of the (01) peak from the  $H_1$  phase of  $C_{12}E_5$  in water at  $w_s=0.39$  observed in reflection geometry as a function of the angle of incidence. Symbols are experimental data and the full lines are fits to the data by the sum of a Gaussian and a Lorentzian on an exponentially decaying background. The inset shows the peak-areas of the respective functions in dependence on  $\alpha_i$ .

incidence is increased, while the detector is kept at a fixed position. This remarkable effect was investigated quantitatively by observing the 01 spot for various  $\alpha_i$  with a position-sensitive detector (PSD). This experiment probes variations of the electron density along the direction perpendicular to the surface only, since the scattering vector is almost parallel to the  $z$ -direction. The observed doublet patterns remain unchanged when moving the sample in the  $xy$ -plane or rotating the sample around its  $z$ -axis at a fixed angle of incidence. However, as to be seen from Figure 11, with increasing  $\alpha_i$  the Bragg spot at smaller  $Q_z$  of each doublet becomes more and more prominent until at  $\alpha_i = 3\alpha_c$  only one asymmetric peak is observed. Accordingly the Bragg spots at larger  $Q_z$  have to be ascribed to a structure which is not present in the bulk sample, since at large angles of incidence mainly bulk properties are probed.

The PSD-spectra displayed in Figure 11 can be fitted by a sum of a Gaussian and a Lorentzian superimposed on an exponentially decaying background. As to be seen from the inset in Figure 11, the relative intensities of the peaks change drastically with increasing  $\alpha_i$  i.e. with increasing penetration depth of the  $x$ -ray beam. As long as the angle of incidence is smaller than  $\alpha_c$  the Gaussian peak has about half the intensity of the Lorentzian peak, while at  $\alpha_i = 3\alpha_c$  the Gaussian is by a factor of three more intense than the Lorentzian.

The basic features of the real-space lattice may be deduced from the shape of the fit function, since the electron density distribution function in real space and the scattering curve are related by a Fourier transformation. As the Fourier transform of a Lorentzian is an exponential and the Fourier transform of a Gaussian is a Gaussian again, we are lead to conclude that there are two coexisting lattices, one with an

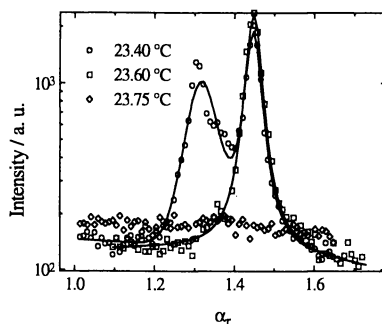


Figure 12: PSD-spectra of the (01) peak from the  $H_1$  phase of  $C_{12}E_5$  in water at  $w_S=0.39$  observed in reflection geometry at  $\alpha_i = 0.8\alpha_c$  for three different temperatures. Symbols are experimental data and the full lines are fits to data by the sum of a Gaussian and a Lorentzian.

exponentially decaying positional correlation, and the other with a Gaussian distribution of correlation lengths. The former is present only in a surface layer with finite thickness while the bulk sample consists of a three-dimensional powder with a Gaussian distribution of domain sizes. Corresponding to the different positions of the Bragg peaks, different  $d$ -spacings[26] for the bulk  $d_B=5.11$  nm and the surface lattice  $d_S=5.05$  are calculated by Bragg's equation  $d = 2\pi / Q$ . Since the Bragg-spacing is proportional to the square root of the area of the two-dimensional unit cell this difference in spacings corresponds to a packing density in the surface layer which is increased by about 2.5% as compared to the bulk. Simulations of the scattered intensity based on a box model of the electron density perpendicular to the surface show that the surface layer has to comprise at least 30 micellar layers with constant spacing, corresponding to a thickness of about 150 nm, to account for the occurrence of a peak doublet.

**4.3. Surface induced shift of the hexagonal to isotropic phase transition.** In addition to the structural changes in the boundary layer, the free surface also effects the transition temperature of the  $L1 \rightarrow H1$  phase transition[5]. This effect was investigated for a surfactant/water mixture with a surfactant content of 39 wt%. In Figure 12 PSD-spectra of the (01) Bragg spot are plotted for three different temperatures. The curves were recorded at a fixed scattering geometry with an angle of incidence  $\alpha_i = 0.8\alpha_c$  where both the bulk and the surface signal are visible in the diffraction pattern.

At a temperature 23.4°C two well-separated peaks are observed which again can be approximated by the sum of a Gaussian for the spot at smaller reflection angle and a Lorentzian (for the one at larger  $\alpha_r$ ). As discussed in the preceding section the left peak corresponds to the bulk lattice and the right peak to a lattice present only in a surface layer of about 100–200 nm thickness. As the temperature is raised by 0.2 K there remains only one peak at the position corresponding to the surface lattice. This shows that the scatterers in the sample bulk have lost their positional correlation, i. e. the bulk is already in the isotropic state, while the surface layer is still in the

hexagonally ordered state. Heating the sample again by 0.2 K causes melting of this surface layer. From these data it is evident that the free surface stabilizes the higher ordered H<sub>1</sub>-phase to higher temperatures, i. e. the hexagonal phase of C<sub>12</sub>E<sub>5</sub> in water shows surface crystallization

We thus conclude that the liquid/air interface exerts an influence on the hexagonal H<sub>1</sub>-phase of C<sub>12</sub>E<sub>5</sub> in water in a threefold way. (i) The lattice planes of the hexagonal unit cell are strongly aligned parallelly to the free surface, even down to a depth of several micrometers away from the surface. (ii) The surface causes a shrinkage of the unit cell by about 2.5 percent in a surface layer of a thickness of about 100-200 nm. (iii) The melting point of the hexagonal phase is shifted to slightly higher temperatures in the surface layer as compared to the bulk. Measurements of the phase transition temperature and the lattice spacing of the surface layer at various bulk compositions of the C<sub>12</sub>E<sub>5</sub>/water system may thus reveal a surface phase diagram which is different from the bulk diagram in the temperature/composition plane. Experiments are in progress to establish this phase diagram.

## 5. References

1. Dosch H. 'Critical Phenomena at Surfaces and Interfaces' Vol.126 of Springer Tracts in Modern Physics, Springer, Berlin, 1992.
2. Dietrich, S.; Findenegg, G.H.; Freyland, W.(Eds.) 'Phase Transitions at Interfaces, Ber. Bunsenges. Phys. Chem. **1994**, *98*, 297-527.
3. Ocko, B.M.; Braslau, A.; Pershan, P.S.; Als-Nielsen, J.; Deutsch, M. *Phys. Rev. Lett* **1986**, *57*, 94.
4. Ocko, B. M.; Wu, X. Z.; Sirota, E. B.; Sinha, S. K.; Gang, O.; Deutsch, M. *Phys. Rev. E* **1997**, *55*, 3164.; Deutsch, M.; Wu, X.Z.; Sirota, E.B.; Sinha, S.K.; Ocko, B.M.; Magnussen, O.M. *Europhys. Lett.* **1995**, *30*, 283.
5. Braun, C.; Lang, P.; Findenegg, G. H. *Langmuir* **1995**, *11* 764.
6. Strey, R. *Ber. Bunsenges. Phys. Chem.* **1996**, *100*, 182.
7. Strey, R.; Schomäcker, R.; Roux, D.; Nallet, F.; Olsson, U. *J. Chem. Soc. Faraday Trans. 1* **1990**, *86*, 2253.
8. Mitchell, D. J.; Tiddy, G. J. T.; Waring, L.; Bostock, T.; MacDonald, M. P. *J. Chem. Soc. Faraday Trans. 1* **1983**, *79*, 975.
9. Király, Z.; Börner, R. H. K.; Findenegg, G. H. *Langmuir* **1997**, *13*, 3308; see also the references given in this paper.
10. Findenegg, G. H.; Pasucha, B.; Strunk, H. *Colloids and Surfaces* **1989**, *37*, 223.
11. Király, Z.; Findenegg, G.H. *J. Phys. Chem.*, **1998**, *102*, 1203; see also the references given in this paper.
12. Manne, S.; Gaub, H.E. *Science*, **1995**, *270* 1480
13. Chu, B.Y.; Gu, T. *J. Chem. Soc. Faraday Trans.* **1991**, *87* 2745.
14. Lee, E.M.; Thomas, R.K.; Cummins, P.G.; Staples, E.J; Penfold, J.; Rennie, A.R., *Chem. Phys. Lett.* **1989**, *162*, 196.
15. McDermott, D. C.; Lu, J. R.; Lee, E. M.; Thomas, R. K.; Rennie, A. R., *Langmuir* **1992**, *8*, 1204.
16. Lee, D. D.; Chen, S. H.; Majkrazk, C. F.; Satjia, S. K. *Phys. Rev. E* **1995**, *52*, R29.

17. Fragneto, G; Lu, J. R.; McDermott, V; Thomas, R. K.; Rennie, A. R.; Gallagher, P. D.; Satjia, S. K. *Langmuir* **1996**, *12*, 477.
18. Als-Nielsen, J *Physica B+C* **1984**, *126* 145.
19. Russell, T.P. *Materials Science Reports* **1990**, *5*, 171.
20. Kunz, K.; Reiter, J.; Götzelmann, A.; Stamm, M. *Macromolecules* **1993**, *26*, 4316.
21. Braun, Chr.; Bowers, J.; Lang, P.; Steitz, R.; Findenegg, G.H. unpublished results.
22. Jonströmer, M; Strey, R *J. Phys. Chem.* **1992**, *96* 5993.
23. Steitz, R.; Braun, Chr.; Bowers, J.; Lang, P.; Findenegg, G.H. *Ber. Bunsenges. Phys. Chem.*, **1989**, *102* (11) in press.
24. Marra, W. C.; Eisenberger, P.; Cho, A. Y. *J. Appl. Phys* **1979**, *50*, 6927; Eisenberger, P.; Marra, W. C. *Phys. Rev. Lett.* **1981**, *46*, 1091.
25. Als-Nielsen, J.; Kjaer, K. in *Phase Transitions in Soft Condensed Matter*, Riste, T.; Sherrington, D. (eds.) Plenum Press, New York 1989.
26. Lang, P.; Braun, Chr.; Steitz, R.; Findenegg, G. H.; Rhan, H. *J. Phys. Chem.* **1998** *102* 7590.
27. Dietsch, O.; Findenegg, G. H. Iwan-N.-Stranski-Institut für Physikalische und Theoretische Chemie, Technische Universität Berlin, 10623 Berlin, Germany, unpublished work.

## Chapter 3

# Structural Transitions in Colloidal Suspensions in Confined Films

Darsh Wasan and Alex Nikolov

Department of Chemical and Environmental Engineering, Illinois Institute  
of Technology, Chicago, IL 60616-3793

The phenomenon of nanosized particle structuring and structural transitions due to confinement in thin liquid films is of considerable interest in both science and technology. Our recent experimental observations on thinning of single liquid films containing monodispersed nanosized colloidal particles with diameters varying from 5 to 1,000 nm clearly establish the presence of long-range (non-DLVO) oscillatory structural forces induced by the confined boundaries of the film. The effective particle interaction potential is oscillatory with both the period of oscillation and the decay length equal to about an effective particle diameter. At low particle concentrations, the long-range oscillatory structural force leads to an attractive depletion effect which gives rise to phase separation in colloidal systems. However, at high particle concentrations, the oscillatory structural force induces particle structural transitions inside the film and the formation of two-dimensional crystalline layers with hexagonal interplanar ordering which offers a new mechanism for stabilizing particle suspensions, foams and emulsions. Our experimental, theoretical and computer modeling results have shown the phenomenon of particle structural transitions in confined films as a function of film thickness, particle concentration, and polydispersity in particle size. This paper presents an overview of our findings.

The iridescent colors produced by light interference phenomenon in a thinning soap film have fascinated scientists for a long time (1-4). Thinning soap film is a simple model to demonstrate the effect of highly confined surfactant micelles on their structural behavior over distances of the order of 100nm (5-15). Our more recent experiments in foam, emulsion and pseudoemulsion films using particles as large as 1,000 nanometers have shown the phenomenon of particle layering and in-layer structural transitions in both plane-parallel and curved films, and also in the film-meniscus region, i.e. in a wedge film (16-21).



This is largely a review paper which summarizes research conducted in our laboratory over the last decade on understanding the nature of interactions within thin liquid films formed from suspensions of colloidal particles such as polymeric latexes and silica hydrosols, surfactant micelles, swollen micelles, microemulsions, and globular proteins.

We have developed two experimental techniques to investigate particle structuring phenomena inside thin liquid films. The particle layering inside the films was probed by using the microinterferometric technique, and the in-layer particle structuring was revealed by the light diffraction method. Details of these methods are given in our previous papers (17,18).

We have also used the Monte Carlo simulations to reveal particle layering and in-layer structural transitions in colloidal systems confined between the film surfaces and verified the numerical results with experimental observations.

## Experimental

The experimental set-up for investigating particle layering in a microscopic horizontal liquid film is shown in Figure 1. The formation of a film includes several steps. The first step is to form a biconcave drop of the liquid colloidal suspension inside a cylindrical tube (of radius  $R=1.5 \times 10^{-1}$  cm) with hydrophilic inner walls. Next, liquid is slowly sucked out of the drop through a capillary orifice in the tube wall, creating a microscopic, horizontal flat film (of radius about  $5 \times 10^{-3}$  cm) encircled by a biconcave liquid meniscus. The cell assembly is enclosed in a thermostat and a constant temperature is maintained ( $\pm 0.1$  °C). The entire assembly is placed on the stage of a differential interference microscope (Epival interphako) which is mounted on a vibration free table to keep any external disturbances from affecting the film thinning process. Mono-chromatic light (wavelength 546nm) from the top of the glass cell is incident on the film's surface and the light reflected from a small portion of the thinning film area is conducted through a fiber optic probe to a photomultiplier. Here the optical signal is converted to an electrical signal, amplified through an electrometer and, finally, recorded on a strip chart recorder which represents photocurrent as a function of time. As the film thins the thickness changes, producing interference patterns. The film thickness,  $h$ , at any instant of time can be estimated from the intensity of the photocurrent using the expression derived elsewhere (22-23).

$$h = \frac{\lambda}{2\pi n_0} \left( l\pi \pm \arcsin \sqrt{\Delta / \left[ 1 + (4\beta / (1 - \beta))(1 - \Delta) \right]} \right) \quad (1)$$

where

$$\beta = \frac{(n - l)(n - n_0)}{(n_0 + l)(n + n_0)} \quad (2)$$

$\lambda$  = wavelength of monochromatic light (546nm)

$l$  = order of interferences

$n, n_0$  = refractive index of film liquid and dispersed phase, respectively

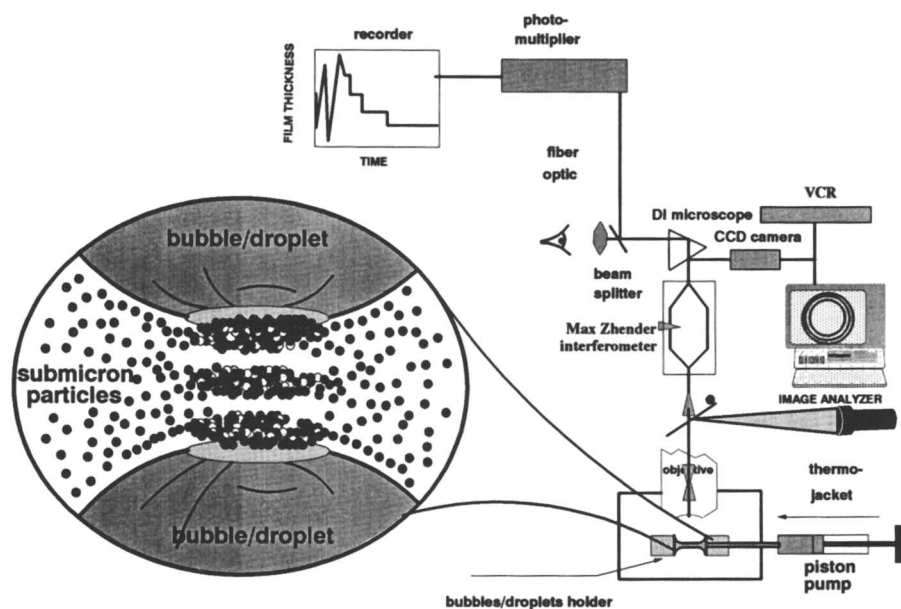


Figure 1. A sketch of the experimental set-up for monitoring particle layering within the microscopic horizontal films.

$$\Delta = \frac{I - I_{\min}}{I_{\max} - I_{\min}} \quad (3)$$

$I$  = instantaneous value of the photocurrent

$I_{\min}$ ,  $I_{\max}$  = value of the photocurrent at the last interferential minimum and maximum, respectively.

The video, in conjunction with a monitor and VCR, records in detail the process of film thinning. The method described here is a general one, appropriate for studying microscopic horizontal film thinning from micellar surfactant solution, suspensions of latex, silica particles, and other suspensions.

Using the microinterferometric technique, a microscopic film from an aqueous suspension (ionic strength of about  $4 \times 10^{-3}$  mol/l) of 20V% silica particles with a diameter of 19nm at 25°C was formed. The following phenomenon was observed: as soon as the film is formed, it starts to decrease in thickness. Initially, interference patterns (circles) appear, representing the dimple formation due to the hydrodynamic interactions between the approaching surfaces of the film. The dimples disappear after a film thickness of about 400nm is reached. The film thinning interferogram is shown in Figure 2. The film thins through several maxima and minima in the intensity of reflected light (the successive maximum and minimum represent a change in thickness of about 100nm). After the maximum (at about 300nm), the first step-transition, at a film thickness of about 230nm, is observed. The film rests for a few seconds in a metastable state with uniform thickness of 230nm. Then, the film begins to change its thickness by stepwise transitions (stratify) as seen in the photomicrographs shown in Figure 2.

After several seconds, a bright spot appears inside the film near the three-phase contact region. This bright spot begins to increase its area (see Figure 2) and more of the film area becomes brighter. We monitored four light intensity transitions before the stratifying film reached its final equilibrium stage which corresponded to a bright, white film with a thickness of about 100nm. The interferogram depicts these four thickness transitions at 230, 200, 167 and 133nm, respectively. The film stops thinning after about 2 minutes, at about 100nm. In this particular case, during the last stage of film thinning, the light intensity increases by steps which indicates that the stratification phenomenon is occurring at a larger film thickness (i.e., before the last light intensity maximum). The thinning stages of the film appear in the interferogram as steps whose width is proportional to the lifetime of the respective states. The mean height of the step is about 30nm. It is noteworthy that a stable film, with a film thickness of about 100nm and containing three layers of particles inside it, can exist in this case. The film interferogram shown in Figure 2 reveals that the horizontal microscopic film in the presence of particles is thinning in a stepwise manner, and this is due to the formation of particle layered-structure inside the film.

The particle self-layering phenomenon inside the film was also probed by studying vertical macroscopic film thinning behavior. This time, the film is formed by pulling a thin glass plate ( $5 \times 10^{-2}$ cm) from a monodispersed colloidal suspension of 20Vol% of silica particles with a diameter of 19nm. A vertical film of about  $0.5\text{cm}^2$  formed at 25°C as shown in Figure 3. After formation, the film is observed in a white (polychromatic)

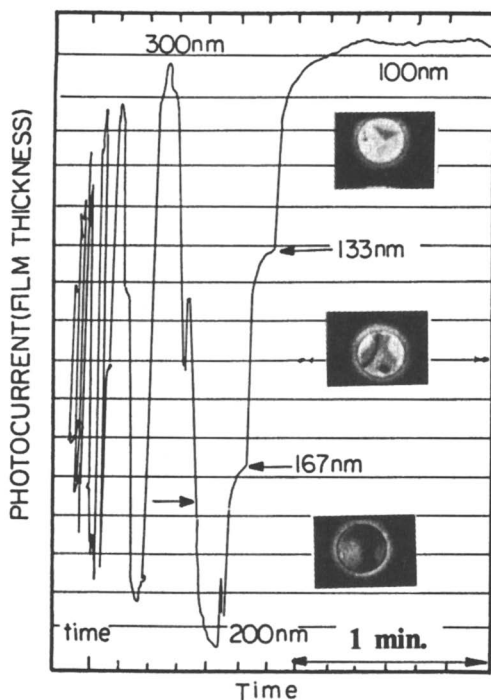


Figure 2. Photocurrent versus time interferogram of film thinning process of microscopic horizontal film (film diameter  $6 \cdot 10^{-2}$  cm) stabilized by silica particles (20 v%) with particle diameter, about 19nm. The thicknesses at which the transitions begin are marked with arrows. The successive movie frame photographs depict the film thickness transitions. (Reproduced from reference 17. Copyright 1992 American Chemical Society.)

reflected light by using a horizontal microscope. A set of well-defined, horizontal stripes of different colors appears first in the upper part of the film and, with time, the boundaries of the stripes expand and move downward. As a result, the area of the colored stripes increases. Each color stripe contains a different number of particle layers inside the thinning film. There are six to seven stratified layers in this film (see Figure 3). Generally, in both horizontal microscopic and vertical macroscopic films we observed the same number of stepwise film thickness transitions.

Figure 4 shows a similar photograph for the 44Vol% latex particles having a diameter of 156nm. In this case, the boundaries between the stripes are sharp—a consequence of the stepwise profile of the film thickness in this region—and the liquid meniscus below the film appears as a region with gradually changing color. When observed in reflected light, the top stripes have the following, sharply distinguished colors: white, yellow, blue, red and green-yellow. Following these stripes, a sequence of diffuse, alternating green and red bands indicates the gradual change in film thickness (the film has a wedge profile) where the particles' layered structure gradually becomes disordered. The thickness of the stripes as determined by the difference in film reflectivity are marked on Figure 4.

We observed similar, sharply defined stripes with films formed from micellar solutions of non-ionic surfactant with a micellar diameter of about 10nm (10).

We used the reflected light microinterferometric method to measure the total film thickness and the amplitude of the film thickness transition. However, this technique is not suitable for studying the type of particle packing structure formed inside a liquid film. Therefore, we used a low-angle transmitted light diffraction technique to study the same latex system as described above. In this case, we varied the angle of light intensity from 1 to 90°. A vertical macroscopic film of diameter 2.5 cm was formed from a 44Vol% aqueous latex suspension on a vertical plate formed inside of a glass cell which was especially designed to prevent film thinning caused by mechanical disturbances and evaporation. The monodispersed charged latex particles had a diameter of about 150nm and a charge of  $5\mu\text{cm}^2$ . Figure 5 shows the diffraction pattern obtained from a vertical macroscopic latex film. Diffraction patterns corresponding to a predominantly 2D hexagonal packing structure appeared only at film thicknesses corresponding to two and one particle layers. No such in-layer structure was observed for film corresponding to three particle layers thick.

In order to further investigate the dependence of the in-layer particle structuring phenomenon on film thickness, we carried out Monte Carlo simulations. These results are summarized below.

### Monte Carlo Simulation Results

A detailed investigation of particle layering and in-layer structure formation in thin films composed of two parallel hard walls using both the hard sphere and Leonard-Jones potentials by grand-canonical-ensemble Monte Carlo simulations was reported by us earlier (24). Typical density distributions of particles across a film thickness three times the particle diameter are shown in Figure 6, for the average particle concentration in the film ranging from 15Vol% to 35Vol%. The three peaks (at -1, 0, and +1) indicate that particles inside the film form three layers parallel to the film surfaces.

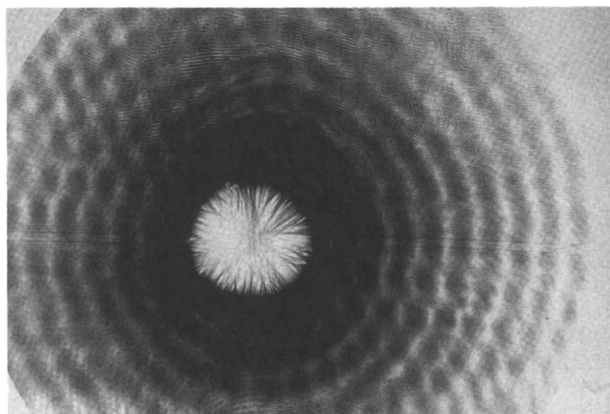


Figure 5. Diffraction patterns from a macroscopic vertical foam film at a film thickness of two particle layers (yellow color) formed from a 44 v% latex suspension, with a particle diameter of 156nm.

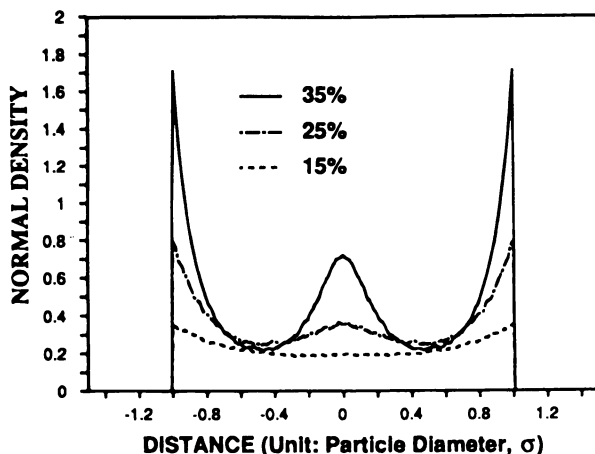


Figure 6. Normal density distributions of particles across a film thickness three times the particle diameter calculated from the hard-sphere-hard-wall mode. Three peaks indicate the formation of three particle layers. The average particle volume fractions are 15, 25 and 35 v%. (Reproduced from reference 24. Copyright 1994 American Chemical Society.)

Also, the figure shows that at a given film thickness, as the particle concentration inside the film increases, the particle-layering becomes more pronounced.

The pressure exerted by the particles on the surfaces of the film (i.e. the structural disjoining pressure) for the hard-sphere-hard-wall model at different bulk concentrations is shown in Figure 7. It can be seen that the structural disjoining pressure exerted by particles in a thin film oscillates around zero and that it can be positive or negative, depending on the thickness of the film. The period of the oscillation is the effective diameter of the particle. When film thickness is about an integer multiple of the particle diameter, the disjoining pressure is positive and when the film thickness is around 1.5, 2.5, 3.5, the effective particle diameter, the disjoining pressure is negative. The states with negative particle disjoining pressure are intrinsically unstable from a thermodynamic point of view, thus film changes its thickness during a thinning process by stepwise transitions and stays at thicknesses with positive particle disjoining pressure. As seen in Figure 7, the amplitude of the oscillation of the of the particle disjoining pressure becomes weaker as the film thickness increases, and beyond a certain film thickness, oscillation ceases. Therefore, a system of given particle concentrations has only a finite number of maxima in the particle disjoining pressure isotherm and one should expect to observe the same corresponding number of stepwise transitions during the actual film drainage experiments.

In order to reveal the particle structure inside the layer parallel to the film surface, the radial distribution function (RDF) of the particles in a layer has been examined. Figure 8 shows a surface plot of inlayer RDF versus inlayer distance and concentration. When the particle concentration is low, the particles inside a layer pack randomly and form a liquid-like 2D structure without order, that is, damped peaks near the integers,  $1\sigma$ ,  $2\sigma$ ,  $3\sigma$  (in the unit of particle diameter). When the average effective concentration increases to somewhere between 40 and 45 Vol%, new peaks begin to appear in the inlayer RDF especially near  $r=\sqrt{3}$  and  $r=\sqrt{7}$ , which indicates the formation of 2-D hexagonal structures inside the layer. This peak grows as the concentration increases, indicating a structural transition from a liquid-like inlayer structure to the colloid crystal-like inlayer structure. Both the hard-sphere-hard-wall and the Leonard-Jones models predict that the disorder-order transition for the surface layers for a film thickness of two particle diameters starts at about 40 to 45Vol% particle concentration.

The inlayer structure depends not only on the position of the layer in the film but also on the film thickness. Figure 9 is a plot of the inlayer RDF of surface layers for different film thicknesses,  $2\sigma$ ,  $3\sigma$ ,  $4\sigma$  and  $5\sigma$ , at the same concentration of 46Vol%. The degree of ordered 2-D hexagonal structure can be detected by the height of the peak near  $\sqrt{3}$ . It is clearly seen that the inlayer particles in thinner films of thicknesses  $2\sigma$  and  $3\sigma$  are better organized than those in films of thickness  $4\sigma$  and  $5\sigma$ .

Figure 10 shows the inlayer RDFs for different layers in a film of particle concentration of 46Vol%. One can see a peak near  $\sqrt{3}$  for the surface layer which indicates the formation of 2-D hexagonal packing. This peak becomes weaker in the next layer and disappears in the middle layer. The difference in the inlayer RDFs of different layers illustrates that there exists, in a single film, more ordered structure in the surface layer and disordered structure in the middle layer. The sequence of the transitions in a thin film of fixed thickness with increasing particle concentration is as

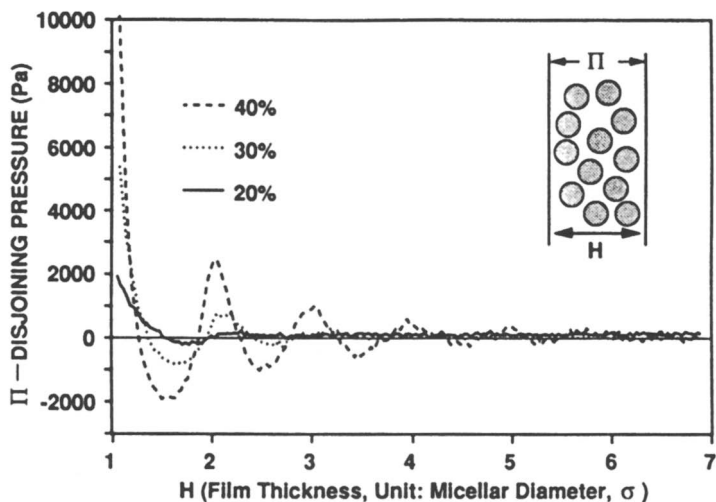


Figure 7. Structural disjoining pressure versus film thickness. Three curves are results for three different bulk concentrations: 20, 30 and 40 v%. The values for disjoining pressure are for a system with the particle of 10nm effective diameter, at a temperature of 300 K°. (Reproduced from reference 24. Copyright 1994 American Chemical Society.)

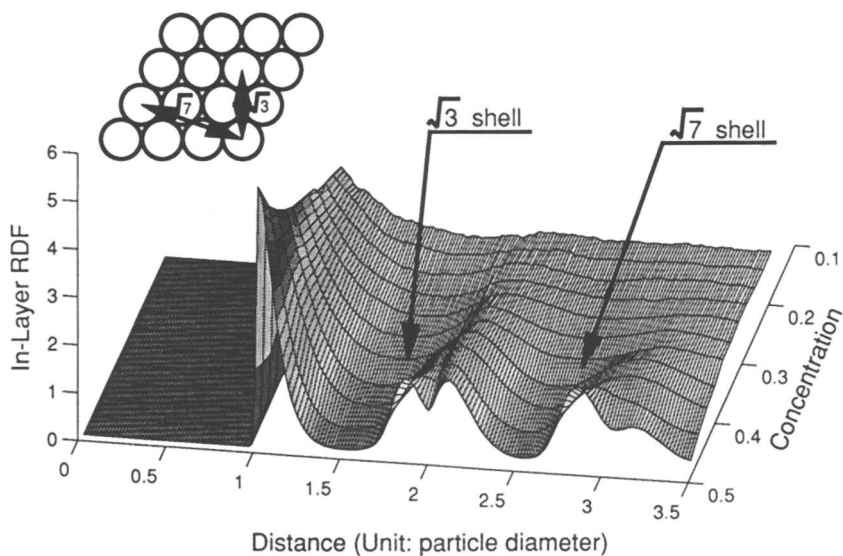


Figure 8. Surface plot of inlayer RDF versus inlayer particle distance and concentration. At low concentrations, the particles inside a layer pack randomly and form a liquid-like 2D structure. At high concentration limit ( $> 43$  v%), two new peaks near  $\sqrt{3}$  and  $\sqrt{7}$  can be seen, indicating the hexagonal packing. The film thickness is two particle diameters. (Reproduced from reference 24. Copyright 1994 American Chemical Society.)



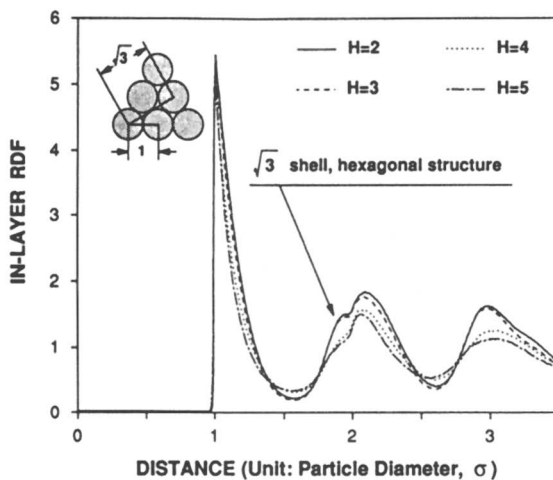


Figure 9. Inlayer radial distribution function for the surface layer of hard-sphere-hard-wall films of the average particle concentration of 46 v%, but at different thicknesses. It shows that the thinner the film is, the better the order in the 2D structure. (Reproduced from reference 24. Copyright 1994 American Chemical Society.)

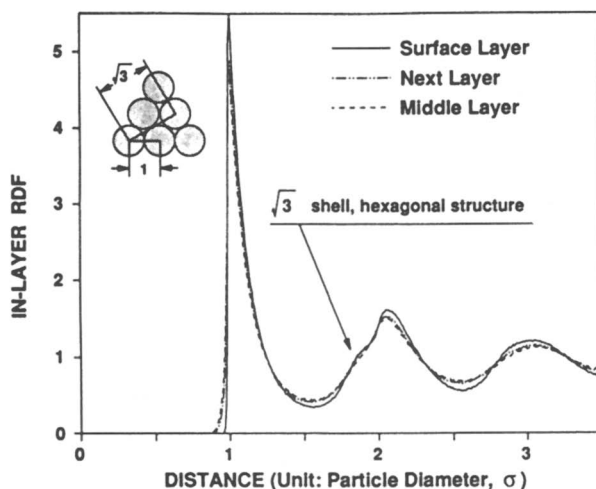


Figure 10. Inlayer radial distribution function for different layers in hard-sphere-hard-wall film of thickness five particle diameters. The solid line is the RDF for the surface layer, the broken line for the layer next to it, and the dotted line for the layer in the middle. The average concentration is 46 v%. (Reproduced from reference 24. Copyright 1994 American Chemical Society.)

follows: disorder  $\rightarrow$  layering  $\rightarrow$  inlayer ordering for surface layers  $\rightarrow$  inlayer ordering for middle layers  $\rightarrow$  bulk type ordering, i.e. Kirkwood-Alder type transition (25,26).

Figure 11 is the inlayer RDF for a film of thickness of  $1.7\sigma$  and the particle concentration of 46Vol%. Contrary to the inlayer RDF for free liquid films (Figure 8-10), there is no  $\sqrt{3}$  peak in this case, but there is a peak instead at  $\sqrt{2}$ , indicating the existence of a 2-D square structure.

### Comparison of Numerical Results with Experiments

We studied the structuring phenomenon inside thin films formed from surfactant micellar solutions or suspensions of Brownian particles such as polymeric latexes and silica hydrosols. We modeled the film by hard-sphere-hard-wall and Leonard-Jones systems.

Experimentally, we observed that the number of film thickness transitions depends on the colloidal particle effective volume. At a high effective particle concentration, we observed more stepwise thickness transitions and consequently more particle layers inside the film were induced. Figure 12 shows the number of stepwise transitions, as a function of particle concentration, we observed compared to those predicted by the Monte Carlo simulations. One notices the good agreement between the numerical results and our experimental observations.

Our experimental observations for stepwise transitions demonstrate the existence of long-range (non-DVLO) oscillatory structural forces which are induced by the confined boundaries of the film. At low particle concentrations, the oscillatory structural force leads to the depletion force which is known to destabilize various dispersions. At high particle concentrations, the long-range structural forces can improve dispersion stability (27).

The numerical results predicted an inlayer 2-D hexagonal particle structure for a film of thickness of two particle diameters (Figures 8 and 9), and this is consistent with our transmitted light diffraction experiments using monodispersed, highly charged latex particles of 150 nm (Figure 5).

We have also used the transmitted light multiple light scattering imaging technique to directly observe the disorder-ordered structural transition during film thinning and verified the predicted numerical results (17).

Pieranski, et al. (28) observed square-type inlayer packing structure for the case of thin film confined by two solid walls where they could control the film thickness at an arbitrary value. Such a square type inlayer structure is predicted by our Monte Carlo simulations (Figure 11). However, it should be noted that for a liquid film with fluid surfaces, such a thickness is not favorable, and hence there is no peak at  $\sqrt{2}$ .

More recently, Basheva, et al. (29) used interference methods to independently verify the presence of hexagonal packing structure inside the vertical liquid films containing latex particles. However, the effect of film thickness on the type of inlayer structure was not observed by these authors.

Murray and Grier (20) observed that latex aqueous suspensions, at concentrations of a few percent and trapped between two solid surfaces, ordered themselves into colloid crystals (30).

It is noteworthy that the direct force measurement experiments performed by Kekicheff, et al. (31) in micellar solutions and microemulsions confined between two mica

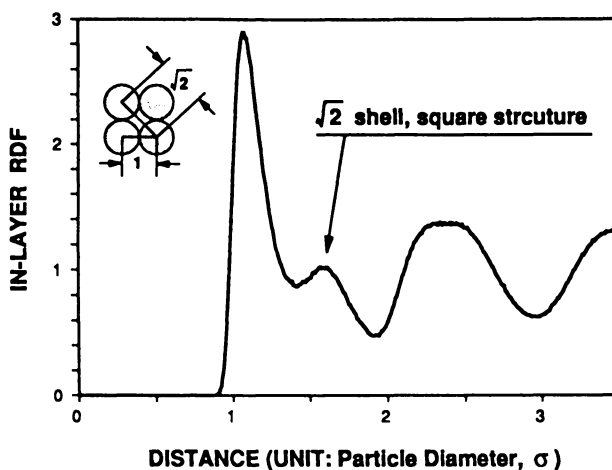


Figure 11. Inlayer radial distribution function for a film of thickness of 1.7 particle diameters at concentration of 46 v%. A film of such thickness can only be realized in a system with two solid walls; a peak near  $\sqrt{2}$  is the indication of square type inlayer structure. (Reproduced from reference 24. Copyright 1994 American Chemical Society.)

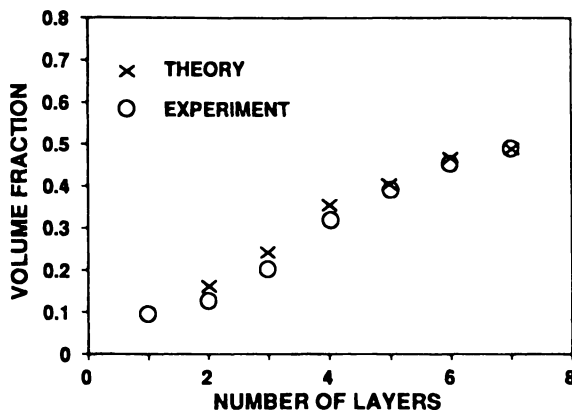


Figure 12. Number of film thickness transition steps versus particle concentration: comparison of theory and experiment. Experimental system consisted of film made of 10.6nm particle size.

sheets in a surface force apparatus have independently confirmed our experimental and theoretical results in thin films.

More recently we have investigated the particle structural transition phenomenon in the liquid film-meniscus region, i.e. in a wedge film, using digital videomicrography and found the coexistence of hexagonal and cubic packing structures inside the film (32). These experimental observations are being verified by us using the Monte Carlo simulations and the density functional methods.

The effects of polydispersity in particle size on layering and structural transitions in a thin film have also been observed by us experimentally and verified theoretically (33). It should be pointed out, however, in all the theoretical calculations carried out thus far we have used the hard-sphere-hard-wall and Leonard-Jones models. Our more recent theoretical work in progress takes into account the effects of solvent and electrolytes. These results will be reported at a later date.

### Acknowledgments

This work is supported by the National Science Foundation and, in part, by the U.S. Department of Energy. The Monte Carlo calculations were performed by Dr. X. L. Chu.

### Literature Cited

- (1) Porter, A. *Encyclopaedia Britannica*. 1964, 21, 595.
- (2) Plateau, J. *Statique Experimentale at Theorique des Liquides aux Seules Forces Moleculaires*; Gauthier-Villars: Paris, 1873; pp 163.
- (3) Newton, *Optiks*; Smith & Walford: London, 1704.
- (4) Laplace, P. *Mecanique celeste (Impr. Imperiale)* Suppl to 10th book, 1806.
- (5) Johnnott, E.S. *Philos. Mag.* 1906, 70, 1339.
- (6) Perrin, J. *Ann. Phys (Paris)* 1918, 10, 160.
- (7) Bruil, H.G.; Lyklema, J. *Nature* 1971, 232, 19.
- (8) Friberg, S.; Linden, St.E.; Saito, H. *Nature*, 1979, 251, 494.
- (9) Wasan, D.T.; Nikolov, A.D.; Huang, D.D.; Edwards, D.A. *ACS Symposium Series 373 Surfactant-Based Mobility Control Progress in Miscible-Food Enhanced Oil Recovery*, Editor, D.H. Smith, A.C.S. Washington, D.C., 1988 pp136-162.
- (10) Nikolov, A.D., Wasan, D.T., Kralchevsky, P.A. and Ivanov, I.B., in "Ordering and Organization in Ionic Solutions," *Proceedings of Yamada Conference XIX*, N. Ise and I. Sogami, Eds., World Scientific Publishing Co.: Singapore, 1988; pp302-314.
- (11) Nikolov, A.D.; Wasan, D.T. *J. Colloid Interface Sci.* 1989, 133, 1-12.
- (12) Nikolov, A.D.; Kralchevsky, P.A.; Ivanov, I.B.; Wasan, D.T. *J. Colloid Interface Sci.* 1989, 133, 13.
- (13) Nikolov, A.D.; Wasan, D.T.; Denkov, N.D.; Kralchevsky, P.A.; Ivanov, I.B. *Prog. Colloid Polym. Sci.* 1990, 82, 87-98.
- (14) Bergeron, V; Radke, C. *Langmuir* 1992, 8, 3020.
- (15) Langevin, D; Sonin, A. *Advances in Colloid and Interface Science* 1994, 51, 1.

- (16) Basheva E.; Nikolov, A.D.; Kralchevsky, P.; Ivanov, I.B.; Wasan, D.T. In *Proceedings of 8th International Symposium on Surfactants in Solution*, Gainesville, FL, U.S. 1991 Ed. by K. Mittal **1992**.
- (17) Nikolov, A.D.; Wasan, D.T. *Langmuir*, **1992**, 8, 2985-2994.
- (18) Wasan, D.T.; Nikolov, A.D. In *Particulate Two-Phase Flow*, M.C. Roco, Ed., NSF, Butterworth-Heinemann, **1993** pp325-354.
- (19) Lobo, L.; Wasan, D. *Langmuir* **1993**, 9, 1668-1677.
- (20) Koczko, K.; Nikolov, A.; Wasan, D.T.; Borwankar, R.; Gonsalves, A. *J. Colloid and Interface Sci.* **1996**, 178, 694-702 .
- (21) Manev, E.D.; Sazdanova, S.V.; Wasan, D.T. *J. Dispersion Sci. and Tech.* **1984**, 5, 111.
- (22) Vasicek, A. *Optics of Thin Films*; North-Holland: Amsterdam; **1960**.
- (23) Lyklema, I., Scholten, P.S. and Mysels, K. *J. Phys. Chem.* **1965**, 69, 116.
- (24) Chu, X.; Nikolov, A.; Wasan, D.T. *Langmuir* **1994**, 10, 4403-4408
- (25) Kirkwood, J.G.; Maun, E.K.; Adler, B. *J. Chem. Phys.* **1950**, 18, 1040.
- (26) Adler, B.J.; Wainwright, T.E. *J. Chem. Phys.* **1957**, 27, 1208.
- (27) Xu, W.; Nikolov, A.D.; Wasan, D.T. *AIChE Journal* **1997**, 43,12, 3215-3222.
- (28) Pieranski, P. *Contemp Phys.* **1983**, 24, 25; Pieranski, P.; Strzelecki, L.; Pansu, B. *American Physical Soc.* **1983**, 50, No. 12, 900.
- (29) Basheva, E.; Danov, K.; Kralchevsky, P. *Langmuir* **1997**, 13, 4342.
- (30) Murray, C.; Grier, D. *Amer. Sci.* **1995**, 8, 238.
- (31) Kekicheff, P.; Richetti, P. *Progress in Colloid and Polymer Science* **1992**, 88, 8.
- (32) Wasan, D.T. Invited Lecture, 72nd Colloid and Surface Science Symposium, Pennsylvania State University, June 22, 1998.
- (33) Chu, X.; Nikolov, A.; Wasan, D. *Journal Chem. Phys.* **1995**, 103, 6653-6661.

## Chapter 4

# Lamellar Droplet Capillary Condensed from a Bicontinuous Microemulsion

L. Moreau-Biensan<sup>1</sup>, P. Barois<sup>1</sup>, and P. Richetti<sup>1,2</sup>

<sup>1</sup>Centre de Recherche Paul Pascal, Avenue Schweitzer, 33600 Pessac, France

<sup>2</sup>Complex Fluids Laboratory, CNRS/Rhodia UMR-166, Prospect Plains Road, Cranbury, NJ 08512-7500

Using a surface forces apparatus (SFA), we have measured the force profiles between two surfaces immersed in a microemulsion solution ( $\mu_e$ ) in the vicinity of the lamellar phase ( $L_\alpha$ ) domain. We find attractive short range oscillatory profiles. At the onset of the  $L_\alpha/\mu_e$  transition, the force range and the number of oscillations increase together. We ascribe these profiles to the condensation of a lamellar droplet from the confined  $\mu_e$  phase. We propose a modeling force for the profiles consisting in two contributions. The first one proceeds from capillary condensation and yields an attraction varying linearly with the surface separation. The second contribution is elastic and specific to the lamellar order. The induced stack of layers experiences an elastic strain in the restricted spacing of the confinement. The oscillations in the force profiles originate from this elastic distortion. From the force profiles, we estimate the compressibility modulus of the induced phase and the interfacial tension between the  $L_\alpha$  and  $\mu_e$  phases.

Capillary condensation is a current phenomenon, abundantly described in the literature. The condensation of a liquid from its vapor in a wetting capillary is a common occurrence (1-4). A related behavior is the phase separation of a single liquid from a mixture in a confined geometry (5). A similar phenomenon occurs with complex fluids as well, confining them may induce phase transition (6). All these phenomena belong to the same class referred to as surface-induced phase transition.

The capillary condensation continues to be the focus of experimental and theoretical interest, especially for complex fluids like liquid crystals (7,8), polymer melts (9,10) or concentrated lyotropic solutions (11,12). Scattering experiments are techniques of choice to study this phenomenon developing either in a porous

medium (8) or thin film (7,13,14). An alternative technique is the surface forces apparatus (15). In this device, the confinement geometry is well controlled and the thickness between the surfaces is tunable with molecular accuracy.

Fisher and Israelachvili have first used a SFA to investigate a capillary condensation (16). They studied the condensation of a liquid droplet from a vapor phase. Later, Christenson and co-worker (4,17) resumed and expanded this kind of study with a SFA. The authors have tested the range of validity of the Kelvin law and measured the capillary adhesion forces between surfaces bridged by a condensed droplet. However, it is only recently that an integral force profile specific to a capillary condensation has been obtained by Grassous *et al.* (18). Using a SFA with a different technology allows them to avoid the intrinsic mechanic instability occurring with classical devices when attractions between surfaces are relatively large.

The condensation of a liquid droplet from mixture has also been observed with the SFA. The group of Canberra in Australia has intensively examined the nucleation of water droplets between the hydrophilic mica surfaces from organic liquids (5,19). In these experiments, the authors characterized the modification of force profiles induced in a dry non-polar liquid by a gradual introduction of water.

More recently, phase transitions for confined complex fluids have also been considered with the SFA. Both first-order (11,12,20) and second-order phase transition (21) have been examined. Until now, the samples studied have always been lyotropic solutions and the induced phase was every time a  $L_\alpha$  phase, with a smectic order. In these systems, a capillary condensation has been triggered from isotropic membrane phases near a first order phase transition with the  $L_\alpha$  phase. Two phases of similar topology have been considered. Antelmi *et al.* (11) and Petrov *et al.* (12) have investigated the sponge phase, and more recently capillary condensation from a bicontinuous microemulsion phase has been tested by Petrov *et al.* (20).

In the present paper, we report a capillary condensation of lamellar droplet from a bicontinuous microemulsion. The system investigated is different from that of Petrov *et al.* (20). Our observations are overall in good agreement with their results. Our results are however more complete and lead to a different interpretation. An attempt is also made to directly compare a modeling force and the experimental data.

The article is organized as follows: the experimental observations are first examined in Section 2. Modeling of the force profiles is presented in Section 3. In Section 4, we analyze and discuss our results. A comparison between the prediction of the model and the experimental data is made. The compressibility modulus of the induced lamellar phase and its interfacial tension with the microemulsion are then estimated. Section 5 is devoted to concluding remarks.

## Experimental Results

**Surface Forces Apparatus.** Using a Mark IV surface forces apparatus (22), we have examined a symmetrical microemulsion on approaching the lamellar phase. The device has been fully described elsewhere (15, 22). The instrument is capable of measuring the separation between two mica surfaces immersed in a solution with an

accuracy of about 0.3 nm and the force within a sensitivity of  $10^{-7}$  N. Molecularly smooth sheets of freshly cleaved mica are glued onto cylindrical lenses having a radius  $R \approx 2$  cm. In the device, the two lenses are mounted in a crossed configuration with their axis perpendicular. The temperature in the enclosure surrounding the SFA was controlled to  $\pm 0.04$  °C, but stability was better in the SFA due to its large mass and thermal inertia. Although the temperature between the mica surfaces was not probed during the experiments, previous tests have shown a constant offset of few tens of degrees compared to the outside temperature ( $T$ ). Hereafter, the temperature difference between the outside and the bulk  $L_{\alpha}/\mu_e$  transition,  $\Delta T = T - T_{L_{\alpha}}$ , is chosen as the control parameter. Owing to inherent evaporation during the filling of the SFA and also during an experiment (usually an experiment lasts between one and two weeks) or because the temperature controller device was not systematically calibrated, the accuracy of  $\Delta T$  is estimated to be about 0.2 °C.

**Lyotropic System.** The lyotropic system was a solution of a nonionic surfactant (tetraethylene glycol decyl ether,  $C_{10}E_4$ ), water and octane. The volumes of both solvents were kept equal while the surfactant weight fraction was fixed at 0.21. A phase diagram cut including this composition can be found in Reference 23 and is schematically reproduced in Figure 1. A narrow strip of microemulsion surrounds a lamellar phase domain both at high and low temperature. Only the upper microemulsion domain, corresponding to the temperature range from about 27 to 29 °C has been investigated. Conductivity measurements reveal that the microemulsion at the studied composition is bicontinuous. An obstruction factor close to 2/3 has been found over the entire temperature range. Above 29 °C a two-phase domain extends up to high temperatures, a water rich phase emerges from the microemulsion phase.

The samples were prepared by weighing. The surfactant  $C_{10}E_4$  (from Nikko, >99% pure) and the octane (from Aldrich, 99+% pure) have been used as received without further purification, while deionized water was passed through a Milli-Q water system (from Millipore).

**Force Profiles.** Figure 2 shows the evolution of the force profiles recorded in the lamellar phase (Figure 2a) and in the symmetrical microemulsion (Figure 2b-e) as  $\Delta T$  is increased over few degrees. The profiles display oscillations with quite constant period. Since one surface is suspended at the end of a cantilever spring of stiffness  $K$ , unstable regimes without recorded data appear when the force slope is greater than  $K$ . Under these conditions, the system jumps from unstable to next stable position, leaving unexplored and inaccessible regions. An inward jump occurs from oscillation maxima upon approaching the surfaces, while an outward jump occurs from positions close to minima upon separation. The  $L_{\alpha}$  force profile, Figure 2a, is qualitatively different from the  $\mu_e$  profiles. This is a long-range profile exhibiting a large number of oscillations. The oscillations have parabolic shape and they line up on a constant zero baseline. In contrast, the  $\mu_e$  force profiles, Figure 2b-e, are short-range oscillatory profiles, the number of oscillations is limited and they are superimposed over an attractive background. Heating up the system has noticeable consequences on the  $\mu_e$



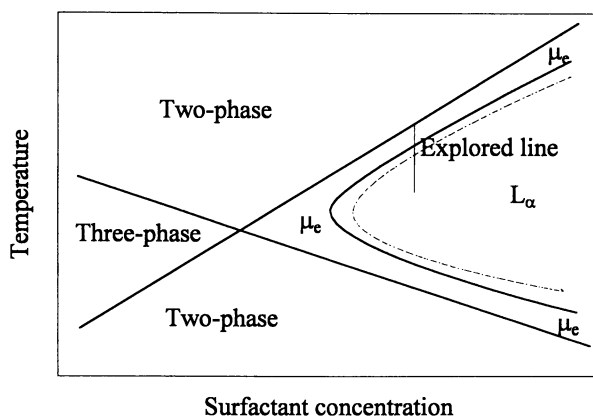


Figure 1. Schematic representation of the  $C_{10}E_4$ /octane/ $H_2O$  phase diagram adapted from Reference 23. (Adapted with permission from reference 23. Copyright 1992 American Physical Society.)

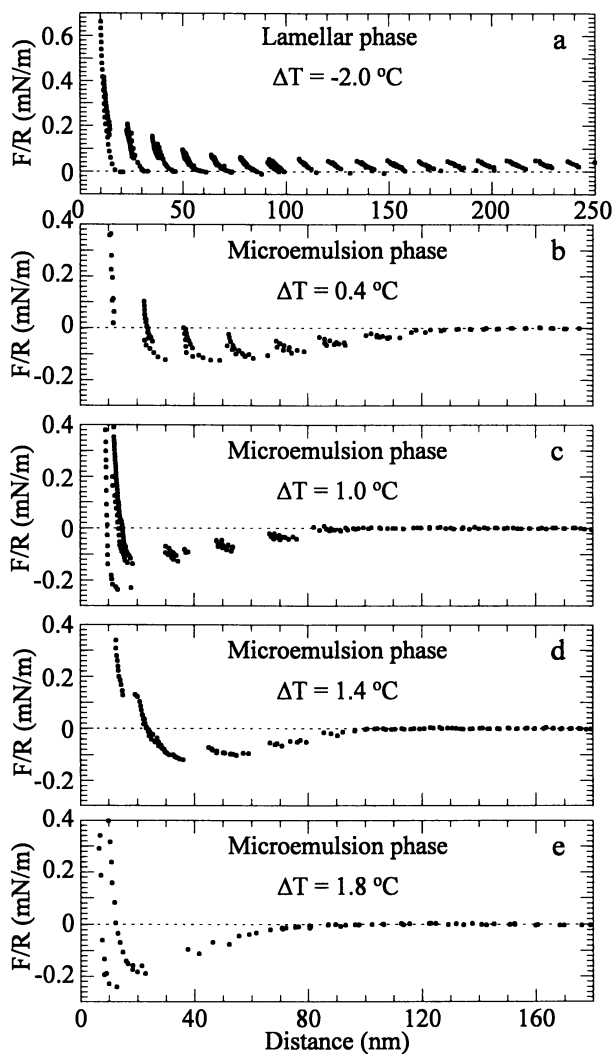


Figure 2. Force profiles upon increasing the temperature between two mica surfaces immersed in a solution of  $\text{C}_{10}\text{E}_4/\text{octane}/\text{H}_2\text{O}$  in the vicinity of the bulk lamellar/microemulsion transition. a) In the lamellar phase about  $2\text{ }^{\circ}\text{C}$  below the bulk transition temperature. In the microemulsion phase about b)  $0.4$ , c)  $1.2$ , d)  $1.4$  and e)  $1.8\text{ }^{\circ}\text{C}$  above the transition temperature.

force profile features. The number of oscillations then decreases, falling from a maximum of 9 very close to the lamellar domain, to 4 at the onset of the upper one-phase microemulsion boundary. Similarly, the amplitude and the period of oscillations change as the temperature is increased. At high temperature, Figure 2e, the amplitudes have so diminished that the oscillations are hardly detectable on the force profile. The oscillation period, which is fairly constant at every temperature, increases from about 15 nm to more than 20 nm when  $\Delta T$  increases from 0.4 to 1.8 °C. Note that the measured periods in the lamellar phase are slightly smaller. For the profile presented in Figure 2a,  $\Delta T = -2$  °C, a period of  $14.2 \pm 0.4$  nm has been estimated.

A difficulty occurs at high temperature, very close to the temperature of demixing for which a water rich phase separates (Figure 1). After having approached the surfaces sufficiently close one to the other, during the subsequent separation, we often observe the condensation of water droplet. This condensation is revealed by a distortion in interference fringes used to measure the separation between surfaces. These fringes also allow the measurement of the refractive index of confined material and then to identify it. At large separations ( $>500$ nm), the droplet is gradually resolubilized after a few minutes. This random phenomenon has been observed only if  $\Delta T > 1.5$  °C and when the surfaces have been previously approached towards separations shorter than about 20 nm. However its frequency increases significantly at the onset of the transition temperature. Note that the force profile presented in Figure 2.e has not been measured under such conditions. The fringes did not exhibit any distinguishing distortion.

## Modeling

**Lamellar phase.** When a lamellar phase sample is confined between two walls, the layers naturally tend to align parallel to the surfaces. Between two parallel plates, an homeotropic alignment may therefore be easily achieved. Between two curved surfaces, because the separation is now varying in the gap, an homeotropic alignment can be only completed if structural defects develop. We can consider a sphere against a plate for the SFA, that equivalent to the crossed cylinders when their separation is small compared to the radii,  $d \ll R$ . Nallet and Prost (24) have shown that a  $L_\alpha$  sample confined between a sphere and a plate orients spontaneously in an homeotropic way by developing edge dislocation defects. The defects build up an array of concentric dislocation loops. The array is centered along the symmetry axis of the confinement. Note however that this kind of defect is thought more stable when the separation between the surfaces is small, less than a few microns. For thicker confinements, screw dislocation lines may develop as reported by Herke *et al.* (25). By taking into account an array of dislocation loops, the interaction between the two surfaces can be calculated as discussed in Reference 26. The force between a sphere and a plate confining a perfectly aligned lamellar sample is the sum of two elastic contributions,

$$F / 2\pi R = \frac{1}{2} \bar{B} \frac{(d - na_0)^2}{na_0} + \gamma \sum_{i=1}^N r_i^{-1} \quad (1)$$

$\bar{B}$  is the layer compressibility modulus of the smectic phase,  $d$  and  $n$  are the spacing and the number of lamellar layers at the center of the gap respectively.  $a_0$  is the lamellar layer thickness at the equilibrium,  $\gamma$  is the line tension density of dislocation, and  $r_i$  is the radius of the  $i^{\text{th}}$  dislocation loop of the array having  $N$  loops. Equation 1 assumes that every defect is an elementary dislocation of Burgers vector 1, meaning that a defect loop is just a circular pore of radius  $r_i$  in a lamella. Such an assumption has frequently been verified provided that the separation between the surfaces is smaller than a micron (24,26-28).

**Derjaguin-like term.** The first term in Equation 1, which is a Derjaguin-like term (29), is the restoring elastic force of the part of sample confined at the center of the gap (26). When the separation between the sphere and the plate at the center of the confinement is not commensurate with an integral multiple of smectic layer thickness,  $d \neq na_0$ , the  $n$  central layers are elastically deformed, stretched or compressed according to the sign of the imposed strain  $(d-na_0)/d$ . The second term arises from the elastic distortion undergone by the rest of the sample and reduces to a defect dependent contribution (26).

**Relaxation Mechanism.** Actually  $n$  the number of layers at the center is dependent on the spacing  $d$ . Let us examine how the sample behaves at the center of the confinement when the separation  $d$  is changed. It is straightforward to show that at some separations, the elastic energies of  $n$  layers compressed and of  $n-1$  layers stretched are equal. Therefore, under compression, the confined system should expel a layer in order to relax the induced elastic stress. This may be accomplished by the nucleation of a new dislocation loop at the center of the confinement, becoming then the central loop of the concentric defect array. The structural defect is expected to be thermally activated. On the other hand, on separating, beyond some threshold separations, the system should introduce a new layer into the stack in order to release the stretching energy. This is achieved with the shrinkage of the central dislocation loop. The pore reduces gradually as the separation increases and eventually collapse at the threshold separation, bringing a new layer at the center of the confinement. In the framework of the dislocation loop array model, the separations at which the relaxation mechanism occurs can be calculated (26). Every time the applied strain is about a half layer,  $(d-na_0) \approx \pm a_0/2$ , a layer is squeezed out or introduced at the center of the confinement according to the sign of the applied strain. The Derjaguin-like term of Equation 1 then leads to a series of parabolas. Every parabola corresponds to an integer of smectic layers at the center of the confinement. The parabolas are centered at separations matching exactly an integral multiple of lamellar layer thickness,  $d_n = na_0$ , and they intersect at separations at which the relaxation mechanism occurs,  $d'_n \approx (n + \frac{1}{2})a_0$ .

**Sum term.** As discussed in Reference 26, on average, the right hand term of Equation 1 is almost constant over a separation range spanning from the contact to a few microns. The variation is expected to be lower than the sensitivity of the SFA with

common  $L_{\alpha}$  phases. Although this term predicts a non-zero background, slightly larger than the SFA sensitivity, a classical SFA does not allow its measurement. Indeed, the technique provides only relative force profiles with respect to the forces at large separations, the distance range over which the device is calibrated. Usually, far from the contact, the surfaces do not experience any interaction; an absolute force profile is then determined. However, no difference can be made when the force is not nil, but weak and constant.

In conclusion, the modeling force, Equation 1, practically reduces to the Derjaguin term. The series of parabolas lines up on a zero-background as displayed in Figure 3a. That is a long-range force profile, since the oscillation amplitudes decrease like  $d^{-1}$ . The oscillations have the same period. Between two successive minima, the separation is equal to  $a_0$ , the lamellar layer thickness.

**Lamellar Droplet Capillary Condensed from the Microemulsion Phase.** In order to account for the force profiles measured in the  $\mu_e$  phase, Figure 2b-e, let us assume that these profiles result from a capillary condensation of a lamellar droplet. This means that the lamellar/microemulsion phase transition occurs at a higher temperature in a confinement than in bulk. Below a threshold separation, the sample transits from the disordered state to the ordered one. Such a transition temperature shift is made possible thanks to an energy gain brought about by surfaces when the surfaces have greater affinity with the induced phase.

**Capillary Condensation.** The hydrophilic mica surfaces are preferentially wet by water. Then they locally break the isotropic symmetry of the  $\mu_e$  phase. Owing to the finite correlation length between membranes in this phase, a layering near the surfaces is expected, involving layers of surfactant and oil, presumably no more than one or two. An ordered film of lamellar symmetry would then wet each surface although the sample is maintained in  $\mu_e$  phase.

With such pre-wetting films, when the capillary condensation occurs, the system gains some energy by giving up the two interfaces (of whole area  $A$ ) between the pre-ordered films and the disordered material, at the cost of ordering the interior of the droplet (of volume  $V$ ) and of creating a new lateral interface (of area  $S$ ) between the lamellar droplet and the microemulsion. With the SFA confinement geometry, the interfacial penalty can be neglected in good approximation (5,18,20). Indeed, the large radius of curvature of mica surfaces leads to condensed droplets of larger area in contact with mica than of lateral area,  $A \gg S$ . Therefore a single balance between a favorable interfacial contribution,  $-\gamma A$ , and an unfavorable volume contribution,  $\mu V$ , monitors the capillary condensation.  $\gamma$  is the interfacial tension between the bulk phase and the induced phase, and  $\mu$  is the difference in chemical potential between these two phases. By considering the SFA surface geometry, the capillary force exerted by a bridging droplet has been derived by different authors (5,18,20) and can be written to a good approximation as

$$F / 2\pi R = -2\gamma \left( 1 - \frac{d - 2d_1}{2R_k} \right) \quad (2)$$

$d_1$  is the thickness of the pre-wetting films covering the surfaces, and  $R_k$  which fixes the range of the linear attraction (Equation 2) is the so-called Kelvin radius,  $R_k = \gamma/\mu$ . When the condensed droplet is lamellar, the interfacial tension to consider in Equation 2 is the parallel component,  $\gamma_{||}$ . The related term arises from the cancellation of interfaces between the microemulsion and the lamellar pre-wetting films, which are supposed to be homeotropically aligned.

**Specific Lamellar Order.** Once the condensation has been completed, the induced stack of lamellar layers undergoes an elastic strain imposed by the confinement of finite thickness, as discussed previously. Then, summing the capillary force (Equation 2) and the elastic Derjaguin-like term in Equation 1 gives a modeling force for the capillary condensation of a lamellar droplet.

$$F / 2\pi R = -2\gamma_{||} \left( 1 - \frac{d - 2d_1}{2R_k} \right) + \frac{1}{2} \bar{B} \frac{(d - na_0)^2}{na_0} \quad (3)$$

This force profile (Equation 3) is displayed in Figure 3b. It consists in a short-range oscillatory profile. The oscillations have a parabolic shape, with a period equal to the thickness of the induced lamellar layers, superimposed on a linear attractive background.

## Analysis and Discussion

**Lamellar Phase.** In the literature, a few force profiles between surfaces confining a smectic phase (30) or a lamellar phase (26-28,31) have been reported. As a rule, long-range oscillatory profiles are measured. The oscillation period is directly related to the reticular distance of the smectic phase. These oscillations are often superimposed upon a non-zero background. Horn *et al.* found a repulsive long-range background (30) whereas medium-range attractive baselines are reported in two other studies (27,28). No definitive interpretation about the non-zero background origin has been advanced up to now.

**Force Profile Analysis.** No such background is present in the lamellar force profile displays in Figure 2a. Within the accuracy of the device, the oscillations rest on a constant zero-force. According to the elastic model, Equation 1, the minimum position would scale like  $d_n = na_0 + 2d''$  while the maximum position varies like  $d'_n \approx \sqrt{n(n+1)}a_0 + 2d''$ .  $2d''$  is an offset in the extremum positions caused by the two layers covering the surfaces. Owing to specific interaction between surfaces and the monolayers of surfactant, the thickness of these adjacent layers does not necessary match the bulk layer thickness. The scaling laws are well verified giving a lamellar

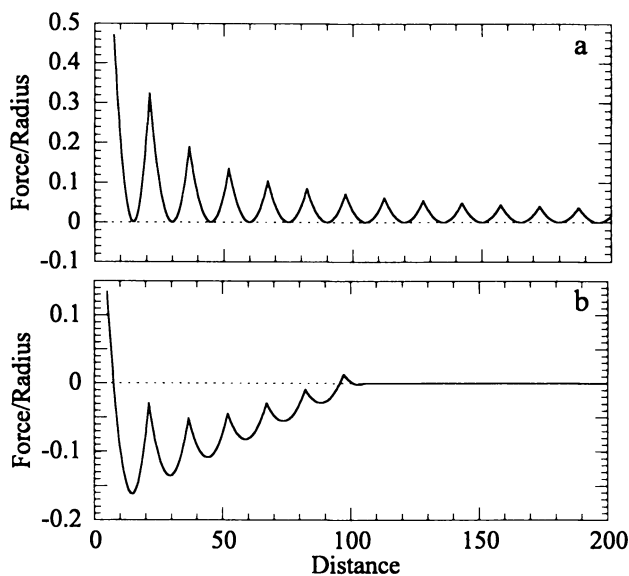


Figure 3. Modeling force profiles between a sphere and a plate confining a lamellar phase when an array of concentric elementary dislocation loops allows an homeotropic alignment. a) When the sample in the surrounding reservoir is lamellar and b) when the sample is non-lamellar and that a lamellar droplet is condensed between the surfaces.

layer thickness  $a_0 = 14.2 \pm 0.4$  nm and an extra thickness  $2d'' = 2.2 \pm 0.5$  nm. We then conclude that the measurements have been performed at (or nearly) thermodynamic equilibrium. The elastic stress has been released by the dislocation loop mechanism at the expected separations. This also supports the initial assumption that the Burgers vector of defects is one, i.e. defects are pores or more precisely channels going through a layer of water or oil. As displayed in Figure 4a, the predicted parabolic shape of oscillations is in good agreement with the experimental data. In this figure, every oscillation has been fitted with the Derjaguin-like term of Equation 1, by substituting  $d$  by  $d - 2d''$ . The compressibility modulus  $\bar{B}$  is measured to be equal to  $3.5 \pm 0.5 \cdot 10^4 \text{ Jm}^{-3}$ . As seen in Figure 4a, the first oscillation ( $d_1 = 20.7$  nm) is right shifted with respect to the modeling profile. This indicates that the thickness of the first layer is smaller than the equilibrium thickness (14.2 nm) and therefore that the thickness  $2d''$  of layers covering the surfaces is actually larger than 2.2 nm as obtained previously.

In summary, the dislocation loop array model is sufficient to account for the whole force profile measured in the lamellar phase. Therefore, we conclude that the studied system naturally aligns its layers parallel to the mica surfaces, structural defects are nucleated or annihilated maintaining the constraint sample in thermodynamic equilibrium. Two characteristic parameters of the system have been determined from the fitting curves, namely the layer spacing and the layer compressibility modulus.

**Microemulsion Phase.** The force profiles measured in the  $\mu_e$  phase are now analyzed in terms of capillary condensation. From the measurements carried out in the  $L_\alpha$  phase, we know that SFA surfaces naturally orient the solvent layers parallel to the surfaces. They are ordering surfaces in regards to the lamellar order. The hydrophilic mica surfaces are actually wet by a water layer. In the  $\mu_e$  phase, the preferred wetting by water is a priori preserved, leading to a local layering. The induced 1D order does not propagate far from the surfaces, even at the onset of the first order  $L_\alpha/\mu_e$  transition,  $\Delta T \rightarrow 0^+$ . On the other hand, the threshold separation at which a capillary condensation would occur should increase on approaching the bulk transition boundary since the free energy difference ( $\mu$ ) between the two phases is progressively reduced. The same trend is observed in the evolution of force profiles on approaching the  $L_\alpha/\mu_e$  transition. The interaction range increases significantly when  $\Delta T$  is reduced. The number of oscillations increases from 4 to 9 over the temperature range scanned in the microemulsion. The trends predicted by the lamellar condensation model, Equation 3, are also qualitatively recovered. Oscillations with constant period resting on a linear attractive background are the features of the  $\mu_e$  profiles displayed in Figure 2. A parabolic shape of oscillations is more difficult to figure out due to the weak magnitude of oscillations, excepted close to the bulk temperature transition.

**X-ray Scattering.** As previously mentioned, the oscillation periods obtained from the force profiles increase progressively with the temperature. The periods have been measured as being the mean separation between two successive minima. We find



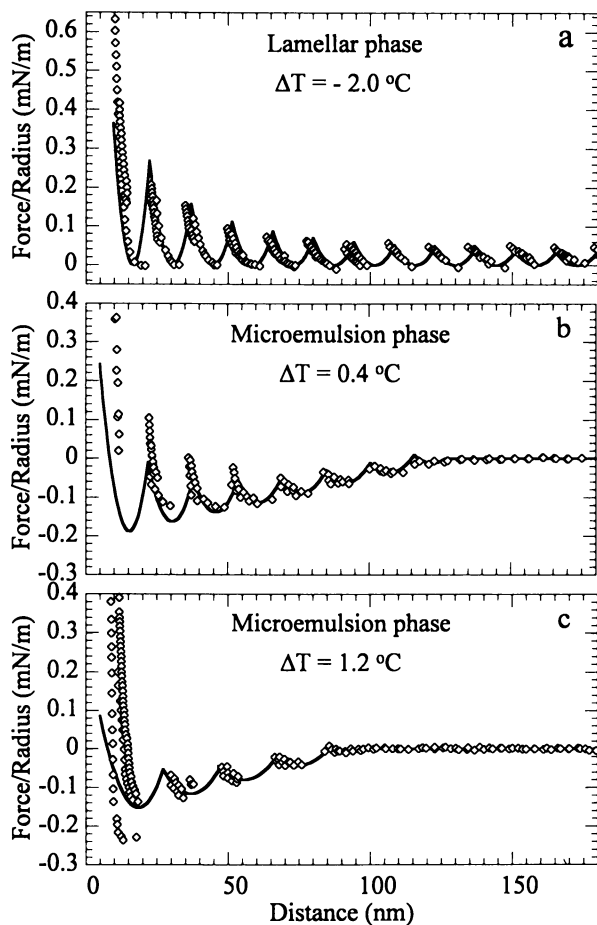


Figure 4. Comparison between experimental force profiles ( $\diamond$ ) and the modeling forces below and above the bulk phase transition. a) In the lamellar phase, the line is the Derjaguin-like term of the modeling force (Equation 1) with  $a_0 = 14.2$  nm,  $2d'' = 2.2$  nm and  $\bar{B} = 3.5 \cdot 10^4$  Jm $^{-3}$ . In the microemulsion phase, b) close to the transition. The line is the modeling force (Equation 3) with  $a_0 = 15.5$  nm,  $2d'' = 0$  nm,  $\bar{B} = 2.0 \cdot 10^4$  Jm $^{-3}$ ,  $2\gamma_{il}(1 - 2d_1/2R_k) = 1.710^{-5}$  Jm $^{-2}$  and  $2R_k - 2d_1 = 130$  nm, c) farther from the transition. The parameters are  $a_0 = 19.2$  nm,  $2d'' = 0$  nm,  $\bar{B} = 0.8 \cdot 10^4$  Jm $^{-3}$ ,  $2\gamma_{il}(1 - 2d_1/2R_k) = 1.510^{-5}$  Jm $^{-2}$  and  $2R_k - 2d_1 = 98$  nm.

14.2±0.4, 15.5±0.5, and 19.2±0.5 nm for  $\Delta T = -2.0, 0.4$  and  $1.2$  °C respectively. In order to compare these values with the characteristic sizes of the system, X-ray diffraction spectra of the sample have been measured, Figure 5. The reticular distance  $a_0$  of the  $L_\alpha$  phase has been found to slightly decrease as the temperature is raised, evolving from 16.5 nm for  $\Delta T = -2.0$  °C to 15.0 nm for  $\Delta T = -0.3$  °C. These lamellar spacings are in good agreement with the oscillation periods of force profiles measured near the transition, both above and below it. On the other hand, in the symmetric microemulsion the mean separation between domains of the same solvent,  $D$ , has been measured to be constant whatever the temperature,  $D = 21.1$  nm. This value is now substantially larger from the oscillation periods of force profiles obtained in the same phase, especially close to the transition. The microemulsion spectra have been analyzed according to the phenomenological model proposed by Teubner and Strey (32). A noteworthy result is the discontinuity in the characteristic sizes at the bulk phase transition. The spectrum of Figure 5b illustrates this discontinuous change well. The spectrum corresponds to a two-phase sample in which the microemulsion coexists with the lamellar phase for  $\Delta T = -0.1$  °C. The narrow Bragg peak of the  $L_\alpha$  phase contrasts markedly with the wide correlation peak of the microemulsion. The two corresponding characteristic sizes,  $a_0$  and  $D$ , are sufficiently different to be separated. This abrupt change at the transition contrasts with the regular evolution of oscillation periods on the both sides of the bulk transition temperature. This continuity indicates that the oscillatory profiles measured in the  $\mu_e$  temperature range are related to a lamellar domain condensed from the  $\mu_e$  sample. On the other hand, we do not have any interpretation to account for the increase in period above the transition while the opposite evolution is observed in bulk for the  $L_\alpha$  phase. However we note that the period gradually tends to the characteristic size of the microemulsion in bulk upon increasing the temperature.

**Refractive Index Profiles.** In addition to the force profile determination, the SFA also allows measurement of the refractive index of a sample confined between the two mica surfaces. The result is reported in Figure 6a for the  $L_\alpha$  phase ( $\Delta T = -2$  °C). The data are analyzed in terms of three-layer film. Two external layers of water having the same thickness,  $d_w$ , sandwich an homeotropic lamellar film. The mean refractive index of a three-layer film (33) as a function of thickness and refractive index of each layer is given by

$$\bar{n} = \eta_{H_2O} \eta_{L_\alpha} \left( \frac{d}{2d_w \eta_{L_\alpha}^2 + (d - 2d_w) \eta_{H_2O}^2} \right)^{1/2} \quad (4)$$

The best fit gives a lamellar refractive index  $\eta_{L_\alpha} = 1.395$  and a thickness  $d_w = 4.2$  nm for each water film covering the mica surfaces, Figure 6a. For purely technical reasons, measurements on both sides of separation about 200 nm are not reliable with the SFA and at separations lower than 15 nm the accuracy progressively worsens. From the new value of  $d_w$ , we can estimate the thickness of the first lamellar layer,  $d_1 - d_w \approx 12.5$  nm

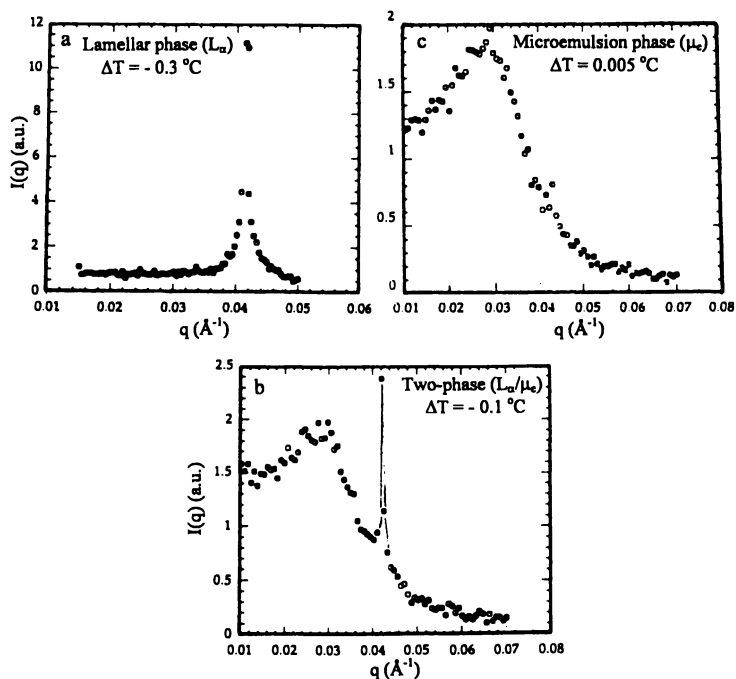


Figure 5. X-ray spectra upon increasing the temperature from the lamellar to the microemulsion phase. a) In the lamellar phase with a sharp Bragg peak, c) in the microemulsion where a broad correlation peak emerges and b) in the coexisting two-phase domain where the Bragg and the correlation peak reveal distinct characteristic size for each phase.

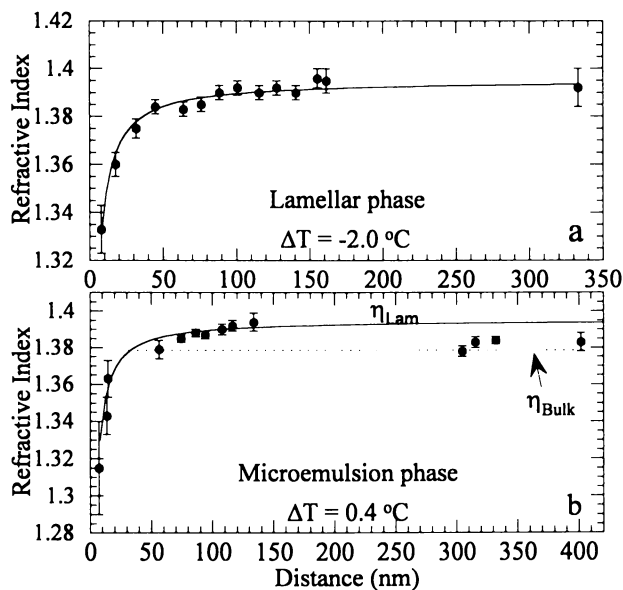


Figure 6. Refractive index profiles. a) For the lamellar phase. The experimental data (●) are fitted by a three-layer film model (Equation 4) with two outer water layers of thickness  $d_w = 4.2$  nm and a sandwiched lamellar film of refractive index equal to 1.395. b) For the microemulsion phase. At small separation the data (●) are still reasonably well fitted by the three-layer film model with the previous lamellar parameter values (full line) but not at larger separations where the measured values are now close to the bulk microemulsion refractive index (dotted line).

(<  $a_0=14.2$  nm). It appears that the layer thickness increase from the surfaces to the bulk, however the asymptotic value  $a_0$ , is promptly reached as shown in Figure 4a.

Equivalent measurements have been performed at a higher temperature  $\Delta T=1.4$  °C, in the  $\mu_e$  phase, Figure 6b. In this Figure, we have reported the fitting curve obtained with the lamellar data. The agreement is reasonable at short separations,  $d<15$  nm, whereas the data are systematically smaller at large separations,  $d>30$  nm. The refractive index of the microemulsion measured independently with a refractometer is also reported in Figure 6b (dotted line). The corresponding value agrees fairly with that in the confinement measured at large separations and deviates significantly at smaller separations. These results are again in agreement with a lamellar condensation from the  $\mu_e$  phase even if no direct evidence of the transition is present in the refractive index profile of Figure 6b.

**Force Profile Analysis.** Fits with the full modeling force (Equation 3) have been completed on the microemulsion profiles for which the oscillations are well marked, Figure 4b and 4c. The agreement is very reasonable, even if the oscillation before the contact is never well adjusted. As mentioned previously, the lamellar model does not take in account the variation of the period for the ultimate oscillations before the contact. As illustrated by the diminution of oscillation amplitudes, the layer compressibility modulus is found to decrease as the temperature rises.  $\bar{B}$  is found to be equal at  $2.0 \cdot 10^4$  and  $0.8 \cdot 10^4 \text{ Jm}^{-3}$  for  $\Delta T=0.4$  and  $1.2$  °C respectively. This result is consistent with the simultaneous increase in oscillation period (15.5 and 19.2 nm) since the Helfrich interaction (34) between nonionic surfactant monolayers is supposed to stabilize the  $L_\alpha$  phase. Because we do not know the thickness  $d_1$  of the pre-wetting films, we can only estimate the order of magnitude of the interfacial tension  $\gamma_{||}$ . The magnitude of the attractive background seems quite constant whatever the temperature. The order of magnitude of the interfacial tension is of  $10^{-5} \text{ Jm}^{-2}$ . According to our knowledge, no measurement of parallel layer interfacial tension has been reported in the literature. Quillet *et al.* have however studied the interfacial tension between a  $L_\alpha$  phase and an isotropic phase (35) (sponge phase). They have analyzed the equilibrium shape of lamellar droplets dispersed in the isotropic phase in the coexisting domain. They have shown that the perpendicular component is much weaker than the parallel one,  $\gamma_{\perp} < \gamma_{||}$  and they have estimated  $\gamma_{\perp}$  to be about  $10^{-7} \text{ Jm}^{-2}$ . Our estimation of  $\gamma_{||}$  is consistent with these results.

**Previous Experimental Studies.** Three other studies with a SFA examining the condensation of lamellar droplet from an isotropic phase (11,12,20) have been reported in the literature. In two of them, the authors have evidenced a lamellar capillary condensation from a sponge phase (11,12). In the last study, the sample was also a bicontinuous microemulsion (20). In the former studies, two distinct force regimes were determined. At large separations, a weak oscillatory profile is ascribed to be due to the internal correlation of solvent micro-domains pre-ordered by the surfaces. At shorter separation, a second regime occurs related to the capillary condensation. Highly repulsive barriers are measured. This kind of behavior is often

met with regular  $L_{\alpha}$  phases (31). Two explanations are then advanced to account for that; either the lamellar sample is poorly aligned between the surfaces with frozen textural defects or the activation barriers (26,36) to nucleate relaxing structural defects (as dislocation loops for instance) are much larger than many  $k_B T$ . Out of equilibrium measurements are then performed with these systems, yielding irregular and stochastic force profiles, consisting of many repulsive barriers of random height. This behavior has been met with our three-compound system neither in the  $L_{\alpha}$  phase and nor in the  $\mu_e$  phase. Moreover, unlike with the sponge phase, only one oscillatory regime is present in the microemulsion force profiles. A second regime at larger separations, with period related to the characteristic size of the bicontinuous phase has never been observed with the  $\mu_e$  phase. This result is consistent with the conclusion reported by Petrov *et al.* with the other bicontinuous microemulsion system (20). Like us, the authors report only one oscillatory regime at short separations. However, their number of oscillations is very limited even close to the  $L_{\alpha}/\mu_e$  transition. Along a dilution line going towards the transition, this number seems frozen at three. With so few oscillations, a linear attractive background supporting them does not clearly emerge. As claimed by the authors, their profiles are not characteristic of a lamellar condensation in a confinement. They may be rather interpreted as presmectic profiles (21,37). As is quite usually, the surfaces may induce a local layering, a presmectic film consisting of no more than two layers for their system, whatever the distance to the transition since the transition is first order. A capillary condensation is never triggered off before the preordered films overlap at shorter separations, yielding then an oscillatory profile with a small fixed number of oscillations.

Petrov *et al.* have also found that by taking away the system from the bulk  $L_{\alpha}/\mu_e$  transition, the oscillation amplitudes gradually decrease and seem to vanish (20) at the onset of the demixing boundary where the water rich phase appears. A water droplet can be them trapped between the two surfaces near this second phase transition. However, in our case, this event occurs randomly only when the surfaces are separated apart after they have been first pushed together sufficiently close. Never the presence of a water droplet has been observed on approaching the surfaces. Therefore, we think that the attractive profile with no resolved oscillations (Figure 2e) is more likely reminiscent of the lamellar condensation rather than the condensation of water droplet. Indeed the range and the intensity of this attraction are similar to those of the oscillatory profile measured at a slightly lower temperature, see Figure 2d.

## Conclusion

In this work, we have studied the force profiles on both sides of a lamellar/microemulsion phase transition. In the  $L_{\alpha}$  phase, we have measured long-range oscillatory profiles. An elastic model successfully accounts for the features of these profiles. Physical parameters are then extracted, as the compressibility modulus or the reticular distance. In the  $\mu_e$  phase, we have measured short-range oscillatory profiles. We conclude that the microemulsion profiles result from a capillary condensation of lamellar droplet between the surfaces. A modeling force consisting in two contributions has been developed. A capillary force yields a linear attraction on

which oscillations superimpose due to the elastic deformation of the induced layers. The quantitative agreement between the model and the data allow us to measure the evolution both of the compressibility modulus and the layer spacing of the condensed phase at different temperatures and to estimate the interfacial tension between the two phases.

### Literature Cited

1. Derjaguin, B.V. *Acta Physicochim. URSS* **1940**, *12*,181.
2. Derjaguin, B.V.; Chauraeu, N.V. *J. colloid Interface Sci.* **1976**, *54*, 157.
3. Evans, R.; Marinin Bettolo Marconi, U.; Tarazona, P. *J. Chem. Phys.* **1986**, *84*, 2376.
4. Christenson, H. K. *Phys. Rev. Lett.* **1994**, *73*, 1821; Wanless, E. J.; Christenson, H. K. *J. Chem. Phys.* **1994**, *101*, 4260.
5. Christenson, H. K. *J. Colloid Interface Sci.* **1984**, *104*, 234; Christenson, H. K.; Blom, C. E. *J. Chem. Phys.* **1987**, *86*, 419.
6. Sheng, P. *Phys. Rev. A* **1982**, *26*, 1610.
7. Ocko, B. M.; Braslau, A.; Pershan, P. S.; Nals-Nielsen, J.; Deutsch, M. *Phys. Rev. Lett.* **1986**, *57*, 94.
8. Clark, N. A.; Bellini, T.; Malzbender, R. M.; Thomas, B. N.; Rappaport, A. G.; Muzny, C. D.; Schaefer, D. W.; Hrubesh, L. *Phys. Rev. Lett.* **1993**, *71*, 3505.
9. Menelle, A.; Russell, T. P.; Anastasiadis, S. H.; Satija, S. K.; Majkrzak, C. F. *Phys. Rev. Lett.* **1992**, *68*, 67.
10. Milner, S. C.; Morse, D. C. *Phys. Rev E* **1996**, *54*, 3793.
11. Antelmi, D. A.; Kékicheff, P.; Richetti, P. *J. Phys. II* **1995**, *5*, 103.
12. Petrov, P.; Olsson, U.; Christenson, H. K.; Milkovic, S.; Wennerström, H. *Langmuir* **1995**, *11*, 3928.
13. Als-Nielsen, J.; Christensen, F.; Pershan, P. S. *Phys. Rev. Lett.* **1982**, *48*, 1107; Pershan, P. S.; Als-Nielsen, J. *Phys. Rev. Lett.* **1984**, *52*, 759.
14. Mayes, A. M.; Russell, T. P.; Bassereau, P.; Baker, S. M.; Smith, G. S. *Macromolecules* **1994**, *27*, 749.
15. Israelachvili, J. N.; Adams, G. E. *J. Chem. Soc. Faraday Trans. 1* **1978**, *74*, 975.
16. Fisher, L. R.; Israelachvili, J. N. *J. Colloid Interface Sci.* **1981**, *80*, 528.
17. Christenson, H. K. *Phys. Rev. Lett.* **1995**, *74*, 4675; Christenson, H. K.; Yaminsky, V. V. *Langmuir* **1993**, *9*, 2448.
18. Crassous, J.; Charlaix, E.; Loubet, J.L. *Europhys. Lett.* **1994**, *28*, 37.
19. Christenson, H. K.; Fang, J.; Israelachvili, J. N. *Phys. Rev. B* **1989**, *39*, 11750.
20. Petrov, P.; Olsson, U.; Wennerström, H. *Langmuir* **1997**, *13*, 3331.
21. Moreau, L.; Richetti, P.; Barois, P. *Phys. Rev. Lett.* **1994**, *73*, 3556; Richetti, P.; Moreau, L.; Barois, P. *Phys. Rev. E* **1996**, *54*, 3556.
22. Parker, J. L.; Christenson, H. K.; Ninham, B W. *Rev. Sci. Instrum.* **1989**, *60*, 3135.
23. Zhou, X.; Lee, L.; Chen, S.; Strey, R. *Phys. Rev. A*, **1992**, *46*, 6479.
24. Nallet, F.; Prost, J. *Europhys. Lett.* **1987**, *4*, 307.
25. Herke, R. A.; Clark, N. A.; Handschy, M.A. *Phys. Rev. E* **1993**, *56*, 3028.
26. Richetti, P.; Kékicheff, P.; Barois, P. *J. Phys. II* **1995**, *5*, 1129.
27. Richetti, P.; Kékicheff, P.; Parker, J. L.; Ninham, B. W. *Nature* **1990**, *346*, 252.
28. Kékicheff, P.; Christenson, H. K. *Phys. Rev. Lett.* **1989**, *63*, 2823.
29. Derjaguin, B. V. *Kolloid Z.* **1934**, *69*, 155.
30. Horn, R. G.; Israelachvili, J. N.; Perez, E. *J. Physique* **1981**, *42*, 39.
31. Abillon, O.; Perez, E. *J. Physique* **1990**, *51*, 2543.

32. Teubner, M.; Strey, R. *J. Chem. Phys.* **1987**, *87*, 3195.
33. Ninham, B. W.; Sammut, R. A. *J. Theor. Biol.* **1976**, *56*, 125.
34. Helfrich, W. *Z. Naturforsch.* **1978**, *33a*, 305.
35. Quillet, C.; Blanc, C.; Kléman, M. *Phys. Rev. Lett.* **1996**, *77*, 522.
36. Pershan, P. S.; Prost, J. *J. Appl. Phys.* **1975**, *46*, 2343.
37. de Gennes, P. G. *Langmuir* **1990**, *6*, 1448.



## Chapter 5

# Near Surface Small Angle Scattering as a Means of Probing the Effects of Fluid Flow on Surfactant Aggregates Near a Solid Surface

Paul D. Butler

NIST Center for Neutron Research, National Institute of Standards and Technology, Building 235, Room E-151, Gaithersburg, MD 20899

A proximate wall imposes an anisotropic constraint on complex fluid systems. This constraint can lead to some interesting behavior in the liquid in the vicinity of the interface, particularly under flow. Flow near a surface is especially relevant to transport phenomena which are common in industrial applications and materials processing in general. Adsorbed layers have so far proven to be relatively impervious to flow. However, the near surface ordering of supramolecular aggregates can be dramatically influenced by the proximity of the surface, up to tens of microns from the wall. The recently developed near-surface SANS technique which addresses this issue is reviewed along with some successful applications of the technique.

Many of the technological applications of viscoelastic surfactant solutions depend on their drag reducing and shear thinning properties. While such systems have been extensively studied for some time now (1-11) the focus has almost always been on the bulk solution, whereas these important phenomena clearly must be governed by the interactions at the interface between the fluid and the wall. It is well known for example that a shear field can impart enough energy to a surfactant solution for it to exhibit a phase change (12-16). Not so well appreciated is the fact that, particularly for non Newtonian fluids, the near surface structure may differ significantly from the bulk structure and that the system may in fact undergo a quasi phase separation due to the vastly different shear rates between the bulk and near surface regions.

In order to probe these phenomena one needs a technique, or set of techniques, which can distinguish between interfacial and bulk effects. Reflectivity is one such

technique. However, it only gives information in the direction parallel to the interface normal. Recently developed non-contact atomic force microscopy (AFM) techniques (17-19) visualize structures in the plane perpendicular to the interface normal which are adsorbed onto the surface. Thus the combination of reflectivity and AFM shows promise for elucidating the morphologies of adsorbed layers (20,21). It is not clear however how to view these structures under flow or in viscoelastic solutions, as AFM is not capable of working in those environments at present. Viewing the structures in the near surface region (e.g. 10 to 50 microns from the surface) is more problematic. The near surface small angle neutron scattering (NSSANS) technique recently developed at Oak Ridge (22,23), in combination with standard SANS of bulk samples (24,25), addresses the problem of structures adjacent to the interface.

### The Near Surface SANS Technique

In the near surface SANS technique (22,26), the neutron beam is incident on a solid/liquid interface at an angle slightly above the critical angle for total external reflection, thus allowing a fraction of the beam to penetrate the solution and scatter from structures therein (Figure 1). NSSANS relies on attenuation of the beam by the liquid sample, and on the very small incident angle, to limit the depth which is probed. The distance traveled by the neutron in the solution increases dramatically as the depth of the scattering event increases. For example, for a  $0.3^\circ$  incident angle on a quartz/D<sub>2</sub>O interface ( $\theta_c = 0.23^\circ$ ), the angle of the incident beam in solution after correction for refraction is  $0.19^\circ$ . For  $4.75 \text{ \AA}^{-1}$  neutrons, simple geometric arguments dictate that neutrons scattered at a  $Q$  of  $0.02 \text{ \AA}^{-1}$ , near the middle of the  $Q$  range studied, from scattering events at a depth of  $50 \text{ }\mu\text{m}$ , must travel  $1.9 \text{ cm}$  in the D<sub>2</sub>O solution. Neutrons scattering from a depth of  $250 \text{ }\mu\text{m}$  must travel  $9.6 \text{ cm}$  in solution, nearly the full length of the cell. The path length for  $1/e$  attenuation at  $4.75 \text{ \AA}^{-1}$ , as measured from the sample transmission (the total cross-section for the solution  $\mu = 0.86 \text{ cm}^{-1}$ ), is only  $1.2 \text{ cm}$  (26). Thus contributions to the scattering from structures at a depth greater than  $50 \text{ }\mu\text{m}$  are minimal.

The cell, which is described in detail in reference (23) and represented schematically in Figure 2 consists of a  $1 \text{ mm}$  deep trough covered by a  $1 \text{ inch}$  thick slab of highly polished single crystal quartz. To ensure good laminar flow in the scattering region, the flowing fluid enters the trough through a series of small, evenly spaced holes from a large reservoir ( $10 \text{ mL}$  to  $15 \text{ mL}$ ), and exits through a large slit into another reservoir. The fluid is circulated and pumped with a gear pump.

After the usual SANS corrections for background and sensitivity, special corrections need to be applied due to the unique geometry of the cell. These corrections are detailed in ref (26). The corrections are for refraction, element of solid angle, reflections at the interfaces, effective scattering volume, and absolute intensity. The first term affects the  $Q$  values while the other corrections affect the pixel intensities.

In order to obtain the correct  $Q$  value corresponding to each detector pixel, the apparent scattering angle (the angle between the undisturbed primary beam and a line

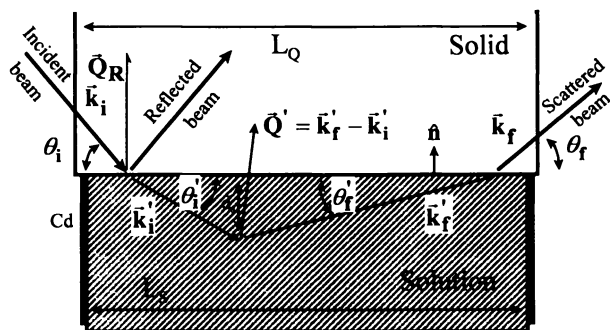


Figure 1. Schematic of the “optics” of the NSSANS experiment.

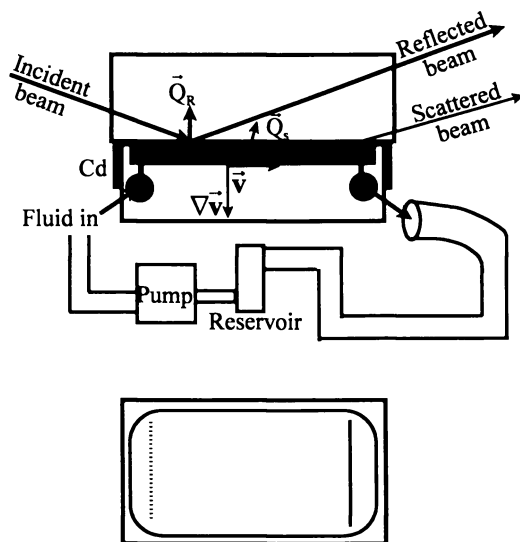


Figure 2. Schematic of the Poiseuille flow cell used in the NSSANS experiments.

drawn from the sample to the detector pixel) must be corrected for refraction as does the apparent incident angle. This transform can be expressed in Q space as follows:

$$\bar{Q}' = \bar{Q} + \hat{n} \left[ -\bar{Q} \cdot \hat{n} + \sqrt{(\bar{Q} \cdot \hat{n} - Q_r / 2)^2 - (Q_c / 2)^2} + \sqrt{(Q_r / 2)^2 - (Q_c / 2)^2} \right]$$

where  $\bar{Q}'$  is the true, or in-solution, momentum transfer and  $\bar{Q}$  is the apparent momentum transfer as reported by any standard SANS reduction program.  $Q_c$  is the critical Q (The Q below which there is total external reflection),  $Q_r = -2\mathbf{k} \cdot \hat{n}$  is the reflectivity Q, and  $\hat{n}$  is a unit vector normal to the interface. This correction is  $Q_y$  dependent with the strongest correction being at lower  $Q_y$  (closer to the horizon).

The refraction correction also affects the effective solid angle subtended by a given detector pixel, which in turn, affects the absolute cross-section value. However, the loss of intensity due to transmission effects from reflections at the interfaces nearly cancels the solid angle effect and neither of these corrections have been applied to date (see reference 26).

The volume of sample contributing to the scattering at a given pixel, which affects the absolute cross section value, depends on both the incident angle, which is fixed, and the exit angle, which varies with  $Q_y$ . Thus a larger sample volume contributes to the high  $Q_y$  scattering than contributes to the low  $Q_y$  scattering (close to the horizon). A secondary effect is that the higher  $Q_y$  data probes somewhat deeper into the solution than the low  $Q_y$  data. The effective sample volume (corrected for transmission) contributing to the scattering at a given  $Q_y$  (or  $\theta_f'$ ) is given by:

$$V_{\text{eff}}(\theta_f') = V(\theta_f') e^{-\mu_Q(L_Q - L_S)} \frac{1}{2} \left[ e^{-\mu_S L_S} + \left( \left[ \mu_S - \mu_Q \right] L_S - 1 \right) e^{-\mu_Q L_Q} \right] \times \left( \left[ \mu_S - \mu_Q \right] L_S \right)^{-2}$$

where  $V(\theta_f')$  is the geometrically accessible volume and can be calculated as:

$$V(\theta_f') \cong \frac{1}{2} W L_S^2 \left( \frac{1}{\tan(\theta_f')} + \frac{1}{\tan(\theta_f')} \right)$$

with  $\mu$  the total cross section (and  $e^{-\mu d}$  is the transmission through thickness  $d$ ) and the Q subscripts refer to superstrate quantities while S subscripts refer to solution quantities. W is the width of the neutron beam. Other quantities are defined in Figure 1.

Finally, the correction for beam flux cannot be made with calibrated standards in the usual way due to the geometry of the setup. However, in this geometry the data

contain the specularly reflected beam. This is an irritation in terms of making sure to keep important features away from it, but it does provide the opportunity to normalize the data to incident flux assuming the reflectivity curve has been measured previously. By reading off  $R(Q_r)$  from a reflectivity scan and taking into account the transmission through the solid superstrate and the effective beam area, one can calculate the incident beam flux.

### CTA Wormlike Micelles

Cetyltrimethylammonium surfactants (CTA) with certain aromatic counterions form viscoelastic solutions at quite low concentrations (below a mass fraction of 1%) (27). 3,5 dichlorobenzoate (35ClBz) is one such counterion (28). Further, mixing CTA35ClBz and CTAB provides a way of studying mixed counterion systems (i.e. a single surfactant moiety with a mixture of bromide and chlorobenzoate counterions with no added electrolyte). Due to the much greater affinity of the chlorobenzoate over the bromide for the micellar surface, it is expected that the degree of counterion binding is decreased as the proportion of bromide counterion increases, with the effect that, at least at high chlorobenzoate content, the wormlike micelles are stiffened by the increase in bromide counterion (29).

A system of 0.02 Mol/L surfactant, containing 0.7 mole fraction of CTA35ClBz and 0.3 mole fraction of CTAB, has been relatively extensively studied as it was the first system to show a very remarkable near surface ordering (22,24,25). Reflectivity measurements of this mixed counterion (MC) system shows that a relatively thin layer of surfactant of  $(25 \pm 5)$  Å is absorbed onto the quartz surface and is apparently impervious to flow (24). The structure of this layer while originally analyzed as a homogenous monolayer or intercalated bilayer is now suspected to be a layer of wormlike micelles absorbed onto the surface (24,21). Unfortunately, AFM cannot be used to clarify the lateral structure of this film due to the viscoelasticity of the solution.

NSSANS from this system at rest (22,24) gives rise to a rather diffuse featureless pattern without even any evidence of the isotropic interaction ring of scattering seen in the bulk. As soon as the system begins to flow however, a rather spectacular hexagonal pattern emerges indicating that even at relatively low average flow rates of several mm/s, the rods near the surface align themselves in the flow and arrange themselves such as to form a 'single crystal' undistorted hexagonal lattice oriented parallel to the adjacent surface (Figure 3). This lattice has the remarkable properties that the rods which sit at the lattice sites, separated by 45 nm from their nearest neighbors (or nine times their diameter of 5 nm), are presumably flowing past each other at many thousands of Angstroms per second (26). A more complete crystallographic analysis of the data (24) shows that the planes are separated by 39 nm with a peak  $\Delta Q/Q = (29 \pm 5)\%$  FWHM leading to a  $\Delta d/d$  of 27%. From the Debye-Waller factor,  $r_z$ , the amount of lateral motion of the rods around their lattice position in the direction normal to the interface is found to be  $(5.9 \pm 0.5)$  nm while a much less well defined  $r_x$ , the motion in the direction perpendicular

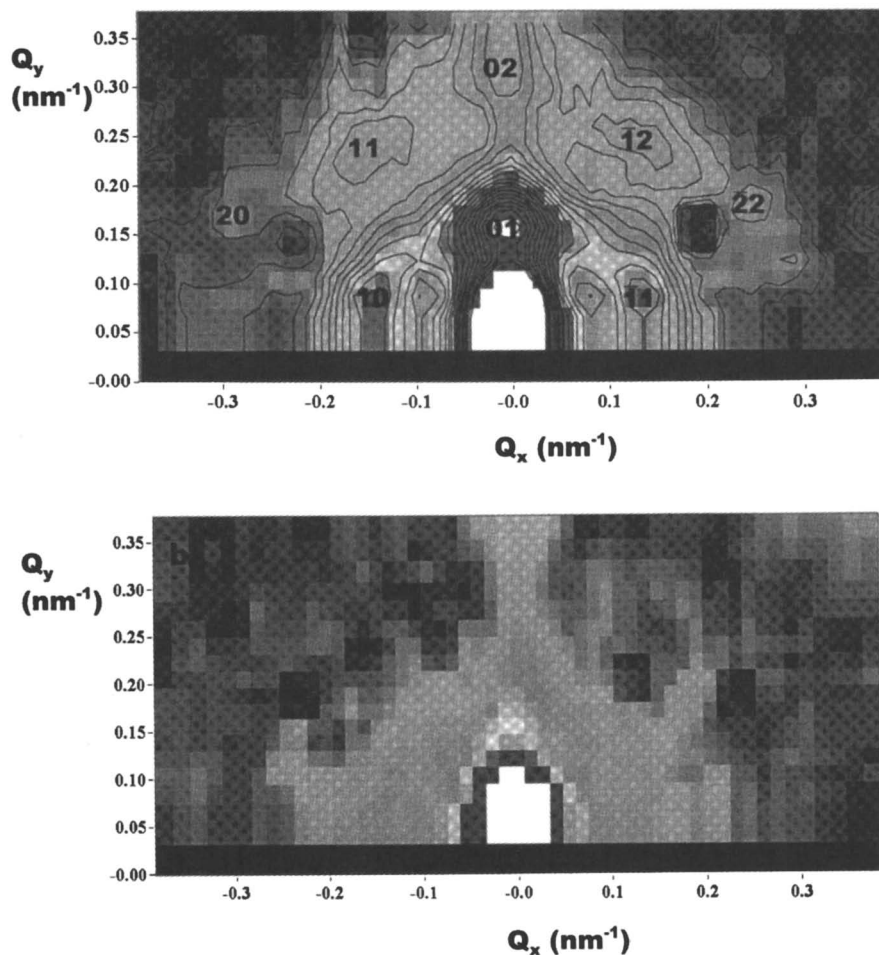


Figure 3. Corrected 2D data sets for the MC system (see text for details). a) shows the hexagonal pattern which forms under a flow rate of 9 mm/s. b) is a zero flow run (Reproduced with permission from reference 24. Copyright 1997 Royal Society of Chemistry.)

to the interface normal-flow direction plane is measured to be  $(6\pm 2)$  nm. The average orientational order over the depth probed is  $(25\pm 5)^\circ$  FWHM and the mosaic width of the 10 and 11 peaks are measured to be  $(7.5\pm 2.5)^\circ$ .

NSSANS only indicates the structure near the surface. In order to determine to what extent the hexagonal structure is a surface driven phenomenon, normal SANS measurements from bulk samples in a Couette shear cell were also performed (24). These indicate in fact that the rods in the bulk only align with the flow and act as a 2D liquid in the plane perpendicular to the flow. The existence in the shear SANS pattern of a second peak (Figure 4), consistent with a hexagonal lattice, is attributed to the near surface region of the sample. Thus it appears that the wall imposes more than a simple pinning constraint on the hexagonal ordering. Rather, it, and not the shear field, is solely responsible for driving the aligned rods into the hexagonal lattice.

Finally, time resolved measurements of the onset and decay of orientation of both the bulk SANS and the NSSANS reveal completely different relaxation kinetics between the surface hexagonal phase and the bulk 2D liquid phase (25,29,30), with a time constant on the order of 1500 s for the bulk phase relaxation and only 0.7 s for the near surface phase relaxation. The difference is not so dramatic for the onset of alignment with the surface phase alignment taking place in a few seconds whereas the bulk phase alignment though not well determined, is likely on the order of a few minutes (29,30).

### Nonionic (and "Doped" Nonionic) Wormlike Micelles

In the conclusion to reference 24, mention is made that a systematic study of different rodlike systems is necessary to get a handle on a theoretical framework for the interactions which lead to this remarkable behavior. In that vein, a study of a nonionic micelles of hexaethylene glycol hexadecyl ether ( $C_{16}E_6$ ) doped with small amounts of sodium hexadecylsulfonate ( $C_{16}NaSO_3$ ) ionic surfactant to controllably vary the micellar surface charge has been undertaken (31). The variation in persistence length of these micelles as a function of ionic dopant concentration has been studied extensively by Schurtenberger and Jerke (32) and thus was thought to provide an ideal model system with which to begin.

The original plan was to first find a point in phase space where the near surface shear induced isotropic-to-hexagonal phase transition is observed, and then to systematically change the persistence length and observe the effect on that transition. The system chosen was 0.03 Mol/L in  $C_{16}E_6$ . The mass of  $C_{16}NaSO_3$  dopant used was 6% of the mass of the nonionic surfactant (henceforth referred to as 6%) at  $35^\circ\text{C}$ . This system showed no near surface structure under shear. The amount of doping and the temperature were then varied with no success. Finally, small amounts of NaCl were added to the system in order to increase the overall contour length.

What was discovered at 0.008 Mol/L NaCl (10% ionic and  $26^\circ\text{C}$ ) was not a hexagonal phase but a lamellar phase (see Figure 5). Furthermore, this phase does not disappear up to at least 0.1 Mol/L NaCl as one might expect just from electrostatic

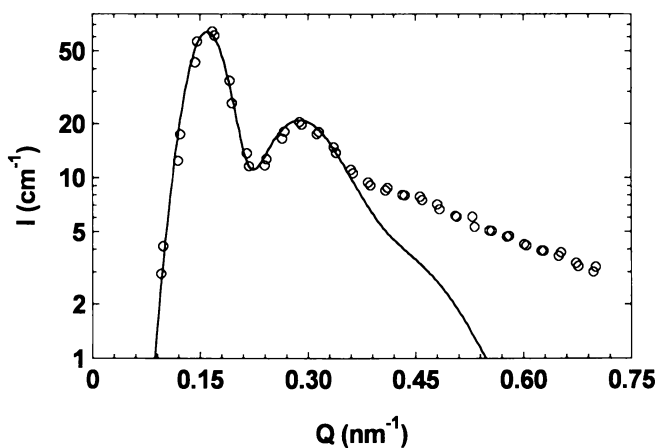


Figure 4. A 1D slice through the bulk Couette data set for the same system as in figure 3. The open circles are the data and the solid line represents the best fit to a hexagonal model. The undershoot at high  $Q$  indicates that the system is NOT hexagonal in the bulk and that the second peak most likely comes strictly from the near surface region. (Reproduced with permission from reference 24. Copyright 1997 Royal Society of Chemistry.)



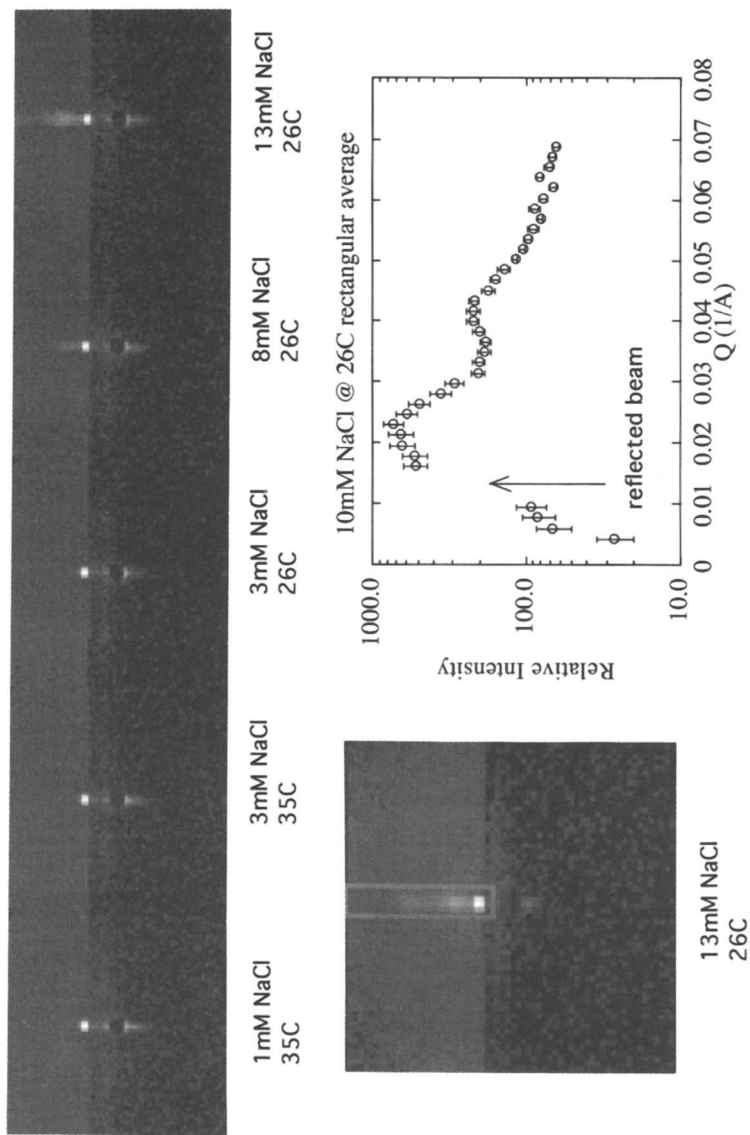


Figure 5. NSSANS from a solution 30 mmol/L in  $C_{16}E_6$  nonionic surfactant, with 10% (see text for detail) added  $C_{16}SO_3Na$  ionic surfactant with increasing amounts of NaCl. The inset graph is a 1D vertical slice through the highest salt concentration data set. Two distinct peaks are visible.

screening effects though there is evidence that the layers are undulating, thus smearing out the peaks into vertical streaks. There was also evidence for two distinct relaxations, one being very slow. Whether these extremely well ordered layers are due to a sheeting phenomenon or to a true micellar phase transition from rodlike to lamellar, is unclear. However, subsequent preliminary Couette experiments showed that the solution is in the isotropic micellar phase at rest and that in the bulk, the rods align only weakly with shear (see Figure 6). No alignment whatsoever is observed in the tangential mode, and no evidence for a lamellar structure was visible even at the highest shear rates available of roughly  $8000 \text{ s}^{-1}$ . Thus the alignment observed in this experiment is strictly a near surface phenomenon and represents a totally new near surface effect on flowing wormlike micelles.

### Limitations and Potential

This technique does have several limitations. First is the limited volume being sampled which means the signal must be quite strong. Practically this has meant it is limited to systems exhibiting Bragg scattering. Fortunately, the flat solid wall constraint seems to be conducive to the formation of very well ordered structures. Another limitation is the sample horizon effect which means that the symmetry around the  $Q_y=0$  line must be assumed. Worse, any inverse space structure near the  $Q_y=0$  line cannot be seen at all. Also, while it was possible to do a rocking curve on the hexagonal system and obtain the crystal mosaic, the rotation axes are limited by the geometry. For example it is not possible to get the mosaic of the lamellar phase since rotation about that axis would lose the signal either by going below the angle for total external reflection (no more beam in solution to do any scattering) or by raising the horizon over the Bragg peaks.

Nonetheless this technique has already proved to be a valuable tool in discovering ordering induced by the solid liquid interface in two systems and should be applicable to many other complex fluid systems including polymer solutions. While there have been relatively few applications of the technique so far, the author is aware of at least one group attempting to apply the technique to ceramic systems. This technique would be useful in observing near surface ordering even in the absence of flow if such ordering exists, or ordering in the presence of other applied fields such as magnetic or electric fields. Different surfaces can also be used to vary the contrast between the substrate and the solvent and they can be chemically modified to present different types of surfaces to the underlying solution. It is becoming clear that this relatively recent technique holds considerable promise for understanding the effects of surface proximity to ordering in solution under a variety of conditions.

### Acknowledgments

Some of the neutron scattering work was done on the 30m SANS and the MIRROR reflectometer at Oak Ridge National Laboratory (ORNL) which are supported by the U.S. Department of Energy under contract No. DE-AC05-96OR22464 with Lockheed Martin

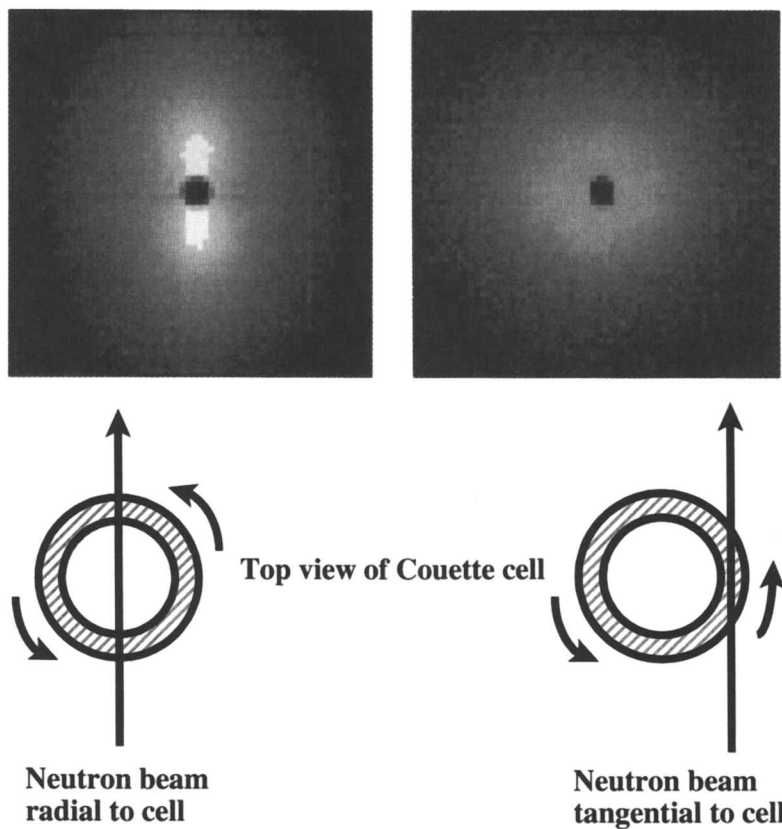


Figure 6. Data from a standard Couette SANS experiment on the same system as for figure 5 (13 mmol/L in NaCl at 26 °C). The nominal shear rate is 7780 s<sup>-1</sup>. Some alignment of the rods is observed in the radial view, while the tangential view is essentially isotropic. The tangential view is the closest to the orientation observed in the NSSANS geometry.

Energy Research Corp. The rest of the scattering measurements were performed at the National Institute of Standards and Technology (NIST), U.S. Department of Commerce, using the NG3 30m SANS. The NIST work is based upon activities supported by the National Science Foundation under agreement no. DMR-9423101. Development of the Poiseuille cell and the early work on the chlorobenzoate was a collaboration between the author, Shenda Baker, now at Harvey Mudd, Greg Smith and Roger Pynn of Los Alamos National Laboratory, William Hamilton and John Hayter of ORNL and Lee Magid of UT, the rest of the CTA chlorobenzoate work is a collaboration involving the author, William A. Hamilton and John Hayter of ORNL, Lee Magid of the University of Tennessee (UT), and Tania Slawewski of NIST. The nonionic work is a collaboration between the author and Lee Magid of UT, William A. Hamilton of ORNL, and Peter Schurtenberger and Cornelia Sommer of the ETH in Zürich.

Identification of certain equipment or materials does not imply recommendation by NIST.

## References

1. Laing, M. E.; McBain, J. W. *J. Chem. Soc.* 1920, *117*, 1506.
2. Nash, T. *Nature* 1957, *177*, 948.
3. Pilpel, N. *J. Phys. Chem.* 1956, *60*, 779.
4. Reis-Husson, F.; Luzzati, V. *J. Phys. Chem.* 1964, *68*, 3504.
5. Barker, C. A.; Sau, I. D.; Tiddy, G. J. T.; Wheeler, B. A.; Willis, E. *Faraday Transaction* 1973, *70*, 154.
6. Strivens, T. A. *Coll. Pol. Sci.* 1989, *267*, 269.
7. Rehage, H.; Hoffmann, H. *Faraday Discussions* 1983, *76*, 363.
8. Wunderlich, I.; Hoffmann, H.; Rehage, H. *Rheologica Acta* 1987, *26*, 532.
9. Makhloufi, R.; Hirsch, E.; Candau, S. J.; Binana-Limbele, W.; Zana, R. *J. Phys. Chem.* 1989, *93*, 8095.
10. Imae, T. *J. Phys. Chem.* 1990, *94*, 5953.
11. Rehage, H.; Hoffmann, H. *Molecular Physics* 1991, *74*, 933.
12. Rehage, H.; Hoffmann, H. *Rheologica Acta* 1982, *21*, 561.
13. Rehage, H.; Wunderlich, I.; Hoffmann, H. *Progress in Colloid and Polymer Science* 1972, *51*.
14. Kalus, J.; Hoffmann, H.; Chen, S.-H.; Lindner, P. *J. Phys. Chem.* 1989, *93*, 4267.

15. Hu, Y.; Matthys, E. F. *Journal of Rheology* 1997, *41*, 151.
16. Mendes, E.; Oda, R.; Manohar, C.; Narayanan, J. *J. Phys. Chem. B* 1998, *102*, 338.
17. Manne, S.; Cleveland, J.P.; Gaub, H.E.; Stucky, G.D.; Hansma, P.K. *Langmuir* 1994, *10*, 4409.
18. Manne, S.; Gaub, H.E. *Science* 1995, *270*, 1480.
19. Manne, S.; Schäffer, T.E.; Huo, Q.; Hansma, P.K.; Morse, D.E.; Stucky, G.D.; Askay, I.A. *Langmuir* 1997, *13*, 6382.
20. Schulz, J. C.; Warr, G. G.; Hamilton, W. A.; Butler, P. D. presented at the *20th Australian Colloid and Surface Chemistry Student Conference "Neutron Reflectometry of Thin Surfactant Films"*, Handorf, South Australia, Australia. Feb 9-13, 1998.
21. Schulz, J. C.; Warr, G. G.; Hamilton, W. A.; Butler, P. D. submitted to *Journal of Physical Chemistry B*.
22. Hamilton, W. A.; Butler, P. D.; Baker, S. M.; Smith, G. S.; Hayter, J. B.; Magid, L. J.; Pynn, R. *Phys. Rev. Lett.* 1994, *72*, 2219
23. Baker, S. M.; Smith, G.; Pynn, R.; Butler, P. D.; Hayter, J. B.; Hamilton, W. A.; Magid, L. *Review of Scientific Instruments* 1994, *65*, 412.
24. Butler, P. D.; Hamilton, W. A.; Magid, L. J.; Hayter, J. B.; Slawewski, T. M.; Hammouda, B. *Faraday Discussion* 1997, *104*, 65.
25. Butler, P.D.; Hamilton, W. A.; Magid, L. J.; Slawewski, T. M.; Han, Z.; Hayter, J. B. *Physica B* 1997, *241-243*, 1074.
26. Hamilton, W. A.; Butler, P. D.; Hayter, J. B.; Magid, L. J.; Kreke, P. J. *Physica B* 1996, *221*, 309.
27. Gravsholt, S. *J. Coll. Int. Sci* 1976, *57*, 575.
28. Carver, M.; Smith, T. L.; Gee, J. C.; Delichere, A.; Caponetti, E.; Magid, L. J. *Langmuir* 1996, *12*, 691.
29. Butler P. D., Magid L. J., Hamilton W. A., Hayter J. B., Hammouda, B., Kreke P. J. *J. Phys. Chem.* 1996, *100*, 442.
30. Hamilton, W. A.; Butler, P. D.; Magid, L. J.; Han, Z.; Slawewski, T. M., *submitted to Physical Review* as well as other very recent, as yet unpublished results measuring the near surface hexagonal alignment onset and decay times.
31. Work in progress. Details will be published elsewhere in the near future.
32. Jerke, G. Ph.D. dissertation, "Structure and Flexibility of Polymer-like Micelles", ETH-Zürich, #12168, 1997.

## Chapter 6

# Phase Diagram of Positively Charged Catanionic Surfactant Aggregates: The Myristic Acid–Cetyltrimethylammonium Hydroxide–Water System

M. Dubois<sup>1</sup>, J.-C. Dedieu<sup>2</sup>, B. Demé<sup>3</sup>, Th. Gulik-Krzywicki<sup>2</sup>,  
and Th. Zemb<sup>1</sup>

<sup>1</sup>Service de Chimie Moléculaire (CEA/Saclay),  
F91191 Gif sur Yvette Cedex, France

<sup>2</sup>CGM, CNRS, F91191 Gif sur Yvette Cedex, France

<sup>3</sup>Institut Laue-Langevin, F38042 Grenoble Cedex, France

**Abstract:** Mixing anionic surfactants with H<sup>+</sup> counter-ions and surfactants with OH<sup>-</sup> counterions produces positively charged surfactant aggregates in strong electrostatic interactions. The phases found are a dilute phase of uncorrelated discs of finite size (U), a nematic phase (N<sup>+</sup>), a lamellar phase (L <sub>$\beta$</sub> <sup>+</sup>), and an isotropic phase of giant micelles. We show that the extension of the single phase regions in this pure catanionic surfactant system is critically dependent on the efficiency of the ion exchange and the amount of dissolved CO<sub>2</sub> in the sample. The ternary phase diagrams obtained when the cationic component is in excess and the samples open to the atmosphere are compared to the corresponding case under nitrogen.

Our aim in this work was to produce surfactant aggregates with strong electrostatic interactions. Strong long range interactions of electrostatic origin are present if dissociated ionic species are reduced as much as possible in the solvent. A good system to produce such aggregates is therefore provided by mixtures of cationic and anionic surfactants (catanionic surfactants) which generally have a cmc at least one order of magnitude lower than the cmc of anionic or cationic surfactants alone<sup>1</sup>.

By mixing anionic and cationic surfactants, the reduction in area per headgroup due to ion pairing induces the formation of molecular bilayers which become the preferred microstructure at low concentration. Thus, vesicles may be the thermodynamically stable state in dilute solution. Indeed, Kaler and coworkers have shown that vesicles produced in catanionic surfactant systems are a thermodynamically stable state<sup>2</sup>. In the absence of electrostatic repulsion stabilizing the system, the catanionic bilayers spontaneously form closed vesicles<sup>3</sup>.

Upon mixing, for example, the common sodium or chloride salts of an anionic and a cationic surfactant the resulting ionic strength due to the counter-ions is higher than 0.1M, for a typical catanionic weight content of 5%. Due to the high ionic strength between aggregates, electrostatic repulsions are screened. The osmotic pressure of these aggregates is lower than 100 Pa and thus difficult to measure. Hoffmann and coworkers have published pioneering studies of catanionic without excess salt having obtained strongly repulsive charged cylinders of limited length<sup>4</sup>.

« Pure », i.e. salt-free, catanionic solutions in the absence of excess salt have a high osmotic pressure due to strong electrostatic interactions between adjacent bilayers. These interactions vary as  $w^{-2}$ , where  $w = D^* \cdot t$  is the thickness of the water layer,  $D^*$  the periodicity and  $t$  the bilayer thickness. When the concentrations of ions present is reduced to the dissociation equilibrium of water, there is an increase by a factor of 10 to 100 in the repulsive pressures stabilizing the colloidal assembly. A catanionic solution of high stability induced by osmotic pressure would contain only the anionic and the cationic surfactant. We use the counter-ions  $H^+$  and  $OH^-$  to produce water molecules instead of excess salt. In the « pure » catanionic systems we describe here, the ionic strength remains lower than the millimolar range. Moreover, the phase diagram can be drawn as a triangle, with only two degrees of freedom. We use the weight fraction and the molar ratio as coordinates.

## MATERIALS AND METHODS

### a) Sample preparation

Pure catanionic solutions are obtained by mixing myristic acid ( $C_{13}COOH$ ) and the hydroxide ion-exchanged form of cetyltrimethylammonium hydroxide ( $C_{16}N(CH_3)_3^+ OH^-$ ). Capillary electrophoresis analysis of the impurities ions present in the commercial form of the surfactant, have shown that in myristic acid, the ionic impurities are Sodium (0.1% molar fraction) and calcium (0.05% molar fraction). Obtaining pure carbonate-free hydroxide surfactant requires the use of a glove box under nitrogen to avoid contact with atmospheric carbon dioxide. An aqueous solution (0.1M) of the bromide form of the surfactant (Sigma) was mixed with  $Ag_2O$  powder. The precipitated silver bromide was then centrifuged (2000rpm). In the remaining solution, the only detectable impurity was bromide at a level less than 0.1%. The ion exchange with hydroxide is higher than 99%.

### b) Wide angle and small-angle X-ray scattering

Wide angle SAXS experiments were used to identify the state of the surfactant tail groups in the aggregated structures<sup>5</sup>. The shape of the 001 peak, occurring at  $q$  close to  $1.5 \text{ \AA}^{-1}$ , is determined using an image plate in the focal plane of a Guinier-Méring camera, using copper  $K\alpha$  radiation, for a sample thickness of 1 mm and typical exposure time of 4 hours.

c) Small angle neutron scattering was performed on installations D11 and D22 at ILL with velocity selectors such that  $\Delta\lambda/\lambda \approx 0.1$ . Data reduction to an absolute scale ( $\text{cm}^{-1}$ ) was done using standard ILL procedures.

d) Freeze fracture electron microscopy experiments were performed using a procedure described previously for the swollen lamellar or vesicle phase of other cationic double tail surfactant solutions<sup>6</sup>.

## RESULTS AND DISCUSSION

Two quantities only control the composition of the quasi-ternary system. In the absence of excess counter-ions, the location of a sample in the ternary phase triangle will be calculated using the total amount of dry surfactant,  $w$  (in weight%), and the molar fraction of cationic surfactant  $r$ :

$$r = [C_{13}COOH]/([C_{16}N(CH_3)_3^+OH^-] + [C_{13}COOH])$$

Since myristic acid is insoluble in water, we have focused our attention on compositions where hydroxide is in excess ( $r < 0.5$ ,  $pH > 7$ ). The conductivity is dominated by the excess hydroxide counter-ions and the monomeric cationic surfactant, but both are at very low levels. Figure 1a shows the pH and conductivity of the samples with constant surfactant content (2%) and for different values of molar ratios  $r$ . When the sample is prepared via the standard ion exchange procedure, the lowest conductivity that can be obtained is close to 1 mS/cm. When bromide as well as carbonate anions are avoided, the conductivity is ten times lower and when  $r \rightarrow 0.5$ , this shows that the dominant residual ions are dissociated monomers at the cmc in the mixed system, of the order of 10-100  $\mu\text{mol/l}$ . The Debye length is thus larger than 30 nm and the aggregates are strongly coupled such that the interactions are not limited to the first neighbor.

When  $r \rightarrow 0.5$ , the surface charge decreases. As will be shown later, hydrocarbon chains are in the solid state. This ensures that the area per headgroup is close to 0.25  $\text{nm}^2$ , independent of the nature of the charge, i.e.  $\Sigma^+ = \Sigma^- \equiv 0.25 \pm 0.02 \text{ nm}^2$ . The structural charge, defined as the formal charge once all counter-ions are stripped off, is therefore one charge per headgroup. Assuming ideal mixing, the balanced structural charge of the bilayer formed is given in charge/ $\text{nm}^2$  by:  $Z = r\Sigma^+ + (1-r)\Sigma^-$ , where the area per molecule is expected to be reduced to 0.25  $\text{nm}^2$  via ion pair formation when hydrocarbon chains are frozen. Hence, one can estimate the surface potential using the Grahame equation<sup>7</sup>. Without information about the eventual binding of counter-ions which should be negligible in the case of  $H^+$  or  $OH^-$  species<sup>8</sup>, we introduce the full surface charge into the Grahame equation. The case of residual parasitic ions is more delicate since counter-ions like bromide are bound and reduce surface charge, but we neglected this term. The result is shown in figure 1b. If the osmotic pressure is evaluated assuming that a



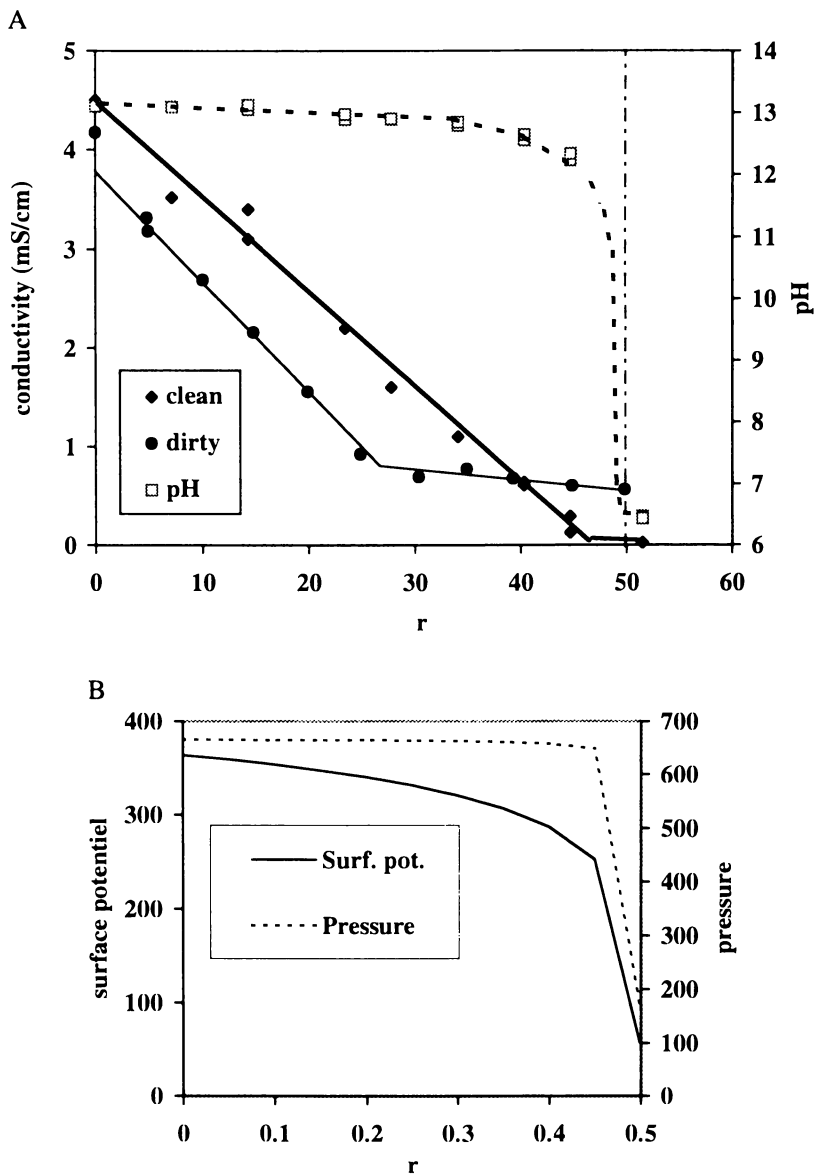


Figure 1. (a) pH and electrical conductivity of a  $w = 2\%$  solution of the cationic system described here, as a function of  $r$ , the molar ratio of the carboxylic acid. Dots are for the ion exchanged hydroxide form; filled squares are results obtained in the absence of bromide and carbonate. pH remains close to 12 for  $r < 0.45$ . (b) Estimated surface potential and osmotic pressure for the same samples.

lamellar phase is the microstructure<sup>9</sup>, an exceptionally large value of the order of 500 Pa is obtained.

**Rigid platelet characterization:** First, we consider the case of an optically isotropic dilute sample ( $w = 0.1\%$ ). Observed with the naked eye, the sample shows no evident turbidity compared with other catanionic solutions which have a bluish appearance due to the formation of spontaneous vesicles in these samples<sup>10</sup>. The sample turbidity is at least one order of magnitude less than for vesicles. Thus we could perform light scattering, experiments avoiding multiple scattering of concentrations less than  $2 \cdot 10^{-4}$  mg/ml and sample thicknesses of 8mm. However, an exceptionally intense neutron scattering signal has been measured in these samples. Within the  $q$ -range at the lower end of SANS experiments, static light scattering (Rayleigh ratio) varies as  $q^{-2}$  in the angular range accessible. These observations have established that the shape of the aggregates are flat on any scale less than a micron, thus, the in-plane persistence length is in the order of one micron<sup>11</sup>.

For the anionic and the cationic component, chain melting temperatures are above room temperature. We have investigated the state of the chains as a function of molar ratio  $r$ . At high excess of cationic surfactant, the chains melt at  $50^\circ\text{C}$ . From the shape of the wide angle X-ray scattering peak corresponding to the average interchain distance shown in figure 1b<sup>12</sup>, we can see that the hydrocarbon chains are frozen at room temperature. The scattering observed at  $50^\circ\text{C}$  is similar to the one observed in the spontaneous vesiculation case described by Kaler, when the hydrocarbon chains are in the liquid state. Closer to equimolarity, chain melting is not obtained at  $50^\circ\text{C}$ . Ion pair formation induces two dimensional crystallization of the chains. In these dilute samples, the scattering of the frozen chains was extremely low and could only be detected using an image plate detector and a focusing SAXS camera. The scattering intensity at the maximum of the Bragg peak given by the hydrocarbon chains, given on absolute scale, is only ten times larger than the incoherent scattering due to water compressibility ( $I = 0.016 \text{ cm}^{-1}$ )

In-plane crystallization of the hydrocarbon chains is one of the reasons for the high rigidity of the platelets. SANS experiments have demonstrated that the bilayer thickness is close to 4nm, thus a two dimensional array of alternating charges stabilize the bilayer in a sandwich-like structure. This layered structure of nanodiscs is responsible for the exceptionally high stiffness of the catanionic nanodiscs.

The stiffness of the discs has a counterpart in the concentrated regime, since a lamellar phase (positively charged bilayers with frozen chains:  $[L_{\beta_1}]$ ) is obtained. A typical scattering pattern obtained for a sample to detector distance of  $2.8 \text{ m}^{13}$ , is shown in figure 3a. After radial averaging, four reflection orders for this swollen phase are observed, as shown in figure 3b. The peaks are extremely sharp, with a FWHM of  $\Delta q/q_H \ll 10$  and spacings  $D^* = 2\pi/q_H$  much larger than bilayer thickness. These observations confirm the predominance of strong electrostatic repulsions, consistent with the calculation results shown in figure 2.

**The electron microscope pictures obtained after cryofracture** confirm the existence of discs, as well as a swollen lamellar phase with rigid chains. Figure 4a shows the most common situation: a swollen lamellar phase at maximum swelling in coexistence with nanodiscs. The same sample, heated to 50°C, consist of nanodiscs alone, as show on figure 4b. Figure 4c shows a giant rigid disc of several micrometers in diameter formed in a dilute solution at low cationic surfactant excess. Figure 4d shows the shrinking of those discs when the cationic excess molar ratio is increased Figure 4e shows a pure swollen lamellar [ $L_{\beta}$ .] Only micelles are obtained if the pure cationic component ( $L_1$ ) is present, as shown in figure 4f. Figure 4g shows the coexistence in terms of microphase separation between nematic and lamellar domains. Microphase separated nematic domains have anisotropic dimensions. The texture of this phase is similar to the one obtained in clay dispersions<sup>14</sup>.

**Disc size control:** If the edges of the nanodiscs were not covered by surfactant, rigid nanodiscs of bilayers could form only at high energy cost, of the order of  $\pi\gamma.t.D$ , where  $\gamma$  is the oil-water surface tension and  $D$  the disc diameter<sup>15</sup>. Indeed, we observe by electron microscopy a systematic decrease in disc diameter with molar ratio  $r$  at constant concentration  $w$ . The rapid decrease in size of discs in the region where  $0.45 > w > 0.35$  is due to charge separation: part of the excess of the cationic surfactant forms the edges of the discs. Adding excess cationic surfactant produces edges more easily and reduces the equilibrium size of nanodiscs. The final size is a balance between the entropy of mixing and electrostatic coupling between discs. Excess charge favors small discs until an abrupt change towards wormlike micelles. The situation here is similar to the abrupt transformation of vesicles in micelles described for flexible bilayers in the presence of salt<sup>16</sup>. Thus, the molar ratio of the two components gives us a direct way to control the nanodisc diameter.

## TERNARY EQUILIBRIUM PHASE DIAGRAM

Considering the results obtained on more than 100 samples of different composition ( $w,r$ ), we can locate the single phase regions in the water rich corner on the cationic side of the phase diagram (figure 5). Figure 5a shows the location of phases if sample preparation occurs in the absence of dissolved  $CO_2$ . Figure 5b shows the results obtained without preventing the sample from coming into contact between the sample and the air in the laboratory. In the presence of  $CO_2$ , and at low cationic excess ( $r < 0.7$ ), a diluted isotropic solution ( $U$ ) to nematic, then to smectic [ $L_{\beta}$ .] phase sequence is observed. The maximum concentration where unbound discs  $U$  are observed is  $w = 0.01$ . At  $r \approx 0.5$ , the lamellar phase in equilibrium collapses corresponding to  $w > 60\%$  (not shown on figure). When  $r$  decreases, the lamellar phase in equilibrium with uncorrelated platelets swells up to spacings  $D^*$  of 80 nm (25 nm in the absence of  $CO_2$ ). In the absence of dissolved carbonate, a nematic region is present and centered around  $w=10\%$ ,  $r = 0.4$ . At  $r < 0.35$ , the [ $L_{\beta}$ .] phase is in competition with giant micelles. Osmotic competition imposes a rapid shrinking of the maximum swelling of the lamellar phase. This effect has already been observed in other surfactant system in two phase regions, when a lamellar phase

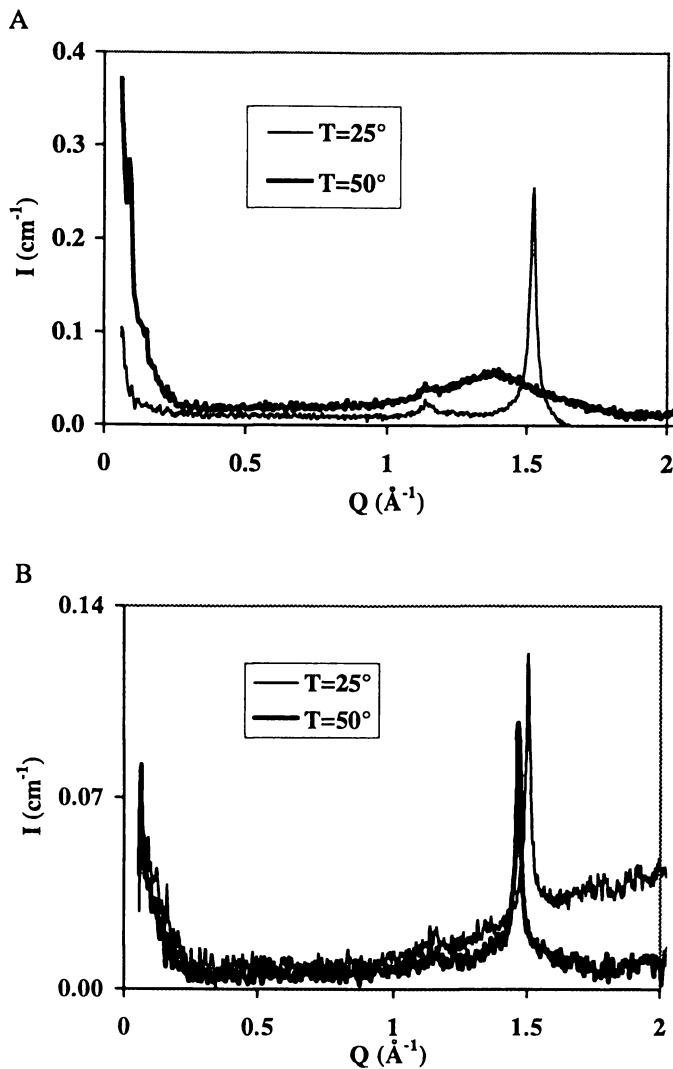


Figure 2. Wide angle X-ray scattering signal obtained on a Guinier-Mering camera at 25°C and 50°C using image plates. Sample compositions: 2a: ( $w = 0.17, r = 0.30$ ), 2 b: ( $w = 0.17, r = 0.40$ ). Broadening of the peak width demonstrates that the temperature of the transition from  $L_{\beta^+}$  (frozen chains) to  $L_{\alpha^-}$  (liquid chains) depends on molar ratio  $r$ .

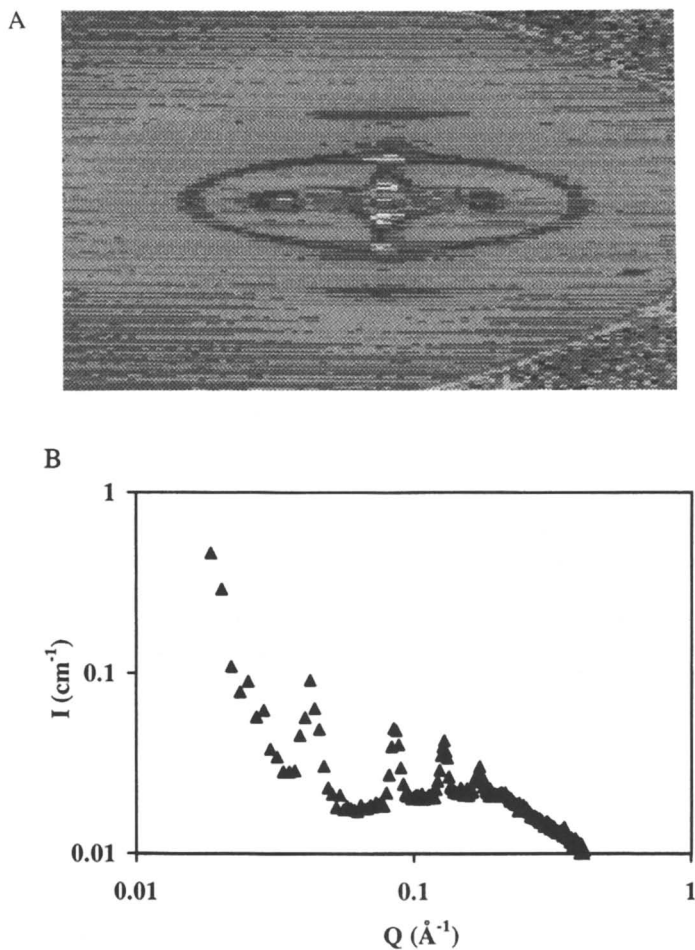


Figure 3. Small angle X-ray scattering spectra obtained for an  $L_{\beta}'$  phase: (a) raw data above chain melting temperature at  $T = 50^{\circ}\text{C}$  with two reflections (b) data when chains are frozen, four orders are observed, after radial averaging, a periodicity  $D^*$  of 20 nm is evidenced by the presence of four Bragg peaks. (sample composition:  $\phi = 17\%$ ,  $r = 0.296$ )

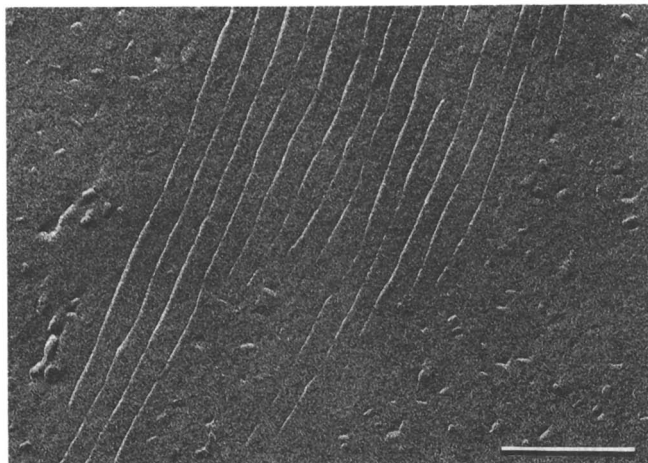
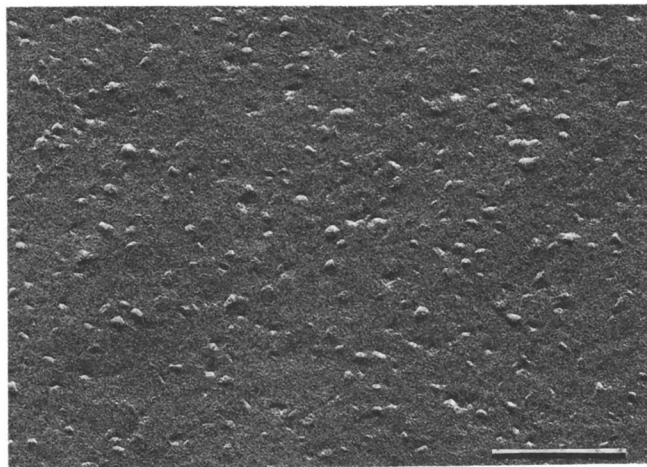
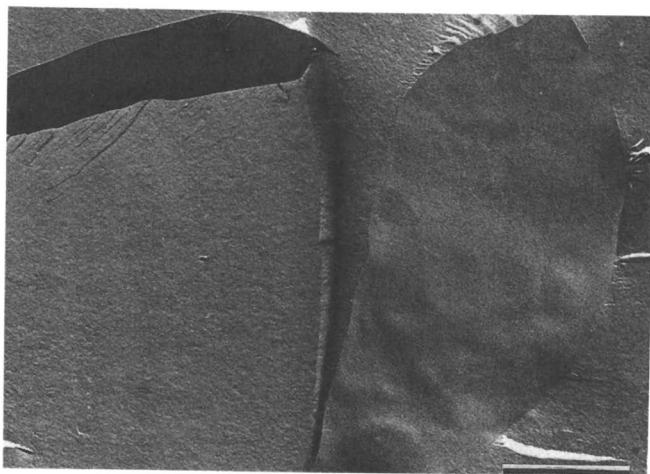


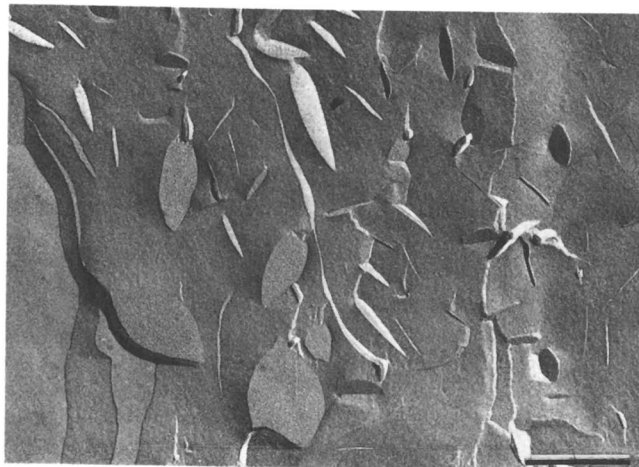
Figure 4. (a) image of an  $L_{\beta}^+$  phase with large nanodiscs; sample composition  $w = 3\%$ ,  $r = 0.39$ ; freeze fracture of a sample equilibrated at  $20^{\circ}\text{C}$ ; the scale bar is 250 nm.



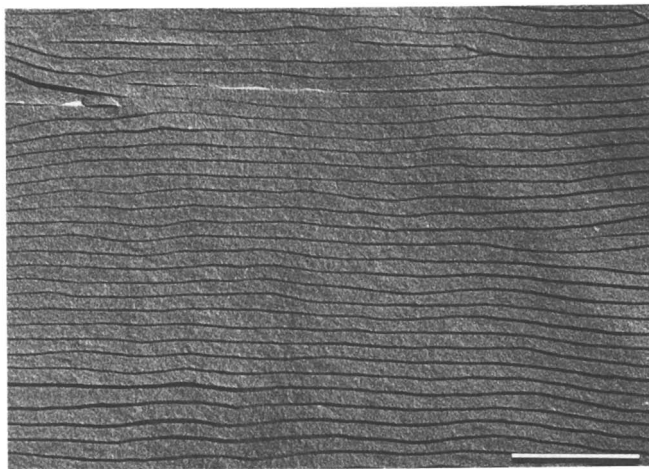
(b) nanodiscs alone; sample composition  $w = 3\%$ ,  $r = 0.39$  (same composition than a); freeze fracture for a sample equilibrated at  $50^{\circ}\text{C}$ ; the scale bar is 250 nm.



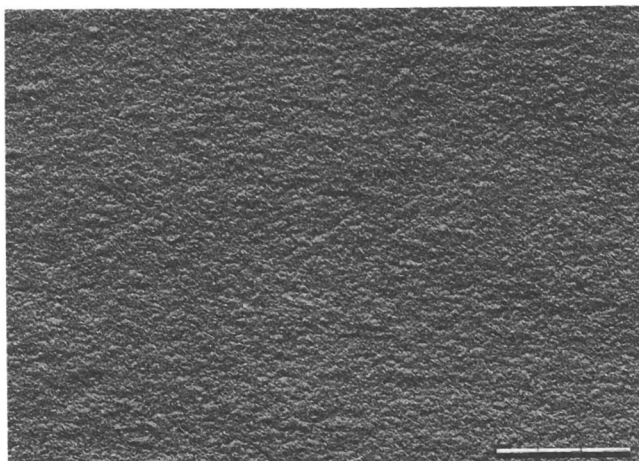
(c) typical giant stiff nanodiscs obtained at  $w = 0.17\%$  and  $r = 0.454$ ; the scale bar is  $1\ \mu\text{m}$ .



(d) large nanodiscs obtained for a sample composition  $w = 2.65\%$ ,  $r = 0.416$ ; the scale bar is  $500\ \text{nm}$ .

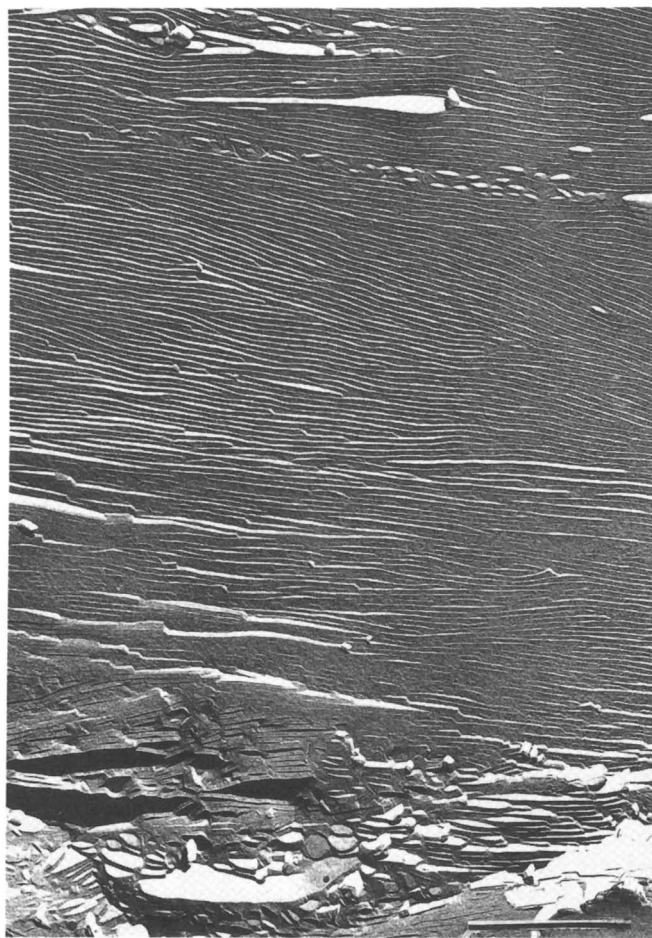


(e) extremely swollen  $L_{\beta}^+$  phase for  $w = 3.9\%$  and  $r = 0.447$ ; spacing is 80 nm; bar is 500 nm.



(f) giant micelles obtained with the pure hydroxide surfactant ( $w = 2\%$ ,  $r = 0$ ); bar is 250 nm.





(g) two inclusions of microphase separated nematic phase in a bulk lamellar phase; sample composition:  $r = 0.395$ ,  $w = 0.925$ ; bar is  $1 \mu\text{m}$ .

competes with smaller aggregates<sup>17</sup>. At low content of myristic acid ( $r < 0.1$ ), only giant micelles are obtained.

The charged  $L_n$  phase swells up to spacings of hundreds of Angstroms; even with frozen hydrocarbon chains. Its macroscopic appearance is a clear birefringent gel with surfactant in the range 1-10% mass content. For most phospholipids, including mixtures of charged and uncharged phospholipids, the swelling is limited to water thicknesses of only a few nanometers, ten times smaller than those reported here. Again, the only explanation is the complete absence of screening and ionic impurities such as carbonates. If the samples come into contact with the atmosphere, the order in a sample is present between bilayers are the excess hydroxide counter-ions of the positively charged nanoplatelet surface. In the absence of salt, the addition of a strong hydration force and an electrostatic repulsion overcomes the dispersion effect at any distance. This unique feature of the catanionic bilayers appears only with hydroxide ions in excess since there is no ion-interface dispersion force in the case of hydroxide ion<sup>8</sup>.

Since the diameter of the nanodiscs versus excess molar ratio is known, it is possible to evaluate the concentration of the semi-dilute regime of these objects. Excluded volume of a platelet of diameter  $D$  is of the order of  $D^3$ . For a diameter of 400 nm, the semi-dilute regime for rigid nanodiscs starts at volume fraction  $\phi \approx w = 2t / \xi$ . The thickness of the frozen chain hydrocarbon bilayer is 4 nm. For charged discs, an Onsager -type phase transition is expected to occur at a weight fraction around 1%<sup>18</sup>. The presence of dissolved carbonate and residual bromide ions probably charges the faces of the nanodiscs, as well as introducing some screening of electrostatic interaction, thus masking the nematic region and the nematic-isotropic coexistence.

**Comparison with other surfactant microstructures.** Other surfactant microstructures having some structures similar to nanodiscs have been previously described. For instance,

- finite sized needles of well defined persistence length<sup>19</sup> obtained in a pure catanionic system or platelets obtained in the presence of excess salt<sup>20</sup>
- mixing long and short chain zwitterionic phospholipids produces uncharged discs which orient in magnetic field<sup>21</sup>.

How do the nanodiscs described here differ from the range of microstructures seen for self-assembly of surfactants and lipids below the chain-melting transition? Solid colloidal particles are known to appear as fibers, helices or multilayered tubules made from flat sheets<sup>22</sup>. All these structures have a molecular length and a macroscopic size set by the low but finite curvature and produce myelinic figures in optical microscopy. To our knowledge, no microstructure of dispersed isolated flat discs with a thickness of nanometers and a diameter in the micron range has been reported.

The origin of the stiffness for this molecularly flat object is the 2D crystallization of an equal amount of positive and negative charges on both sides of the bilayer. A hexagonal lattice is formed on each surface. Bending the nanodisc to form tubules

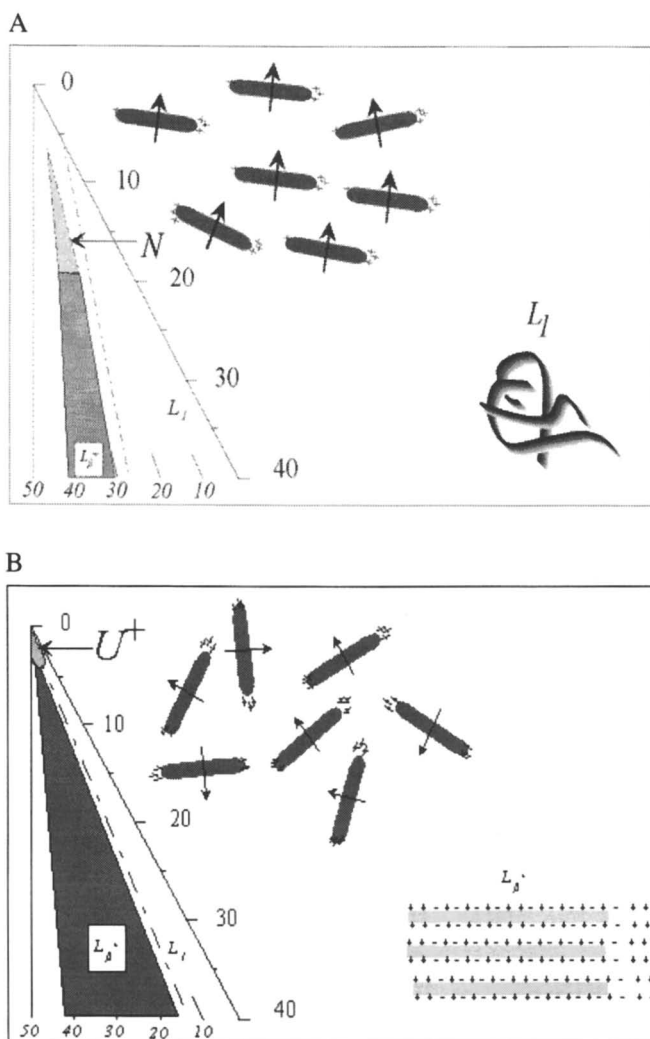


Figure 5. Partial ternary phase diagram; cationic half (right axis in total surfactant weight %, horizontal axis in molar ratio  $r$ ) obtained in the absence of dissolved  $\text{CO}_2$  (5a), and in contact with atmosphere (5b), showing the location of the micellar phase ( $L_1$ ), the swollen lamellar phase ( $L_\beta^*$ ), the nematic phase ( $N$ ) and the unbound phase containing randomly oriented nanodiscs ( $U$ ).

or fibers would require compression of the hexagonal lattice on one face and extension on the other.

### CONCLUSION: POSSIBLE USES OF NANODISCS

The main features of rigid nanodiscs are:

- A rigid outer layer of low charge and ion pairs forming the faces.
- The edge contains a larger quantity of the excess ion.
- The chains are frozen at room temperature.
- In-plane correlation length of discs can be as large as a micrometer.

The nanodiscs form spontaneously upon mixing an anionic surfactant with H<sup>+</sup> counter-ion and cationic surfactant with an OH<sup>-</sup> counter-ion. Provided that the ionic headgroup sizes and chain length are compatible, stiff discs of nanometric thickness and micron-size lateral extension are formed. The observation of still nanodiscs instead of closed vesicles in the diluted region of the phase diagram is due to chain crystallization. These discs are at thermodynamic equilibrium whose their size is controlled by the competition between mixing entropy and the coverage of the lateral faces. A similar competition between mixing entropy and bending energy in flexible bilayers has been shown to be the origin of the formation of spontaneous vesicles<sup>23</sup>.

Since the morphology obtained with catanionic mixtures is suitable for producing mesoporous materials or orienting solubilized molecules, the size, surface potential and electrokinetic properties of this new type of rigid colloidal particles may be considered for molecular templating. The colloidal properties should present some similarity with clay systems, such as flocculation via salt-induced tactoids.

The nematic phase of rigid nanodiscs includes an exceptionally high amount of water (up to 95%). This may be used to obtain anisotropic movement for non-polar molecules dissolved in the solvent, such as oligopeptides<sup>24</sup>.

Finally, it is likely that this type of stiff catanionic platelet could be used as an easy-to-remove template surface for inorganic polymerization of inorganic oxides: for example as flat or folded silica platelets of nanometric thickness, such as those produced using a surfactant aggregate as a template<sup>25</sup>.

### REFERENCES:

- 1 Khan, A.; Marquès, E.; *Specialist surfactants*, I. D. Robb Ed. (Chapman et Hall, Glasgow), **1996**, pp. 37
- 2 Kaler, E. W.; Kamalakara, A.; Murthy, B. E.; Rodriguez, J. A.; Zasadzinski, *Science*, **1989**, *245*, pp. 1371
- 3 Kaler, E. W.; Herrington, K. L.; *J. Phys. Chem.*, **1992**, *96*, pp. 6698; Brasher, L. L. and Kaler, E. W. *Langmuir* **1996** *12*, pp. 6270.

- 4 Hoffmann, H.; Kalus, J.; Schwander, B., *Ber. Bunsenges. Phys. Chem.*, **1987**, *91*, pp. 99
- 5 *Handbook of Lipid Research IV*; D. M. Small ed. , Plenum Press, London, **1986**, Chapter 3
- 6 Dubois, M.; Zemb, Th., *Langmuir*, **1991**, *7*, pp. 1352
- 7 J. Israelachvili; Intermolecular and surface forces; Academic Press, London, **1991**, 2nd edition
- 8 Ninham, B. W.; *Langmuir*, **1997**, *13*, 2097
- 9 Dubois, M.; Zemb, Th.; Levitz, P.; Belloni, L.; *J. Chem. Phys.* **1992**, *96*, pp. 227
- 10 Dubois, M.; Zemb, Th.; Demé, B.; Gulik-Kryzwicki, Th.; *Comptes-rendus Acad. Sci. Paris*, **1998**, in press
- 11 Dubois, M.; Gulik-Kryzwicki, Th.; Demé, B.; Zemb, Th. *Comptes-rendus de l'Acad. Sci. paris III*, **1998**, in press
- 12 Tardieu, A.; Luzzati, V.; Raman, F. C.; *J. Mol. Biol.* **1973**, *75*, pp.711
- 13 Le Flanchec, V.; Gazeau, D.; Taboury, J.; Zemb, Th.; *J. Appl. Cryst.* **1996**, *29*, pp. 1
- 14 Van Damme, H.; Levitz, P.; Fripiat J.J.; Alcover, J.F.; Gatineau, L.; Bergaya, F.; "Clay minerals: a molecular approach to their fractal microstructure", N. Boccara and M. Daoud Eds, Springer-Verlag, Berlin, 1985, pp. 24-30
- 15 Fromherz, P.; *Ber. Bunsenges. Phys. Chem*, **1985**, *85*, pp. 891
- 16 Södermann, O.; Herrington, K.L.; Kaler, E.W.; Miller, D.D.; *Langmuir*, **1997**, *13*, pp. 5531
- 17 Ricoul F. et al., *European Phys. J.*; **1998**, *4*, n°3, pp333-340
- 18 Forsyth, P. A.; Marcelja, S.; Mitchell, D.J.; Ninham, B. W.; *J. Chem. Soc. Farad. Trans. II*, **1977**, *73*, 84 .
- 19 Hoffmann, H.; Kalus J. and Schwander, B. *Ber. Bunsenges. Phys. Chem.*, **1987**, *91*, 99
- 20 Tamori K. et al., *Colloid and polymer Sci.*, **1992**, *270*, 885
- 21 Vold, R.R. and Prosser R.S., *J. of Magn. Resonance*, **1996**, *B113*, 267
- 22 Furhop, J. H. and Helfrich, W. ; *Chem. Rev.* , **1993**, *93*, 1565-1582
- 23 Safran, S.; Pincus, P.; Andelmann, D.; *Science*, **1990**, *248* ,354
- 24 Tjandra, N. and Bax, A., *Science*, **1997**, *278*, 1111
- 25 Dubois M; Cabane B; *Langmuir* **1994**, *10*, 1615; Mc Grath, K. M. et al., *Science* **1997**, *277*, 552

## Chapter 7

# On the Microscopic Nature of Stick–Slip Behavior in Lubricating Films

Peter Harrowell

School of Chemistry, University of Sydney, Sydney,  
New South Wales 2006, Australia

The experimental characterisations of the static and dynamic properties of thin liquid films between solid surfaces are reviewed, along with the theoretical models that have been proposed to account for their rich phenomenology. A critical discussion is presented of the degree to which the proposed models make connection with the experimental studies and the questions that remain to be resolved.

### I. Introduction

The aim of this essay is to provide a critical review of the current models of stick-slip motion of solid surfaces separated by thin liquid films. The present interest in this phenomenon has been driven by extensions (1,2) of the surface force apparatus (SFA) which permit the study of boundary lubrication on microscopic scales. These remarkable experiments have, in turn, inspired a wealth of computer simulations and mathematical modelling. Among the intriguing structural and dynamics features of confined liquids, it is the appearance of film rigidity at temperatures well above the bulk freezing or vitrification points which has generated perhaps the greatest interest. The appearance of stick-slip dynamics in such films under shear provides valuable model systems to study this ubiquitous process without the irreversible surface wear typically accompanying stick-slip sliding between dry surfaces. This paper will examine the various physical models which have been invoked to account for the mechanical properties of the thin liquid films and their rheology in the hope of sorting out what connection these models make with the experimental studies, what issues can be regarded as resolved and what questions remain.

### II. The Experiments

**A. Liquid Layering.** Most of the experiments described in this review will involve the behaviour of smooth solid surfaces moving laterally with respect to one another. It is useful to start, however, by considering the response of the intervening liquid to the

relative motion of the surfaces in the normal direction. The force between mica surfaces separated by a liquid of quasi-spherical non-polar molecules, such as octamethylcyclotetrasiloxane (OMCTS) (3,4), cyclohexane (5), tetrachloromethane, benzene and 2,2,4-trimethylpentane (6), is found to oscillate as a function of the separation once the surfaces are within roughly 5 molecular diameters of each other. The wavelength of the oscillation is constant, approximately equal to the molecular diameter, and the amplitude increases with decreasing distance. The oscillatory force is interpreted as a consequence of the layering of the liquid molecules against the mica surfaces. Rather than being continuously expelled from the intervening gap, the liquid tends to be squeezed out in quanta corresponding to single complete layers. This tendency increases with decreasing separation between the surfaces, a consequence of the increasing layered structure, which, in turn, gives rise to the observed growth in the amplitude of the normal force. The maxima in the normal force correspond to the build up of pressure sufficient to expel the next liquid layer.

Impurities and surface roughness will disrupt this layering. Increasing the water content of an OMCTS film (7) decreased the number of force oscillations observed. The smoothness of mica surfaces can be modified with monolayer coatings. The effect of monolayers of hexadecyltrimethylammonium bromide (CTAB) and dioctadecyldimethylammonium bromide (DOAB) on the force profile of an OMCTS film has been reported (8). In the case of the high density DOAB coatings, force oscillations remained although with fewer oscillations. The more disordered and lower density CTAB system disrupted layering completely.

The role of molecular configurations on layering have been explored in experiments on linear (9) and branched (10,11) isoparaffins. The linear isoparaffins have an oscillatory force profile similar to OMCTS, the wavelength of the oscillation being equal to the width of the carbon chain. This indicates that the chain molecules arrange themselves parallel to the boundaries when confined. The branched alkanes, in contrast, showed little to no oscillations. Squalene (18) exhibited a monotonic increase in the force from a separation of roughly 18 Å. The shorter branched molecule 2-methyloctane (10).

The expulsion of the layer from the liquid film requires a time which will depend on the effective viscosity of the film and the nature of the flow process by which the layer is removed. Chan and Horn (12) have calculated the viscous force arising for a Newtonian liquid as the surfaces approach one another. The faster the surfaces are pushed together, the greater is the amplitude and range of this nonequilibrium force (13). Holding the mica surfaces at a fixed separation, the observed force arising from a film of polybutadiene was observed to relax towards the equilibrium value (14). These hydrodynamic effects, it should be noted, are observed over length scales on the order of  $10^2$  nm while the oscillatory forces typically occur over length scales less than 5 nm. The oscillatory forces, however, also appear to include nonequilibrium contributions. As evidence, Horn *et al* (13) observe that the measured depth of the force minimum in films of polydimethylsiloxane can be doubled by vibrating one of the surfaces as the separation is decreased.

**B. Rigidity in Thin Films.** Understanding the origin and characteristics of the rigid state of the confined film must underlie any analysis of stick-slip motion. The layering indicated by the oscillatory normal force profiles described above does not necessarily result in rigid response to a shear force. The onset of rigidity is distinct from layering and is associated, presumably, with structural correlations in the plane of the surface. No experiments to date have directly probed such structure within the lubricating films due to the small volumes concerned and the restricted accessibility to the confined film.

Friction involves the transformation of mechanical energy into heat. A conceptually appealing aspect of the phenomenon of stick-slip motion is the physical resolution of this transformation process into two physically distinct steps. Mechanical energy is first converted into elastic energy during the "stick" phase as the surfaces and film are brought to their collective yield point. On yielding (the "slip") a fraction of this stored energy is democratically (and, hence, irreversibly) distributed among a spectrum of film and surface degrees of freedom. While the weight of experimental and theoretical studies have been directed at the nonequilibrium phenomenon, it could be argued that the heart of the stick-slip process lies with the ability of the thin films to accomplish the transient storage of elastic energy. The generality of this property is evident from the range of liquids that give rise to rigid films, a list that includes  $M_gCl_2$  solutions (15) and cyclohexane (16) as well as linear and branched polymers. It is thus the appearance, below a given film thickness, of film rigidity and its microscopic origins which poses the central problem.

**1. The Transition to Rigidity.** The key control parameter for the transition between liquid and solid behaviour is film thickness. The transition to rigidity of OMCTS between clean mica surfaces provides an interesting case study. There are currently two different pictures of the onset of rigidity in films with decreasing surface separation. Granick and coworkers (17-19) have measured the elastic and viscous response of OMCTS films as a function of film thickness. At 27° C (19) they report a continuous increase of the longest relaxation time with decreasing thickness. (This time is the reciprocal of the crossover frequency at which viscous and elastic shear moduli equal one another.) At transitions from 7 → 5, 4 → 3 and 3 → 2 layers thickness, the relaxation time increases by 0.5, 1.0 and 1.5 orders of magnitude, respectively. Similar behaviour is reported for OMCTS films between mica surfaces coated with monolayers of octadecyltriethoxysilane (OTE), suggesting that neither the periodic surface structure nor strong adsorption are necessary for film rigidity (11). The elastic modulus, measured at the crossover frequency, exhibits a roughly exponential decay with respect to film thickness.

It has been concluded that the rigidity arises from the continuous slowing down of the confined liquid rather than from any abrupt structural transition as a function of layer thickness. An analogy is drawn with a glass transition in which the usual roles of temperature or pressure are played here by the film thickness. It remains to be seen, however, whether this analogy reflects little more than superficial similarities. Demirel



and Granick (19) have examined frequency-thickness superposition of the viscoelastic response in OMCTS films (drawing on the analogy with the temperature-frequency superposition found in bulk glass formers). Unlike many bulk glass-formers, superposition was not observed using a thickness-dependent frequency scaling alone. Scaling of both frequency and response amplitude, however, did result in superposition of the spectra. The resulting master curves indicated two clusters of relaxation times separated by a constant distance on the reduced frequency scale. This differs from the case of  $\alpha$  and  $\beta$  relaxation in bulk glasses whose separation increases with increasing pressure or decreasing temperature. As thorough as the evidence is for the continuous slowing down, there is also the problem of the abrupt jump seen in the time dependence of the transition into the rigid state following compression of the film (11). This effect points strongly to metastable states of some sort, entities that do not sit comfortably with continuous transitions.

These results and conclusion have recently been called into question by Klein and Kumacheva (16,20,21). In ref.16 evidence is presented of an abrupt increase, 7 orders of magnitude, in the effective viscosity in an OMCTS film when going from a thickness of 7 to 6 layers. Similar abrupt transitions are reported for toluene and cyclohexane. The authors conclude that a structural phase transition, akin to epitaxial crystallisation, is responsible. The difference between these results and the earlier ones is attributed to possible contamination of the earlier systems by trace impurities such as water. It is not clear, however, that the results of the two groups are so different. Unlike ref.19, Klein and Kumacheva probe their films at a single frequency of about  $10^2$  rad/s. At this frequency, the viscous/elastic force in OMCTS films measured by Demirel and Granick (19) seems to indicate an abrupt transition from liquid to solid behaviour at about 6 layers, in agreement with the observation in ref.16. The point here is that as the probing frequency is increased, the transition to rigid response occurs more abruptly and at larger film thicknesses. With its roughly spherical shape, OMCTS represents one of the best candidates for crystallisation in the film and, hence, the experimental resolution of the manner in which rigidity appears in this system is of some significance. We shall return to consider the possibility of crystallisation in the confined film in the context of computer simulations.

In the case of branched and linear polymers there appears to be a consensus that rigidity results from a continuous slowing down of relaxation as the film thickness decreases until, at the frequencies being probed, the film is capable of elastic response only. The absence of layering in these films for all but short linear chains essentially precludes any suggestion of crystallisation. Granick and coworkers (22-29) have measured the viscous and elastic linear response of a range of polymer films to small amplitude shear oscillations of the surfaces relative to one another. The properties of a polymer film (e.g. adhesion) can change significantly as a result of sliding and relaxation back to the static properties can be slow. For this reason, characterisation of the 'equilibrium' properties of the film requires the measurements involve the linear response. Characteristics of the sliding film, such as stick-slip behaviour, are examined in the section below on nonlinear behaviour.

The nature of the onset of rigidity of the polymer films can be summarised as follows (17,24,27). (i) The effective shear viscosity increases continuously with decreasing film thickness, starting from a thickness of roughly 7 times  $R_G$ , the unperturbed radius of gyration, until the response becomes solid-like for films thinner than 4-5  $R_G$ . (ii) Due to slow drainage and structural relaxation, the thickness at which the onset of rigidity occurs depends on the rate at which the film is compressed, with rapid compression leading to rigidity at larger separations between the surfaces. (iii) In thick films, the shear loss modulus increases linearly with frequency. With decreasing film thickness, this loss modulus becomes steadily independent of frequency. The elastic shear modulus becomes larger than the loss shear modulus at a crossover frequency characteristic of internal relaxation in the film. This relaxation frequency decreases with decreasing thickness. The resulting shear moduli are rubber-like, with dynamics similar to that associated with entanglement even for molecules too short to exhibit entanglement in the bulk. (iv) For film widths  $< 4 R_G$ , the shear moduli are independent of molecular weight.

What is the origin of this thickness-dependent slowing down of the relaxation within polymer films? Simply referring to it as a "glass transition" is, at best, only descriptive and of little explanatory value. Is it just the result of strong adsorption of polymer onto the surface? Such interactions must be involved, of course, simply to permit the transfer of shear stress between the surfaces and the film. Rigid films, however, can be up to 6  $R_G$  thick and so some additional kinetic correlations are required. Various modifications of mica surfaces have been examined in order to determine the role of adsorption strength on film properties. Granick and coworkers (28,29) studied the behaviour of polyphenylmethylsiloxane (PPMS) films between mica surfaces (strongly adsorbing) and mica surfaces coated with OTE monolayers (weakly adsorbing). They reported similar slowing down of the viscoelastic response for the two surfaces and concluded that geometrical confinement, as opposed to surface adsorption, plays an important role in the film kinetics. Comparison of kinetic friction of a perfluoropolyether (PFPE) film between surfaces of mica, zirconia and alumina show little difference in the absence of water (30). The role of surface adsorption on the character and thickness-dependence of film rigidity remains to be clearly established.

The dependence of the film relaxation time on molecular weight  $M$  can potentially shed light on the kinds of cooperative processes involved the slow processes. Granick and Hu (27) have studied films of PPMS with chain lengths of 31 and 65 bonds. They found that the shear moduli in films of thickness  $\approx 4 R_G$  were roughly independent of molecular weight. This implies that the relaxation frequencies, identified by the crossover of the loss and storage shear moduli, are equal for different length chains as long as the film thickness is scaled by the unperturbed  $R_G$ . It is not obvious how to translate this result to the dependence of the relaxation time on  $M$  at a fixed film thickness. It has been proposed that the slow relaxation process involved chain adsorption and desorption. One study (31) has established that the polystyrene desorption rate at a single surface (oxidised silicon) varies as  $M^{2.3}$ , a dependence interpreted as indicating entanglement. It has been suggested (17) that the slowing down with increasing confinement was the result of a loss of free volume. That this is

specifically an effect of the heterogeneous systems is supported with the observation that the effective viscosity in the film is very much greater than that of the bulk at the same pressure (32). This proposal has been expanded upon in recent discussions of the origin of this enhanced entanglement which include the additional configurational constraints arising from tethering of polymer chains to the surface (27) and the geometrical restrictions in going from 3D to 2D with decreasing thickness (33). In support of the entanglement picture, the rubber-like character of the frequency independent shear moduli in thin films have been cited (see, for example, ref.33). This interpretation should be qualified, however, by the fact that OMCTS films, for which entanglement is not an option, exhibit a similar plateau feature (11).

**2. Properties of the Rigid Film.** Thin lubricating films represent an intriguing state: rigid at high temperatures under sufficient confinement, highly heterogeneous and anisotropic, and influenced by the external field of the confining surfaces. In this section we describe a number of film properties with the aim of building up a picture of the rigid film state.

The thin film in its rigid state resembles a *soft* solid. This characterisation is based on the magnitudes of both the elastic shear modulus and the yield stress. The elastic modulus in rigid squalene films (25) was found to be 3 orders of magnitude smaller than that expected for a crystal or glass. The stored elastic energy at the yield point added up to only  $0.1k_B T$  per molecule. As noted for the case of OMCTS (19), if one looks for a single degree of freedom associated with  $k_B T$  of elastic energy, this collective coordinate will involve between 60 and 300 molecules. Already mentioned above, the appearance of rigidity is generally accompanied by the development of a frequency-independent plateau in the loss and storage shear moduli. These features have been described as rubber or gel-like. Typical strains of 0.1 are required to see the onset of nonlinear response, considerably larger than in the case of bulk solids (24). This, too, is reminiscent of rubber or gel-like response. Finally, the relationship between the normal compressibility and the storage shear modulus has been used to estimate Poisson's ratio  $\mu$ . In rigid films of PPMS (24),  $\mu = 1/2$  corresponding to no volume change on shear distortion, another property associated with rubber-like behaviour (34).

The frequency at which the storage and loss moduli are equal provides a relaxation time associated with linear response of a film (19) and so can be regarded as a property of the static film. Identifying the degrees of freedom associated with the slowest of these relaxation processes constitutes the central object of many of the models discussed in this review. The dependence of this time on film thickness has already been discussed above. Many of the features of the nonlinear response of thin films depend on the rate of relaxation of the perturbations to the resting state. These features include adhesion hysteresis, the recovery of the yield stress (or static friction) following the cessation of sliding, the time-dependence of the sliding friction following sudden changes in load or sliding velocity, and the existence of a critical sliding velocity, above which stick-slip response disappears. Each of these nonlinear phenomena is discussed below. The slowing down of relaxation with decreasing film

thickness unavoidably raises the question of whether a given film property can be regarded as an equilibrium property (i.e. its value largely independent of its history) or not. There is certainly clear evidence of nonequilibrium effects, e.g. the dependence of film thickness at the onset of rigidity on the rate of film compression and the presence of high frequency vibrations (35) and the increase observed in polymer film viscosity with increasing temperature (36).

### C. Nonlinear Response of the Rigid Film.

**1. An Overview.** At strains of 0.1 or greater, a film cannot respond elastically. This yield point can be characterised by a yield stress  $\sigma_c$  or, in terms of the shear force, the static friction  $F_s$ . The resulting relaxation of the strain can take place through processes ranging from creep flow to undamped motion of one surface past the other.

The range of nonlinear response of the rigid films to a shear force is a complex one, sensitive to a considerable number of variables. The general features are as follows (35). To begin, it is useful to distinguish those liquids which exhibit layering (i.e. relatively small molecules of spherical or linear structure) from those which exhibit a monotonic normal force (branched molecules and polymers). The layered films exhibit 1) a marked variation of properties with changing numbers of layers (a "quantisation of properties"), 2) a tendency to exhibit stick-slip dynamics at low sliding velocities, 3) abrupt increases in frictional force during sliding as a layer is expelled from the between the sliding surfaces and 4) a transition, with increasing sliding velocity, to a constant sliding friction without the stick-slip oscillations. The unlayered films display a different behaviour. On yielding, the frictional force typically drops smoothly to a constant sliding friction without the oscillatory stick-slip behaviour. The resulting peak in the shear force associated with the yield event is referred to as a stress overshoot. In the case of linear chain molecules, an initial liquid-like friction can develop the sawtooth force oscillations associated with stick-slip behaviour during prolonged sliding. This appears to be the result of shear-induced alignment of the molecules at the surface as the stick-slip behaviour is accompanied by the appearance of oscillations in the normal force. These structures relaxed if the surfaces were moved apart. On stopping the sliding motion, the shear stress remains at its sliding value (unlike the case of a liquid where this shear stress decays).

The relative alignment of the two mica surfaces can strongly influence the observed sliding behaviour. Yoshizawa and Israelachvili (37) have compared the time dependent frictional force for a 3 layer film of tetradecane at two different relative orientations of the mica surfaces, differing by a  $10^\circ$  twist. One configuration shows the sawtooth profile of stick-slip while the other shows no sign of stick, the sliding frictional force equal to the force minimum of the stick-slip. This is a remarkable result with important implications regarding the role of surface-surface registry in friction. It is also a little unnerving. It suggests that reproducibility of the sliding behaviour between mica requires that the relative orientation between the two surfaces also be reproduced. Gee *et al* (35) note that data can vary from run to run by up to 50%, a variability attributed to different angles between mica sheets and differing sliding directions relative to these lattices. Experimental clarification of the role of

surface alignment relative to each other and to the direction of sliding would seem to be a prerequisite for any quantitative comparison of data between different experiments.

**2. Static Friction.** The static friction  $F_s$  is the maximum shear force that the film can sustain before sliding. It is related to the yield stress  $\sigma_c$  by  $\sigma_c = F_s/A$ , where  $A$  is the area of contact. Its existence is a crucial aspect of friction, accounting for the grip of tires on roads and the mechanical integrity of woven fabrics.

The yield stress increases with increasing pressure, even in the absence of discernible changes in the film thickness (17). For thin films, however, it should be noted that thickness changes of the order of 1-2 Å, too small for earlier measurements to resolve, can correspond to significant changes in the film volume. Note that if the measurement of the pressure dependence was taken before equilibrating the films, the pressure dependence of the yield stress was found to be an order of magnitude smaller (17). The yield stress also increases with decreasing film thickness (35,38). The sensitivity of the static friction on film thickness can lead to a dramatic change in the sliding behaviour if a liquid layer is expelled during sliding. Transitions from smooth sliding to stick-slip behaviour have been observed during sliding in films of OMCTS (32,35,39), cyclohexane (35) and hexadecane (39). Limited data exists regarding the temperature dependence of the static friction in films. A 12 Å film of hexadecane exhibits a transition temperature of around 25°C (7° above the bulk melting temperature) (39). Below this temperature, stick-slip behaviour is observed while at higher temperatures only smooth sliding is found. This temperature appears to be independent of load but does depend on film thickness and the relative orientation of the mica surfaces.

The time dependence of the yield stress in a film following the cessation of sliding motion exhibits a striking functional form and range of time scales. With either tetradecane or of 2-methyloctadecane (MOD) (35), if the sliding is stopped for less than some internal relaxation time, no change is found in the frictional force on resuming the motion. If the stoppage is longer than this relaxation time, however, a single spike is observed before the constant sliding friction is recovered corresponding to a static friction. The time dependence of this spike amplitude is an interesting one. After this lagtime which increases with normal load and molecular size, the spike amplitude abruptly jumps to a value (a decreasing function of the sliding velocity prior to the stop) which, subsequently, continues to increase slowly. The value of the static force immediately following this rapid rise is a decreasing function of the sliding velocity prior to the stop (35). If the direction of the shear is reversed, the film response resembles that of a film in which shearing had just been initiated. In siloxane polymers (22), the time dependence of the increase in the yield stress has been fitted with two exponential functions with time constants of 70 min and 650 min. In contrast, the lag times observed in tetradecane and MOD (35) varied from 0.3 to 20 sec, depending upon the load, while the abrupt increase in the static friction took place within a second. These dynamics suggest a cooperative process in which the return of rigidity is a self-accelerating process whose initiation takes up the lag time. The

kinetics of the slow approach to the final value of the yield stress is reminiscent of an aging or coarsening mechanism.

The finite time required to re-establish the static friction suggests a stick-slip analogue to shear thinning in liquids in which the amplitude of the  $F_s$  decreases with increasing sliding rate as the imposed rate of shear stress build up outstrips the kinetics governing the growth of yield stress. Yoshizawa and Israelachvili (39) have proposed such an explanation to account for the observed disappearance of stick-slip behaviour above a critical sliding velocity  $v_c$ . Identifying the critical velocity with the equality of the stick-slip frequency and the frequency of static friction recovery  $1/\tau$ , the following expression for  $v_c$  was obtained,

$$v_c \propto \frac{F_s - F_k}{K/\tau} \quad (1)$$

where  $K$  is the elastic modulus of the SFA. The transition from stick-slip to smooth sliding is found to vary between two extremes (43); (i) a continuous convergence of the values of  $F_s$  and  $F_k$ , the minimum in the force oscillation and referred to as the kinetic friction, and (ii) an abrupt disappearance of the static friction at  $v_c$  with little change to  $F_k$ . In hexadecane films, the transition was similar to type (ii), with a critical velocity which decreased with load (39). The critical velocity is found to increase with load in the better layered OMCTS films (39). Given the same conditions (42), polymers generally have a lower critical velocity than quasi-spherical molecules.

Recent experiments appear to contradict the earlier observation of a critical velocity and rheological transition. Kumacheva and Klein (20) have re-examined the velocity dependence of stick-slip in OMCTS and cyclohexane films and found no transition to smooth sliding, despite sliding velocities of up to 4000 nm/s. The authors suggest that one source of the difference between these and earlier measurement is the improved force resolution in the recent study. Given the importance placed on modelling the transition to smooth sliding (see the section on constitutive equations below), we need to understand the significance of these new results.

The time dependence of force oscillations on sliding, including their disappearance at high velocity, cannot be regarded as arising from the film and its interactions with the surfaces alone. The macroscopic dynamics of the apparatus are intimately entangled with the microscopic processes of the film. This has been most elegantly demonstrated in experiments on sliding sheets of paper by Heslot *et al* (42) in which the space of apparatus variables (spring constant, slider mass and driver velocity) was carefully explored. While somewhat removed from the topic of this review, this work provides valuable insight into the general role of the apparatus parameters in stick-slip behaviour. The observation of the creep flow immediately preceding yield demonstrated the possibility of exploring the characteristic length and time scales involved in the yield event itself. In a preliminary application of these ideas to lubricating films, Berman *et al* (43) consider the role of system parameters in establishing the nature of the transition from stick-slip to smooth sliding with

increasing temperature. They also demonstrate the possibility of stick-slip behaviour for which the slip times are on the order of seconds.

While the mechanism by which the film yields remains poorly understood, the stick-slip is a macroscopic process and both the yielding and the stick processes must consist of some complex cascade of microscopic events. Evidence for this complexity is provided by the long-lived memory seen in friction fluctuations of a squalene film under an oscillatory shear force (19). These interesting observations have yet to be related to possible structural or thickness fluctuations in the sliding film.

**3. Kinetic Friction.** The magnitude of the kinetic (or sliding) friction  $F_k$  is, of course, the key issue in lubrication and a considerable amount of experimental effort has gone into characterising the  $F_k$  for liquid films and polymer-coated surfaces (44).

The kinetic friction is observed, in general, to be proportional to the applied load  $L$ , as is the case for dry friction. This linear relation  $F_k = \mu L$  ( $\mu$  being the friction coefficient) is known as Amontons's Law. There are, however, a number of interesting classes of films for which the Amontons-like relation between load and friction breaks down. In well layered films consisting of small compact molecules such as cyclohexane, octane and OMCTS (35), the shear stress has been observed to increase in a series of well defined steps with increasing load, with the stress independent of load between the steps. This behaviour is clearly associated with "quantized" changes in film thickness.

Polymer brushes attached to one or both of the mica surfaces provide a more important class for which load and friction appear to be, at least partially, decoupled. Klein and coworkers (44,45) have shown that the normal force on surfaces bearing polymer brushes can increase by 3 orders of magnitude with no increase in the kinetic friction. These results are of obvious significance in the context of lubrication. It has been proposed that steric repulsions between chains on opposite surfaces inhibit interdigitation, providing effectively a fluid-like interface over a range of loads. Similar results have been obtained by Dhinojwala *et al* (15).

What correlation exists between the net normal force observed to act between the solid surfaces and the kinetic friction? Amontons's law represents an empirical correlation between the applied load and sliding friction. Do the normal attractive forces observed in thin films act on the kinetic friction as additional contributions to the load? Normal forces represent the accessible information concerning surface-surface and surface-film interactions. Connecting these observables with the behaviour of the shearing film could represent a useful economy of information.

The interaction between surfaces can be quantified in terms of the surface adhesion, the work required to completely separate two surfaces from some initial film thickness. This energy is associated with the free energy of the liquid-solid interface (46). No general correlation exists between surface adhesion and kinetic friction. This can be demonstrated with much the same examples used previously to show that film layering and film rigidity were not equivalent phenomena. The normal force

oscillations due to layering provide an effective attraction between surfaces and so contribute to the work required to separate them.

The lack of correlation between adhesion and kinetic friction is underlined by the behaviour of surfactant-coated mica surfaces under different amounts of water vapour (47). The sliding friction of these systems is found to decrease dramatically with increasing humidity with little change in the surface adhesion. A clear correlation has been reported, however, between kinetic friction and adhesion hysteresis. This latter quantity is the difference in the adhesion energy measured during pulling surfaces apart and pushing them together. (The former measurement is typically the larger of the two.) Large adhesion hysteresis correlates positively with large kinetic friction. It is not clear how this correlation is to be interpreted. Certainly, one contribution to the adhesion hysteresis is the lateral flow of liquid into and out of the volume between the surfaces as there are pulled and pushed respectively. Increasing the kinetic friction will slow down such flow and, hence, increase the hysteresis in a straightforward manner. Hysteresis, however, can also involve contributions from other rearrangements with no simple connection to liquid flows. Klein and Luckham (48), for example, have demonstrated the existence of a nonstationary attractive interaction between surfaces separated by a polymer film. The attraction, attributed to the bridging of polymers between the surfaces, increases and then decreases over a time interval of hours. Establishing a connection between the kinetics of such molecular configurations and sliding friction would be an important result. Frequency dependent measurements of both the normal force and the kinetic friction could be valuable in sorting out the various contributions.

### III. The Models

**A. Overview.** The origin of the rigidity of a confined film is the fundamental microscopic question. The answer is a prerequisite for any detailed understanding of the manner in which a film loses and regains this rigidity during stick-slip. While the kinetic features of stick-slip present all the problems in characterisation one would expect for phenomena which are heterogeneous, nonequilibrium and transient, a number of basic questions can be posed concerning the nature of the yield event, the slip stage and the recovery of adhesion in the 'stick' event. (i) The onset of slip motion is a macroscopic process requiring a yield mechanism that spans the contact area. What kinds of spatial and temporal correlations are involved? (ii) Following this yielding, the film must rapidly alter its behaviour from a solid to a sliding medium. What are the structural or configurational changes that account for this alteration? (iii) The sliding film quite abruptly regains a substantial portion of its initial rigidity. This rapid transition from sliding to lateral adhesion is perhaps the most intriguing aspect of the phenomenon. It must be associated with the relaxation of the degrees of freedom identified in question (ii). What governs the dynamics of this relaxation process and so determines the onset of the 'stick'? By what kinds of microscopic sequences does this adhesion take place and how is it translated into the macroscopic arrest of the slider motion? We begin by looking at proposals for the origin of rigidity in a confined film.



**B. On the Origins of Rigidity in a Thin Film.** In order to transfer shear stress from solid to film, there must be some sort of surface structure capable of laterally restraining molecules in the surface layer of the film. This adhesion is sufficient in itself to account for the immobility of the liquid directly adjacent to the surfaces. Rigid response, however, is evident for surface separations equal to 7 molecular diameters. A number of explanations have been proposed.

**1. Crystallisation.** Layering of a liquid adjacent to a hard flat wall is well established, both through oscillatory dependence of force vs plate separation as measured by the SFA, and through simulation and theory. As discussed above, however, layering cannot account for the observed rigidity to shear. A number of workers have proposed that the film rigidity is the result of crystallisation of the confined liquid. Crystallisation refers specifically to the appearance of in-plane periodic order in the layered liquid. In the case of crystalline solid surfaces, the film order will be either commensurate with the surface structure (ie. epitaxial crystallisation) or incommensurate. These transitions would be taking place at temperatures well above the bulk freezing temperature and so these models must reproduce such substantial freezing point elevation. The experimental evidence (49) on freezing in porous media (with pore sizes  $\sim 10^{-6}$  m compared with the surface separations of  $\sim 10^{-9}$  m) suggests that freezing point *suppression* is the more typical outcome of such confinement.

In the absence of any clear experimental evidence for an abrupt transition in a static property of a confined liquid, the study of film crystallisation rests heavily on computer simulation studies of confined liquids set up so as to optimise crystal formation. The confining walls typically consist of the same crystallographic planes, aligned with one another and with lattice spacings commensurate with those of the crystalline film. (Relaxation of this last restriction has been considered, as discussed below.) While these conditions do not describe the general reality of the SFA, the model is of value in providing a film for which the fundamental origin of the rigidity is understood.

The thermodynamics of the order-disorder transition of thin films of Lennard-Jones particles between 100 fcc surfaces have been characterised under explicit constraints in an important series of simulation studies by Schoen, Diestler and coworkers (50-56). Shear strains were imposed by translating one wall a fraction  $\alpha$  of a lattice spacing with respect to the other. At  $\alpha = 0.0$  crystal films with odd numbers of layers are stable while for  $\alpha = 0.5$  even layered crystals are stable, a consequence of the *...ababab...* stacking of the 100 planes. At a load-dependent critical strain, intermediate between these two values, the shear stress drops abruptly from its maximum value and the film disorders. Under a constraint of fixed chemical potential, this disordering is accompanied by either a draining or inflow of one liquid layer. Metastable states, corresponding to different numbers of layers, exist with the free energy gap between them and the equilibrium state. This gap reaches a minimum as the strain  $\alpha$  approaches the critical value. If the normal load is fixed, then the disorder transition also involves a continuous increase in the film thickness. The continuous character of the

disordering transition is not the only difference between the strain-induced transition and bulk melting. The strain-disordered film remains rigid, able to sustain a non-negligible shear stress. Thermally-induced disordering, on the other hand, is accompanied by a discontinuous change in the film thickness and appears to be first order.

To examine the sensitivity of these results to the ratio of surface and film lattice spacing, variations of the ratio have been examined (56). Expanding the surface lattice spacing by 6% with respect to that of the film was sufficient to destroy translational, but not orientational, order in the film and to substantially decrease the shear stress which the film could sustain. The relationship between the reduced order and the persistent rigidity in these disordered films is an interesting one, deserving of more study. It is possible that rigidity in real films may involve such states, any translational order disrupted by incommensurate interactions, relaxation in these 'disordered' films would be constrained by the imposed orientational order of the surfaces. (Such disrupted structures could incorporate a significant amount of inherent stress, a point of some interest with regards the microscopic mechanism of the yield process.) The significance of the imposed structure (as opposed to that arising from interactions between film particles) has been nicely underscored by the demonstration (56) that a monolayer of ideal gas can sustain a shear stress. It is useful to note here that the yield behaviour of such a film cannot be described as a phase transition. The implication of this result that rigidity involves the interaction between surfaces, with 'pinned' film particles acting as intermediaries, will be taken up below in considering bridging in polymer films.

In an interesting development, it has demonstrated (57-61) that crystallisation alone does not necessarily imply an increase in friction. In simulations of adsorbed monolayers on a single solid surface, an ordered film with a structure incommensurate with that of the surface can slide with a smaller friction than even that of a disordered film. The reason is that the periodic driving force felt by the film due to the substrate over which it is being driven, does not couple with the modes of the incommensurate structure. Any change to this incommensurate order will lead to an increase in friction; for the commensurate structure the driving oscillations come into resonance with the film, while disordering the film broadens the spectrum of modes, facilitating energy transfer from the sliding process. Persson (60) identifies the importance of even a small concentration of substrate imperfections or pinned particles in destroying this incommensurate structure. This two dimensional model also provides a useful 'laboratory' for understanding the collective spatial character of the onset of sliding and the onset of sticking under an applied lateral force. A lattice model of this process indicates a complex avalanche of detachments (62).

**2. Slow Relaxation in Disordered Films.** Granick and coworkers have argued that the observed increase in relaxation time in the confined liquids is sufficient to account for the onset of rigid behaviour. As the relaxation time exceeds the time scale of the applied shear stress, the liquid response becomes substantially elastic. Push this high frequency response into the nonlinear regime, argues Granick, and yield

behaviour results. In a sense, this model encompasses the previous crystallisation proposal as a special case, long range transverse ordering being just one mechanism by which the relaxation time within the film can be increased. In practice, however, these two pictures differ significantly. The experimental evidence presented above strongly supports the picture of a continuous approach to rigidity via decreasing film thickness, with an associated continuous increase in relaxation times. The possible exceptions are the compact molecules such as cyclohexane and OMCTS.

Films consisting of hydrocarbon chains make up the most important class of systems with respect to lubrication. Simulations have been carried out for a number of linear polymers: a 5-mer(63), n-pentane (68), n-octane (64-67,70), n-decane (68) and n-hexadecane (69). The results indicate that there is no 'universal' behaviour, details of the thermodynamic state and solid-hydrocarbon interaction strength (65), in particular, appear to strongly influence whether or not lateral order is observed. The study on n-hexadecane (69) observed a high degree of in-plane ordering, accompanied by layering amplitudes enhanced of those arising from the branched squalene molecule.

The octane results embody this diversity of behaviour. Harris and coworkers (66,67,70) have carried out MD simulations of thin octane films between walls made up of static crystalline hydrocarbons (modelling surfactant-coated mica). The walls extend a finite length (2.5 nm) in one direction so that the film molecules can exchange with bulk liquid. A result of these calculations, carried out at 297K, is that, despite the strong layering observed in the segment density and the clear stretching of chains next to the surfaces, the layers remain liquid-like in terms of particle mobility. (It is also noted that while the layering in a branched octane film is reduced compared to the linear molecule, there is little difference in the amplitude of the force oscillations. This raises the possibility that the experimentally observed decrease of these oscillations for branched chains might be a nonequilibrium effect.) While finite size effects on structure have been checked for, it is possible that the molecular mobility is enhanced in these calculations due to the fact that many of the molecules straddle the confined and bulk liquid regions.

Bitsanis and coworkers have examined thick (64) and thin (65) n-octane films using constant NVT MD simulations. In the thick films, layering associated with stretching of the chain (i.e. enhancement of *trans* configurations at the surface) is observed with no reports of inplane structure. The authors do note that including a realistic carbon-carbon torsional potential (as opposed to assuming a freely rotating chain) is important to properly capturing the slowing down associated with segment adsorption on the surface. In the thin film simulations (75), the crystalline wall is replaced by smooth wall potential with no inplane variation. (The walls retain a normal layer structure.) Here, strong surface adsorption does involve domains of local alignment and periodic arrangement of the stretched alkane chains, similar to that observed in n-hexadecane (69). Significant slowing down of segment diffusion and torsional motion accompanies the appearance of this structure. One interesting conclusion is that epitaxial effects (i.e. the role of the inplane surface structure) are secondary, with respect to this ordering process, to the role of the surface-alkane interaction strength.

The difference between these results for thin films of n-octane and those of Harris and coworkers (67,70) who found no large drop in segment diffusion appears to be due to the stronger surface-alkane interaction employed in ref. 65. Smooth walls cannot, of course, transmit shear stress. The lateral structure required for this transverse coupling will, as acknowledged in ref. 65, also perturb the stability of the film's inlayer order. In the n-hexadecane case (69), the surface structure acts to align domains.

What might cause the substantial slowing down in the confined films? Certainly, if ordered domains can develop on the solid surface, they will contribute to the increasing relaxation time. Other proposed mechanisms relate specifically to polymeric films and include (i) interdigitation and entanglement of tethered chains (27), (ii) entanglement arising from the confinement of chains into a quasi-2D space (33), and (iii) bridging between the two surfaces by individual chains. Of these three proposals, only the last one has been examined in any detail.

If molecules can span the wall separation, with their ends adhering to opposite surfaces, the effective film rigidity would reflect the elasticity of individual molecules (up to stresses at which surface-molecule attachment breaks). While this effect relates chiefly to polymer films, it is worth noting that even spherical molecules will bridge, i.e. interact with both surfaces simultaneously, in films thinner than 3-4 molecular diameters (56). While theoretical treatments of the statistics of bridging have been presented (73,74), it remains to be established in experiment and simulation the relative magnitudes of the inter- and intramolecular stress contributions through a thin polymer film. A treatment of bridging between sliding surfaces has been presented by Subbotin *et al* (75). In MD simulations of the pulling apart of a glassy film of short chain molecules, Baljon and Robbins (76) found that roughly a third of the adhesive energy was associated with molecular bridges.

**3. Interaction of Stick Boundary Conditions.** The liquid adjacent to a surface can typically be treated as immobile (the stick boundary condition of hydrodynamics). While this section does not really examine an alternative proposal for thin film rigidity, it is useful to ask whether the thin film rigidity is specifically one of confined liquids or just the overlap of two pre-existing pinned boundary layers. At issue here is how thick are these rigid boundary layers at a single surface? Addressing this question experimentally poses something of a conundrum. In order to directly probe the behaviour of liquid films adjacent to the surface with the SFA requires that the two surfaces be brought together, so demolishing the very information sought about the single surface. Chan and Horn (12) have provided one answer, demonstrating that by measuring the drainage kinetics of thick films (> 100 nm) and analysing the dynamics with linear hydrodynamics (and the surface potential), the thickness of the stationary layer at the surface could be estimated to within 0.2 nm. Applying this analysis to drainage data for OMCTS, tetradecane and hexadecane, it was concluded that roughly two molecular layers against the solid did not undergo shear

A number of simulations have addressed the question of the microscopic nature of the shear flow boundary condition. Up to two liquid layers can be held immobile in MD

simulations of a Lennard-Jones liquid flowing through a cylindrical pore (77) for sufficiently strong surface-liquid attractions. Thompson and Robbins (78) have studied the velocity fields and liquid structure in simulations of a Lennard-Jones liquid flowing between two widely spaced planar crystal surfaces. They also observed that up to two liquid layers became locked to the surface, associating this with epitaxial crystallisation. These results suggest that in some cases, the rigidity observed in a confined film may essentially just correspond to the pre-existing locked boundary layers.

The role of surface roughness plays a central role in the theory of dry friction. While lubricating films are supposed to reduce this effect by separating the surfaces, rough surfaces will alter the hydrodynamic flow within the lubricating film. Daikhan and Urbakh (80) have examined the effective friction arising due to the perturbation of the linear hydrodynamics of shear flow between rough surfaces. Assuming random roughness with a root mean squared height of 1 nm, the contribution due to the perturbation in flow is of the order of 20% of the contribution from smooth surfaces. While this effect cannot account for the large increases in the effective viscosity of thin films under increasing confinement observed in the SFA experiments, it could become important at higher shear rates.

**C. On the Nature of Stick-Slip Motion.** Once sufficient stress is applied to a rigid film so that one surface is displaced with respect to the other by a distance equal to the film thickness, the film or the adhesion between film and surface must yield. The subsequent dynamics of the walls depends on whether the frictional force acting on the shearing motion (the kinetic friction) is similar to the yield stress (the static friction) or considerably smaller. In the former case, plastic flow will result. In the latter case, the combination of low friction and released elastic energy results in an abrupt transition to a high shear rate. As this energy is dissipated, the rigidity is recovered. The description of these macroscopic processes in terms of phenomenological equations and the explanation of the phenomenological coefficients in terms of molecular degrees of freedom constitute the two themes of friction modelling.

**1. Constitutive Equation for Friction.** Stick-slip behaviour arises from a combination of macroscopic elements, a slider of mass  $M$  coupled elastically to a driver, and the interface between slider and the stationary surface. A general class of lubrication experiments can be modelled with the following equation of motion (43,81,82) for the slider displacement  $x$ ,

$$M\ddot{x} = K(X - x) + F \quad (2)$$

$K$  is the force constant of the elastic driver-slider coupling,  $X$  is the displacement of the driver and  $F$  is the friction force. As  $F$  provides the only source of dissipation in this equation, it will include dissipative elements other than those at the interface (e.g. glue used to fix the mica to the SFA). In order for the slider to undergo stick-slip, the friction force must be capable of undergoing large changes during the time evolution

of the system. The various models for stick-slip can be organised in terms of the variable on which  $F$  depends.

One of the earliest approaches (81) involves considering  $F = f(x)$ . In these models, the changes in friction are associated with the varying surface topologies explored by the slider as it moves. This approach is reviewed in the following section. In an elegant and valuable analysis, Rabinowicz (82) has argued that the friction between two surfaces reflects the time dependence of the adhesion process. The yield force (static friction force) due to the adhesion contacts increases as a function of contact time  $\tau$  as  $\sim \log(\tau)$ . To define contact time for moving surfaces, the contact regions must have a nonzero dimension; the characteristic length a surface must be moved to break adhesive attachments. Earthquake models have motivated more recent developments along these lines, stick-slip on the geological scale (85). Ruina (86) introduced an additional interfacial state variable with its own characteristic time scale. This model has been successfully applied by Heslot *et al.* (42) to their data for sliding of sheets of paper in which they find support for Rabinowicz's characteristic length. While developed for solid-on-solid friction, they appear to offer a valuable framework within which to analyse stick-slip in thin films. The rapid decrease in the amplitude of force oscillations above a critical velocity, for example, can be explained as the result of a shear rate in excess of the short-time yield stress recovery rate. Recently, Carlson and Batista (87) has presented model similar to Ruina's for thin film rheology where the internal parameter is associated with film order and its relaxation kinetics and the history dependence of the film can be included.

A related class of models involves a velocity dependent friction force,  $F = f(v)$ . The simplest of these consists of a static friction force  $F_s$  when  $v = 0$  and a smaller kinetic friction force  $F_k$  for  $v > 0$ . While able to describe stick-slip, this model cannot account for the transition to steady sliding above a critical velocity. To model this critical velocity behaviour, it is sufficient that the kinetic friction  $F_k$  increases with sliding velocity. Berman *et al.* (43) have analysed the case of  $F_k \propto v$ . Persson (71), taking into account the elastic deformation of the slider block itself, has arrived at a more complex form for  $F_k$ . A valuable feature of these models is their power to separate in the data the apparatus response from that of the film. To go beyond these constitutive equations we must consider the dynamics associated with the microscopic origins of rigidity.

**2. Surface Topology.** The qualitative similarity between stick-slip as seen in dry friction and that observed in thin lubricating films suggests that surface-surface interactions, mediated by the intervening film, may play a significant role in the rheology of the confined fluids. Coulomb (83) proposed the "cobblestone" model of solid friction in which the static friction was associated with the lateral force required to push apart two rough surfaces sufficiently to allow movement. This model, which has seen more recent refinements (84), provides an explicit mechanical coupling between transverse and normal motion (a key idea in understanding the slipping state) and a useful picture of energy dissipation as the surfaces collide in recovering their original normal separation (61). The model's shortcomings include the absence of all but one degree of freedom, the slider displacement, and the difficulty in extending the

picture to 2D surfaces except for the case of surfaces arranged to allow perfect registry.

The ideal gas calculation of Schoen *et al.* (56), described above, is a simple example of mediated interaction between surfaces. An interesting dynamical example is the model of Rozman *et al.* (84) who consider a damped 1D harmonic chain of particles between two corrugated walls sliding past one another. There is no direct interaction between the walls. The resulting dynamics is quite rich as a result of the excitation of the spring by the sliding periodic potential. The studies of sliding monolayer films (57-59) take this idea considerably further, adding the 2D film and the anharmonic interactions. The number of degrees of freedom is so large, at this point, that the purely mechanical description used in topological models may no longer be appropriate. We shall return to these monolayer studies in the following section on phase transitions.

**3. Stick-Slip Motion as Sequential Phase Transitions.** In this section we return to the epitaxial crystal film, to consider how such a film responds to applied stresses in excess of its yield stress. Again, the caveat here is that such ordering is unlikely to play any general role in thin film behaviour, depending, as it does, on optimal boundary conditions. The model remains, however, of considerable fundamental value as the film rigidity arises from rather simple and, hence, accessible structural correlations which can be monitored throughout the yielding and healing process.

Schoen *et al.* (51) proposed a quasi-static picture of the stick-slip processes. Arguing that the typical sliding velocity used in experiments is  $10^{-9}$  Å/ps and thus considerably slower than any relaxation process which can be observed during a typical MD simulation (of roughly  $10^3$  ps duration), they suggested that the film be treated as being at equilibrium at each value of the time dependent strain. The resulting stick-slip process can thus be described as the equilibrium strain-induced disordering and ordering process. The approach has considerable appeal. All the relevant properties such as yield stress and film viscosity can be evaluated as equilibrium quantities. The existence of the metastable states associated with the 'wrong' number of layers could account for the metastability observed in experiments. The question is whether the quasi-static assumption is appropriate. Such an approach cannot, for example, treat the reported variations of static friction with sliding velocity, i.e. the transition from stick-slip to smooth sliding. It should be noted that this failure is essentially one of MD simulations themselves and the short time window they can provide. The time scale associated with recovery of the static friction is on the order of seconds for 2-methyloctadecane (35), with the time scale for smaller molecules no more than an order of magnitude smaller. Such processes are simply inaccessible to simulation and the process may involve larger length scales than the simulated system provides. The question raised about the very existence of a critical sliding speed and the accompanying transition to smooth sliding (20) should also be kept in mind when using such phenomena to judge the applicability of the quasi-static assumption.

MD simulations (64,88) on a similar epitaxial system have been carried out to model the dynamic response of the film to a constant driver velocity. In light of the previous discussion, how can such calculations model processes that occur on such long time scales? There are, at least, two relevant times, the period of the force oscillation and the inherent relaxation time of the film. The choice of the spring constant and slider mass can be used to adjust the oscillation period and so it can be argued that the large difference between the frequencies of these oscillations in simulations and experiments corresponds to a trivial choice of time scale set by these 'equipment' settings. The relaxation time of the film, however, is not subject to such adjustment except in the ill-defined sense that the smaller contact areas in the simulation may involve faster relaxation processes. One is left to conclude that the relaxation process associated with the simulated stick-slip may have little connection with the much slower process observed in the macroscopic samples.

While questioning (again) the connection of this model simulation with experiments, the dynamic calculations do provide some insight into how the crystalline film responds to these high shear rates. Thompson and Robbins (88) found in the constant particle number calculations that the slip interval was accompanied by a transient separation of the surfaces and a decrease in the in-plane order as measured by the in-plane scattering function. (The magnitude of the slip distance must be the source of some concern in terms of finite size effects. The top surface slips a distance roughly twice the length of the simulation cell, hence running over the site of its original detachment before much in the way of relaxation can occur.) From these observations they concluded that the "origin of stick-slip motion is a thermodynamic instability of the sliding state below a critical force", i.e. a thermodynamic freezing transition. It was proposed that the yield force and stick force corresponded to spinodals of the crystal and liquid. In a later publication (61) this transition is differentiated from the thermodynamic transition described by Schoen *et al.* Instead, a parallel is drawn to the observation of shear melting in colloidal suspensions (89). This connection is tenuous. In colloids, shear melting refers to transition involving suspensions undergoing steady shear flow which retain much of their in-plane order until a critical strain rate is reached. Note that there is a clear separation in strain rate between the yield event that produced the shearing crystal and the disordering event. In the case of the thin films, disordering occurs simultaneously with the yield event itself, behaviour more akin to the mechanical disruption (i.e. fracture) of the ordered phase than a transition between well defined steady states. (It has been proposed that the term "melting" can be extended to cover brittle fracture (39). Only confusion can follow such a redefinition.)

A Lindemann criterion for the yielding of the confined film has been suggested (79). Analogous to the phenomenological parameterisation of bulk melting, an instability is proposed when the mean squared particle displacement exceeds a critical value. It remains to be established whether such a criterion can provide a useful correlation of data.

**4. The Transition to Sliding in Amorphous Films.** We arrive, finally, at the model that probably best describes most of the systems studied experimentally, the



yield/fracture of slowly relaxing liquid films. Modelling the rheology of these soft 'rubbery' films, as characterised by Granick and coworkers, remains, however, an important open problem to which attention is now being turned (90). The phenomenological picture of Subbotin *et al* (75) based on bridging applies only to long chain polymers and does not include the inter-chain component of the shear stress. Modelling of the fracture of ductile materials is still in its infancy (91). Simulation studies of the response to sliding velocities by amorphous films consisting of small molecules could provide a more tractable testbench for ideas about creep and fracture in slow confined liquids.

Simulations of the confined films of chain-like molecules (92,93) have demonstrated a power law shear thinning relation between the viscosity and shear rate similar to that observed experimentally (18). With the increasing 'stiffness' of the amorphous film, Thompson *et al* observe slipping at the surface-liquid interface. This is probably a quite general result for polymeric films. Once the chains can no longer shear past one another in the time set by the imposed sliding velocity, the sliding mechanism would be expected to change to either surface slip or chain breaking.

#### IV. Conclusion.

The SFA experiments have opened a door onto the rich and challenging phenomenology of liquids confined between solid surfaces. One of the key accomplishments of the past decade of experiments has been the characterisation of the mechanical properties of these liquid films. As the film thickness drops below  $\approx 5$  molecular diameters, the film resembles a gel mechanically, with low shear modulus and yield stress. Structurally these films are probably translationally disordered but with some long range orientational order, the latter reflecting the combined effect of the two unaligned crystal surfaces. With virtually nothing known about the thermal properties of these exotic new states, many new questions await experimental resolution. Likewise, simulation studies focused on the static properties of the confined films should be able to shed light on how these new properties arise from the 'awkward' constraints under which the liquid finds itself.

Of the nonlinear response of these films, and stick-slip motion in particular, the very complexity of the phenomena, along with the subtleties of the entanglement of apparatus and film response, make it difficult to assess the current position. This difficulty underlines the pressing need for useful theoretical models of the rheology of soft solids to provide some sort of framework on which to organise the experimental observations. While the strain-induced melting transitions of Schoen *et al* may provide a useful conceptual starting point, it is important to acknowledge the real novelty of the problems posed by these confined films. Ductile fracture (91), rheology of foams (90) and jamming models (94) offer promising insights. A recent experimental study of stick-slip friction in sheared granular layers (95) holds the exciting prospect of direct optical imaging of the mechanisms underlying this ubiquitous phenomenon.

**Acknowledgements.** It is a pleasure to thank Max Horn for valuable and enjoyable discussions on friction without which this review would never have been begun.

## References

1. Israelachvili, J.N.; *Surf.Sci.Rep.*, **1992**, *14*, 109.
2. Granick, S.; *Mater.Res.Soc.Bull.*, **1991**, *16*, 33.
3. Israelachvili, J.N.; Adams, G.E.; *J.Chem.Soc.Faraday Trans. 1*, **1978**, *74*, 975.
4. Horn, R.G.; Israelachvili, J.N.; *J.Chem.Phys.*, **1981**, *75*, 1400.
5. Christenson, H.K.; Horn, R.G.; Israelachvili, J.N.; *J.Colloid Interface Sci.*, **1982**, *88*, 79.
6. Christenson, H.K.; *J.Chem.Phys.*, **1983**, *78*, 6906.
7. Christenson, H.K.; Blom, C.E.; *J.Chem.Phys.*, **1987**, *86*, 419.
8. Christenson, H.K.; *J.Chem.Phys.*, **1986**, *90*, 4.
9. Christenson, H.K.; Gruen, D.W.R.; Horn, R.G.; Israelachvili, J.N.; *J.Chem.Phys.*, **1987**, *87*, 1834.
10. Israelachvili, J.N.; Knott, S.J.; Gee, M.; Witten, T.A.; *Macromolecules*, **1989**, *22*, 4247.
11. Granick, S.; Demirel, A.L.; Cai, L.L.; Peanasky, J.; *Isr.J.Chem.*, **1995**, *35*, 75.
12. Chan, D.Y.C.; Horn, R.G.; *J.Chem.Phys.*, **1985**, *83*, 5311.
13. Horn, R.G.; Hirz, S.J.; Hadziioannou, G.; Frank, C.W.; Catala, J.M.; *J.Chem.Phys.*, **1989**, *90*, 6767.
14. Pelletier, E.; Montfort, J.P.; Lapique, F.; *J.Rheol*, **1994**, *38*, 1151.
15. Dhinojwala, A.; Cai, L.; Granick, S.; *Langmuir*, **1996**, *12*, 4537.
16. Klein, J.; Kumacheva, E.; *J.Chem.Phys.*, **1998**, *108*, 6996.
17. Van Alsten, J.; Granick, S.; *Langmuir*, **1990**, *6*, 876.
18. Hu, H.W.; Carson, G.A. Granick, S.; *Phys.Rev.Lett*, **1991**, *66*, 2785.
19. Demirel, A.L.; Granick, S.; *Phys.Rev.Lett.*, **1996**, *77*, 2261.
20. Kumacheva, E.; Klein, J.; *J.Chem.Phys.*, **1998**, *108*, 7010.
21. Klein, J.; Kumacheva, E.; *Physica A*, **1998**, *249*, 206.
22. Van Alsten, J.; Granick, S.; *Macromolecules*, **1990**, *23*, 4856.
23. Granick, S.; *Science*, **1991**, *253*, 1374.
24. Hu, H.W.; Granick, S.; *Science*, **1992**, *258*, 1339.
25. Reiter, G.; Demirel, A.L.; Granick, S.; *Science*, **1994**, *263*, 1741.
26. Reiter, G.; Demirel, A.L.; Peanasky, J.; Cai, L.; Granick, S.; *J.Chem.Phys.*, **1994**, *101*, 2606.
27. Granick, S.; Hu, H.W.; *Langmuir*, **1994**, *10*, 3857.
28. Granick, S.; Hu, H.W.; Carson, G.A.; *Langmuir*, **1994**, *10*, 3867.
29. Peanasky, J.; Cai, L.L.; Granick, S.; Kessel, C.R.; *Langmuir*, **1994**, *10*, 3874.
30. Hirz, S.J.; Homola, A.M.; Hadziioannou, G.; Frank, C.W.; *Langmuir*, **1992**, *8*, 328.
31. Johnson, H.E.; Douglas, J.D.; Granick, S.; *Phys.Rev.Lett.*, **1993**, *70*, 3267.
32. Van Alsten, J.; Granick, S.; *Phys.Rev.Lett.*, **1988**, *61*, 2570.
33. Hu, H.W.; Granick, S.; Schweizer, K.; *J.Non-Cryst.Solids*, **1994**, *172-174*, 721.

34. Ferry, J.D.; *Viscoelastic Properties of Polymers*, Wiley, New York, 1980.
35. Gee, M.L.; McGuiggan, P.M.; Israelachvili, J.N.; Homola, A.M.; *J.Chem.Phys.*, **1990**, *93*, 1895.
36. Yoshizawa, H.; McGuiggan, P.M.; Israelachvili, J.N.; *Science*, **1993**, *259*, 1305.
37. Yoshizawa, H.; Israelachvili, J.N.; *Thin Solid Films*, **1994**, *246*, 71.
38. Israelachvili, J.N.; McGuiggan, P.M.; Homola, A.M.; *Science*, **1988**, *240*, 189.
39. Yoshizawa, H.; Israelachvili, J.N.; *J.Phys.Chem.*, **1993**, *97*, 11300.
40. Demirel, A.L.; Granick, S.; *Phys.Rev.Lett.*, **1996**, *77*, 4330.
41. Israelachvili, J.N.; *Fundamentals of Friction: Macroscopic and Microscopic Processes*, eds. I.L.Singer and H.M.Pollock, Kluwer Academic Publishers, 1992, p.373.
42. Heslot, F.; Baumberger, T.; Perrin, B.; Caroli, B.; Caroli, C.; *Phys.Rev.E*, **1994**, *49*, 4973.
43. Berman, A.D.; Ducker, W.A.; Israelachvili, J.N.; *Langmuir*, **1996**, *12*, 4559.
44. Klein, J.; *Annu.Rev.Mater.Sci.*, **1996**, *26*, 581.
45. Klein, J.; Kumacheva, E.; Mahalu, D.; Perahia, D.; Fetters, L.J.; *Nature*, **1994**, *370*, 634.
46. Johnson, K.L.; Kendall, K.; Roberts, A.D.; *Proc.R.Soc.London, Ser.A*, **1971**, *324*, 301.
47. Yoshizawa, H.; Chen, Y.L.; Israelachvili, J.N.; *J.Phys.Chem.*, **1993**, *97*, 4128.
48. Klein, J.; Luckham, P.F.; *Nature*, **1984**, *308*, 836.
49. e.g. Brown, D.E.; Sokol, P.E.; Ehrlich, S.N.; *Phys.Rev.Lett.*, **1998**, *81*, 1019 and references within.
50. Schoen, M.; Diestler, D.J.; Cushman, J.; *J.Chem.Phys.*, **1987**, *87*, 5464.
51. Schoen, M.; Rhykerd, C.L.; Diestler, D.J.; Cushman, J.; *Science*, **1989**, *245*, 1223.
52. Diestler, D.J.; Schoen, M.; Cushman, J.H.; *Science*, **1993**, *262*, 545.
53. Schoen, M.; Diestler, D.J.; Cushman, J.H.; *Phys.Rev.B*, **1993**, *47*, 5603.
54. Schoen, M.; Diestler, D.J.; Cushman, J.H.; *Mol.Phys.*, **1993**, *78*, 1097.
55. Schoen, M.; Cushman, J.H.; Diestler, D.J.; *Mol.Phys.*, **1994**, *81*, 475.
56. Schoen, M.; Hess, S.; Diestler, D.J.; *J.Chem.Phys.*, **1995**, *52*, 2587.
57. Sokoloff, J.B.; *Phys.Rev.Lett.*, **1993**, *71*, 3450.
58. Persson, B.N.; *Phys.Rev.Lett.*, **1993**, *71*, 1212.
59. Cieplak, M.; Smith, E.D.; Robbins, M.O.; *Science*, **1994**, *265*, 1209.
60. Persson, B.N.; *J.Chem.Phys.*, **1995**, *103*, 3849.
61. Robbins, M.O.; Smith, E.D.; *Langmuir*, **1996**, *12*, 4543.
62. Rundle, J.B.; Brown, S.R.; *J.Stat.Phys.*, **1991**, *65*, 403.
63. Bitsanis, I.A.; Pan, C.; *J.Chem.Phys.*, **1993**, *99*, 5520.
64. Gupta, S.; Koopman, D.C.; Westermann-Clark, G.B.; Bitsanis, I.A.; *J.Chem.Phys.*, **1994**, *100*, 8444.
65. Ballamudi, R.K.; Bitsanis, I.A.; *J.Chem.Phys.*, **1996**, *105*, 7774.
66. Wang, Y.; Hill, K.; Harris, J.G.; *Langmuir*, **1993**, *9*, 1983.
67. Wang, Y.; Hill, K.; Harris, J.G.; *J.Phys.Chem.*, **1993**, *97*, 9013.
68. Dijkstra, M.; *J.Chem.Phys.*, **1997**, *107*, 3277.

69. Gao,J.; Luedtke,W.D.; Landman,U.; *J.Chem.Phys.*, **1997**, *106*, 4309.
70. Wang,Y.; Harris,J.G.; *J.Chem.Phys.* , **1994**, *100*, 2376.
71. Persson, B.N.; *Phys.Rev.B* , **1994**, *50*, 4771.
72. Lupkowski, M.; van Swol, F.; *J.Chem.Phys.*, **1991**, *95*, 1995.
73. de Gennes,P.G.; *Adv.Colloidal Interface Sci.*. **1987**, *27*, 189.
74. Bonet Avalos,J.; Johner,A.; Joanny,J.F.; *J.Chem.Phys.*, **1994**, *101*, 9181.
75. Hirz,S.; Subbotin,A.; Frank,C.; Hadziioannou,G.; *Macromolecules* , **1996**, *29*, 3970 and references within.
76. Baljon,A.R.C.; Robbins,M.O.; *Science* , **1996**, *271*, 482.
77. Heinbuch,U.; Fischer,J.; *Phys.Rev.A* , **1989**, *40*, 1144.
78. Thompson, P.A.; Robbins, M.O.; *Phys.Rev.A*, **1990**, *41*, 6830.
79. Hersht,I.; Rabin,Y.; *J.Non-Cryst.Solids* , **1994**, *172-174*, 857.
80. Daikhin,L.; Urbakh,M.; *Phys.Rev.E* , **1994**, *49*, 1424.
81. Bowden,F.P.; Tabor,D.; *Friction and Lubrication of Solids* , **1950**, (Clarendon, Oxford)
82. Rabinowicz,E.; *Proc.Phys.Soc.(London)* , **1957**, *71*, 668; *ibid.*, *Friction and Wear*, **1959**, ed. R.Davies (Elsevier, Amsterdam), p.151
83. Dowson,D.; *History of Tribology*, **1979**, (Longman, London)
84. Rozman,M.G.; Urbakh,M.; Klafter,J.; *Physica A* , **1998**, *249*, 184.
85. Scholz,C.H.; *Nature* , **1998**, *391*, 37.
86. Ruina,A.; *J.Geophys.Res.*, **1983**, *88*, 10359.
87. Carlson,J.M.; Batista,A.A.; *Phys.Rev.E* , **1996**, *53*, 4153; Batista,A.A.; Carlson,J.M.; *Phys.Rev.E* , **1998**, *57*, 4986.
88. Thompson,P.A.; Robbins,M.O.; *Science* , **1990**, *250*, 792.
89. Ackerson,B.J.; Clark,N.A.; *Phys.Rev.A* , **1984**, *30*, 906.
90. Sollich, P; Lequeaux, F; Helbrand, F; Cates, M.E.; *Conf. on Jamming and Rheology*, Institute of Theoretical Physics, **1997**, <http://www.itp.ucsb.edu/online/jamming2>
91. Lobkovsky, A.E.; Langer,J.S.; *Phys.Rev.E* , **1998**, *58*, 1568.
92. Thompson,P.A.; Robbins,M.O.; Grest,G.S.; *Thin Films in Tribology*, 1993, eds. D.Dowson et al. (Elsevier) p. 347
93. Thompson,P.A.; Grest,G.S.; Robbins,M.O.; *Phys.Rev.Lett.*, **1992**, *68*, 3448.
94. Cates,M.E.; Wittmer,J.P.; Bouchard,J.-P.; Claudin,P.; *Phys.Rev.Lett.*, **1998**, *81*, 1841.
95. Nasuno,S.; Kudrolli,A.; Bak,A.; Gollub,J.P.; *Phys.Rev.E* , **1998**, *58*, 2161.

## Chapter 8

# Optical Probes of the Glass Transition in Thin Polymer Films

John R. Dutcher<sup>1</sup>, Kari Dalnoki-Veress<sup>1</sup>, and James A. Forrest<sup>2</sup>

<sup>1</sup>Department of Physics, University of Guelph, Guelph,  
Ontario N1G 2W1, Canada

<sup>2</sup>Department of Physics, University of Sheffield,  
Sheffield S3 7RH, United Kingdom

We have used three optical techniques, ellipsometry, Brillouin light scattering and photon correlation spectroscopy, to study the glass transition in a variety of polymer thin film geometries. Following a description of the essential features of these techniques, we summarize the results of our recent glass transition measurements for thin polystyrene (PS) films. In particular, for very thin freely-standing PS films, we have measured  $T_g$  values and corresponding structural relaxations that occur at temperatures that are reduced from the bulk value of  $T_g$  by more than 70 K.

There is tremendous interest in the physical properties of thin polymer films because of their use in technological applications such as coatings, adhesion and tribology, as well as the implications of these studies on fundamental issues such as the confinement of polymer molecules and the interaction of polymer molecules with other materials. New techniques have been developed, and existing techniques have been adapted, to probe the properties of thin polymer films (1, 2). A significant fraction of these techniques are optical in nature and involve analyzing the spectral content and polarization of light which has interacted with the sample. Optical methods have the considerable advantage that they are generally well-established and relatively inexpensive. In this chapter, we describe recent optical measurements of the glass transition temperature and the associated relaxation dynamics in thin polymer films.

As a collection of long-chain polymer molecules is cooled from the melt state through the glass transition temperature  $T_g$ , there is a dramatic reduction in the mobility of the polymer molecules over length scales ranging from the size of an entire molecule to the length of the polymer segments. The corresponding large increase in viscosity is accompanied by a similarly large increase in the relaxation time of the so-called  $\alpha$ -modes which are related to segmental mobility (3). If

the sample is cooled at a certain rate, at some temperature the time scale of the experiment becomes shorter than the time required for motion of the molecules, and the polymer melt is quenched into a disordered or glassy state.

Because of the strong dependence of the kinetics on temperature, the  $T_g$  value measured in a given experiment depends on the cooling (or heating) rate, as well as on the thermal history of the sample. Although the kinetic aspects of the glass transition are well-established, the issue of whether there is an underlying thermodynamic transition is still controversial. For a recent review of these issues, see ref. (4). Typically, the glass transition temperature  $T_g$  is chosen as the temperature corresponding to a measured discontinuity in the thermal expansion.

The possibility of observing finite size effects related to the glass transition was suggested by the postulation of a cooperatively rearranging region (CRR) (5). As a result, motion of a given segment within a polymer melt requires the cooperative motion of neighbouring segments. Experimental studies have provided some evidence for the existence of a CRR with dimensions of the order of 7 nm (6). Another length scale relevant to samples containing long-chain polymer molecules is the overall size of the molecules which can be characterized by the root-mean-square end-to-end distance  $R_{EE}$ . By spincoating solutions of polymer molecules dissolved in a solvent, it is straightforward to prepare films of polymer molecules in which the film thickness is comparable to, or less than,  $R_{EE}$ . This allows the possibility of probing finite size effects related to the confinement of the polymer molecules. For a recent summary of experimental and theoretical investigations of confinement effects on  $T_g$ , see the introduction to ref. (7).

There are two classes of optical experiments which have been developed to probe the glass transition in thin polymer films. The first class of experiment involves analyzing light which is specularly reflected from a homogeneous film supported on a substrate. A particularly important example of this technique is ellipsometry, in which the polarization of the specularly-reflected light is analyzed. Ellipsometry has been used to probe the temperature dependence of the thermal expansion of thin polymer films, and hence  $T_g$ , both for single films and multilayer films. The second class of optical experiment involves detecting and analyzing the light which is diffusely scattered by time-dependent optical inhomogeneities, such as density and surface fluctuations, within the sample. Of these techniques, Brillouin light scattering (BLS) and photon correlation spectroscopy (PCS) have been used to measure the glass transition and the associated relaxation dynamics, respectively. A schematic diagram of the different light scattering mechanisms is shown in Figure 1.

Schematic diagrams of cross-sectional views of the three different film geometries used in this work are shown in Figure 2: a polymer film supported on a substrate with a free upper film surface (uncapped supported), a polymer film supported on a substrate with a thin solid capping layer on the upper film surface (capped supported), and an unsupported or freely-standing polymer film. Careful preparation of the films and control of their thermal history is crucial to ensure reliable, reproducible measurements of the glass transition. Although the complete details of the preparation of the films are provided in refs. (7-10), we summa-

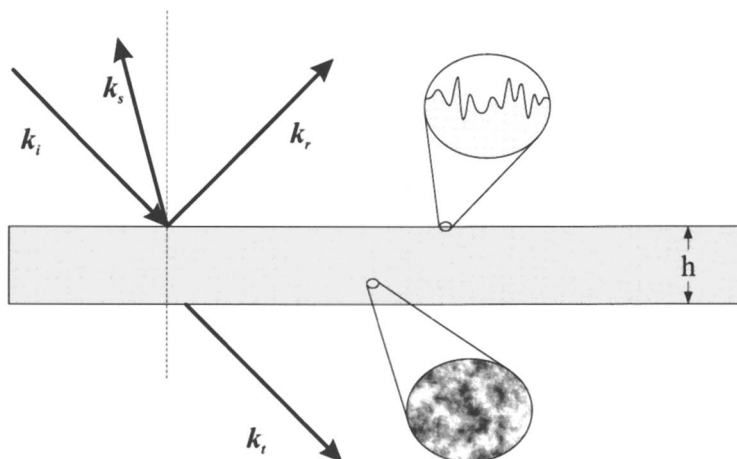


Figure 1: Schematic diagram of light scattering mechanisms. The incident light of wavevector  $k_i$  can be scattered specularly (wavevector  $k_r$ ), or diffusely (wavevector  $k_s$ ) by surface and density fluctuations.

size the important details here. Polystyrene (PS) molecules with a well-defined molecular weight, i.e. polydispersity index  $\sim 1.1$ , were dissolved in toluene with PS concentrations ranging from one to several percent. Freely-standing PS films were prepared by first spincoating the polymer solution onto clean glass slides. The films were then annealed at a temperature greater than the bulk value of  $T_g$  for more than 12 h, and cooled at a well-defined, slow rate to room temperature. The PS films were then floated onto distilled water and transferred to a sample holder containing a small, 3 mm diameter hole, creating a freely-standing PS film. Uncapped and capped supported PS films were prepared either by spincoating the polymer solution directly onto a substrate, or by water-transfer of a PS film onto a substrate. Subsequent evaporation of a thin layer of  $\text{SiO}_x$  onto the top PS film surface resulted in capped supported films. All supported films were annealed at a temperature greater than the bulk value of  $T_g$  and cooled slowly to room temperature before glass transition measurements were performed to ensure a well-defined thermal history.

Below we discuss the aspects of the experimental techniques of ellipsometry, BLS and PCS which are essential for our recent measurements of the glass transition in thin polymer films. In addition, we present a summary of our experimental results.

### Specularly-Scattered Light

Light incident on a material is scattered by inhomogeneities in the dielectric constant of the material. For the simple case of an optically-homogeneous, semi-

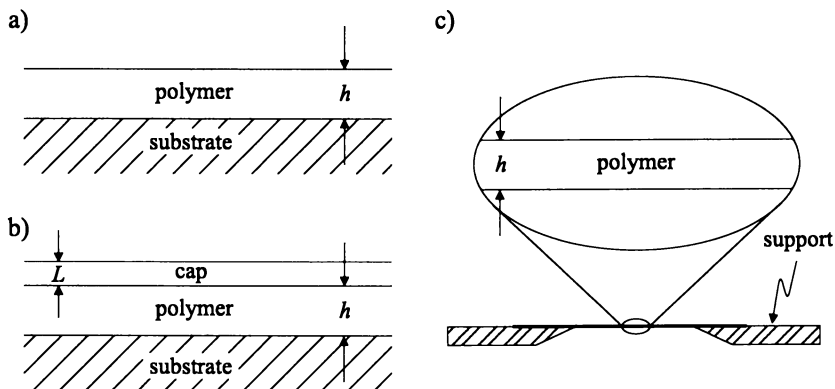


Figure 2: Schematic diagrams of cross-sections of different film geometries: (a) uncapped polymer film supported on substrate, (b) capped polymer film supported on substrate, and (c) freely-standing polymer film.

infinite material, the inhomogeneity which gives rise to scattering is the interface between the material and the surrounding medium. If the interface is perfectly flat, the scattering of light simply leads to the well-known case of specular reflection from the interface, as well as transmission of light for an optically-transparent material. For a sample consisting of a homogeneous, optically-transparent film supported on an optically-absorbing substrate, there are two reflecting interfaces separated by the thickness of the film  $h$ , and the electric fields due to multiple reflections from the two interfaces must be added to calculate the total reflected light intensity.

**Ellipsometry.** One of the most useful specular light scattering techniques for the study of the glass transition in thin polymer films is ellipsometry. In general, the incident light has two polarization components:  $p$ -polarized (parallel to the plane of incidence defined by the incident light wavevector  $\mathbf{k}_i$  and the film normal, see Figure 1) and  $s$ -polarized (perpendicular to the plane of incidence). Both polarization components are reflected and transmitted according to the Fresnel relations (11). For light of arbitrary polarization incident on a film-covered substrate, there are reflection and transmission coefficients for light incident at both interfaces. The total electric field reflected from the film is given by a sum of all electric field contributions for each of the  $p$ - and  $s$ -polarized components (11). Since the reflection and transmission coefficients for the two polarizations at the two film interfaces are generally different, reflection of light from the film-covered surface generally changes the polarization state of the light. The ratio of the total reflection coefficients for  $p$ - and  $s$ -polarized light,  $r_p/r_s$ , can be written in terms



of two ellipsometric parameters  $\Delta$  and  $\Psi$  as (12)

$$\frac{r_p}{r_s} = \tan \Psi \cdot e^{i\Delta}. \quad (1)$$

For the common case of an optically-transparent polymer film with an underlying substrate for which the optical properties are known, it is relatively straightforward to determine the two unknown quantities, the film thickness  $h$  and the refractive index  $n$  of the film, from the measured parameters  $\Delta$  and  $\Psi$ . One typically measures a series of films of the same material with different thicknesses  $h$  to obtain the best fit values of  $h$  and the best fit, common value of  $n$ .

Measurement of film properties using ellipsometry is surprisingly sensitive, due in no small part to the high quality of optical devices which are available. Using light with a wavelength of  $\sim 500$  nm, one can measure film thickness with a precision of  $\sim 0.1$  nm. This high degree of precision is obtained because the ellipsometry measurement accounts for the *relative phases* of the electric fields for the reflected and transmitted light components.

There are two commonly-used schemes for ellipsometric measurements, which differ in the manner in which the polarization of the reflected light is measured. Both schemes employ a light source with variable linear polarization, a compensator (such as a quarter-wave plate or a half-wave plate) placed between the light source and the sample, and a linear polarizer (analyzer  $A$ ) placed between the sample and detector. The first technique is known as nulling ellipsometry, in which the compensator is a quarter-wave plate placed immediately after a linear polarizer  $P$  and before or after the sample. The polarization of the incident beam is varied until the reflected light before the analyzer  $A$  is linearly polarized, as detected by cross-polarizing the reflected light by rotating  $A$  to obtain a null (or zero transmission) at the detector. The values of the angles of the polarizer and analyzer with respect to the plane of incidence corresponding to the null are simply related to  $\Delta$  and  $\Psi$  (12). The second technique is referred to as modulated ellipsometry, and this can be further divided into cases in which the polarization is modulated by a rotation of one of the polarizing elements, and those of phase-modulated ellipsometry in which the phase of the compensator is varied with time. In both of these cases the time-dependent intensity of the light signal transmitted through the optical system can be analyzed to give  $\Delta$  and  $\Psi$  (12). Most modern modulated ellipsometers are of the phase-modulated type for two reasons. First of all, the phase modulation may in general be done much more rapidly than physical rotation of an optical component (typical values of the modulation frequency are 50 kHz for phase modulation versus 100 Hz for rotation of a polarizer), which results in a much greater data acquisition rate. Secondly, phase-modulated devices are not susceptible to aliasing (12) caused by a rotating polarizer, and do not cause any sample vibrations.

Ellipsometry was the first technique used to measure  $T_g$  for thin polymer films (13), primarily because of its sensitivity and the ease of performing the measurements. As discussed in the introduction,  $T_g$  can be identified as the temperature corresponding to a discontinuity in the thermal expansion, i.e. a "kink"

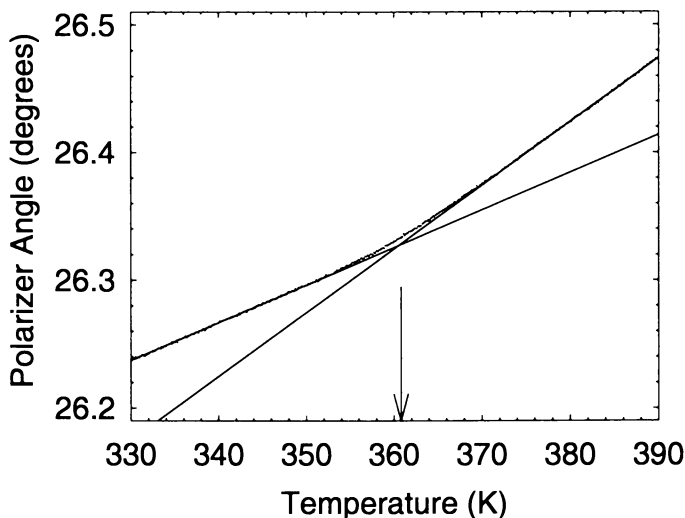


Figure 3. Ellipsometry polarizer angle versus temperature for an uncapped supported PS film ( $\bar{M}_w = 767 \times 10^3$  and  $h = 29$  nm). The vertical arrow indicates the  $T_g$  values for the film. (Adapted with permission from reference 7. Copyright 1997 American Physical Society.)

in the thickness  $h$  versus temperature plot. In addition, the refractive index  $n$ , which also depends on the material density, is expected to exhibit a kink in its temperature dependence at  $T_g$ . Since both  $\Delta$  and  $\Psi$  depend on both  $h$  and  $n$ , one may simply look for a kink in the temperature dependence of  $\Delta$  or  $\Psi$  to obtain a reliable measure of  $T_g$ . Both nulling and modulated ellipsometers have been used to measure  $T_g$  for thin polymer films, for film thicknesses as small as 5 nm. Representative data obtained using a nulling ellipsometer for an uncapped supported polystyrene (PS) film ( $h = 29$  nm) on silicon oxide ( $\text{SiO}_x$ ) is shown in Figure 3. The dependence of the shift in  $T_g$  on polymer film thickness  $h$  as measured using ellipsometry is discussed below. Because ellipsometry is very sensitive to small changes in the properties of the film, it can also be used to measure  $T_g$  values for more complicated sample geometries, such as multilayer films (7).

### Diffusely-Scattered Light

In the previous section we were concerned with smooth, optically-homogeneous materials, in which the optical inhomogeneities are due to the film interfaces. Of course in practice all materials have other inhomogeneities such as surface roughness or local variations in the dielectric constant of the medium (see Figure 1). Light scattered from these inhomogeneities will lead to scattering in directions other than that of the specular reflection, i.e. diffusely-scattered light. These

*higher-order* inhomogeneities can be divided into two types. The first (and typically unimportant) type corresponds to static inhomogeneities, which may be due to, e.g., dust in the sample and static surface roughness. Important information can be obtained by analyzing the light scattered from time-dependent inhomogeneities such as fluctuations in the dielectric constant which result from fluctuations in the mass density, and the dynamic rippling of the film surfaces. Both types of fluctuations are due to thermal noise. From an experimental perspective, these fluctuations can be further divided into propagating and non-propagating fluctuations.

**Brillouin Light Scattering.** Density fluctuations which propagate throughout the film and surface fluctuations which propagate along the film surfaces can be visualized as sound waves or phonons with all possible frequencies and wavevectors. In the Brillouin light scattering (BLS) experiment, laser light is focussed onto the film surface and a small fraction of the light scatters from the propagating fluctuations. The alternating compression and rarefaction of a longitudinal wave (or the longitudinal component of a wave with both transverse and longitudinal character) will scatter the incident light. Because the Brillouin light scattering (BLS) experiment is a scattering experiment, with incident light with a well-defined frequency and wavevector, the light is scattered only from those components of the thermal noise which satisfy energy and momentum conservation, with the Doppler shift in the scattered light frequency equal to the phonon frequency. Typical phonon frequencies are in the GHz ( $10^9$  Hz) frequency range, i.e. only one part in  $10^5$  of the laser light frequency. To separate the small component of frequency-shifted scattered light from the large component of the unshifted scattered light, a very sensitive Fabry-Perot interferometer is used. Recent major advances in Fabry-Perot instrumentation by Sandercock (14) have made it possible to detect BLS from very thin films and interfaces.

For thin films, either supported on a substrate or freely-standing, the phonons which are probed in the BLS experiment are not the familiar longitudinal and transverse phonons characteristic of bulk materials. Instead, the boundary conditions at the film interfaces give rise to a series of film-guided modes which have both longitudinal and transverse character. The film-guided modes are dispersive, i.e. their velocities  $v$  vary as the product of the phonon wavevector component  $Q_{\parallel}$  parallel to the film surface and the film thickness  $h$  (15). The most spectacular success of BLS in probing the glass transition of thin polymer films has been its unique ability to measure  $T_g$  for thin freely-standing polymer films (7, 8). For isotropic freely-standing films, the film-guided phonons are referred to as Lamb waves, and the dispersion relations are relatively simple to derive (15). The phonon modes can be classified according to the symmetry of the displacement vectors across the midplane of the film. The antisymmetric modes are denoted as  $A_i$ , and the symmetric modes are denoted as  $S_i$ , with the index  $i \geq 0$ . Dispersion curves, both calculated and measured, are shown in Figure 4 for freely-standing polystyrene films, with the lowest order modes labelled. The dispersion curves are uniquely determined by two physical quantities, the longitudinal phonon ve-

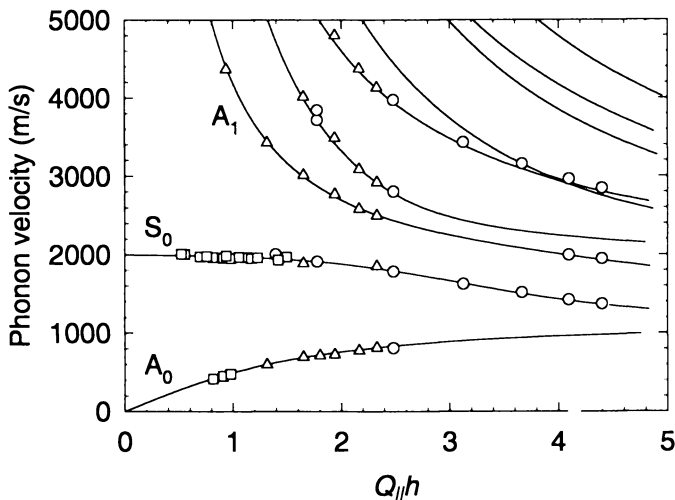


Figure 4. Measured and calculated velocity dispersion curves for freely-standing PS films. Data were obtained for films with thicknesses ranging from  $h = 29$  to  $190$  nm. (Adapted with permission from reference 10. Copyright 1999 American Physical Society.)

locity,  $v_L$  and the transverse phonon velocity  $v_T$ , both of which are given by an expression of the form  $v_i = \sqrt{c_i/\rho}$ , where  $c_i$  is the relevant elastic modulus,  $\rho$  is the mass density and  $i = L, T$ . In addition to the explicit dependence of  $v_i$  on  $\rho$ , the elastic moduli for fragile glass formers such as polymers may also be strong functions of the density (16). Therefore measurements of the film-guided phonon velocities using BLS allow a very sensitive, though indirect, probe of the mass density (10).

In principle any of the film-guided modes may be used to probe the temperature dependence of the mass density and thus measure  $T_g$  for thin polymer films, but there are a number of practical limitations. The biggest limitation for very thin polymer films can be understood from the shape of the dispersion curves shown in Figure 4. For typical values of  $Q_{\parallel} = 2k_i \sin \theta_i \approx 10^7 \text{ m}^{-1}$ , corresponding to green light of wavevector  $k_i$  incident at an angle of  $\theta_i = 45^\circ$ ,  $Q_{\parallel}h < 1$  for  $h < 100$  nm. For small  $Q_{\parallel}h$ , all but two of the phonon mode velocities diverge. In addition, measurement of the  $A_0$  mode can be difficult since its velocity approaches zero for small  $Q_{\parallel}h$  such that the  $A_0$  mode merges with the large unshifted component of scattered light. The remaining mode, the  $S_0$  mode, proves to be very useful indeed. Its velocity approaches a constant, non-zero value, determined by  $v_L$  and  $v_T$ , as  $Q_{\parallel}h$  approaches zero. As a result, the  $S_0$  mode velocity is insensitive to small changes in the film thickness that may result from directing the focussed incident laser beam onto different spots on the same film. It also means that the room-temperature value of the  $S_0$  mode velocity is essentially the same

for the entire film thickness range of interest ( $h < 100$  nm). This insensitivity to the film thickness coupled to very high sensitivity to changes in the material properties makes the study of the  $S_0$  mode ideally suited to probing the small changes in mass density with temperature. By measuring the  $S_0$  phonon velocity or, equivalently, the frequency shift of light scattered from the  $S_0$  phonon, as a function of temperature we can identify  $T_g$  as the temperature corresponding to the “kink” in the  $S_0$  phonon frequency versus temperature plot (as in the ellipsometry data shown in Figure 3). We have performed BLS measurements of  $T_g$  for freely-standing films with  $h$  as small as 29 nm. This lower limit is related to the difficulty in preparing such thin, freely-standing films, and is not a limitation of the BLS technique. Perhaps surprisingly, there is sufficient sensitivity in the BLS experiment to measure the acoustic phonons guided by polymer films with thicknesses much smaller than the acoustic phonon wavelength ( $\lambda \approx 300$  nm). This high sensitivity is due to the large amount of light scattering from dynamic surface roughness, relative to that from bulk density fluctuations. This so-called “surface ripple” scattering (14) is relatively insensitive to the film thickness for the  $S_0$  mode with  $Q_{\parallel}h < 1$ .

Using BLS, we have observed very large reductions in  $T_g$  with decreasing film thickness  $h$  for freely-standing PS films with  $h < R_{EE}$  (see Figure 5) (7). For high molecular weight  $M_w$  polymers, the  $T_g$  reductions for freely-standing PS films depend significantly on the  $M_w$  value of the polymer molecules. This behavior is qualitatively different from the lack of  $M_w$ -dependence of the  $T_g$  reductions with decreasing film thickness observed for supported PS films (17). Quantitatively, the results obtained for freely-standing PS films are very different from those observed for supported PS films. In Figure 6 is shown data obtained for freely-standing, uncapped supported and capped supported PS films with  $\overline{M}_w = 767 \times 10^3$ . The reductions in  $T_g$  observed for freely-standing films are much larger than those observed for supported films, illustrating the large effect of the substrate on the measured  $T_g$  values.

One possible explanation of the large  $T_g$  reductions observed for very thin, freely-standing PS films is a corresponding reduction in mass density of these films. However, precise measurements of the  $S_0$  mode frequency for freely-standing PS films in the glassy state have allowed us to infer that the mass density must be the same as in bulk to within  $\pm 0.5\%$  for all films measured, with  $T_g$  values which differ by as much as 70 K (10). The results of simple calculations suggest that density decreases of  $\approx 2\%$  are required to account for the largest  $T_g$  reductions observed.

It is worth noting that BLS may also be used to measure  $T_g$  for films supported on substrates. Because the substrates must be optically absorbing, the use of a focussed laser beam causes heating of the polymer film. It requires a complicated procedure to determine the sample temperature precisely: performing BLS experiments using different laser powers, and extrapolation of the results to zero laser power. Measurements of  $T_g$  for supported polymer films can be performed much more easily and directly using ellipsometry.

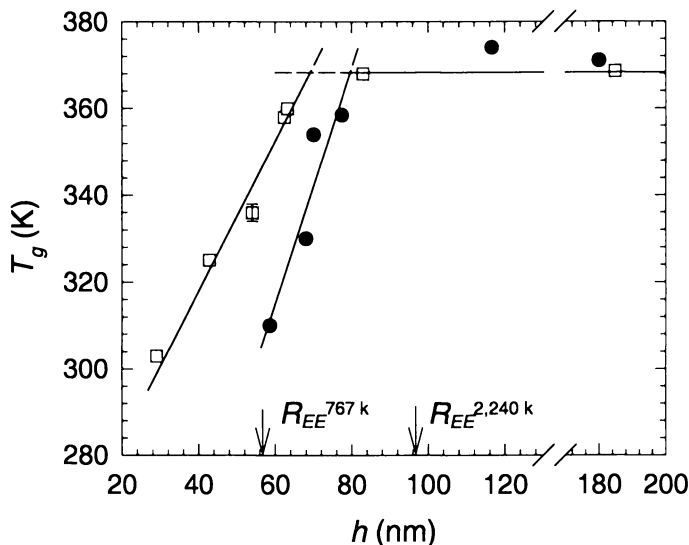


Figure 5.  $T_g$  versus room-temperature film thickness  $h$  for freely-standing PS films with  $\bar{M}_w = 767 \times 10^3$  (open squares) and  $\bar{M}_w = 2240 \times 10^3$  (solid circles). The vertical arrows indicate the  $R_{EE}$  values for the two  $M_w$  values. (Adapted with permission from reference 7. Copyright 1997 American Physical Society.)

**Photon Correlation Spectroscopy.** In addition to light scattering from propagating density fluctuations, as measured in the BLS experiment, light may be scattered by non-propagating fluctuations, which is the basis of the photon correlation spectroscopy (PCS) experiment (18). In principle, the two experiments are identical except for the techniques used to analyze the scattered light. In the BLS experiment, one measures the very small fraction of light which is Doppler-shifted because of scattering from propagating phonon modes in the material, whereas in the PCS experiment, one measures *quasielastic* scattering from time-dependent density fluctuations within the material. The fluctuations studied using PCS have frequencies which are typically  $< 10^8$  Hz and are most effectively analyzed directly in the time domain. In the PCS experiments the time-dependent scattered light intensity  $I(t)$  is used to continuously calculate the intensity autocorrelation function:

$$g_{exp}(t) = \langle I(t)I(0) \rangle / \langle I \rangle^2. \quad (2)$$

Although the intensity autocorrelation function is measured in the PCS experiment, it is the autocorrelation function of the scattered electric field

$$g_1(t) = \langle E_s(t)E_s(0) \rangle / \langle E_s \rangle^2 \quad (3)$$

which is proportional to the density autocorrelation and hence to the structural relaxation function of the material. If all of the light at the detector has scattered

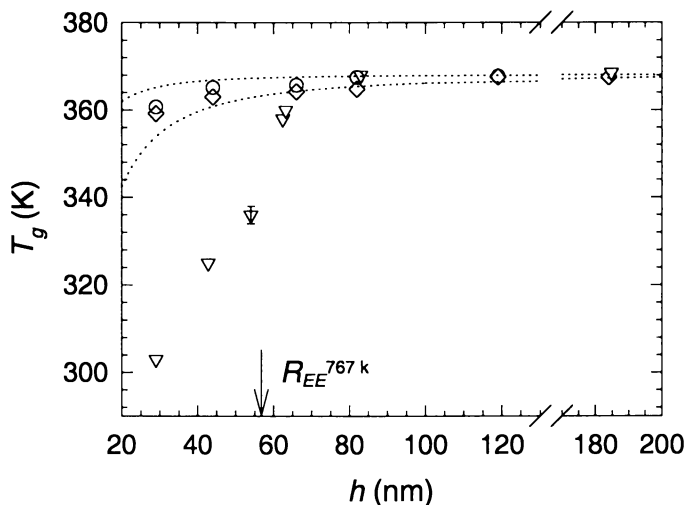


Figure 6.  $T_g$  versus room-temperature film thickness  $h$  for PS films with  $\overline{M}_w = 767 \times 10^3$ . The data for freely-standing, uncapped supported and capped supported films are represented by inverted triangles, circles and diamonds respectively. The dashed curves represent the spread and uncertainty of data for uncapped supported PS films on Si (17). (Adapted with permission from reference 7. Copyright 1997 American Physical Society.)

from dynamic inhomogeneities in the sample, the desired structural relaxation function may be obtained using the simple relation:  $g_1(t) = [(g_{exp}(t) - 1)/\sigma]^{1/2}$ , where  $\sigma$  is an experimental parameter ideally close to 1.

For very thin films, there is very little light scattered from the material, with most of the scattering apparently due to the presence of static inhomogeneities such as surface roughness (9). However, it is possible to measure structural relaxation in very thin films by employing careful sample preparation techniques and diligent exclusion of extraneously scattered light. In particular, the technique has been used by one of us to measure structural relaxation in very thin freely-standing PS films for which the  $T_g$  values had been measured previously using BLS (9). In this case the intensity at the detector contains only a small fraction of light that has scattered from density fluctuations within the material, and the structural relaxation function is proportional to  $[g_{exp}(t) - 1]$ .

The motivation for performing PCS measurements of freely-standing PS films was two-fold. First of all, since the relationship between the  $T_g$  values and the structural relaxation is indirect, it is desirable to have a more direct probe of the relaxation processes. A comparison of the results obtained from the two measurements could help to resolve conflicting ideas which currently exist concerning the glass transition in thin polymer films. Secondly, since the  $T_g$  values for freely-standing PS films are reduced dramatically from that in bulk, it is possible that the relaxation properties of freely-standing PS films are also substantially altered.

The PCS experiments on freely-standing PS films provided the first direct measurements of the relaxation function in polymer films with  $T_g$  values reduced from that in bulk. In Figure 7 are shown intensity autocorrelation functions measured for a freely-standing PS film with  $h = 22$  nm. For the lowest measured temperature of  $T = 291$  K, there is only a very slight hint of relaxation within the time window of the experiment, and for the data collected at  $T = 297$  K, the entire relaxation function is observed within the time window of the experiment. Since the glass transition, as defined by the near-discontinuity in the thermal expansion, occurs at approximately the temperature for which the average relaxation time  $\langle \tau \rangle = 100$  s, the PCS data allow us to state that  $T_g = 294 \pm 3$  K. This  $T_g$  value is in agreement with the value  $T_g = 287 \pm 10$  K obtained by extrapolating the  $T_g$  values determined using BLS to  $h = 22$  nm. The relaxation functions measured using PCS were well-described by a stretched exponential function  $\phi(t) = \exp(t/\tau)^\beta$  with a  $\beta$  value indistinguishable from that of bulk PS.

## Summary and Conclusions

We have described the essential features of three optical techniques, ellipsometry, Brillouin light scattering and photon correlation spectroscopy, that we have used to study the glass transition in a variety of polymer thin film geometries. In addition, we have summarized the results of our recent glass transition measurements for thin polystyrene (PS) films. In particular, for very thin freely-standing PS

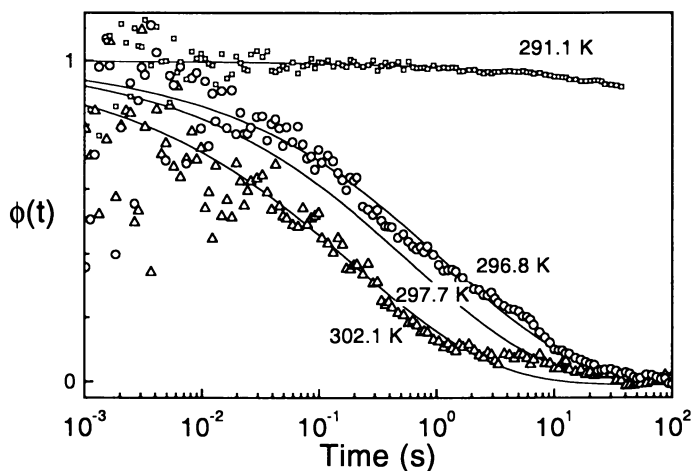


Figure 7. Intensity autocorrelation functions  $\phi(t) = [g_{exp}(t) - 1]/[g_{exp}(0) - 1]$  for a freely-standing PS film with  $h = 22$  nm. The temperature values corresponding to each measurement are indicated in the figure. (Adapted with permission from reference 9. Copyright 1998 American Physical Society.)



films, we have measured  $T_g$  values and corresponding structural relaxations that occur at temperatures that are reduced from the bulk value of  $T_g$  by more than 70 K.

## Acknowledgments

We have benefitted from many useful discussions with Dr. B.G. Nickel. We gratefully acknowledge the financial support of the Natural Sciences and Engineering Research Council of Canada. JAF acknowledges the generous support of Dr. L.M. Torell and the Chalmers University of Technology, Göteborg, Sweden. We would also like to thank C. Svanberg for his assistance with the PCS measurements.

## Literature Cited

- (1) *Physics of Polymer Surfaces and Interfaces*; Sanchez, I.C., Ed.; Butterworth-Heinemann: Boston, 1992.
- (2) Jones, R.A.L.; Richards, R.W. *Polymers at Surfaces and Interfaces*; Cambridge University Press: Cambridge, U.K., 1999.
- (3) Strobl, G. *The Physics of Polymers*, Second Edition; Springer: Berlin, 1997.
- (4) Forrest, J.A.; Jones, R.A.L. In *Polymer Surfaces, Interfaces and Thin Films*; Karim, A.; Kumar, S., Eds.; World Scientific: 1998.
- (5) Adam, G.; Gibbs, J.H. *J. Chem. Phys.* **1965**, *43*, 139.
- (6) Arndt, M.; Stannarius, R.; Groothues, H.; Hempel, E.; Kremer, F. *Phys. Rev. Lett.* **1997**, *79*, 2077.
- (7) Forrest, J.A.; Dalnoki-Veress, K.; Dutcher, J.R. *Phys. Rev. E* **1997**, *56*, 5705.
- (8) Forrest, J.A.; Dalnoki-Veress, K.; Stevens, J.R.; Dutcher, J.R. *Phys. Rev. Lett.* **1996**, *77*, 2002; *ibid.* **1996**, *77*, 4108.
- (9) Forrest, J.A.; Svanberg, C.; Révész, K.; Rodahl, M.; Torell, L.M.; Kasemo, B. *Phys. Rev. E* **1998**, *58*, R1226.
- (10) Forrest, J.A.; Dalnoki-Veress, K.; Dutcher, J.R. *Phys. Rev. E*, in press.
- (11) Born, M.; Wolf, E. *Principles of Optics*, Sixth Edition; Pergamon: Oxford, 1980.
- (12) Azzam, R.M.A.; Bashara, N.M. *Ellipsometry and Polarized Light*; North-Holland: Amsterdam, 1977.
- (13) Beaucage, G.; Composto, R.J.; Stein, R.S. *J. Poly. Sci., Poly. Phys. Ed.* **1993**, *30*, 131.
- (14) Sandercock, J.R. In *Light Scattering in Solids III*; Cardona, M.; Güntherodt, G., Eds.; Springer-Verlag: Berlin, 1982, pp. 173-206.
- (15) Farnell, G.W.; Adler, E.L. In *Physical Acoustics, Principles and Methods*; Mason, W.P.; Thurston, R.N., Eds.; Academic: N.Y., 1972; Vol. 9, Chap. 2.
- (16) Masnik, J.E.; Kieffer, J.; Bass, J.D. *J. Chem. Phys.* **1995**, *103*, 9907.
- (17) Keddie, J.L.; Jones, R.A.L.; Cory, R.A. *Europhys. Lett.* **1994**, *27*, 59.
- (18) *Dynamic Light Scattering: Applications of Photon Correlation Spectroscopy*; Pecora, R., Ed.; Plenum Press: New York, 1985.

## Chapter 9

# Manipulating Copolymers with Confinement and Interfacial Interactions

O. K. C. Tsui, L. Rockford, E. Huang, and T. P. Russell<sup>1</sup>

Polymer Science and Engineering Department, University of Massachusetts,  
Amherst, MA 01003

Fully utilizing the morphologies present in polymeric materials requires simple, robust methods for manipulating the spatial organization of the morphology over many length scales. In the absence of an external applied field, control over the morphology is achieved by tailoring the interfacial interactions and film thickness. In thin films, incommensurability between the natural polymer length scale and film thickness will tend to disorder the polymer, resulting in a corresponding shift in the ordering transition temperature. The phase transition behavior of a symmetric diblock copolymer is used to demonstrate this point. In addition, two different cases are discussed which demonstrate the influence of interfacial interactions. In the first, the surface is laterally homogeneous but can be made effectively neutral which results in an orientation of the morphology normal to the surface. In the second, the surface is laterally heterogeneous where the chemical composition of the surface is altered in a periodic manner. The wavelength of the period is made comparable to the size of the polymer chain and, hence, manipulates the polymer on a molecular scale. Molecular recognition of the surface by the polymer is shown to yield control over the morphology both parallel and normal to the surface.

The morphologies observed in polymeric materials span length scales from the nanoscopic to macroscopic. Taking advantage of naturally developing structures, however, requires the ability to manipulate their spatial orientation. Bates and coworkers (*1*) have described the use of shear to achieve this end and have shown that mechanical forces can be effectively coupled into the polymer, to produce well-defined, highly oriented morphologies with very high persistence. In the case of thin

<sup>1</sup>Corresponding author.

films, however, the use of mechanical force is difficult, if not impossible, to utilize in any practical manner. Consequently, other routes are needed to manipulate the spatial arrangement of the polymer morphology. While electric fields have been shown to be ineffective in orienting bulk polymers (2,3), in thin films, very high field strengths can be achieved at low applied voltages (due to the small separation distance between the electrodes) to produce highly oriented morphologies (4). Magnetic fields, though not studied in detail, can also be used (5). However, practical use of magnetic fields for controlling polymer morphology may be limited due to the cost of the magnets which produce sufficiently high fields, and the need to have non-magnetic processing equipment. An attractive, alternative route is to tailor both the film thickness and the interfacial interactions, such that the polymer morphology will spontaneously orient in a predetermined manner without the need of any applied, external field. Here, diblock copolymers of poly(styrene), PS, and poly(methyl methacrylate), PMMA, denoted P(S-*b*-MMA), and of PS and poly(*n*-butyl methacrylate), PnBMA, denoted P(S-*b*-nBMA), are used as simple model systems to demonstrate the idea and its feasibility.

Diblock copolymers, in the bulk, can microphase separate into morphologies ranging from spherical to cylindrical to lamellar having a characteristic period,  $L_0$ , on the tens of nanometer size scale (6). In the particular case of a symmetric, diblock copolymer, the copolymer microphase separates into a lamellar microdomain morphology. Locally, the lamellar microdomains are parallel to one another, as shown schematically in Figure 1a. However, the local orientation is only confined to single grains which are randomly oriented in the sample forming an isotropic structure globally. Adjacent to an interface, the preferential interactions of one of the blocks will force an orientation of the lamellar microdomains parallel to the interface (7-10). This orientation will persist into the bulk of the sample for some characteristic distance, whereupon, defects will cause a loss of a preferred orientation. If a thin film is prepared where there is a strong segregation of the blocks to both interfaces, as shown in Figure 1b, a global orientation of the block copolymer morphology parallel to the surface occurs (11-13). If the initial film thickness,  $t$ , is not commensurate with  $L_0$ , ( $nL_0$  for the case where the same component preferentially segregates to both interfaces or  $(n+1/2)L_0$  when one block segregates to one interface and the other block to the other interface), the diblock copolymer is frustrated as is evident from the observed difference between the measured period and the bulk value  $L_0$  for P(S-*b*-MMA) lamellae confined between two solid interfaces (15). For this system, when  $nL_0 < t < (n+1/2)L_0$ , the period of the copolymer is expanded in comparison to the bulk period, *i.e.* the individual copolymer chains stretch at the interface between the microdomains, but when  $(n+1/2)L_0 < t < nL_0$  the period is compressed in comparison to the bulk. In all cases, however, the strong interfacial interactions force the morphology to be parallel to the surface. The amount of compression or expansion depends upon the degree of incommensurability or frustration. If one of the surfaces is free, as in the case of a thin film on a solid substrate, this frustration is relieved by the formation of a terraced surface topography with a step height of  $L_0$ , commonly referred to as 'island' and 'hole' formation.

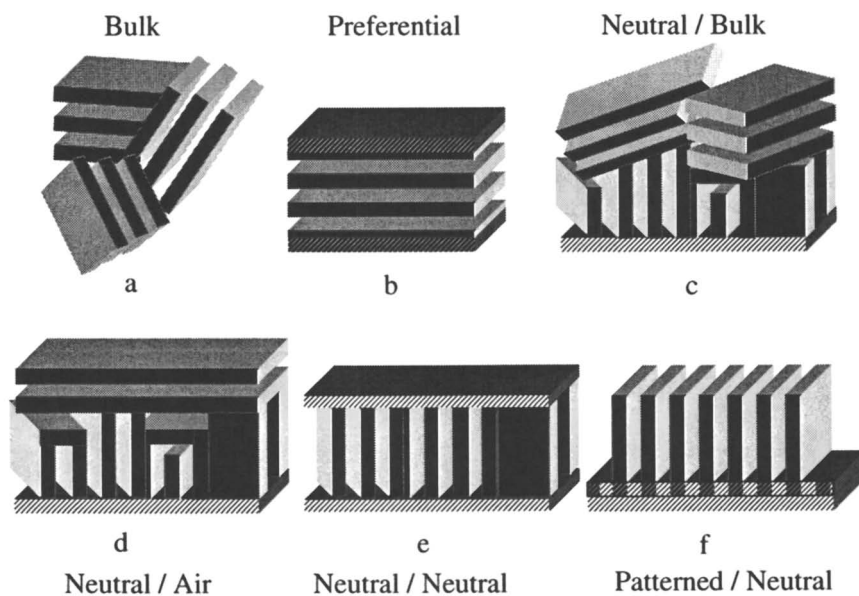


Figure 1. Schematic diagrams of the lamellar microdomains of a block copolymer in: a) the bulk, b) between two surfaces with preferential segregation by one of the components, c) at a neutral surface, d) between a neutral surface and the air surface, e) between two neutral surfaces, and f) between a heterogeneous and neutral surface.

While the thickness of the film can be used as a constraint on the system, it is evident that without modifying the interfacial interactions, controlling the orientation of the morphology in polymers is not possible (16-19). If the interfacial interactions can be tuned, such that interactions at one interface are balanced, as shown in Figure 1c or 1d, the lamellae adjacent to the neutral interface will orient normal to the interface (20). As one proceeds away from the interface into the bulk of the film, the orientation of the lamellae normal to the surface is lost and a random orientation is found (Figure 1c). For a thin film if there is a preferential interaction of one of the blocks at the other interface, as for example at the polymer/air interface where the lower surface energy component will segregate to the surface, then the lamellae will bend over to accommodate this constraint and orient parallel to the surface as shown schematically in Figure 1d (21). If interactions are balanced at both interfaces, then the lamellar microdomains will orient normal to each interface, and if the sample is not too thick, the preferential orientation of the lamellar microdomains normal to the interfaces will persist through the entire sample, as indicated schematically in Figure 1e. In each of these cases, the orientation of the lamellar grains in the plane of the interface is random. To gain further control over the orientation of the lamellar microdomains, a directionality must be placed in the interactions at the interface. One extreme case of this is shown in Figure 1f where a copolymer is placed in contact with a striped surface where the interactions along one stripe are favorable to one block and the interactions along the second stripe are favorable to the second block. Provided the stripe widths are comparable to the size of the individual blocks, a recognition of the substrate patterning occurs; the lamellar microdomains order normal to the substrate and are aligned by the striped surface (23-25).

Three different examples will be given where constraints are used to manipulate the morphology and thermodynamics of diblock copolymers. In the first the film thickness will be used to alter the phase behavior of a P(S-*b*-nBMA) symmetric diblock copolymer. By controlling the film thickness, the temperature at which P(S-*b*-nBMA) undergoes a transition from the disordered to ordered state can be changed. In the second, an asymmetric diblock copolymer of P(S-*b*-MMA), comprised of PMMA cylinders in a PS matrix, is placed in contact with a substrate where the interfacial interactions have been balanced forcing the cylinders to orient normal to the film surface. Finally, a symmetric P(S-*b*-MMA) diblock copolymer is placed in contact with a surface where the favorable interactions between the PS and PMMA blocks are periodically varied over a distances comparable to the size of the individual blocks. The recognition of the substrate patterning by the copolymer is shown to produce an ordered array of lamellar microdomains normal to the surface.

### Confinement Effects on Ordering

The order parameter for a diblock copolymer in the disordered state is by definition zero everywhere in the sample, with the equilibrium composition at any point in the sample equal to the average composition of the copolymer. Concentration fluctuations will occur though, due to the connectivity of the two blocks, which are

oscillatory in nature with a period given by the molecular weight of the copolymer, *i.e.* the size of the copolymer chain. The fluctuations are exponentially damped with a decay length,  $\xi$ , that depends upon the difference between the measurement temperature and the ordering transition temperature (26). At an interface, however, the preferential interactions of one of the components will pin a particular fluctuation at the plane of the interface. The composition profile normal to the interface can then be described by an exponentially damped cosine function with a period given by the size of the copolymer chain and a decay length identical to the bulk, mean field value at the same temperature (27). It is this pinning of a composition fluctuation at an interface that gives rise to surface-induced ordering in a disordered copolymer.

Interesting questions regarding the order-disorder transition arise when one reduces the sample thickness to a value comparable to  $\xi$ . Menelle *et al.* (28) studied the temperature and thickness dependence of the ordering of symmetric diblock copolymer thin films of P(S-*b*-d-MMA) using neutron reflectivity. As the temperature of the disordered copolymer film was decreased,  $\xi$  was found to increase corresponding to an increase in the distance over which the decaying oscillatory concentration profile propagated away from the surface. For a film of thickness  $t$ , the decay length diverged at a temperature  $T_{\infty,t}$  that was substantially different from the ordering transition temperature in the bulk  $T_{ODT,B}$ . It is interesting to note that the phase transition temperature  $T_{\infty,t}$  defined in Reference 28 for the thin film corresponds to an order to disorder transition temperature in the mean field sense. The results of this study showed that concentration fluctuations pinned at the interface may induce full ordering in a block copolymer thin film well above the ordering transition temperature in the bulk.

Unexpectedly, however, effects on the ordering transition associated with the frustration of the copolymer were not observed. In general, the film thickness will not be commensurate with the natural microdomain period, and concentration fluctuations propagating from either surface will destructively interfere in the center of the film. This induced disorder suppressing oscillations should cause the ordering transition temperature to decrease, if disordering occurs on heating, or increase, if the disordering occurs upon cooling. This should produce systematic variations in the ordering transition temperature that are superposed on the effect associated with finite sample size.

Neutron reflectivity measurements were performed on thin films of P(d-S-*b*-nBMA) ( $M_w = 8.5 \times 10^4$ ) to investigate such an effect. The film thickness was varied in steps of  $\sim 5$  nm to capture any systematic changes in the ordering transition temperature as a function of film thickness. Solutions of the copolymer in toluene (3 - 6%) were spin-coated onto polished silicon wafers (5 cm in diameter and 5 mm thick) at various spin-coating speeds to produce films with thicknesses from 228 nm to 280 nm. Independent SANS measurements on the same material in the bulk showed that the natural lamellar period,  $L_0$  is 28.5 nm and the lower critical ordering transition temperature is 155°C. Neutron reflectivity profiles were measured for each sample at temperatures from 128°C to 160°C at  $\sim 3^\circ\text{C}$  intervals. After each temperature change

there was a 10 minute waiting period to allow the sample to equilibrate. A series of neutron reflectivity profiles of the 2806 Å thick sample taken at different temperatures within this temperature range are shown in Figure 2. The scattering vector,  $Q$ , spans from 0.02 to 0.03 Å<sup>-1</sup> ( $Q = 4\pi/\lambda \sin\theta$ , where  $\lambda$  is the neutron wavelength and  $\theta$  the incidence angle) and contains the first order Bragg peak corresponding to lamellar ordering of the copolymers. As shown in the figure, the peak intensity is pronounced at high temperatures but diminishes as the temperature is decreased, indicative of a lower order to disorder phase transition. It is noteworthy that the positions of the first and second order Bragg peaks observed at  $Q \sim 0.025$  and 0.045 Å<sup>-1</sup> (not shown) agree with SANS results of  $L_0$  (29). Shown in Figure 3 is a plot of the intensity of the first order Bragg peak as a function of temperature for the different thicknesses shown. Consistent with the data of Figure 2, the intensity of the Bragg peak undergoes an abrupt reduction in intensity as the temperature is decreased from 160°C to 128°C for all samples. The lower order to disorder transition temperature  $T_{LODT,t}$  for a film with thickness  $t$  is taken as the inflection point of these curves. For all the samples studied,  $T_{LODT,t}$  is below the value for the bulk in agreement with the results of Menelle *et. al.* on P(S-*b*-d-MMA) copolymer thin films. In addition, the majority of the films have a transition temperature of  $144 \pm 2^\circ\text{C}$ . This shift of 11°C from the bulk value is also consistent with previous results for films with similar reduced thicknesses. A more interesting finding, however, is the noticeably higher value of the transition temperature for the 261.2 nm film and the 239 nm thick film (reduced thickness of  $t/L_0 = 9.16$  and 8.37, respectively). These results show that two different effects are coming into play. First, there is the finite size effect that causes a reduction in the lower order to disorder transition temperature and, second, there is the frustration effect that causes a change in the absolute position of the transition temperature. Consequently, the film thickness has provided a novel means by which the thermodynamics of the ordering transition can be varied systematically.

### Laterally Homogeneous Surfaces

To address the role of the interfacial interactions on the orientation of a block copolymer, a series of end-functionalized random copolymers, TEMPO-P(S-*r*-MMA)-OH, was synthesized via a TEMPO living free radical route (30,31). The random copolymers were end grafted to silicon substrates by reacting the hydroxy termini with the native oxide leaving a random copolymer brush layer of  $\sim 5$  nm (32). This provided a means in which the surface affinity for PS and PMMA can be precisely tuned. For surface anchored random copolymers having a styrene fraction of 0.60, the affinities for PS and PMMA at the random copolymer brush surface are equal, *i.e.* the interfacial energies between PS and PMMA and the random copolymer are equivalent, and the surface is non-preferential or effectively *neutral*.

To remove the preferential interactions at the polymer/air interface, neutral random copolymer brushes were placed at the surface. This was accomplished by

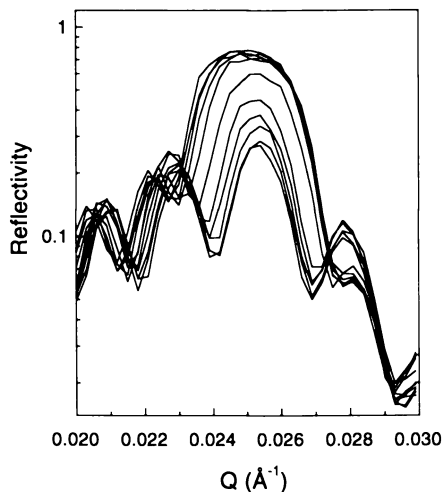


Figure 2. Log of the neutron reflectivity profiles for a symmetric, diblock copolymer film of P(d-S-b-nBMA) ( $t = 2806 \text{ \AA}$ ) at temperatures from  $128^\circ\text{C}$  to  $157.5^\circ\text{C}$ ; and for scattering vectors  $Q$  between  $0.02 \text{ \AA}^{-1}$  and  $0.03 \text{ \AA}^{-1}$  where the first order Bragg peak lies. The temperatures at which individual curve have been taken are (from top to bottom):  $157.5$ ,  $154.4$ ,  $151.2$ ,  $148.2$ ,  $145.3$ ,  $142.3$ ,  $139.5$ ,  $136.5$ ,  $133.1$  and  $130.5$  and  $128.1^\circ\text{C}$ .

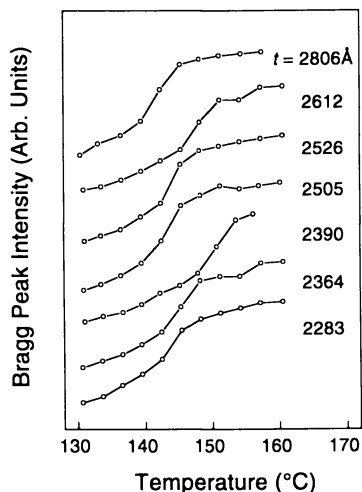


Figure 3. The intensity of the first order Bragg reflection as a function of temperature for P(d-S-b-nBMA) films of different thickness. The thickness of the films are indicated for each temperature run. The ordering transition temperature is taken as the temperature of the inflection point in the data.



applying a thin layer,  $\sim 5.5$  nm, of neutral random copolymer that had been modified with a surface active group, onto the diblock copolymer film prior to annealing. The surface active random copolymer was spin coated directly on the diblock copolymer film from an acetic acid solution. This procedure did not disturb the underlying film as the diblock copolymer was found to be insoluble in acetic acid. The sample was annealed at  $170^\circ\text{C}$  and the resultant structure was found to consist of lamellae oriented perpendicular to the film interfaces throughout the entire film. However, some parallel lamellae were still observed in the interior of the film due, most likely, to the lack of registry between the perpendicular lamellae emanating from the two neutral interfaces.

The behavior of asymmetric, P(d-S-*b*-MMA) diblock copolymer thin films which order into hexagonally packed cylindrical lattices with a period of 44 nm, were also examined on substrates treated with the neutral random copolymer. The neutral surfaces were shown to have a dramatic effect on the orientation of the cylindrical morphology. For a film having a thickness of 43.5 nm, perpendicular cylinders were observed *throughout* the entire film thickness. Phase contrast atomic force microscopy performed in tapping mode revealed the surface structure shown in Figure 4. Here, a well ordered hexagonally packed array of cylinders normal to the surface of the film is observed.

The difference in behavior between the cylindrical and lamellar structures near the polymer/air interfaces may be explained in the following manner. The total surface energy of a thin film having a morphology with a perpendicular orientation,  $\gamma_{\perp}$ , is the sum of the interfacial energy of each component multiplied by the fraction of surface area that each component covers ( $\gamma_{\perp} = x\gamma_{\text{S}} + [1-x]\gamma_{\text{MMA}}$ , where  $x$  is the areal fraction of PS at the polymer/air interface and  $\gamma_{\text{S}}$  and  $\gamma_{\text{MMA}}$  are the surface energies of PS and PMMA, respectively). The surface energy of the parallel orientation,  $\gamma_{\parallel}$ , is simply the surface energy of PS which is the lower surface energy component. If the surface energy difference between the perpendicular and parallel orientations,  $\gamma_{\perp} - \gamma_{\parallel}$ , is larger than the energy to form a mixed structure per unit area, *i.e.* to form internal defects at the interface between perpendicular and parallel orientations of the morphology, then the PS block will wet the surface and the mixed morphology will persist as is the case for the symmetric diblock copolymer (Figure 1d). However, for an asymmetric diblock copolymer having a minority of the higher surface energy component, the total surface energy of a film having a perpendicular morphology would be less than that of the symmetric case. If the surface energy difference between the perpendicular and parallel orientations in the asymmetric system is less than the energy penalty to form a mixed morphology per unit area, the film will consist of a perpendicular morphology as the formation of defects at the interface between perpendicular and parallel orientations of the morphology will be unfavorable.

This appears to be the case for the asymmetric diblock copolymer mentioned above, as the films having a minority fraction of the high surface energy component, *i.e.* PMMA, exhibits perpendicular cylinders at the surface and is more pronounced

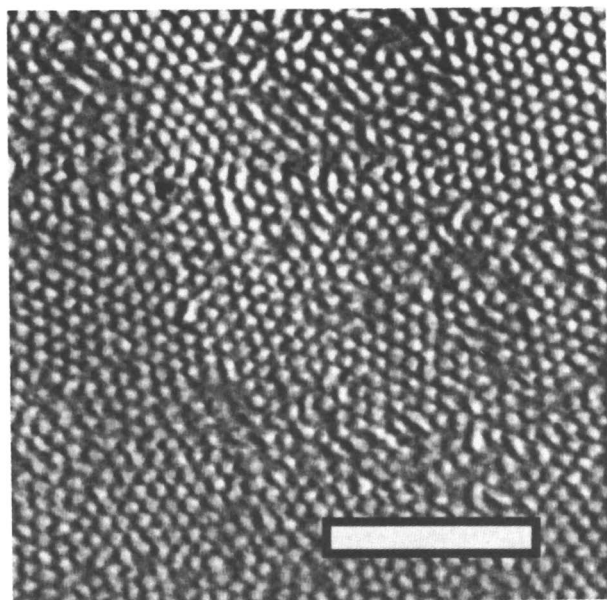


Figure 4. AFM micrograph of an asymmetric diblock copolymer of P(S-*b*-MMA) containing cylinders of PMMA in a PS matrix. The phase contrast image, taken in the tapping mode, shows an ordered array of PMMA cylinders at the copolymer/air interface (scale bar is 0.5  $\mu\text{m}$ ).

for thinner films. Thus, the formation of a morphology with mixed orientations of cylinders is more easily formed for thicker films as these films are more capable of forming internal defects between parallel and perpendicular orientations of the morphology. This is in keeping with mean field theoretical arguments (18,19) and simulations (16).

### Laterally Heterogeneous Surfaces

A particularly attractive route in gaining control of the orientation of the morphologies with respect to a surface is by producing a surface with a laterally periodic affinity for one or both of the components. Such a surface would force an orientation of a microphase separated morphology normal to the surface by pinning fluctuations in two dimensions at the interface. However, it is imperative that the length scale of the periodicity on the surface be of molecular dimension.

Nanoscopically grooved surfaces can be prepared from miscut Si[113] single crystal wafers through resistive annealing, where they are heated by passing a current directly through the Si wafer (33). The period and amplitude of the grooves on the surface are controlled by the misorientation angle of the surface and the annealing conditions. Typically, the lateral period of grooves is tens of nanometers in size with an amplitude or height of about a nanometer. Consequently, the groove amplitude is small in comparison to the size of a polymer coil and can be considered topologically flat. Chemical heterogeneity of the surfaces is achieved by glancing angle metal evaporation where chromium is first evaporated onto the surface, followed by Au (34). This produces a shadowing of the surface features and results in a surface that is comprised of alternating stripes of SiO<sub>2</sub> that interacts favorably with PMMA and Au to which PS preferentially segregates.

Shown in Figure 5 is the AFM phase contrast image of a P(S-*b*-MMA) symmetric, diblock copolymer ( $M_w = 1.13 \times 10^5$  with  $M_w/M_n = 1.10$ ) film that has been solution cast onto a surface with alternating stripes of Au and SiO<sub>2</sub>. A portion of the copolymer film was stripped away to reveal the underlying structure of the substrate. The bright stripes on the substrate are gold. As can be seen there is nearly a perfect registry between the stripes on the substrate and the PS and PMMA microdomains of the copolymer. Consequently, the results in Figure 5 show that it is possible to control the ordering of the copolymer microdomains normal to the interface. Using such means, one should be able to achieve orientation of the copolymer in all directions.

### Conclusions

The three different studies presented here represent three different means by which the structure and morphology of polymeric materials can be controlled and manipulated in thin films. While these experiments have focused on the particular case of diblock copolymers and specific chemical interactions, the extension of these ideas to other systems is straightforward. In the case of polymer mixtures similar

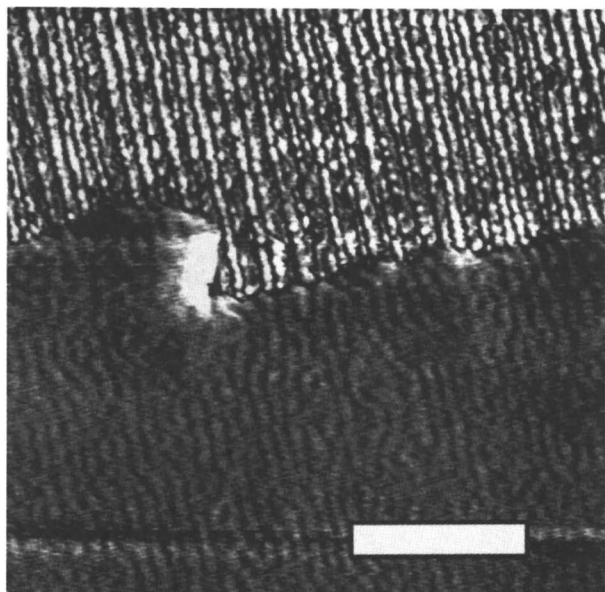


Figure 5. AFM micrograph of a P(S-*b*-MMA) symmetric, diblock copolymer on a striped Au/SiO<sub>2</sub> substrate. A portion of the P(S-*b*-MMA) film was removed to show the patterning of the substrate. The registry between the surface pattern and the copolymer microdomains is evident. Film thickness is 25 nm (scale bar is 0.5 μm).

types of chemical interactions can be used. The challenge here, however, is to force the phase separation of the mixtures onto a size scale not typically seen in the bulk. Rather than chemical interactions, hydrophobic/hydrophilic interactions or polar/nonpolar interactions could be manipulated in a similar manner. An important point to be kept in mind is that no external forces were used in any of the studies discussed and the polymers self-assembled into the structures shown simply by heating to a temperature where the polymer is mobile (*i.e.* above the glass transition temperature or the melting temperature) or by solution casting which provides sufficient time for the copolymer to order in the solvent where the polymer chains are relatively mobile. It is by the use of these natural forces that simple, robust methods can be developed for the generation of nanoscopic structures from polymer materials.

### Acknowledgments

This work was supported by National Science Foundation Materials Research Science and Engineering Center (DMR-9400488) at the University of Massachusetts, the Department of Energy, Office of Basic Energy Science (DE-FG02-96ER45) and the Center for Environmentally Appropriate Materials at the University of Massachusetts. We thank Prof. Simon Mochrie and Mirang Yoon at the Massachusetts Institute of Technology for assistance in the preparation of the heterogeneous surfaces, Prof. Yves Gallot at the Institut Charles Sadron in Strasbourg for the preparation of the P(S-*b*-nBMA), Prof. J. Mays at the University of Alabama for the synthesis of the P(S-*b*-MMA), Dr. C. J. Hawker at IBM Almaden Research Center for synthesis of P(S-*r*-MMA), and Dr. P. Mansky in Symyx Technologies for helpful discussions.

### Literature Cited

1. Koppi, K.A.; Tirrell, M.V.; Bates, F.S.; Almdal, K.; Mortensen, K., *J. Rheol.*, **1994**, *38*, 999.
2. Amundson, K.; Helfand, E.; Quan, X.; Hudson, S.D.; Smith, S.D., *Macromolecules*, **1991**, *24*, 6546; **1994**, *27*, 6559.
3. Amundson, K.; Helfand, E.; Quan, X.; Smith, S.D., *Macromolecules*, **1993**, *26*, 2698
4. Morkved, T.L.; Lu, M.; Urbas, A.M.; Ehrichs, E.E.; Jaeger, H.M.; Mansky, P.; Russell, T.P., *Science*, **1996**, *273*, 931.
5. Muthukumar, M.; Ober, C.K.; Thomas, E.L., *Science*, **1997**, *277*, 1225.
6. Bates, F.S.; Fredrickson, G.H., *Ann. Rev. Phys. Chem.*, **1990**, *41*, 525.
7. Vanzo, E.J., *J. Polym. Sci.*, **1966**, *A4-4*, 1727; Bradford, E.B.; Vanzo, E.J., *J. Polym. Sci., Polym. Chem.*, **1966**, *A1-6*, 1661.
8. Wittmann, J.; Lotz, B.; Candau, F.; Kovacs, A.J., *J. Polym. Sci., Polym. Phys.*, **1982**, *20*, 1341.
9. Hasegawa, H.; Hashimoto, T., *Macromolecules*, **1985**, *18*, 589.
10. Henkee, C.S.; Thomas, E.L.; Fetters, L.J., *J. Mater. Sci.*, **1988**, *23*, 1685.

11. Coulon, G.; Russell, T.P.; Deline, V.R.; Green, P.F., *Macromolecules*, **1989**, *22*, 2581.
12. Russell, T.P.; Coulon, G.; Deline, V.R.; Miller, D.C., *Macromolecules*, **1989**, *22*, 4600.
13. Anastasiadis, S.H.; Russell, T.P.; Satija, S.K.; Majkrzak, C.F., *Phys. Rev. Lett.*, **1989**, *62*, 1852; *J. Chem. Phys.*, **1990**, *92*, 5677.
14. Koneripalli, N.; Singh, N.; Levicky, R.; Bates, F.S.; Gallagher, P.D.; Satija, S.K., *Macromolecules*, **1995**, *28*, 2879.
15. Lambooy, P.; Russell, T.P.; Kellogg, G.J., Mayes, A.M.; Gallagher, P.D.; Satija, S.K., *Phys. Rev. Lett.*, **1994**, *72*, 2899.
16. Kikuchi, M.; Binder, K., *J. Chem. Phys.*, **1994**, *101*, 3367.
17. Turner, M.S., *Phys. Rev. Lett.*, **1992**, *69*, 1788.
18. Walton, D.G.; Kellogg, G.J.; Mayes, A.M.; Lambooy, P.; Russell, T.P., *Macromolecules*, **1994**, *27*, 6225.
19. Matsen, M.W., *J. Chem. Phys.*, **1997**, *106*, 778.
20. Pickett, G.T.; Balazs, A.C., *Macromolecules*, **1997**, *30*, 3097.
21. Mansky, P.; Russell, T.P.; Hawker, C.J.; Pitsikalis, M.; Mays, J., *Macromolecules*, **1997**, *30*, 6810.
22. Huang, E.; Russell, T.P., *Nature*, in press.
23. Balazs, A.C.; Huang, K.; McElwain, P.; Brady, J.E., *Macromolecules*, **1991**, *24*, 714.
24. Halperin, A.; Somers, J.U.; Daoud, M. *Europhys. Lett.*, **1995**, *24*, 297.
25. Petera, D.; Muthukuimar, M., *J. Chem. Phys.*, **1997**, *107*, 9640.
26. Leibler, L., *Macromolecules*, **1980**, *13*, 1602.
27. Fredrickson, G.H., *Macromolecules*, **1987**, *20*, 2535.
28. Menelle, A.; Russell, T.P.; Anastasiadis, S.H.; Satija, S.K.; Majkrzak, C.F., *Phys. Rev. Lett.*, **1992**, *68*, 67.
29. Pollard, M.; Russell T.P.; Ruzette, A.V.; Mayes, A.M.; Gallot, Y., *Macromolecules*, in press.
30. Hawker, C.J., *J. Am. Chem. Soc.*, **1994**, *116*, 11185.
31. Hawker, C.J.; Elce, E.; Dao, J.; Volksen, W.; Russell, T.P.; Barclay, G.G., *Macromolecules*, **1996**, *29*, 2686.
32. Mansky, P.; Liu, Y.; Huang, E.; Russell, T.P.; Hawker, C.J., *Science*, **1997**, *275*, 1458.
33. Mochrie, S.G.J.; Song, S.; Yoon, M.; Abernathy, D.L.; Stephenson, G.B., *Physica B*, **1996**, *221*, 105.
34. Rockford, L.; Liu, Y.; Mansky, P.; Russell, T.P.; Yoon, M.; Mochrie, S.G.L., *Phys. Rev. Lett.*, submitted.

## Chapter 10

# NMR Solvent Relaxation Studies on Concentrated Particulate Dispersions

Terence Cosgrove, Kevin S. Jack, Nicholas Green, Timothy M. Obey,  
and Matthew Wood

Department of Physical Chemistry, School of Chemistry, University of Bristol,  
Cantock's Close, Bristol BS8 1TS, United Kingdom

The technique of  $^1\text{H}$  NMR solvent relaxation has been used to probe the effect of the adsorption of polymers at particle/water interfaces. On inorganic oxide surfaces the pure water relaxation was strongly enhanced but on a latex surface, the effect was much weaker due to its more hydrophobic character. The effect of polymer adsorption on all the oxide materials studied increased the specific relaxation weight of water: the effect for poly(vinyl pyrrolidone) (PVP) adsorption on silica was much stronger than for poly(ethylene oxide) (PEO) and in a competitive adsorption study the PVP was found to displace the PEO. On a clay surface, a strong molecular weight effect was found on the bound solvent probability ( $p$ ). Similar data for a series of PEO samples with a similar molecular weight but different end groups and for a cyclic polymer also showed very different effects. The results are discussed in terms of different surface conformations. The NMR method is shown to be a very simple tool to measure competitive adsorption.

The adsorption of polymers at interfaces has been discussed widely in the literature and a recent text by Fler et al. (1) gives a comprehensive, critical review of the subject. Polymers are used widely in colloidal systems for stability enhancement and for flocculation. Many examples of which can be found in reference 1. In many practical systems both inorganic and polymeric particles are used and the relative propensity for adsorption in these systems is of current interest.

In this paper we examine four aspects of polymer adsorption onto inorganic particles, namely the dependence of adsorption on molecular weight, molecular structure and the nature of end groups, and the displacement of adsorbed polymers by polymers of a differing chemical structure. Several different colloidal particles are used and their relative hydrophilicity is examined by NMR. Moreover, the NMR

solvent relaxation method is shown to give valuable in-situ data in these systems up to relatively high particle volume fractions.

NMR solvent exchange theory makes use of the difference in mobility of the solvent in the bulk solution and the solvent at the interface, to observe (indirectly) the adsorption of polymers at interfaces. For the systems of interest here, where the correlation time for solvent motion ( $\tau_c$ ) is small compared with the nuclear resonance frequency ( $\omega_0$ ), the spin-spin relaxation time ( $T_2$ ) of the solvent molecules will decrease if the solvent becomes less mobile, for instance if it becomes associated with a surface (2). Woessner (3) has shown that the effect of a particle surface on the motions of the solvent occurs over a short spatial range. For example, the range of the surface effect of clay on the rotation of a water molecule is a molecular layer or two.

The NMR relaxation of water in silica was shown experimentally in the 1950s to depend on the rate of exchange between water associated with the surface of the silica particles and water in the bulk (4). For a system in fast exchange the relaxation can be described by a single averaged relaxation time, which is related to the relaxation time of the water bound to the surface ( $T_{2b}$ ) and the longer relaxation time of free (or bulk) water ( $T_{2f}$ ). In the fast exchange limit  $R_2$ , the single relaxation rate measured for the system ( $R_2=1/T_2$ ), is given by (5):

$$R_2 = R_f(1-p) + R_b p \quad [1]$$

where  $p$  is the time-averaged probability of finding a randomly chosen solvent molecule in the vicinity of the surface, i.e. in the “bound” environment. This quantity ( $p$ ) is referred to as the “bound fraction probability”, and is related to both the fraction of water that is present at the interface *and* the fraction of time it spends in this environment.

A useful way of presenting solvent relaxation data for complex systems is to consider the *specific* relaxation rate ( $R_{2sp}$ ), which is defined as:

$$R_{2sp} = R_2/R_2^0 - 1 \quad [2]$$

where  $R_2^0$  is the relaxation rate of a suitable reference sample, e.g. the pure solvent. An important point to realise is that relaxation rates are additive; it is, therefore, possible to normalise the specific relaxation rate with respect to any reference system. For instance, when observing the effect of adsorbed polymer on particulate systems, it is often most convenient to normalise the relaxation rate with respect to the bare particle dispersion. Moreover, this normalisation of the relaxation rate removes the effects of many instrument-dependent variables from  $R_{2sp}$ .

For dilute systems, it can be assumed that the relaxation rate of the free solvent ( $R_{2f}$ ) is independent of the concentration of the dispersion. Substitution of Equation 1 into Equation 2 and setting  $R_2^0 = R_{2f}$  gives:

$$R_{2sp} = p (R_{2b}/R_2^0 - 1) \quad [3]$$



As the bound fraction probability ( $p$ ) is proportional to the surface area of the particle available for adsorption, a plot of  $R_{2sp}$  as a function of surface area (or concentration) of particles, is expected to be linear if the fast exchange model is valid. Indeed, the fast exchange model has been shown to be applicable to a number of systems including sodium hectorite/water (3) and polymer/silica/water (1,5,6). Additionally, the specific solvent relaxation rates measured for silica particles of differing diameters have been shown to be constant for a given total surface area of silica, irrespective of the absolute size of the particles (7,8), as predicted by Equation 3.

By measuring the relaxation time for particle/solvent dispersion as a function of particle concentration it is possible to determine the relaxation time of the bound solvent ( $T_{2b}$ ) by extrapolation from a plot of  $T_2$  versus  $[H_2O]/[particle]$ . Using this value and the relaxation time for pure water as  $T_{2f}$  the value of  $p$ , the bound fraction probability, can be obtained from the equation below:

$$p = (R_2 - R_f)/(R_b - R_f) \quad [4]$$

The adsorption of a polymer at a homogeneous solid-liquid interface can have two possible effects on the ordering and mobility of the solvent at the interface. Firstly, the polymer can displace solvent from the surface upon adsorption, which will give rise to a decrease in the bound fraction probability. Alternatively, as the polymer adsorbs it may bring water associated with it into the vicinity of the surface, effectively increasing the number of the water molecules near the surface. This effect would lead to an increase in the bound fraction probability. These two effects may happen simultaneously and the net effect will be seen in the observed relaxation rate and  $p$ .

### Experimental Techniques

The NMR experiments were performed on a JEOL FX200 NMR spectrometer controlled by a SMIS (Surrey Medical Imaging Systems, UK) console, operating at a  $^1H$  frequency of 200 MHz. The measurements of spin-spin relaxation times were made using the Carr-Purcell-Meiboom-Gill (CPMG) (9,10) sequence with a time of 0.5 ms between the  $90^\circ$  and  $180^\circ$  pulses. For each relaxation decay between 4096 and 8192 data points were collected by extracting the intensity of every alternate echo, i.e. a dwell time of 1 ms between points. The spin-spin relaxation time was extracted from the measured decays by a non-linear least-squares analysis. Signal averaging (typically 8–16 scans) and receiver phase cycling were employed to reduce errors due to random noise and possible DC offsets.

### Materials

**Polymers.** The poly(ethylene oxide) (PEO) used here had a molecular weight of 50,100 ( $M_w/M_n < 1.1$ ) and was supplied by Polymer Laboratories (UK). Poly(vinyl pyrrolidone) (PVP) was obtained from BDH chemicals (UK) and had a molecular weight of 44,000.

The poly(ethylene glycol) (PEG) samples used in this study were obtained from Polymer Laboratories, UK. A range of number-average molecular weights ( $M_n = 194, 600, 4100, 10000$  and  $23000$ ) were studied and all had  $M_w/M_n$  better than 1.07. The methoxy-terminated PEG (mPEG), (Shearwater Polymers, Huntsville, AL), had the chemical formula  $\text{CH}_3\text{O}(\text{CH}_2\text{CH}_2\text{O})_{227}\text{H}$  and  $M_n=10,000$ . The cyclic PEG (cPEG) also had  $M_n=10,000$  and was synthesised by Professor Colin Booth (University of Manchester, UK).

**Particles.** Polystyrene latex particles were prepared at Bristol University by surfactant-free polymerisation of styrene using ammonium persulphate as the initiator (11). For the investigations of water onto bare particles, colloidal silica was prepared by the base hydrolysis of tetraethyl silicate in ethanol and water (12). Silica particles (Ludox HS40) used for the competitive adsorption study were obtained from DuPont Chemicals (Willmington, DE). Alumina particles (Wesolock) were obtained from Wesbond Corp. (Willmington, DE). All of these particles were dialysed against distilled water to remove impurities.

Montmorillonite is a naturally occurring swelling clay with the chemical formula  $(\text{Na}^{+}_{0.74}\cdot n\text{H}_2\text{O}) (\text{Al}^{3+}_{3.1}\text{Mg}^{2+}_{0.50}\text{Fe}^{3+}_{0.40}) (\text{Si}^{4+}_{7.76}\text{Al}^{3+}_{0.24}) (\text{OH})_4 \text{O}_{20}$ . A high quality bentonite (Swy-1, Crook County, Wyoming) was used as a source of montmorillonite. This was purified by forming a suspension in water and removing and rejecting particles greater than  $2 \mu\text{m}$  diameter by sedimentation. Samples for the NMR studies were made at a range of clay concentrations up to 1% (w/w) solids. At these concentrations the samples are dispersions of discrete clay platelets.

Laponite RD (Laporte, UK) is a synthetic, hectorite clay that forms clear, aqueous dispersions, below 2% (w/w) solids. The chemical formula of Laponite RD is  $(\text{Na}^{+}_{0.46}n\text{H}_2\text{O}) (\text{Mg}^{2+}_{5.46}\text{Li}^{+}_{0.46}) (\text{Si}^{4+}_8) (\text{OH})_4 \text{O}_{20}$ . The laponite investigated here was used as supplied by the manufacturers, in its predominantly sodium-exchanged form.

**NMR samples.** For each of the separate NMR investigations presented, a constant batch of distilled water (Milli-Q) was used throughout, as variation in oxygen content of the water can significantly alter the absolute value of the relaxation times. Additionally, all of the montmorillonite samples containing PEG had a polymer concentration of 0.125%(w/w), which corresponds to the plateau on the adsorption isotherm (13).

### The Adsorption of Water onto Particles Surfaces

To demonstrate the sensitivity and simplicity of using solvent relaxation time measurements to probe the surface properties of particles, the measurements have been carried out on a series of particles of varying hydrophobicity. In Figure 1 specific relaxation rates ( $R_{2sp}$ ) for three colloidal surfaces, polystyrene latex (PSL), silica and alumina, in water are presented as a function of the surface area. In this figure  $R_{2sp}$  has been normalised by the relaxation rate of pure water and the surface area has been calculated from the average particle size (determined by transmission

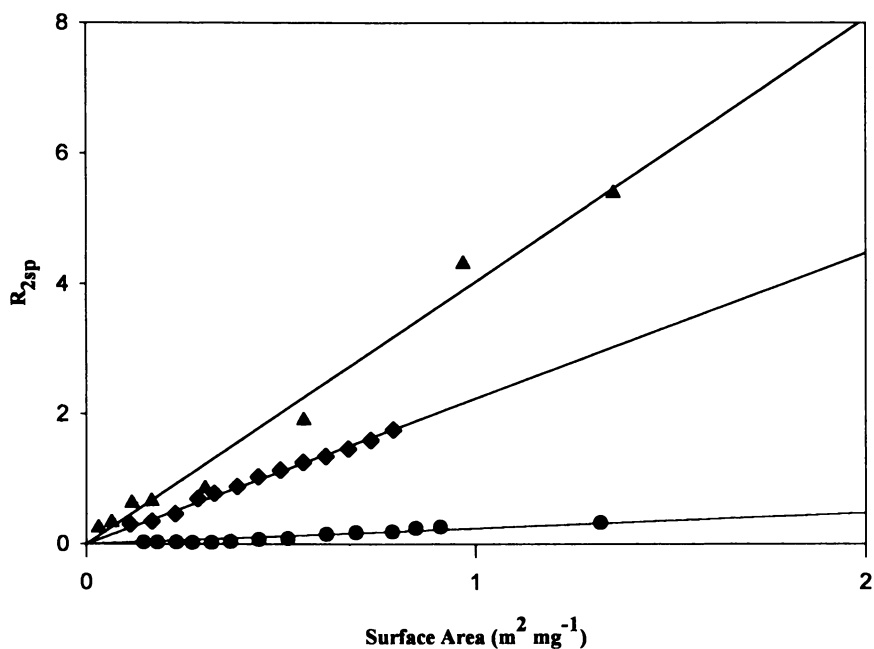


Figure 1. Specific relaxation rates measured for particles of polystyrene latex (●), silica (◆) and alumina (▲) in water, as a function of the relative surface area of the particle.

electron microscopy) and the solids content. As discussed above, the linear relationship observed for each of the colloidal systems is indicative of the validity of the fast exchange model for these systems. More importantly, it can be seen from Figure 1 that the slope of  $R_{2sp}$  as a function of the surface area is small for PSL and increases for the silica and alumina systems. By comparison with Equation 3 this increase in slope must be due to either an increase in the amount of adsorbed water per unit surface area, and/or a restriction of the mobility of the adsorbed water (i.e. an increase in the value of  $R_{2b}$ ). If we consider this affinity of the surface of the particle towards water, determined from the NMR measurements, to be a measure of the hydrophobic nature of the particle surface, then the observed trend in the slopes implies that the hydrophobicity of the particles decreases as; PSL > silica > alumina. The underlying reasons for this change in hydrophobicity may be due to differences in the surface charge density, the chemical structure and/or the porosity of the surface.

In the case of the  $R_{2sp}$  measurements of alumina, however, it must also be noted that it is possible that paramagnetic Fe impurities may be present at the surface of the alumina particle. These impurities can provide an alternative relaxation pathway for the bound water molecules, thereby increasing the value of  $R_{2b}$  and hence the slope of  $R_{2sp}$ . Nonetheless, these results clearly demonstrate the sensitivity of solvent relaxation measurements to the nature of the particle surface, i.e. the hydrophobic nature and surface chemistry.

### The Competitive Adsorption of Polymers onto Silica Particles

In this section the adsorption of poly(ethylene oxide) (PEO) and poly(vinyl pyrrolidone) (PVP) onto dispersions of silica has been investigated indirectly through measurements of solvent relaxation times. Figure 2 shows the  $R_{2sp}$  of these silica/polymer/water systems as a function of the concentration of polymer added, for a constant silica/water composition (5% w/w). Note that  $R_{2sp}$  for these systems has been normalised by the relaxation rate of the pure silica dispersion, hence,  $R_{2sp}$  is by definition zero for the system containing no polymer. Moreover, measurements of the relaxation rates for the polymers dissolved in pure water showed only a negligible enhancement in rate upon addition of polymer over the concentration range shown in Figure 2. The changes in  $R_{2sp}$  observed upon addition of polymer to the silica dispersions can, therefore, be interpreted directly in terms of the effect of polymer adsorption onto the particles; free polymer in solution will not contribute to the measured  $R_{2sp}$ .

The enhancement of  $R_{2sp}$  observed upon addition of both PEO and PVP is typical of the relaxation behaviour previously observed for the adsorption of polymers onto silica particles (1,6-8). The silica particles used in this work, however, show a lower affinity for PEO chains than those used in the previous publications. This lower affinity is due to a combination of effects, i.e. differences in the silica particles and the lower molecular weight of PEO used, and will not affect the interpretation of results presented here. This enhancement of  $R_{2sp}$  can be due to either an increase in the time-averaged fraction ( $p$ ) of water bound at the interface,

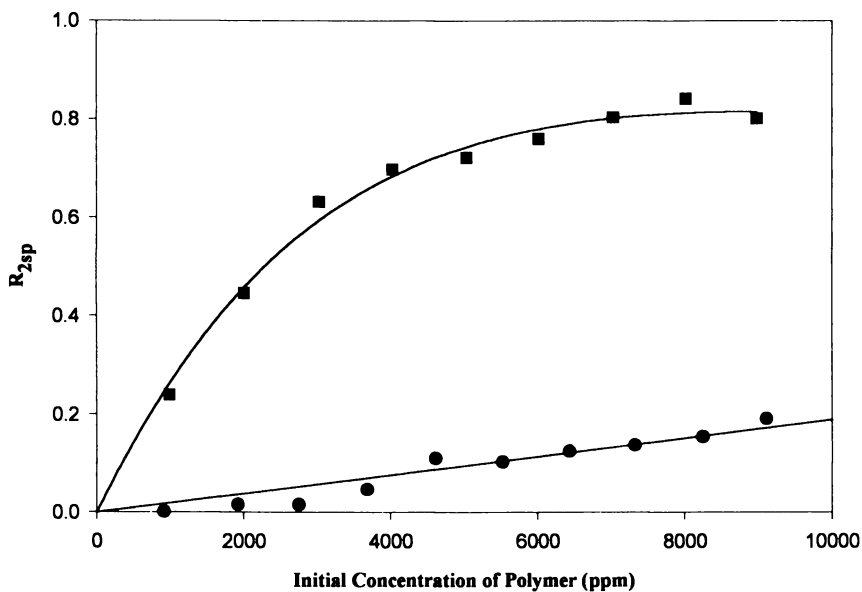


Figure 2. Specific relaxation rates for PEO [●] and PVP [■] adsorbed on silica as a function of the initial concentration of polymer added to the solution.

and/or a decrease in the mobility of the water trapped at the interface (i.e. an increase in  $R_{2b}$ ). Although the exact mechanism for the enhancement in  $R_{2sp}$  cannot be determined from these results, the fact that an enhancement of  $R_{2sp}$  is observed suggests that the polymer-coated particle has a greater affinity toward water than the bare silica particle. Furthermore van der Beek et al. (5) have shown that  $R_{2sp}$  is sensitive to the number of polymer segments directly bound to the particle surface and is not affected by the presence extended conformations (i.e. loops or tails) of the polymer chains. The second trend shown in Figure 2 is the substantial increase in the enhancement of  $R_{2sp}$  observed upon addition of PVP, compared with that of PEO. Such a result is probably because the PVP chains are more hydrophilic than PEO; either they are better at trapping water molecules at the surface of the particle and/or water is bound more strongly at the interface. Finally, it is also worth noting that these measurements of  $R_{2sp}$  as a function of polymer concentration provide a very simple means for determining the adsorption isotherm for the process. Indeed, it can be seen that PVP has begun to reach maximum adsorption at a concentration of ca. 8000 - 9000 ppm, whereas, for PEO the maximum adsorption is only obtained at a concentration of > 10000 ppm. The greater adsorption of PVP is thought to be a consequence of the stronger affinity of the carbonyl groups of PVP to the surface hydroxyl groups of silica, compared with the ether oxygen of PEO. However, it can not be determined from Figure 2 what fraction of polymer added, is adsorbed to the particle and what fraction remains in solution.

The displacement of one polymer (PEO) by another polymer of a similar molecular weight (PVP) can be seen in the solvent relaxation data presented in Figure 3. In this experiment, PVP was added to a silica dispersion of fixed concentration (5%) onto which 10000 ppm of PEO had previously been adsorbed and allowed to equilibrate.  $R_{2sp}$  was then measured (normalised by  $R_2$  of the 5% silica solution) and plotted as a function of the concentration of PVP added. From Figure 3 it can be seen that  $R_{2sp}$  increases rapidly from the value initially measured for pure silica-PEO (ca. 0.2) and appears to reach a plateau at a value close to that of the maximum value measured for silica-PVP (0.8, see Figure 2). These results imply that the PVP chains are displacing PEO chains at the surface of the silica particles, and are preferentially adsorbed to the particle. Moreover, the solvent relaxation time measurements allow us to characterise the isotherm for the displacement process.

It can also be seen from Figure 3 that the value of  $R_{2sp}$  measured for silica-PEO containing 10000 ppm of PVP is slightly smaller than that measured for an equivalent concentration of PVP on pure silica. This implies that the polymer-particle interface in the silica-PEO-PVP system contains less adsorbed PVP than that for the silica-PVP system, most likely due to a coexistence of PVP and a small fraction of PEO chains at the surface of the particle. Although care was taken to ensure that the exchange of PVP and PEO had reached a measurable equilibrium before the relaxation time measurements were carried out, it is possible that the displacement of these residual PEO chains may be slow, and that the maximum adsorption of PVP would be reached after an extended period of time.

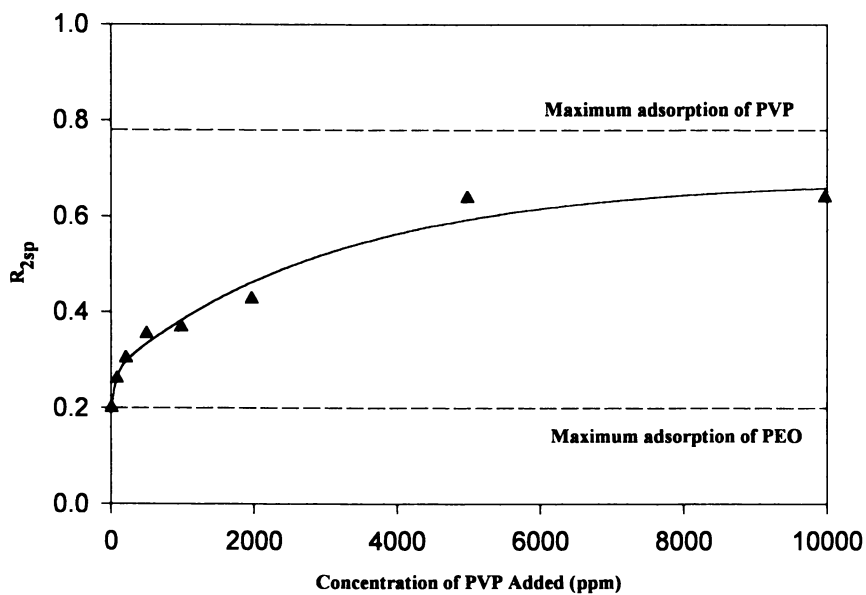


Figure 3. Competitive adsorption of PVP and PEO adsorbed on silica.  $\blacktriangle$  show the change in  $R_{2sp}$  upon addition of PVP to silica particles with PEO previously adsorbed onto its surface. The horizontal lines correspond to the maximum specific relaxation rate enhancement for each the two polymers at initial polymer concentrations of 10000 ppm.

## Polymer Adsorption onto Clay; Molecular Weight and End-Group Effects

The effects of adsorption of poly(ethylene glycol) (PEG) onto the surface of montmorillonite clay on both the bound fraction probability ( $p$ ) and the relaxation time of bound water ( $T_{2b}$ ) have been used to probe the nature of the polymer/clay interface. For each of the clay/polymer systems studied  $T_{2b}$  was determined by extrapolation of a plot of  $T_2$  versus  $[H_2O]/[Clay]$ . Two examples of the determination of  $T_{2b}$  are shown in Figure 4. From the values of  $T_{2b}$  thus determined and by assuming that the relaxation rate of the free water ( $T_{2f}$ ) is equal to that measured for pure water,  $p$  can be calculated from Equation 4. Montmorillonite is a naturally occurring clay and it is known to contain some iron impurities. The effect of the iron is to facilitate faster relaxation of bound water, via nuclear-spin/electron-spin interactions (14), giving the system a relatively short  $T_{2b}$  of 1.9 ms (see Figure 4). Most importantly, the iron in the montmorillonite is fixed within the internal clay structure, giving a constant paramagnetic effect for the surface water and no appreciable effect on  $T_{2f}$ . The presence of this iron will, therefore, not alter the calculated values of  $p$ , as the influence of the iron will be accounted for in the normalisation factor in the denominator of Equation 4. In fact, the presence of this paramagnetic impurity is advantageous as it increases the sensitivity of the solvent relaxation measurements to surface effects.

The effect of the adsorption of PEG on montmorillonite is shown in Figures 5 and 6. There are three striking trends in this data. First, upon adsorption of any of the molecular weights of PEG,  $p$  decreases relative to that of the bare clay. The second trend shown in Figure 5 is that as the molecular weight of the adsorbing PEG increases, so does  $p$ . Finally,  $T_{2b}$  for the low molecular weight PEG is considerably shorter than for the bare montmorillonite, as seen in figure 6, and as the molecular weight of PEG increases,  $T_{2b}$  tends towards the value of bare montmorillonite.

For the bare montmorillonite it is reasonable to assume that the surface can be thought of as hydrophobic with hydrophilic sites (15). These sites will correspond to the exchange cations associated with the surface of the clay. When a low molecular weight PEG adsorbs it will adopt a relatively flat conformation, as predicted by the Scheutjens-Fleer model (1), and will effectively displace the water associated with the hydrophilic surface sites. Water will also be brought down to the surface with the polymer but the net effect will be a displacement of water. The low value of  $T_{2b}$  for the low molecular weight PEG, as seen in Figure 6, implies that the water associated with the adsorbing polymer is either more tightly bound to the surface or that it is less mobile than water directly associated with the hydrophilic surface sites.

In the case of a high molecular weight PEG the polymer adsorbs in greater amounts and will consequently have to adopt a more extended conformation. This conformation should result in a less efficient displacement of water from the surface, and as the polymer is still bringing water to the surface the bound solvent probability will increase relative to that of the adsorbed low molecular weight PEG. As the molecular weight increases the value of  $T_{2b}$  also increases (see Figure 6). This implies that the water associated with the polymer is becoming more mobile as the thickness of the adsorbed layer increases.



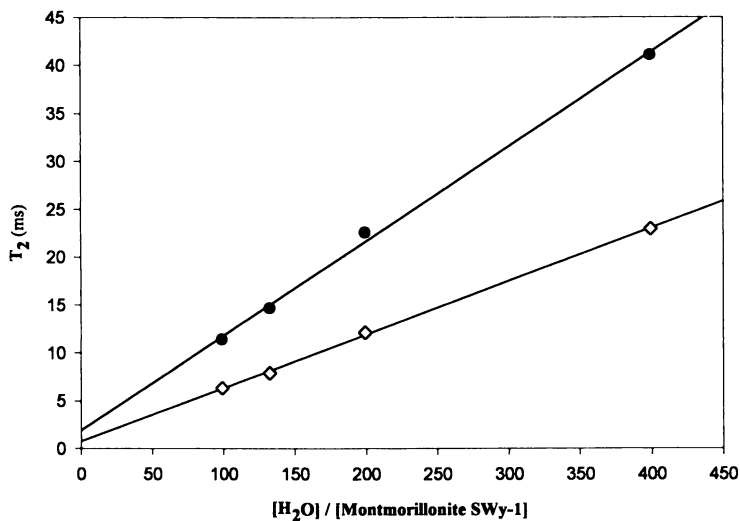


Figure 4. The determination of  $T_{2b}$  by extrapolation of the measured  $T_2$  data as a function of the solids contents. Bare montmorillonite Swy-1 (●) and montmorillonite Swy-1 + PEG (Mn = 10000) (◇) are shown as examples.

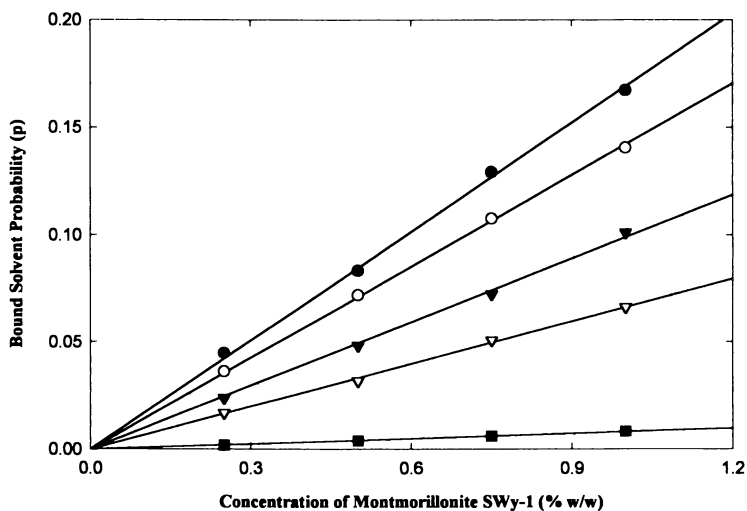


Figure 5. The effect of PEG adsorption on the bound fraction probability ( $p$ ) of water adsorbed onto Montmorillonite: Bare clay (●), +PEG 194 (■), +PEG 600 (▽), +PEG 4.1K (▼), and +PEG23K (○).

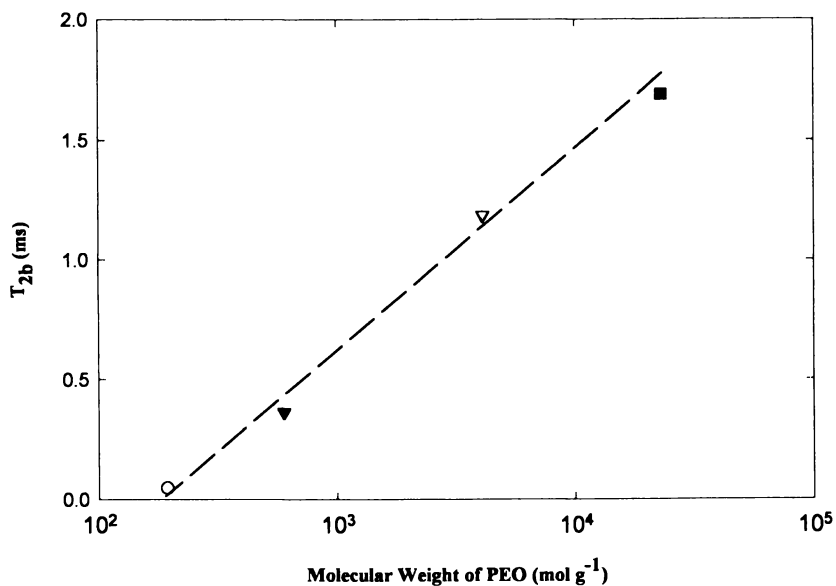


Figure 6. Effect of PEG molecular weight on  $T_{2b}$  of water adsorbed onto Montmorillonite Swy-1. The symbols are the same as those used to represent the different molecular weight PEG in Figure 5.

In Figure 7, the adsorption of three different PEGs onto montmorillonite is presented. All of these PEGs have a similar molecular weight ( $M_n=10,000$ ), but two are linear polymers with differing end groups (i.e., di-hydroxy and mono-methoxy) and the third is a cyclic polymer. For each of the polymers  $p$  has been calculated and is plotted as a function of the concentration of clay, at a constant polymer concentration of 1.25 % (w/w). As was also observed in Figure 5, the addition of PEG to montmorillonite leads to a reduction in  $p$ , that is the adsorption of polymer to the surface of the clay excludes water from the interface. Moreover, it can be seen that a greater reduction in  $p$  results from the adsorption of the cyclic PEG (cPEG) compared to the methoxy-terminated PEG (mPEG), which in turn shows a greater reduction than the OH-terminated PEG (PEG). By comparing Figures 5 and 7 it can also be seen that effect of adsorbing the cPEG is similar to that observed for a linear PEG of  $M_n=194$ . Computer modelling, of the adsorption of different PEG chains onto these clay surfaces, using Scheutjens-Fleer's self-consistent field (SCF) theory, has predicted that the conformation adopted by the PEG becomes flatter as  $M_n$  decreases, or as the end groups of the polymer chains become more hydrophobic in nature (e.g. in moving from PEG to mPEG to cPEG) (16). This is because the more hydrophobic end groups will have a greater affinity for the particle surface, c.f. the aqueous media, and this will have the effect of restricting the conformational freedom of the polymer chains at the interface. Additionally the radius of gyration of cPEG will be much smaller than that of the linear PEGs. The decrease in  $p$  observed in moving from PEG to mPEG to cPEG is, therefore, believed to arise from the flatter, denser, conformation adopted by the polymer at the interface, which leads to a greater displacement of water bound at the interface.

### Phase Transitions in Clay Dispersions

In Figure 8 measurements of  $R_{2sp}$  for water/laponite solutions as a function of the particle concentrations are shown. It can be seen that  $R_{2sp}$  is initially a linear function of the particle concentration, in agreement with the fast exchange model (see Equation 3). However, as the concentration of the dispersions is increased, a deviation from the expected linear behaviour is observed at ca. 2%. This change in gradient corresponds to the region of a sol-gel transition. Below 2% laponite the samples are in the 'sol' regime and the linear dependence of  $R_{2sp}$  on the particle concentration implies that the water is in fast exchange between the bound and free states. However, at concentrations above 2% laponite, the measured  $R_{2sp}$  is smaller than expected. From Equations 1 and 2 we can see that the observed decrease in  $R_{2sp}$  could result from a number of sources:

1. A decrease in  $R_{2b}$
2. A decrease in  $R_{2f}$
3. A decrease in the bound fraction probability per unit surface area, i.e. a decrease in  $p$  for a given total surface area of the particle.
4. That the fast exchange model (Equation 1) is no longer valid.

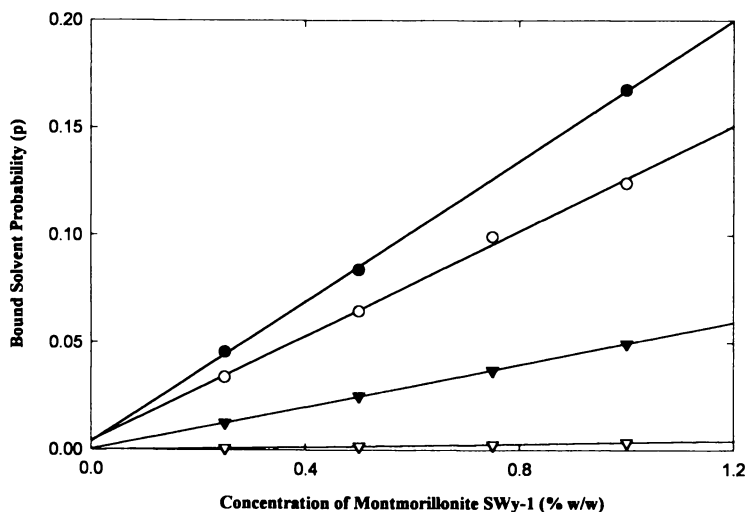


Figure 7. The effect of the end-group structure of PEG adsorbed onto Montmorillonite Swy-1 on the bound fraction probability of water. The polymers PEG (○), mPEG (▼) and cyclic PEG (▽), are all of  $M_n = 10000$ .

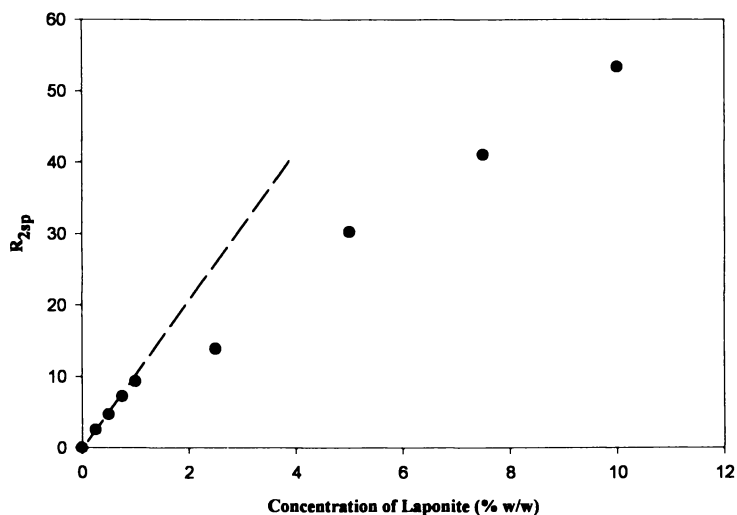


Figure 8. Specific relaxation rate of water adsorbed onto Laponite as a function of the concentration of clay, showing the change in gradient at ca. 2% of Laponite.

Explanations 1 and 2 are both thought to be extremely unlikely, as they imply that the mobility of water (either bound or free) increases as the solutions becomes 'gel' like. Both of explanations 3 and 4, however, are considered to be plausible. It is highly likely that the increase in order of the clay platelets exhibited in the 'gel' would lead to exclusion of water from the surface of the particles, effectively reducing the value of  $p$ . The apparent linear behaviour of  $R_{2sp}$  in the 'gel' region, albeit with a decreased slope compared to the 'sol', supports the hypothesis that the fast exchange model remains valid in this region. However, it can not be ruled out that the two-site fast-exchange model is no longer valid in the gel. That is, it is possible that a third solvent environment exists, and that the most restricted environment cannot be observed in the relaxation decay curves because the relaxation times are too short to be measured by high-resolution NMR, or that the rate of exchange between the environments is no longer fast on the NMR timescale. Most importantly, this system demonstrates the sensitivity of the solution NMR technique to changes in the structure of the dispersions.

## Conclusions

The versatility of solvent relaxation measurements for probing the interfacial effects in particulate dispersions has been demonstrated for a number of particle/water and particle/polymer/water systems. The key advantages of these measurements are their sensitivity to the nature of the polymer surface and their relative simplicity to obtain.

From studies of dispersions of inorganic particles in water it was found that the measurements of the specific relaxation rates can provide valuable information about the relative hydrophobic nature of the particles and changes in the state of dispersion. Although, care must be taken when interpreting relaxation measurements from systems in which paramagnetic impurities may be present.

The relative affinities of PEO and PVP chains of a similar molecular weight to a silica surface were studied by NMR. It was found that the latter polymer showed a much stronger affinity, most likely due to the greater hydrogen-bonding strength of carbonyl groups of PVP compared with the ether oxygens of PEO. Furthermore, the displacement of PEO chains adsorbed to the surface of silica particles by the chains of PVP could be characterised by the NMR method.

The effect of the adsorption of PEG chains (of various molecular weight and end-group functionality) on the fraction of water constrained at a clay/water interface, and the relative mobility of this constrained water was investigated. It was found that the fraction of bound water decreased as the molecular weight of the PEG decreased, or as the polymer chains became more hydrophobic in nature. These observations could be correlated with the flatter, denser, conformations adopted by the PEG at the surface, as predicted by theoretical treatments.

## Acknowledgements

The authors wish to thank Professor Colin Booth of the University of Manchester for kindly supplying the cyclic PEG. Financial support for this work was supplied by Schlumberger Cambridge Research, ICI Research Wilton and the EPSRC.

## Literature Cited

- (1) Fleer, G. J.; A., C. S. M.; Scheutjens J. M. H. M.; T., C.; B., V. *Polymers at Interfaces*; Chapman and Hall: London, 1993.
- (2) Bloembergen, N.; Purcell, E.; Pound, R. *Phys. Rev.* **1948**, *73*, 679.
- (3) Woessner, D. *J. Mag. Res.* **1980**, *39*, 297.
- (4) Zimmerman, J.; Brittin, W. *J. Phys. Chem.* **1957**, *61*, 1328.
- (5) van der Beek, G. P.; Stuart, M. A. C.; Cosgrove, T. *Langmuir* **1991**, *7*, 327.
- (6) Cosgrove, T.; Obey, T. M.; Taylor, M. *Colloids and Surfaces* **1992**, *64*, 311.
- (7) Cosgrove, T.; C.Griffiths, P.; Lloyd, P. M. *Langmuir* **1995**, *11*, 1457.
- (8) Mears, S. J.; Cosgrove, T.; Thompson, L.; Howell, I. *Langmuir* **1998**, *14*, 997.
- (9) Carr, H.; Purcell, E. *Phys. Rev.* **1954**, *94*, 630.
- (10) Meiboom, S.; Gill, G. *Rev. Sci. Instrum.* **1958**, *23*, 68.
- (11) Goodwin, J. W.; Ottewill, R. H.; Pelton, R.; Vianello, R.; Yates, D. E. *British Polym. J.* **1978**, *10*, 173.
- (12) Stober, W.; Fink, A.; Bohn, E. *J. Colloid and Interface Sci.* **1968**, *26*, 62.
- (13) Avery, R.; Ramsay, J. *J. Coll. Int. Sci.* **1986**, *109*, 448.
- (14) Sur, S.; Heinsbergen, J.; Bryant, R. *J. Mag. Res.* **1993**, *8*, 103.
- (15) Boek, E.; Coveney, P. *J. Am. Chem. Soc.* **1995**, *117*, 12609.
- (16) Green, N. *Ph.D. Thesis, The University of Bristol* **1997**, 103.

## Confinement of Polysoaps in Nonionic Surfactant Lyotropic Bilayers

Y. Yang<sup>1</sup>, R. Prud'homme<sup>1</sup>, P. Richetti<sup>2</sup>, and C. M. Marques<sup>2</sup>

<sup>1</sup>Department of Chemical Engineering, Princeton University,  
Princeton, NJ 08544

<sup>2</sup>Rhodia/CNRS Complex Fluids Laboratory, Prospect Plains Road,  
Cranbury, NJ 08512-7500

We study the confinement of hydrophobically modified polyacrylate (HMPA) in lamellar ( $L_\alpha$ ) and sponge ( $L_3$ ) phases of a ternary lyotropic system, comprising n-dodecyl pentaethylene glycol monoether ( $C_{12}EO_5$ ), hexanol and brine. The unmodified polymer cannot be inserted into the membrane solution, but the confinement of HMPA can be achieved with a sufficient amount of hydrophobe substitution. The resulting stapled polymer structure induces pronounced changes in the phase behavior of the surfactant solution as well as in the membrane properties. Neutron scattering and visual observation were used to obtain phase diagrams and information on membrane properties. We found that the confinement of HMPA 1) induces two new phases: a vesicle-like phase and two coexisting  $L_\alpha$  phases, 2) reduces the monophasic  $L_\alpha$  area, and 3) increases the rigidity of the bilayers. The effects of the hydrophobe substitution level and polymer concentration are systematically explored.

Adding polymer into a membrane solution results in changes of both the properties of individual membrane and the inter-membrane interactions. For instance, the smectic compression modulus,  $\bar{B}$ , or the average spacing distance,  $d$ , are functions of the membrane flexibility, that can be changed by the presence of the polymers. Accordingly, new phase regions may appear in the phase diagram. Industrially, polymer-membrane complexes are of importance in the formulation of liquid detergents and cosmetics. In the biological realm, the walls of liposomes and cells are built from phospholipid bilayers that anchor a variety of macromolecular species. Understanding the structure/property relationships for polymer/membrane systems would be a step towards the of polymer architectures to create or enhance a desired phase structure, rheological property, or vesicle stability.

Ionic or nonionic membranes have different interactions with polymers. For example, an ionic lamellar phase can confine a non-charged polymer with the radius of gyration several times larger than the interlayer spacing [1]. In contrast, polymers create phase separation in nonionic surfactant mesophases [2-6]. Miscibility between dissolved polymers and non-ionic surfactant mesophases can, nevertheless, be achieved by grafting hydrophobic side groups onto the backbone: the hydrophobic side chains anchor the polymer to the lyotropic membrane [2-7]. The variation of the bending modulus,  $\kappa$ , the Gaussian bending modulus,  $\bar{\kappa}$ , and the compression modulus,  $\bar{B}$ , upon adding polymers has been theoretically and experimentally studied [8-13]. Polymer induced excess membrane rigidity from an anchoring polymer system was recently reported by our group [14].

This paper focuses on the lamellar  $L_a$  phase consisting of one-dimensional stacks of surfactant bilayers separated by a solvent. The sponge phase  $L_3$ , a bicontinuous isotropic phase of multiconnected membranes [15] is also studied. We systematically investigate the effect of hydrophobe substitution level and polymer concentration on the phase behavior and on the membrane properties of the surfactant membrane solutions. The variation of the elastic constant,  $\kappa$ , and compression modulus,  $\bar{B}$ , of the membranes as a function of added polymer concentration is determined by small angle neutron and x-ray scattering.

## Experiments

Hydrophobically modified poly(sodium acrylate) with 0 to 3 mol% aliphatic chains containing 14 hydrocarbon units is made by grafting alkylamine in the presence of dicyclohexadecarbonimide onto a precursor polymer (polyacrylic acid) using a protocol developed by Illiopoulos [16]. The hydrophobic side chains are randomly distributed along the polymer backbone [17]. The molecular weight of the precursor polymers is 250,000, corresponding to 3400 repeat units. The surfactant membrane solution consists of pentaethylene glycol dodecyl ether ( $C_{12}EO_5$ ), hexanol and brine, which was chosen because previous studies have determined the phase behavior of the neat system without polymer [18-19]. The molar ratio of hexanol to  $C_{12}EO_5$  is kept constant ( $1.43 \pm 0.02$ ).

The study of phase diagrams was conducted in a thermal bath with samples contained in Parafilm® sealed vials. Phases were determined by visual inspection under a crossed polarizer. The lamellar phase is identified by its optical anisotropy: it is birefringent in transmitted light under crossed polarizer. The  $L_3$  phase is optically clear and isotropic. The two coexistent lamellar phases,  $L_{a1}/L_{a2}$  create a turbid mixture under a natural light and shows an interface between two birefringent phases after centrifugation. For samples close to the phase boundary, centrifugation and optical microscopy were used to determine the phase behavior of the solution.

Small angle neutron scattering experiments were performed at the Laboratory Leon Brillouin (Orphee reactor, Central d'étude de Saclay, France) on the neutron lines PACE and PAXE. The non-polarized neutron wavelengths were selected at 5, 8 and 12 Å ( $\Delta\lambda/\lambda$ =about 3 %) while the two dimensional detector was kept at distances 1, 3.2 and 4 meters from samples. The wave vector range varied from  $6 \times 10^{-3}$  to



$3.5 \times 10^{-1} \text{ \AA}^{-1}$ . Samples were held in 1 or 2 mm quartz cells. Relative scale spectra are obtained with respect with  $\text{H}_2\text{O}$ .

## Results and Discussion

**Phase Behavior.** The phase diagram of the reference solution,  $\text{C}_{12}\text{EO}_5/\text{C}_6\text{OH}/\text{brine}$  (0.1 M NaCl) over the temperature ranges from 5 °C to 60 °C is shown in Figure 1. Membrane volume fraction  $\phi$  is defined as the ratio of the volume of surfactant plus alcohol to total volume of the solution. A broad monophasic  $L_\alpha$  domain exists at room temperature for a membrane volume fraction of 6.2 % or higher, corresponding to a maximum interlamellar distance of order of 400 Å. The  $L_3$  phase starts at a membrane volume fraction of 5.9 %. The system phase separates into a lamellar phase and an isotropic phase when the membrane volume fraction is lower than 5.9 %. Compared to the phase diagram of the binary system,  $\text{C}_{12}\text{EO}_5/\text{H}_2\text{O}$  [15], all phase transition temperatures are shifted to lower values by roughly 50 °C.

A minimum amount of hydrophobic side chains is required to confine the polysoap in the membrane solution (Fig.2). Polymer is not soluble in the membrane mesophases when the hydrophobe substitution level is equal to or less than a 0.22 mol% at fixed polymer backbone molecular weight of 300,000. Consequently, a phase separation leads to a surfactant-rich membrane phase and a polymer-rich isotropic phase, even for very dilute membrane solutions. Polymer confinement in the membrane solution is not favored since the polymer loses conformational entropy. In contrast, when the hydrophobe level is higher than 0.7 mol %, the polysoap can be solubilized both in the lamellar phase  $L_\alpha$  and the sponge phase  $L_3$ . The critical hydrophobe substitution level is between 0.22 and 0.7 mol %. For the HM-polymer system hydrophobic interaction energy balances the reduction of entropy due to confinement. The hydrophobic side chains along the polymer backbone aggregate with hydrophobic species in aqueous, e.g., mixed micelles formed by hydrophobic side chains with surfactants [20-24]. The exchange energy for a  $\text{CH}_2$  from a hydrocarbon environment to an aqueous environment is 1.8  $\text{K}_\text{B}\text{T}$  [25]. The hydrophobic side chains of the polymers anchor into the bilayers, forming polymer-coated membranes. Intra- or inter-polymer aggregation among hydrophobic groups is also possible in the solution. At this time we can not estimate the fraction of hydrophobes associated with the membrane relative to the hydrophobes associating in solution.

With the polymer inclusion, two new phases are observed (Fig. 3). They are two coexisting lamellar phases  $L_{\alpha 1}/L_{\alpha 2}$  at high membrane concentration, and  $L_\alpha'$  phase at low membrane concentrations adjacent to the lamellar domain. The  $L_\alpha'$  solution is optically isotropic. Unlike lamellar phase,  $L_\alpha'$  solution is not birefringent at rest, however, it exhibits birefringence under shear. The border between  $L_\alpha$  and  $L_\alpha'$  is determined by this difference in birefringence behavior. The  $L_\alpha'$  solution has a higher viscosity than that of lamellar solution, especially for the solution close to the phase transition. A maximum turbidity exists during dilution, but no phase separation is observed under a microscope or after centrifugation. The flow birefringence gradually disappears upon to further dilution after the maximum turbidity is reached. The behavior of  $L_\alpha'$  phase is similar to that of a vesicle phase reported by several groups

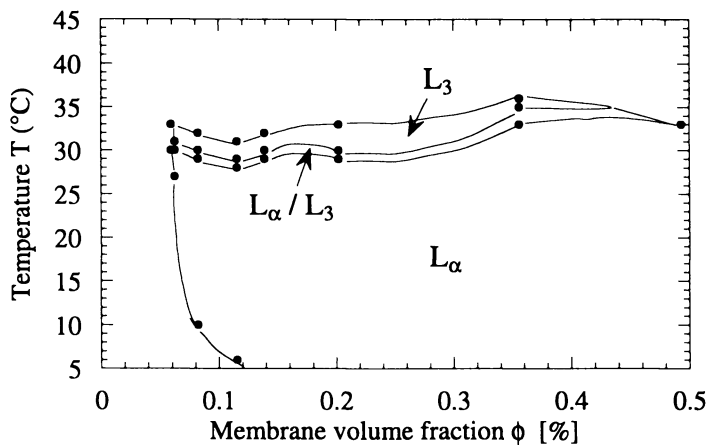


Figure 1. Phase diagram of reference system ( $C_{12}EO_5/C_6OH/brine$ ).

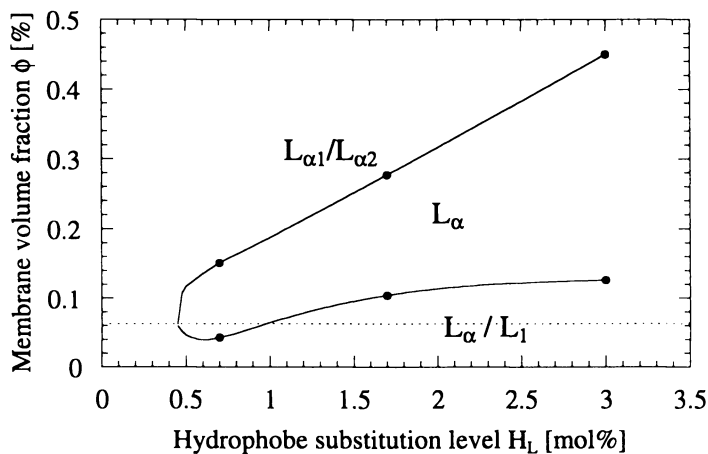


Figure 2. Hydrophobe substitution level effect on monophasic  $L_\alpha$  solution at fixed polymer concentration  $C_p = 0.2$  wt%, temperature  $T = 25$  °C. The dashed line is low  $L_\alpha$  boundary for reference solution.

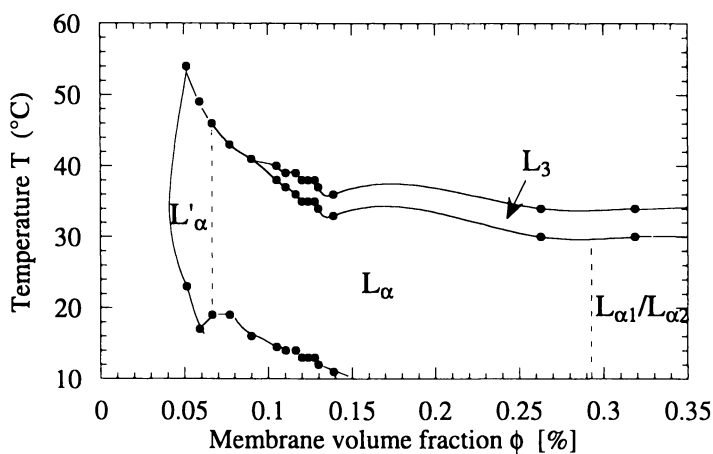


Figure 3. Phase diagram of HMPA doped membrane solution. Polymer concentration  $C_p = 2$  wt%, substitution level  $H_1 = 3$  mol%.

[26-29]. The transition between  $L_\alpha$  and  $L_\alpha'$  is also studied using SANS [30]. The results show that the  $L_\alpha'$  phase is a membrane phase that is different from the lamellar phase. The difference may be related to a curvature change, for example vesicles formed from the membrane solution. Further study is required to fully characterize the  $L_\alpha'$  phase. The  $L_{\alpha_1}/L_{\alpha_2}$  solution is cloudy or turbid and separates into two macroscopic phases after centrifuged for an hour. Under neutron scattering, the  $L_{\alpha_1}/L_{\alpha_2}$  solution shows two Bragg peaks reflecting two interlamellar distances.

The polymer concentration and hydrophobe substitution level determines the monophasic lamellar boundary (Fig.4). The area of the monophasic lamellar regime is reduced with polymer concentration at all substitution levels as has been reported by others [9,31]. The calculated phase diagrams for Helfrich-stabilized lamellar phases show that the two phases region increases with increasing bending modulus,  $\kappa$ . As we will see below, this prediction is consistent with our experimental results that show an increase in  $\kappa$  with polymer concentration. Higher polymer concentrations are accepted by the lamellar phase at lower hydrophobe levels (Fig.4). With HMPA-3 (3 mol % substituted polysoap), phase separation occurs when the polymer concentration is higher than 4.5 wt%. The limits of miscibility are shifted to concentrations of polymer of 6.5 wt% and 10.5 wt% for 2 mol% and 1 mol% substituted polymer (HMPA-2 and HMPA-1), respectively.

**Membrane Properties.** The effect of polymer on the elastic properties of the membranes is studied using scattering techniques. The scattering intensity from a lamellar phase produces a power law singularity of the Bragg peak,  $I(q) \propto |q-q_0|^{-1+\eta}$ , where the exponent  $\eta$  is defined in terms of the smectic elastic constants by Caille et al [32]:

$$\eta = \frac{\kappa_s T q_0^2}{8\pi \sqrt{K \bar{B}}}$$

Where  $K$  is the smectic curvature modulus which is the ratio of membrane elastic constant,  $\kappa$ , to period spacing,  $d$ , (i.e.  $K=\kappa/d$ ), reflecting the rigidity of single bilayer;  $\bar{B}$  is the layer compression modulus related to the bilayer/bilayer interactions. Figure 5 is a neutron scattering spectrum for HMPA-3 coated membranes with different polymer concentration at a fixed membrane volume fraction ( $\phi=20\%$ ). The normalized Bragg peaks of the lamellar solution become narrower with growing polymer concentration (Fig. 5). This implies that the product  $K\bar{B}$  increases with polymer addition. Also the diffuse scattering at small angles is reduced with polymer concentration. This indicates that the strength of the inter-membrane interactions increases with polymer concentration since the scattering intensity at low angle is inversely proportion to  $\bar{B}$ .

The variation of the elastic constant with polymer concentration is calculated using a theory relating the excess area of the membrane to its rigidity [33]. In a perfect one-dimensional stack of membranes, a simple dilution law,  $d=\delta/\phi$ , is followed. However, the fluctuating-membrane systems investigated in this study generate the excess area in a lamellar phase, arising from undulations. The projected area is smaller than that estimated by a one-dimensional model. Therefore, the interlamellar distance,

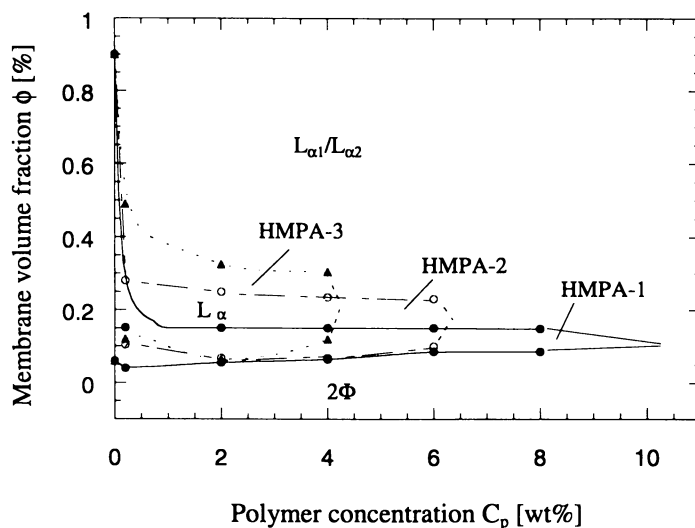


Figure 4. Polymer structure and concentration effect on the phase behavior of polymer doped membrane solutions. (Temperature = 25 °C).

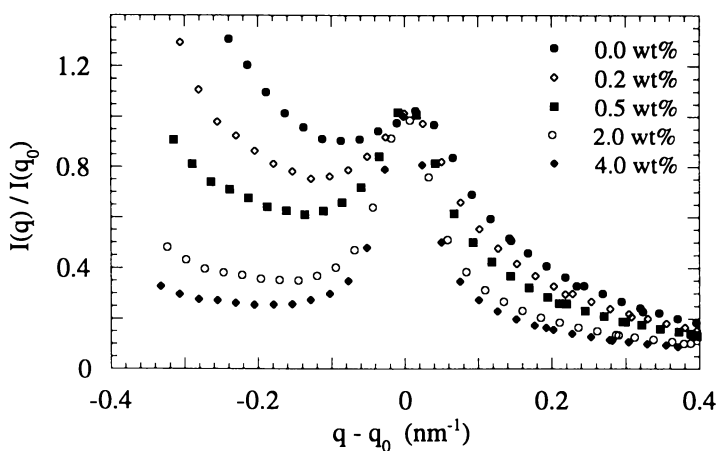


Figure 5. Normalized neutron scattering data of membrane solutions with different polymer concentration. Polymer concentration is indicated in the figure, membrane volume fraction  $\phi = 20\%$ , hydrophobe substitution level  $H_1 = 3 \text{ mol}\%$ . (Reproduced with permission from reference 14. Copyright 1998 American Physical Society.)

$d$ , which also depends on the membrane bending modulus  $\kappa$ , is given by the following relationship with  $\delta$  and  $\phi$  [33]:

$$\frac{d\phi}{\delta} = 1 + \frac{1}{4\pi k} \ln \left[ \frac{\delta}{\phi b} \sqrt{\frac{32k}{3\pi}} \right]$$

where  $b$  is a microscopic cutoff length. Based on this equation, variation of bending modulus can be monitored by simply measuring the interlamellar distance if membrane thickness is known. The value of  $\delta$  is extracted from the high- $q$  region of the neutron scattering spectra (Figure 6). From the peak position given by  $\sin^2(q\delta/2)$ , a membrane thickness  $\delta = 24 \pm 2 \text{ \AA}$  is obtained. Membrane thickness is the same in the  $L_\alpha$  and  $L_3$  phases with different polymer concentrations, as shown in Figure 6. The variation of interlamellar distance,  $d$ , may also arise from the defect in lamellar structure [34]. However, the model developed by Nallet et al [35] for lamellar phase,  $I(q) = q^{-2}P(q)S(q)$ , is in good agreement with the experimental data [30]. It indicates that the effect of defects on variation of interlamellar spacing is not a dominant factor for this system. Hence the membrane elastic constant  $\kappa$  can be considered the only factor determining the interlamellar distance, since the membrane volume fraction is kept constant ( $\phi = 20\%$ ). We show in Fig. 7, the relative elastic constant  $\kappa_r/\kappa_0$  as a function of polymer concentration, where  $\kappa_0$  is the elastic constant of the reference system. The relative elastic constant increases linearly with polymer concentration at low concentrations, then, appears to level off at a polymer concentrations above 2 wt%. The elastic constant almost doubles when polymer concentration increases from 0 to 4 wt%.

Both the elastic constant,  $\kappa$ , and the smectic compression modulus,  $\bar{B}$ , increase with polymer concentration (Figs. 5 and 7). This indicates that the polymer contributes to both inter- and intra-membrane. A large  $\bar{B}$  means a stiffening of the interlayer interaction potential. For a potential which is solely due to the steric Helfrich undulation interactions, the smectic modulus decreases with membrane stiffness  $\bar{B} \sim 1/\kappa$ . However, we find that  $\kappa$  increases with polymer concentration as does  $\bar{B}$  (Fig. 7). We conclude that the embedding of polymer in our system not only modifies the elastic properties of the membranes but also contributes to the inter-membrane potential.

## Summary

In this study, we have demonstrated that polymer structure, polymer concentration and membrane volume fraction are determinate factors governing the phase behavior and bilayer membrane properties of the surfactant/polymer mixture. When the size of the polymer is of same order of the bilayer spacing, the presence of a critical hydrophobe substitution along the polyacrylate-based backbone is necessary to insert the polymer into bilayer stack. The hydrophobic anchoring groups associate with the lyotropic bilayer, therefore allowing for confinement. The anchoring polymer induces two new phases, a vesicle-like phase and two coexisting lamellar phases  $L_{\alpha 1}/L_{\alpha 2}$ . Moreover, the presence of the polymer increases the bending elastic modulus,  $\kappa$ , and compression modulus,  $\bar{B}$ .

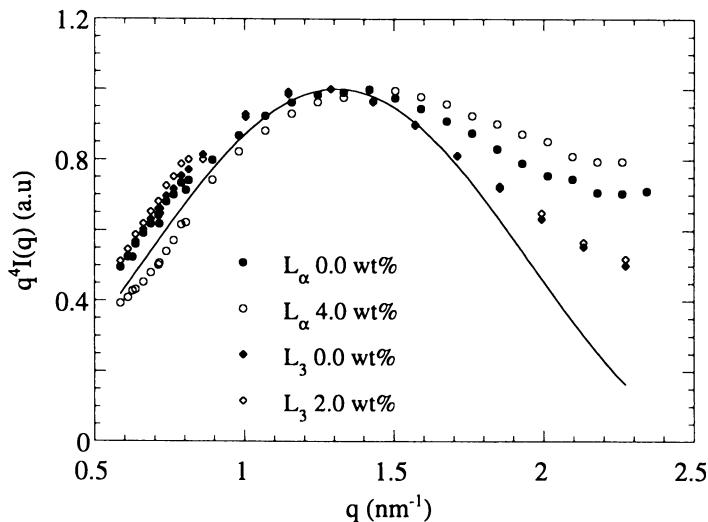


Figure 6. Large- $q$  behavior of  $q^4 I(q)$  in arbitrary units, showing one oscillation from which we extract the bilayer thickness  $\delta = 2.4 \pm 0.2$  nm. The fitting line is the function  $\sin^2(q\delta/2)$ . (Reproduced with permission from reference 14. Copyright 1998 American Physical Society.)

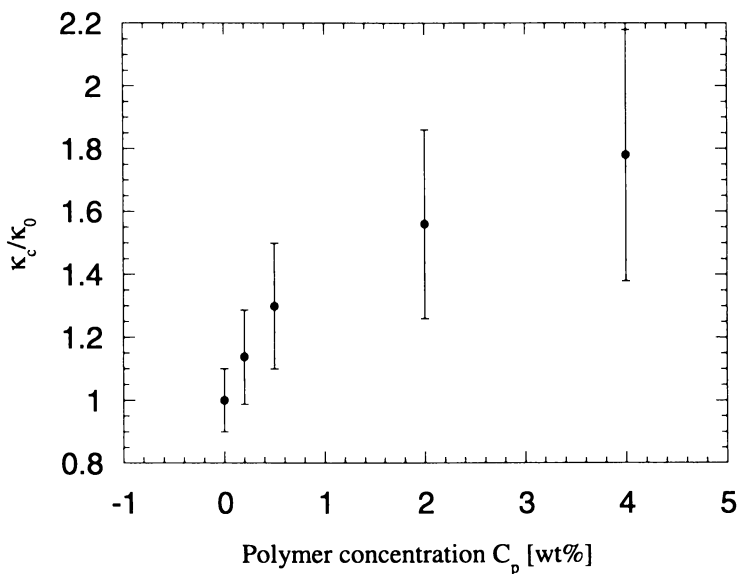


Figure 7. Polymer concentration effect on the membrane elastic constant. Membrane volume fraction  $\phi = 20\%$ , hydrophobe substitution level  $H_1 = 3$  mol%. (Reproduced with permission from reference 14. Copyright 1998 American Physical Society.)

## References

1. C. Ligoure, G. Bouglet, and G. Porte, *Phys. Rev. Lett.* **1993**, *71*, 3600
2. H. Bagger-Jorgensen, U. Olsson and I. Iliopoulos, *Langmuir* **1995**, *11*, 1934
3. Bagger-Jorgensen, U. Olsson, I. Iliopoulos and K. Mortensen, *Langmuir* **1997**, *13*, 5820
4. K. Loyen, I. Iliopoulos, R. Audebert and U. Olsson, *Langmuir* **1995**, *11*, 1053
5. H. Bagger-Jorgensen, U. Olsson and I. Iliopoulos, *Langmuir* **1995**, *11*, 1934
6. V. Rajagopalan, U. Olsson and I. Iliopoulos, *Langmuir* **1996**, *12*, 4378.
7. B. Deme, M. Dubois, T. Zemb and B. Cabane, *J. Phys. Chem.* **1996**, *100*, 3828.
8. R. Lipowsky, *Europhys. Lett.* **1995**, *30*, 197
9. M. F. Ficheux, A.M. Bellocq and F. Nallet, *J. Phys. II France*, **1995**, *5*, 823.
10. E. Z. Radlinska, T. Gulik-Krzywicki, F. Lafuma, D. Langevin, W. Urbach, S. E. Williams, and R. Ober, *Phys. Rev. Lett.* **1995**, *74*, 4237.
11. E. Z. Radlinska, T. Gulik-Krzywicki, F. Lafuma, D. Langevin, W. Urbach and S. E. Williams, *J. Phys. II France* **1997**, *7*, 1393
12. J. T. Brooks, C. M. Marques, and M. E. Cates, *Europhys. Lett.* **1991**, *14*, 713
13. G. Bouglet, C. Ligoure, A.M. Bellocq, E. Dufourc, and G. Mosser, *Phys. Rev. E*, **1998**, *57*,1
14. Y. Yang, R. Prudhomme, K. M. McGrath, P. Richetti and C. M. Marques, *Phys. Rev. Lett.* **1998**, *80*, 2729
15. R. Strey et al., *J. Chem. Soc. Faraday Trans.* **1990**, *86*, 2253
16. T. K. Wang, I. Iliopoulos, R. Audebert, *Polym. Bull.* **1988**, *20*, 577
17. I. Iliopoulos, T. K. Wang and R. Audebert, *Langmuir* **1991**, *7*, 617
18. R. Strey and M. Jonstromer, *J. Phys. Chem.* **1992**, *96*, 5993
19. E. Freyssingeas, F. Nallet and D. Roux, *langmuir*, **1996**, *12*, 6028
20. A. J. Dualeh and C. A. Steiner, *Macromolecules* **1990**, *23*, 251
21. R. Tanaka, J. Meadows, P. A. Williams and G. O. Phillips, *Macromolecules*, **1992**, *25*, 1304
22. I. Iliopoulos, T. K. Wang and R. Audebert, *Langmuir*, **1991**, *7*, 617
23. B. Nyström, H. Walderhaug, F. K. Hansen and B. Lindman, *Langmuir*, **1995**, *11*, 750
24. L. Piculell, F. Guilenet and K. Thuresson *Advances in Colloid and Interface Science*, **1996**, *63*, 1
25. T. Annable, R. Buscall, R. Ettelaie, and D. Whittlestone, *J. Rheol.* **1993**, *37*, 695
26. M. H. G. M. Penders and R. Strey, *J. Phys. Chem.* **1995**, *99*, 6091
27. R. Strey, *Ber. Bunsenges. Phys. Chem.* **1996**, *100*, 182
28. H. Hoffmann, U. Munkert, C. Thunig, and M. Valiente, *J. Colloid and Interface Sci.* **1994**, *163*, 217
29. P. Herve, D. Roux, A. M. Bellocq, F. Nallet and T. Gulik-Krzywicki, *J. Phys. II France*, **1993**, *3*, 1225
30. Y. Yang, R. Pud'homme, A. Zirkel, C. M. Marques, and P. Richetti, prepared for *langmuir*
31. K. Zhang and P. Linse, *J. Phys. Chem.* **1995**, *99*, 9130



32. A. Caille, C.R. Jeb. Sean, *Acad. Sci.* **1972**, B274, 1733
33. D. Roux, F. Nallet, E.Freyssingas, G. Porte, P. Bassereau, M. Skouri and J. Marignan, *Europhysics Letters*, **1992**,17 (7), 575
34. S. T. Hyde, *Langmuir*, **1997**, 13 842
35. F. Nallet, R. Laversanne and D. Roux, *J. Phys. II France*, **1993**, 3, 487

## Chapter 12

# **Biomimetic Surface Engineering: Synthesis and Surface-Induced Assembly of Novel Oligosaccharide Surfactant Polymers**

**Yongxing Qiu<sup>1,3</sup>, Nolan B. Holland<sup>2</sup>, Mark Ruegsegger<sup>1</sup>,  
and Roger E. Marchant<sup>1,2</sup>**

**Departments of <sup>1</sup>Biomedical Engineering and <sup>2</sup>Macromolecular Science,  
Case Western Reserve University, Cleveland, OH 44106**

Physical adsorption and surface induced assembly of oligosaccharide surfactant polymers on graphite creates a biomimetic, glycocalyx-like surface, which is effective in suppressing protein adsorption and provides a potential solution to clinical problems (e.g. thrombosis) with polymer implants. The novel surfactant polymers consist of a flexible poly(vinyl amine) backbone with two types of side chains: hydrophilic oligosaccharide and hydrophobic alkanoyl. The surface induced assembly is driven by hydrophobic interaction and epitaxial adsorption of alkanoyl side chains. This gives rise to hexagonal ordering of adsorbing polymers, in which assembly propagates laterally, with preferential adsorption at the edge of previously adsorbed polymer. This yields a highly ordered monolayer of polymer backbone and alkanoyl side chains assembled on the surface, while solvated oligosaccharide chains protrude into the aqueous phase, creating a glycocalyx-like oligosaccharide coating. A range of biomimetic surfaces may be engineered by extending the same approach to include different oligosaccharides and other hydrophobic surfaces.

One of the well-known clinical problems for blood-contacting biomaterial devices and implants is surface-induced thrombosis (1). The first step in surface-induced thrombosis is the spontaneous and non-specific adsorption of plasma proteins, followed by adhesive interactions of adsorbed protein with blood components (e.g. the adhesion and activation of platelets), and finally the formation of thrombus. Accordingly, tremendous effort has been devoted to minimizing the initial non-specific protein adsorption, by surface modification of the biomaterials (2).

An ideal surface modification should be an optimal combination of two basic elements: an effective surface modifying substance and a simple yet well defined

<sup>3</sup>Current address: CIBA Vision, 11460 Johns Creek Parkway, Duluth, GA 30097.

surface modification method. Among the variety of modifying substances explored so far, poly(ethylene glycol) (PEG) has been the most widely used, due to its ability to suppress protein adsorption by entropic repulsion (3). We have approached the problem of inhibiting protein adsorption from the perspective of how the body controls adhesive and non-adhesive interactions. The external region of a cell membrane, known as the glycocalyx, is dominated by glycosylated molecules (4). Cell and molecular interactions are strongly influenced by pendant oligosaccharides that are clustered on many plasma proteins and cell surface glyco-molecules of a cell's glycocalyx. The densely-packed, highly hydrated oligosaccharides provide a physical basis for maximizing entropic repulsion and preventing undesirable molecular and cellular adhesions. However, it still facilitates desirable adhesive interactions and biological specificity achieved through specific interactions. A biomimetic, glycocalyx-like surface modification provides a potential solution to the clinical problems related to non-specific protein adsorption, such as surface-induced thrombosis.

Existing surface modification methods are far from ideal in achieving a well-defined modified surface for practical biomaterial devices. Typical biomaterials are hydrophobic, with no labile functional groups available for direct chemical modification (5). Functionalization of biomaterials by wet chemistry (6), oxidation (7) or radio frequency plasma treatments (8) and subsequent derivatization are traditional methods to modify polymer surfaces. However, because of several steps involved in the chemical reactions, it is inherently difficult to achieve well-defined and reproducible modified surfaces. Self-assembled monolayers (SAMs) (9) derived from organotrichlorosilanes on silica and organosulfur compounds on gold represent well-defined model surfaces to study protein-surface interactions, but are unlikely to find application on practical polymer biomaterials that normally cannot meet the requirements needed in the formation of SAMs.

In following the biological perspective of the glycocalyx and pursuing a simple yet well-defined practical modification method, we have explored physical adsorption/surface-induced assembly of oligosaccharide surfactants onto hydrophobic biomaterials in an attempt to mimic the non-adhesive properties of a glycocalyx (10). That is, using the hydrophobic interaction between surfactant and solid surface to create a new biomimetic oligosaccharide-rich interface capable of minimizing protein adsorption. In our initial work, we reported on the synthesis and surface active properties of structurally well-defined linear oligosaccharide surfactants with different molecular geometries: AB diblock and ABA bolaform-type surfactants, where "A" represents the sugar head group and "B" represents the hydrophobic alkyl tail, and different hydrophobic and hydrophilic chain lengths (11). Our reports on novel oligosaccharide surfactants laid emphasis on manipulating surfactant structure to achieve desired interfacial behavior (10, 11).

In this report, biomimetic surface engineering using novel oligosaccharide surfactant polymers is demonstrated. We describe here the synthesis, characterization, surface activity at air/water interface, surface-induced assembly at solid surface/water interface, and protein resistance of a novel series of well-defined, comb-like, surfactant polymers. The surfactant polymers have a low molecular weight poly(vinyl amine) (PVAm) backbone with two types of side chains: hydrophilic dextran and hydrophobic alkanoyl (hexanoyl or lauroyl). Selective attachment of dextran is accomplished by reacting amine groups with dextran lactone, while alkanoyl groups are attached using N-alkanoyloxy succinimide, the N-

hydroxy succinimide active ester of alkanoyl acid. The alkanoyl side chains serve as physical binding ligands to a hydrophobic substrate, and oligosaccharide side chains protrude into the aqueous environment to provide a glycocalyx-like interface. The macromolecular design of surfactant polymers presented here provide a glycocalyx-like surface when adsorbed under aqueous conditions on a hydrophobic highly-oriented pyrolytic graphite (HOPG) surface. The glycocalyx-like surfaces exhibit excellent resistance against non-specific protein adsorption. The synthetic and biomimetic approach described in this chapter offers numerous possibilities for quantitative manipulation of composition and molecular architecture for achieving desired interfacial properties and ultimately to structures that may realistically mimic a glycocalyx.

### **Synthesis and characterization of comb-like dextran surfactant polymers.**

The surfactant polymers, poly(N-vinyl dextran aldonamide-co-N-vinyl alkanamide) (PNVDA-co-PNVA, or PVAm/Dex-Alk) are synthesized from well-defined poly(vinyl amine) by attaching oligosaccharides of dextran and alkanoyl (hexanoyl or lauroyl) chains simultaneously and selectively to reactive amine sites, as previously reported (12). Low molecular weight poly(vinyl amine) ( $M_n \sim 6000$ ) was prepared from the hydrolysis of poly(N-vinylformamide) (12). Dextran lactone with 9  $\alpha$  (1 $\rightarrow$ 6) glucose residues ( $M_w = 1600$ , polydispersity = 1.16) was prepared according to the method reported previously (11a). N-Alkanoyloxy (N-hexanoyloxy or N-lauroyloxy) succinimide was prepared from alkanoyl acid (hexanoic acid or lauric acid) and N-hydroxysuccinimide in the presence of dicyclohexylcarbodiimide (DCCI). Selective attachment of dextran is accomplished by reacting amine groups with dextran lactone, while alkanoyl groups are attached using N-alkanoyloxy succinimide, as shown in the synthetic scheme along with a molecular model for the surfactant polymer in Figure 1. The aminolysis of dextran lactone is selective, and thus protection of dextran hydroxyl groups is not necessary (11a). Surfactant polymers were purified by extensive dialysis against water to remove residual unreacted dextran lactone, using Spectra/Pro 3 regenerated cellulose membrane with a 3500 molecular weight cutoff. Then the surfactant polymers were characterized by Fourier transform infrared (FTIR) and  $^1\text{H-NMR}$  spectroscopies and elemental analysis to confirm purity and structure (12). The molar feed ratios of dextran lactone to N-alkanoyloxy succinimide was varied to produce different ratios of hydrophilic dextran to hydrophobic alkanoyl side chains on the polymer backbone. In this manner, five surfactant polymers were prepared with different side chain ratios of dextran to hexanoyl (PVAm/Dex-Hex 1:1, 1:4 and 1:5) and dextran to lauroyl (PVAm/Dex-Lau 1:0.6, 1:1.5). All of the five surfactant polymers are soluble in DMF and DMSO. PVAm/Dex-Hex 1:1, PVAm/Dex-Hex 1:4 and PVAm/Dex-Lau 1:0.6 are soluble in water at room temperature, while PVAm/Dex-Hex 1:5 and PVAm/Dex-Lau 1:1.5 are not readily soluble in water but a low level of solubility ( $\sim 1$  mg/ml) can be achieved by vigorous sonication.

### **Surface active properties at air/water interface.**

The surface activity of the comb-like surfactant polymers in solution at an air/water interface was demonstrated by water surface tension measurement. Surface tensions



of aqueous surfactant solutions were measured at 25°C and ambient pressure, using a Du Nouy ring tensiometer. The tensiometer was calibrated with Millipore ultrapure water (18.2 M $\Omega$ ·cm resistivity) before use. The platinum ring was cleaned by flaming, while the glassware was cleaned with a NaOH/2-propanol basic solution and rinsed with tap water and ultrapure water. A concentrated surfactant solution (up to 5 wt%) was freshly prepared as a starting solution and then diluted to the desired concentration for each measurement. After the solution was equilibrated for 5 min., surface tension was measured three times at each concentration.

Surface tension plotted against the logarithm of surfactant concentration is shown in Figure 2 for PVAm/Dex and the PVAm/Dex-Hex surfactant polymers. As expected, PVAm/Dex, a homopolymer composed of PVAm with pendant dextran molecules only, showed virtually no surface activity, as indicated by the small decrease (~2 mN/m) in water surface tension with increasing surfactant concentration (Figure 2a). In contrast, the surfactant polymers PVAm/Dex-Hex (1:1) and PVAm/Dex-Hex (1:4) exhibit significant surface active behavior, as indicated by the substantial decrease in surface tension with increasing surfactant concentration (Figures 2b, 2c). The lowest surface tension is about 41 mN/m, a decrease of 31 mN/m compared with pure water. In both cases, no critical micelle phenomenon was observed within the measured concentration range.

Both surfactants gave similar curves for surface tension versus concentration. Since PVAm/Dex-Hex (1:1) and PVAm/Dex-Hex (1:4) exhibit similar effects on water surface tension reduction, we may assume that packing of hexanoyl groups at the air/water interface, which is responsible for reducing the surface tension, is similar in both cases. The results suggests the surfactants have considerable conformational freedom in order to facilitate comparable hexanoyl packing at the air/water interface. Thus, to achieve further reductions in surface tension suggests increasing the length of the alkanoyl ligand in the molecular design, rather than further increasing the density of hexanoyl ligand groups. This is a useful finding, because it should also permit increased oligosaccharide to alkanoyl ratios in the polymer surfactants, an important consideration for maximizing oligosaccharide density while maintaining surface activity.

### Surface induced assembly of oligosaccharide surfactant polymers on HOPG.

The observed surface active properties of the surfactants at the air/water interface may lead to similar properties at a solid/water interface. To test this hypothesis, *in situ* adsorption of surfactant polymers on highly oriented pyrolytic graphite (HOPG) was studied.

The surface induced assembly of surfactant polymers was demonstrated in real time using atomic force microscopy (AFM). *In situ* adsorption of surfactant polymers on HOPG under aqueous medium was imaged using a Nanoscope III Multimode atomic force microscope equipped with a glass fluid cell attachment and silicon nitride (Si<sub>3</sub>N<sub>4</sub>) cantilevers with integrated Si<sub>3</sub>N<sub>4</sub> tips (Digital Instruments, Santa Barbara, CA). HOPG cleaves across a single atomic plane, and is therefore extremely smooth, except for occasional step edges. This allowed topographical features of adsorbed surfactant molecules to be easily distinguished from the underlying HOPG surface. AFM images were collected at ambient temperature in

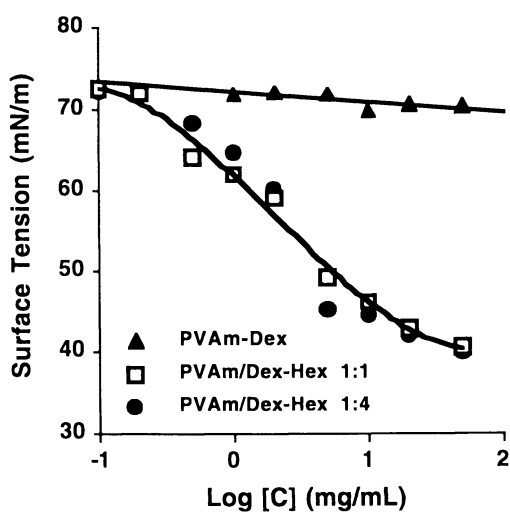


Figure 2. Plots of surface tension versus logarithm of the concentration of aqueous PV Am-Dex and PV Am/Dex-Hex surfactant polymer solutions.

tapping mode. A freshly cleaved HOPG substrate was first imaged in water as a reference before the addition of surfactant solution in each experiment. Surfactant solution (0.5 mg/mL) was then flowed into the fluid cell without withdrawing the AFM probe, so that the same surface region of HOPG, before and after adsorption of surfactant molecules, could be imaged. Imaging of adsorbed surfactant polymer began after the microscope had equilibrated with the new solution (about 10 minutes) and was carried out in the presence of the surfactant polymer solution.

The time-dependent adsorption of the surfactant polymer with a ratio of 1:5 dextran to hexanoyl groups (PVAm/Dex-Hex 1:5) is shown in Figure 3. Initially, the surfactant polymer adsorbed on HOPG as strands, as shown in an image obtained after about 25 minutes (Figure 3a). As adsorption time progressed, the strands broaden (Figure 3b, c) and by about 7 hours (Figure 3d) most of the surface is covered. Residual surface roughness disappears by 20 hours leaving a complete and compact monolayer. The thickness of the adsorbed surfactant polymer increases slightly with increasing surface coverage up to a maximum of 7 - 12 Å. This indicates a single monolayer on the surface, consistent with our estimate for the dextran side chain diameter of ~9 Å, obtained from surface tension data of N-dodecyl dextran aldonamide (11b), and ~2.5 Å for the polymer backbone. Evidence that the adsorption is stable was obtained from observing no discernible change in the monolayer after keeping pure water over the adsorbed surfactant for 1-2 hours and scanning with high AFM imaging forces.

The ordering of adsorbing surfactant polymer on HOPG was unexpected. Polymers with relatively short chain branches do not tend to crystallize, because branches prevent close intermolecular alignment of the polymer backbone. On the HOPG, however, we observe an ordered adsorption pattern in which adsorbed polymer strands align themselves in three symmetric directions 60 degree out of each other (Figure 3c), as verified by the hexagonal angular dependence pattern in the 2-dimensional Fourier transform of the image (Figure 4). The underlying HOPG has a hexagonal atomic lattice structure. This result suggested an epitaxial adsorption of surfactant polymer PVAm/Dex-Hex 1:5 on HOPG. By comparing images of the HOPG lattice with that of surfactant polymer on HOPG, it was verified that the strands align perpendicular to the substrate atoms. Surfactant polymer ordering on HOPG propagates laterally, with preferential adsorption at the edge of previously adsorbed polymer.

A mechanism of epitaxial adsorption of surfactant polymer on HOPG is proposed. Driven by a large enthalpic force, alkanoyl side chains adsorb in registry with the graphite atoms, which constrains the polymer backbone to the surface and orients dextran side chains away from the substrate into the aqueous solution. The large enthalpic driving force (6.28 kJ/mol per methylene group) (13a) for epitaxial ordering of hydrocarbons is supported by numerous reported examples (13-15), including paraffin chain alignment on graphite (13) and epitaxial crystallization of linear polyethylene (14). The relatively high density of randomly spaced hydrocarbon side chains requires the polymer backbone to extend to allow each hexanoyl to be in registry. The entropy lost in extending the polymer chain is offset by the enthalpic energy gained from epitaxial adsorption. Hexanoyl side chains can align to three symmetric directions on the graphite lattice, leading to the alignment of the polymer backbone in three directions as observed by AFM (Figure 3c, 5a). The growth direction of adsorbing surfactant polymer is perpendicular to the backbone,



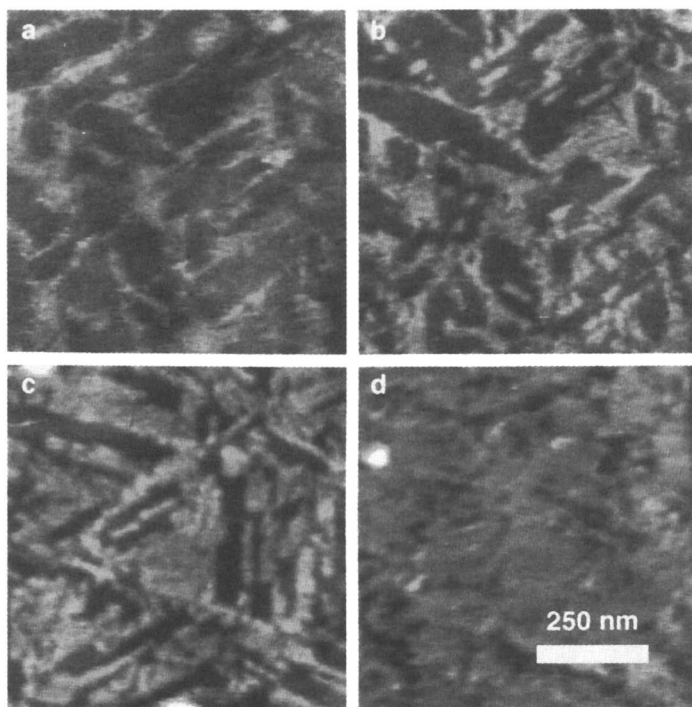


Figure 3. AFM images of PV Am/Dex-Hex 1:5 surfactant polymer adsorbed on the HOPG. The images show the progression of adsorption from: a, ~25 minutes; b, ~1 hour; c, ~5.5 hours; and d, ~7.5 hours; as imaged in 0.5 mg/mL aqueous polymer solution.

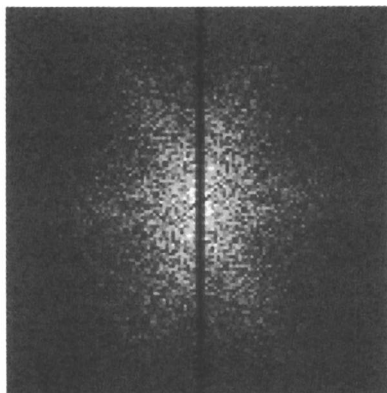


Figure 4. A 2-D fourier transform of an AFM image in Fig. 3c showing epitaxial adsorption of surfactant polymer PV Am/Dex-Hex 1:5 on HOPG, as evidenced by the hexagonal pattern.

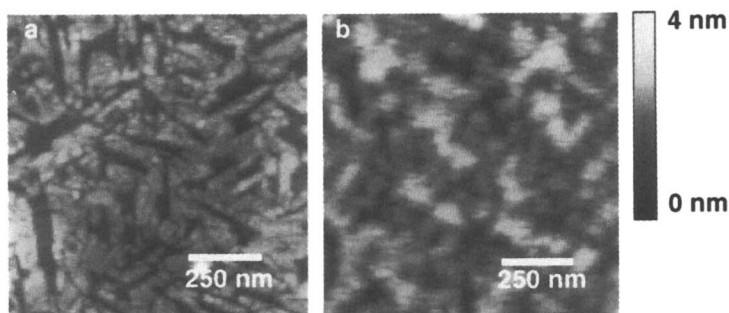


Figure 5. AFM topographic images of surfactant polymers with different hydrophobic/hydrophilic ratio adsorbed on the HOPG. a. Ordered structure of PV Am/Dex-Hex 1:5; b. Molecular aggregates of PV Am/Dex-Hex 1:1.

with preferential adsorption along the edge of the previously adsorbed polymer molecules. In this way, the surface is fully covered after certain adsorption time and modified into a biomimetic, glycocalyx-like surface.

Epitaxial adsorption patterns were observed for the three surfactant polymers (PVAm/Dex-Hex 1:5 and 1:4 and PVAm/Dex-Lau 1:1.5) that contain a relatively high hydrophobic alkanoyl chain concentration (>15 methylene units per dextran) (Figure 5a). The surfactant polymers with a relatively low alkanoyl concentration (PVAm/Dex-Hex 1:1 and PVAm/Dex-Lau 1:0.6, <8 methylene units per dextran) adsorbed to the HOPG surface as molecular aggregates (Figure 5b), but not in an ordered pattern. In this case, alkanoyl chains may bind in registry to achieve energy minimization but are too far apart to induce the polymer backbone to extend.

The total enthalpic energy gain of adsorption is dependent on the relative total number of methylenes in alkanoyl side chains. Therefore, surfactant polymers with the longer lauroyl side chains have the advantage of needing fewer binders (~1.5 lauroyl) per dextran, compared to hexanoyl (~4), to induce epitaxial ordering. To achieve ordering, enthalpic energy gained from epitaxial adsorption of alkanoyl side chains offsets the entropy loss in extending the polymer backbone and forcing dextran side chains into close proximity. Steric repulsion between dextrans may result in a "brush-like" conformation, although there is little comparison with the extended conformations exhibited by surface-anchored synthetic random coil polymers interacting with good solvents (16). Dextran has a stable helical structure that is unlikely to be perturbed by nearest neighbor effects.

### **Protein resistance of the biomimetic, glycocalyx-like surface.**

A design feature of the biomimetic surface is to use the protruding dextran oligosaccharides to mimic the non-adhesive properties of a glycocalyx. The steric barrier provided by the highly hydrated dextrans is designed to suppress non-specific adsorption of plasma proteins (17), while the high energy of desorption and low water solubility of the adsorbed surfactant polymer is designed to minimize possible displacement or exchange reactions with highly surface-active plasma proteins. This biomimetic concept was tested by studying the protein resistance of surfactant polymer modified HOPG.

Freshly cleaved HOPG was modified with PVAm/Dex-Hex surfactant polymers in a 24 hour adsorption from aqueous solution, then air dried overnight. Protein adsorption on surfactant polymer modified HOPG and HOPG control were studied using a parallel plate laminar flow cell. The flow cell insert was designed in such a way that the vertical position of sample could be adjusted to level the sample surface with the flow track. A 50% solution of fresh human platelet poor plasma in phosphate buffered saline (pH 7.4) anticoagulated with sodium citrate, was adsorbed on HOPG samples under static conditions for 30 minutes at 37°C. This provided a rigorous *in vitro* test, since the solution contained all plasma proteins in blood at a concentration that was sufficient to cover a surface with proteins every second of exposure. The protein solution was replaced by PBS and the samples were rinsed under a controlled shear stress of 100 mN/m<sup>2</sup> for 5 minutes to remove the loosely-attached proteins from the sample surface. The sample was exposed to air after replacing PBS slowly with 100 ml of water and air dried overnight in a Class-100 clean hood. In order to minimize the interference of residual water molecules, the

sample was further vacuum dried (60 millitorr) at room temperature using a liquid nitrogen sorption pump. Then the sample was immediately analyzed by ATR (attenuated total reflectance)-FTIR using a BIO-RAD FTS 575C IR spectrometer, with a UMA 500 microscope accessory and a MCT detector. IR spectra (4000 - 700  $\text{cm}^{-1}$ ) were collected by co-adding 100 scans with a resolution of 8  $\text{cm}^{-1}$  using germanium as the internal reflective element. Nine spectra from different areas of each sample were collected.

Protein adsorption was quantified from the relative IR absorbance intensity of the characteristic protein Amide I (1650  $\text{cm}^{-1}$ ) and Amide II (1550  $\text{cm}^{-1}$ ) bands. HOPG has a characteristic sharp negative absorption peak at 1590  $\text{cm}^{-1}$  due to "in-plane" vibration mode of hexagonal atomic lattice of graphite (18). To reveal the protein adsorbate (Fig. 6), spectra were normalized to this sharp negative peak (1590  $\text{cm}^{-1}$ ), followed by digital subtraction of water vapor and the graphite substrate. On bare HOPG, the Amide I and II bands are attributed entirely to adsorbed proteins, whereas on modified HOPG amide bonds in both the surfactant polymer and adsorbed proteins contribute to the absorbance. Amide I and II protein bands are very strong on bare HOPG and almost negligible on the biomimetic surfactant modified HOPG. By subtracting the contribution from the surfactant polymer, the absorbance due to adsorbed protein is isolated and determined (Table 1). We estimate that plasma protein adsorption is suppressed by at least 90% on the PVAm/Dex-Hex 1:5 modified surface, 85% on the PVAm/Dex-Hex 1:4 modified surface and 70% on the PVAm/Dex-Hex 1:1 modified surface (Table 1), compared with the bare HOPG. The small difference in three surfactant polymer modified surface may be attributed to their different degree of adsorption ordering.

Table 1: The relative average absorbance values of amide I and amide II bands and percentile reduction in protein adsorption for surfactant polymer modified HOPG.

Sample	Relative absorbance		% Reduction in Protein adsorption	
	Amide I	Amide II	Calculated from Amide I	Calculated from Amide II
HOPG	1.838	0.773	/	/
PVAm/Dex-Hex 1:5 modified HOPG	0.166	0.086	91.0	91.4
PVAm/Dex-Hex 1:4 modified HOPG	0.254	0.109	86.2	85.9
PVAm/Dex-Hex 1:1 modified HOPG	0.544	0.217	70.4	71.9

## Conclusion.

A novel series of nonionic oligosaccharide surfactant polymers with well-defined structure and adjustable hydrophilic/hydrophobic balance were synthesized by incorporating dextran oligosaccharide molecules and hydrophobic hexanoyl groups simultaneously into poly(vinyl amine). The surfactants demonstrate surface activity at an air/water interface, as determined by water surface tension measurements, and surface-induced assembly at HOPG/water interface, as visualized directly by AFM. Physical adsorption and surface induced assembly of oligosaccharide surfactant

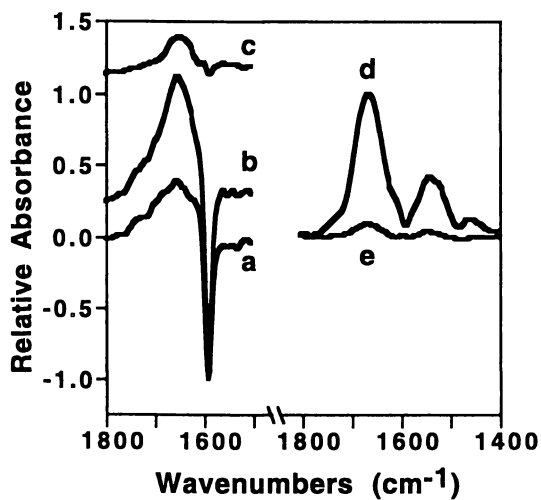


Figure 6. ATR-FTIR spectra. a: HOPG; b: Surfactant polymer coated HOPG; c: Surfactant polymer obtained by subtracting a from b; d: Protein adsorbed on HOPG after subtracting the contribution of HOPG; e: Protein adsorbed on surfactant polymer coated HOPG after subtracting the contribution of HOPG and surfactant polymer.

polymers on HOPG creates a biomimetic, glycocalyx-like surface. The glycocalyx-like modification of HOPG demonstrates effective suppression of non-specific protein adsorption, although testing under *in vivo* conditions is needed to confirm the utility of this approach on implantable devices. The synthetic and biomimetic approach offers numerous possibilities for manipulating the surfactant polymer design, ligand composition, and hydrophilic/hydrophobic ratios, to accommodate a wide range of potential applications that require surface modification with well-defined molecular structures. It should also be possible to develop biomimetic designs that adhesive, rather than non-adhesive biological interactions are desired, such as by incorporating the anticoagulant pentasaccharide sequence of heparin, specific cell adhesion receptors (selectins) or adhesive peptides.

**Acknowledgments.** We acknowledge the financial support of this work provided by the National Institute of Health and the Whitaker Foundation and use of facilities at the Center for Cardiovascular Biomaterials.

## References

1. (a) Hanson, S. R. and Harker, L. A. *Blood Compatibility*, Williams. B. D. F. Ed., CRC Press, Boca Raton, FL, 1987, Vol.1; pp 37-86. (b) Horbett, T. A. *Cardiovasc. Pathol.* **1993**, 2 (suppl.), 137-148. (c) Courtney, J. M.; Lamba, N.M.K.; Sundaram, S. and Forbes, C. D. *Biomaterials* **1994**, 15(10), 737-744. (d) Salzman, E. W.; Merrill, E. W.; Hent, K. C. in *Hemostasis and Thrombosis*, 3rd ed. Colman, R. W., Hirsh, J., Marder, V. J., Salzman, E. W., Eds.; J. B. Lippincott Co., Philadelphia, PA, 1994; pp 1469-1485.
2. (a) Fougnot, C.; Labarre, D.; Jozefonvicz, J.; and Jozefowicz, M. *Macromolecular Biomaterials*; Hastings, G. W. and Ducheyne, P. Eds., CRC Press, Boca Raton, FL, 1984, pp 216-233. (b) Ikada, Y. *Biomaterials* **1994**, 15(10), 725-736. (c) Hoffman, A.S. *Macromol. Sym.* **1996**, 101, 443-454. (d) Elbert, D. L. and Hubbell, J. A. *Annu. Rev. Mater. Sci.* **1996**, 26, 365-394.
3. (a) Harris, J. M. *Poly(ethylene glycol) Chemistry, Biotechnical and Biomedical Applications*; Plenum Press, New York and London, 1992. (b) Harris, J. M. and Zalipski, S. *Poly(ethylene glycol) Chemistry and Biological Applications*; American Chemical Society, Washington, DC, 1997.
4. (a) Evans, W.H. & Graham, J.M. *Membrane Structure and Function*; Oxford University Press, New York, NY, 1991, pp 1-86. (b) Fukuda, M. & Hindsgaul, O. *Molecular Glycobiology*; Oxford University Press, New York, NY, 1994, pp 1-52. (c) Bongrand, P. *Intermolecular forces, Physical Basis of Cell-Cell Adhesion*; Bongrand, P. ed., CRC Press, Boca Raton, FL, 1987, pp 1-37.
5. Helmus, M.N. & Hubbell, J.A. *Cardiovasc. Pathol.(Suppl.)*, **1993**, 2, 53S-71S.
6. Park, K.D.; Okano, T.; Nojiri, C.; Kim, S.W. *J. Biomed. Mater. Res.* **1988**, 22, 977
7. (a) Whitesides, G. M. and Laibinis, P. E. *Langmuir* **1990**, 6, 87-96. (b) Rasmussen, J. R.; Stedronsky, R. R.; and Whitesides, G. M. *J. Am. Chem. Soc.*,

- 1977, 99, 4736-4745. (c) Rasmussen, J. R.; Bergbreiter, D. E.; and Whitesides, G. M. *J. Am. Chem. Soc.* **1977**, 99, 4746-4756. (d) Holmes-Farley, S. R.; Bain, C. D.; Whitesides, G. M. *Langmuir*, **1988**, 4, 921-937.
8. (a) Qiu, Y.; Klee, D.; Plüster, W.; Severich, B.; Höcker, H. *J. Appl. Polym. Sci.*, **1996**, 61, 2373-2382. (b) Yu, S. and Marchant, R. E. *Macromolecules*, **1989**, 22, 2957-2961. (c) Johnson, S. D.; Anderson, J. M.; and Marchant, R. E. *J. Biomed. Mater. Res.* **1992**, 26, 915-935. (d) Yuan, S.; Szakalas-Gratzl, G.; Ziats, N. P.; Jacobsen, D. W.; Kottke-Marchant, K.; and Marchant, R. E. *J. Biomed. Mater. Res.* **1993**, 27, 811-819.
9. (a) Sagiv, J., *J. Am. Chem. Soc.* **1980**, 102, 92-98. (b) Wasserman, S. R.; Tao, Y.-T.; and Whitesides, G. M. *Langmuir* **1989**, 5, 1074-1087. (c) Bain, C. D. and Whitesides, G. M. *Science*, **1988**, 240, 62-63. (d) Mrksich, M. and Whitesides, G.M. *Annu. Rev. Biophys. Biomol. Struct.* **1996**, 25, 55-78.
10. (a) Marchant, R. E.; Yuan, S.; Szakalas-Gratzl, G. *J. Biomater. Sci., Polymer Edn.* **1994**, 6(6), 549-564. (b) Holland, N.B.; Ruegsegger, M.; Marchant, R. E. *Langmuir* **1998**, 14, 2790-2795. (c) Holland, N. B.; Qiu, Y.; Ruegsegger, M.; Marchant, R. E. *Nature*, **1998**, 392, 799-801.
11. (a) Zhang, T.; Marchant, R. E. *Macromolecules* **1994**, 27(25), 7302-7308. (b) Zhang, T.; Marchant, R. E. *J. Colloid Interface Sci.* **1996**, 177, 419-426. (c) Ruegsegger, M.; Zhang, T.; Marchant, R. E. *J. Colloid Interface Sci.* **1997**, 190, 152-160.
12. Qiu, Y.; Zhang, T.; Ruegsegger, M.; Marchant, R. E. *Macromolecules* **1998**, 31(1), 165-171.
13. (a) Groszek, A. *Proc. Roy. Soc. Lond. A* **1970**, 314, 473-498. (b) McGonigal, G.C.; Bernhardt, R.H. & Thompson, D.J. *Appl. Phys. Lett.* **1990**, 57, 28-30. (c) Rabe, J.P. & Buchholz, S. *Science* **1991**, 253, 424-427.
14. (a) Wellinghoff, S.; Rybnikar, F. & Baer, E. *J. Macromol. Sci. Phys.* **1974**, B10, 1-39. (b) Whitman, J.C. & Lotz, B. *Prog. Polym. Sci.* **1990**, 15, 909-948.
15. (a) Manne, S. & Gaub, H.E. *Science* **1995**, 270, 1480-1482. (b) Manne, S.; Cleveland, J.P.; Gaub, H.E.; Stucky, G.D. & Hansma, P.K. *Langmuir* **1994**, 10, 4409-4413.
16. (a) Milner, S.T. *Science* **1991**, 251, 905-914. (b) Sharma, R. *ACS Symp. Ser.* **1995**, 615, 1-20. (c) Golander, C.-G.; Herron, J.N.; Lim, K.; Claesson, P.; Stenius, P.; & Andrade J.D. in *Ref. 3a*, **1992**, 221-246.
17. Österberg, E.; Gergström, K.; Holmberg, K.; Schuman, T.P.; Riggs, J.A.; Burns, N.L.; Van Alstine, J.M.; Harris, J.M. *J. Biomed. Mater. Res.* **1995**, 29, 741-747.
18. Nemanich, R.J.; Lucovsky, G. & Solin, S.A. *Solid State Comm.* **1977**, 23, 117-120.

## Chapter 13

# Single-Molecule Hydrodynamics of Tethered and Released DNA Molecules

R. G. Larson<sup>1</sup>, T. T. Perkins<sup>2</sup>, D. E. Smith<sup>3</sup>, and S. Chu<sup>3</sup>

<sup>1</sup>Department of Chemical Engineering, University of Michigan,  
Ann Arbor, MI 48109-2136

<sup>2</sup>Princeton Materials Institute, Princeton University, Bowen Hall,  
70 Prospect Avenue, Princeton, NJ 08540

<sup>3</sup>Department of Physics, Stanford University, Stanford, CA 94305

Recent advances in molecular manipulation and imaging methods, combined with advances in computational speed, now make it possible to compare directly the predictions of detailed micromechanical models of polymers in flow fields with experimental images of long DNA molecules, thereby establishing the accuracy of the models. The examples reviewed here are that of a single DNA molecule tethered to a sphere confined by a laser-optical trap, and a freely suspended DNA molecule convected and stretched by an extensional flow field. The first example permits validation of the drag model for DNA, while the second considers transient unraveling processes. Excellent agreement is found between experiments and computer simulations based on the micromechanical model. With the model and simulation method validated, the source of heterogeneity in stretching behavior of DNA at high flowrates can be traced to Brownian-induced variations in molecular conformation at the start of flow.

The behavior of long polymer molecules in flow fields that can deform the polymer has long been a subject of great scientific and practical importance (1). The simplest such problems involve dilute concentrations, and hence non-interacting polymers. Even for this "simple" case, conventional experimental and theoretical methods have not provided an adequate description of molecular deformation. Experiments have been limited to the measurement of macroscopic quantities such as stress or birefringence, which are averages over many molecules and provide too coarse-grained a description to answer some of the most basic questions about polymer conformations under flow, such as whether or not the polymer molecules become fully extended (2,3). Conventional polymer theory suffers from an analogous limitation; it too is restricted to macroscopically averaged quantities, which are



possible, but the most accurate of these, molecular dynamics, can't cope with the large length scales and long time scales inherent in the dynamics of long polymer molecules. The most rigorous of these, atomistic molecular dynamics, is almost certainly accurate enough to describe polymer molecules under flow in enough detail to be accurate, but is far too slow to be a feasible method. The least rigorous model, a pre-averaged dumbbell, is too crude to be accurate (4).

Recent developments, however, have changed this outlook entirely. Steven Chu and his group at Stanford University have developed single-molecule experimental methods by which the conformation of single, long, DNA molecules can be imaged with fluorescent microscopy under well defined flow conditions (5,6). At the same time, over the last few years, computational resources have become fast enough and abundant enough to permit Monte Carlo and Brownian dynamics simulations of relatively large ensembles of model polymers that are sufficiently refined to capture detailed molecular configurations, such as random coils, "folded" and "kinked" states, etc (7,8). Thus, comparisons between theory and experiment can now be made literally on a molecule by molecule basis. Excellent agreement has been recently reported between extensional-flow experiments on lambda phage DNA by Smith et al. and corresponding multi-bead Monte Carlo and Brownian dynamics simulations of Larson et al. (7,9), with zero adjustable parameters

**Micromechanical Model of DNA** The micromechanical model used for the DNA molecule is based on the "worm-like chain," which is equivalent to a rod with a uniform bending stiffness. If a long portion of the worm-like chain of length  $L_s$  is subjected to a tension  $F$  tending to straighten it out, then the average end-to-end distance of separation between the two ends of the portion is given approximately by the Marko-Siggia expression (10):

$$F \lambda / kT = 0.25(1 - x/L_s)^{-2} - 0.25 + x/L_s \quad (1)$$

where  $\lambda$  is the "persistence length" of the molecule and is a measure of its stiffness. This expression is valid when the length of the piece of DNA  $L_s$  is much greater than the persistence length  $\lambda$ . In a flow field, the tension  $F$  on each piece of the chain tends to cause it to curl up so that it is unextended. However, the drag force acting along the DNA molecule tends to stretch it out. We can represent this drag force by a series of drag-producing "beads" placed uniformly along the backbone of the DNA molecule; see Figure 1. The more beads we use, the more nearly continuous is the distribution of drag force along the chain. However, we do not want to use too many beads, because if  $N$  is the number of beads, the distance along the backbone between adjacent beads decreases with the number of beads as  $L_s = L/(N-1)$ , where  $L$  is the total contour length of the DNA molecule. As  $N$  becomes larger,  $L_s$  becomes smaller; yet  $L_s$  must remain much larger than  $\lambda$  for equation 1 to apply. Since the persistence length of stained DNA is around 0.066 microns, we find that  $N = 20$  gives accurate results for DNA molecules with  $L = 20$  microns or more, if the persistence length  $\lambda$  is adjusted upward slightly to account for deviations to equation 1 produced by the introduction of beads.

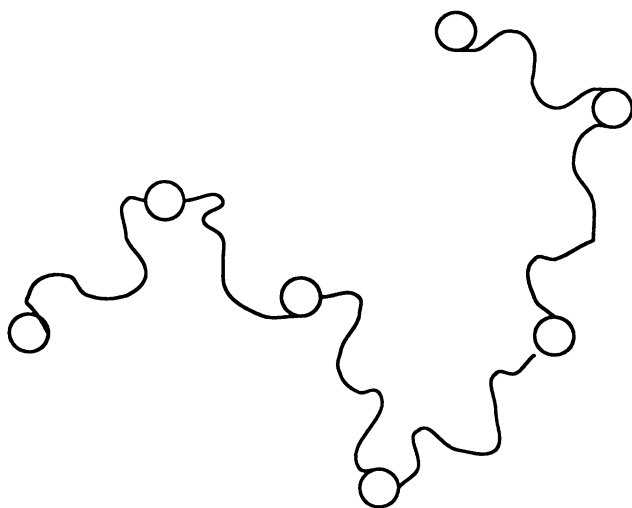


Figure 1. Illustration of bead-spring chain. Each bead provides frictional drag, while the springs each satisfy Equation 1.

The drag coefficient for each bead is set by two criteria. The drag on a freely suspended DNA molecule must match the value established by measurements of the center-of-mass diffusivity of a freely suspended DNA molecule (11). A second criterion is that the drag on a fully stretched DNA molecule must be equivalent to that on a long, thin, filament (9). Using these two criteria, the drag coefficients of the beads can be obtained, as well as the degree of hydrodynamic coupling among the beads produced by the influence one bead has on the drag exerted on the other beads. We have found that for lambda phage DNA represented by 20 beads, the drag coefficient on all beads can be taken to be almost equal to each other and hydrodynamic coupling among them is small, practically negligible (9). For longer DNA molecules, the hydrodynamic coupling is not insignificant but can be represented accurately by the hydrodynamic model (9).

**Tethered DNA Molecules.** To test this model of DNA, we compared its predictions against measurements of Perkins et al. (5) for fluorescently stained DNA tethered at one end to a small, 1 micron polystyrene sphere, held in place by a laser-optical trap; see Figure 2. A simple uniform flow was then imposed, which stretched out the DNA molecule. With the microscope objective, highly magnified images of the DNA molecule were acquired. From these images, the intensity of light emitted by the stained DNA could be measured as a function of position downstream of the tethering point. Figure 3 shows the measured mass distribution as a function of position downstream of the tethering point, for various imposed velocities. Note that the mass density is highest at the downstream end of the DNA molecule. The lines in Figure 3 are the predictions of the computer simulation using the beads-and-springs model. The predicted mass distribution is in good agreement with the measured one, showing that the micromechanical model of DNA is accurate.

**Released DNA Molecules.** In a second set of experiments, extensional flow was imposed on freely suspended DNA molecules in a crossed-slot device, which has two opposing inlet channels and two opposing outlet channels, as shown in Figure 4 (6, 12). The flowrate in each channel is identical. At the center of this device there is then a stagnation region where the local velocity is small, but where the gradient of velocity is large, leading to molecular stretching along the outflow axis. The gradient of velocity along the outflow axis,  $\partial v_x / \partial x$  is defined as  $\epsilon$ , the extension rate. The velocity gradient along the inflow axes,  $\partial v_y / \partial y$ , is equal to  $-\epsilon$ , because of fluid volume conservation. Because  $\partial v_z / \partial z = 0$ , this is a planar extensional flow. In this flow, the molecules are observed to stretch out via various different modes; in some cases the molecule takes on a “dumbbell” configuration in which a taut central portion connects two coiled up balls of DNA at either end; see Figure 5. In other cases, the molecule becomes “folded” as depicted in Figure 6. (In the images in Figures 5 and 6, the outflow axis of the planar extensional flow is vertical.) Other configurations include the “half dumbbell” with a ball of DNA at only one end, the “kinked” configuration with a ball in the center, and a “coiled” configuration, in which the molecule hardly stretches at all (6). These configurations are also observed in Brownian dynamics simulations, using the DNA micromechanical model described above (7). Figures 5

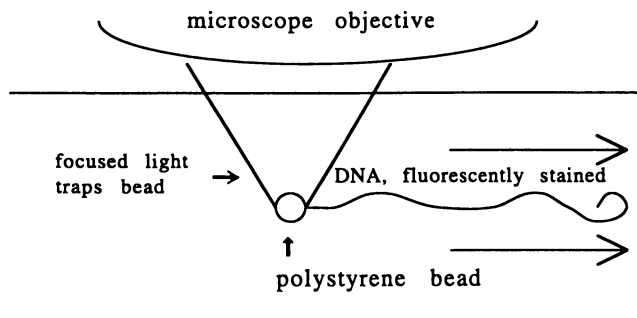


Figure 2. Configuration of tethered DNA molecule used by Perkins et al. (5). A focused beam of laser light traps a small bead to which a DNA molecule is attached by one end. Translation of the cell in which the DNA and bead are immersed produces a uniform flow, stretching the DNA.

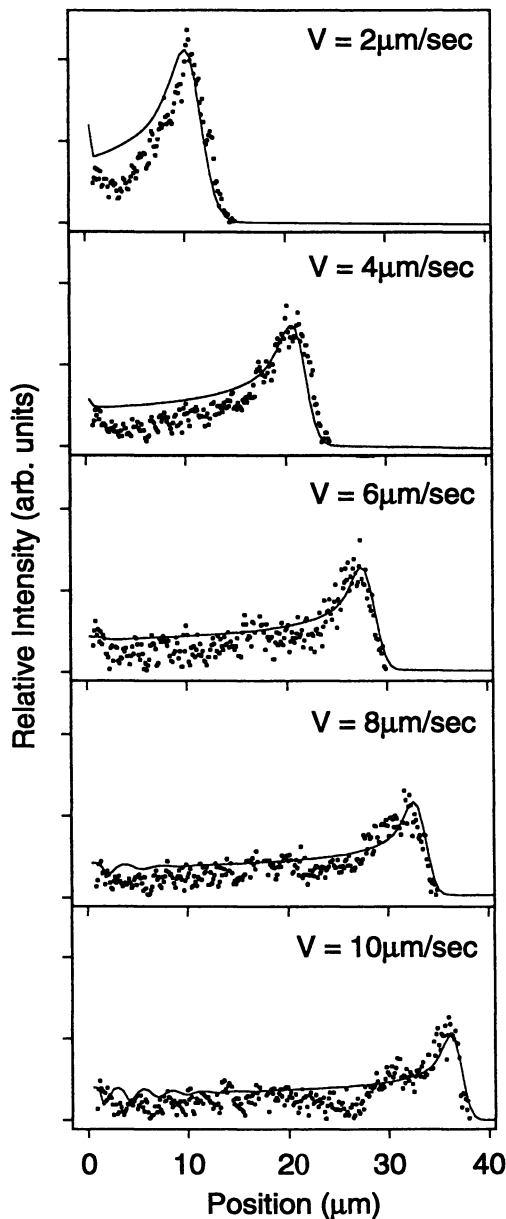


Figure 3. Distribution of DNA mass (symbols) as a function of position downstream of the tether point for DNA contour with length of 67 microns for the velocities indicated. The lines are predictions of the bead-spring model with 80 beads, using bead drag coefficients computed a priori, as discussed in the text. The bead-spring chain was simulated using Monte Carlo sampling (Reproduced with permission from reference 9. Copyright 1997 American Physical Society.)

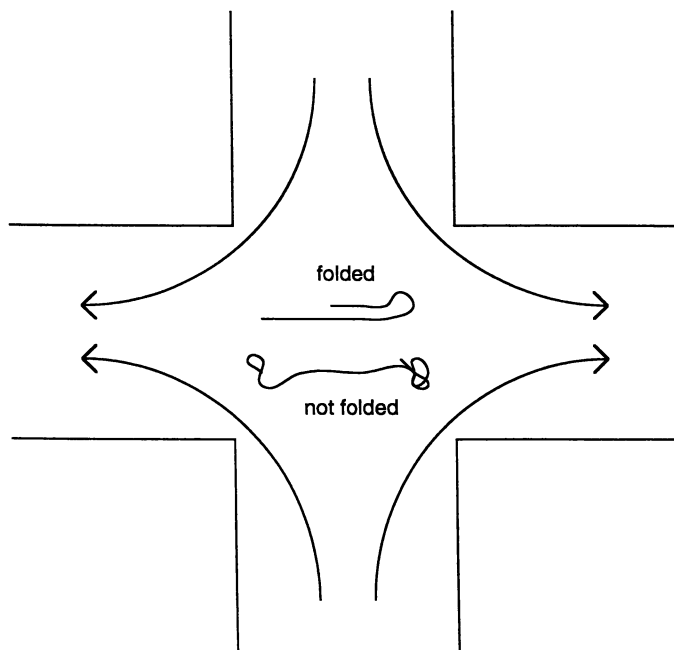


Figure 4. Illustration of crossed-slot device used to generate a planar extensional flow near the stagnation point at the center of the device in the experiments of Perkins et al. (6) and Smith and Chu (12). Molecular configurations during stretching were video recorded and categorized.

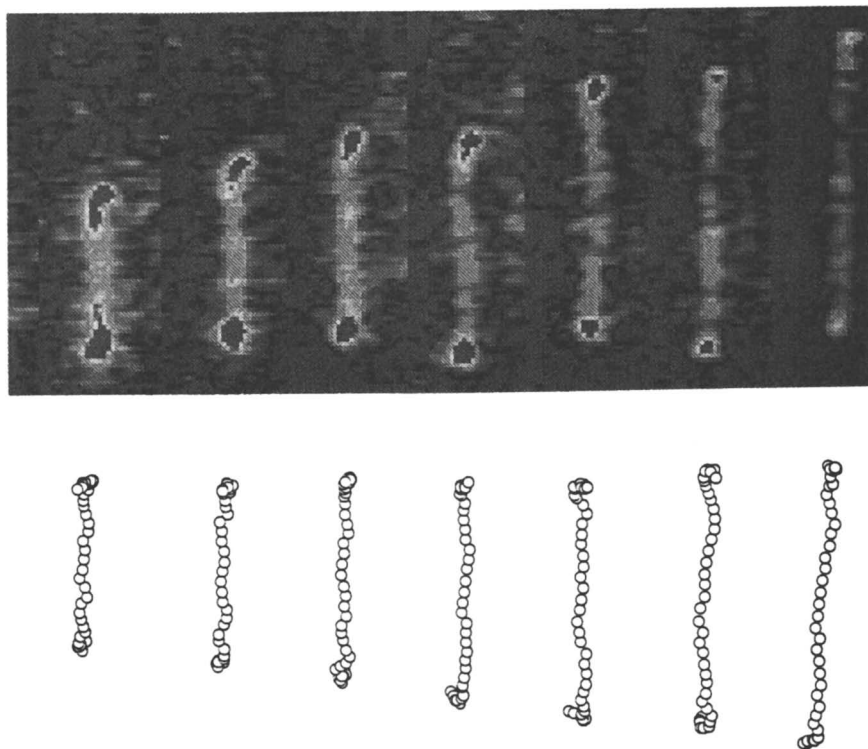


Figure 5. Comparison of a time sequence of experimental images of DNA in an extensional flow with the simulated images from bead-spring Brownian dynamics simulations. The outflow axis of the extensional flow is vertical. The spacing between images corresponds to around 0.1 Hencky strain units. In this case, the DNA unraveled via a “dumbbell” conformation. (Reproduced with permission from reference 7. Copyright 1999.)

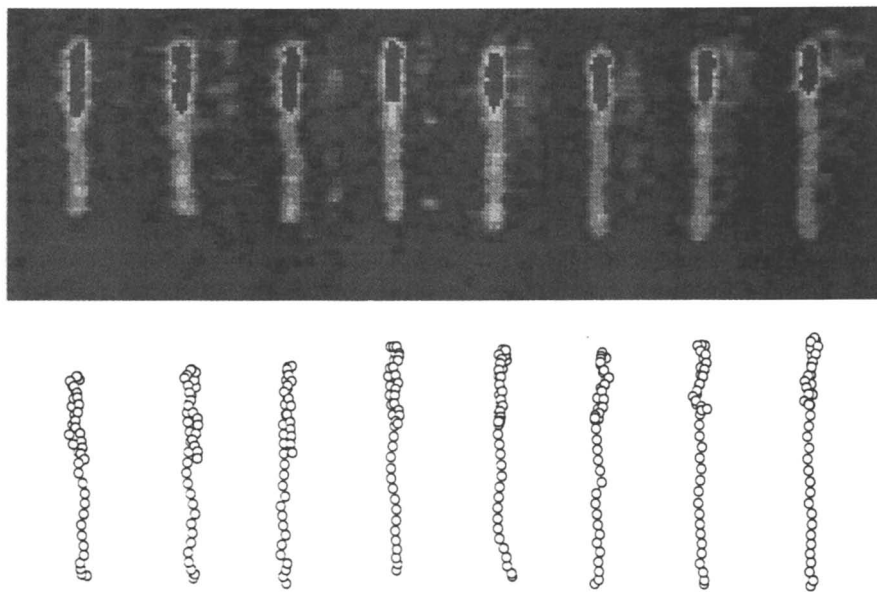


Figure 6. As in Figure 5, except in this case the unraveling occurs via a “folded” intermediate state. (Reproduced with permission from reference 7. Copyright 1999.)



and 6 show that configurations seen in the simulations closely match the experimental ones.

There is also a close quantitative agreement between experiment and simulations. Figure 7, for example, plots the percentages of chains that become folded during extensional flow as a function of the Deborah number  $De$  for a large ensemble (100 or more) of lambda phage DNA molecules, whose contour length (maximum stretch)  $L$  is 21 microns, and whose persistence length  $\lambda$  is around 0.066 microns. Comparisons are made at Deborah numbers  $De = \tau \dot{\epsilon}$  ranging from unity to 55. Here  $\tau$  is the time constant governing the relaxation of the molecular stretch in the absence of flow. It is obtained in both experiments and simulations by fitting the square of the stretch averaged over many molecules to an exponential decay function, as described in Perkins et al. (6) and Larson (7). Two criteria for a "folded" conformation are used in both experiment and simulation. In the "2/5 criterion," the location of the fold along the chain contour is such that at least 2/5 of the chain is taken up in the two halves of the fold (12). More precisely, if the distance from the fold to the nearest free end of the chain is defined as  $a$ , and the distance from the fold to the point on the chain farthest removed (upstream or downstream) from the fold is  $b$ , then the 2/5 criterion implies that  $2a/(a+b) > 2/5$ . An analogous definition applies for the 2/3 criterion. In both experiments and simulations, these criteria are considered satisfied if they are satisfied at any time after a Hencky strain of 2.3 has been applied to the chain to give it a chance to begin deforming. Note that the percentages of "folded" chains according to these criteria predicted by simulation are within experimental error of the measured values. The simulated conformations agree with the experimental ones in many other respects as well (7). For example, the predicted time-dependence of the molecular stretch (i.e., distance from the upstream-most to the downstream-most part of the molecule), averaged over an ensemble of chains, is in good agreement with the corresponding measured average stretch. Since the simulations in Figure 7 and elsewhere (7) were performed using the known properties of DNA molecules, the good agreement is without adjustable parameters.

**Analysis of Unraveling Mechanisms** The success of the simulations gives us confidence that they reflect the true behavior of polymer molecules under flow, and prompts us to use the simulation method to begin answering some long-standing basic questions about polymer deformation. One question that can immediately be answered is the source of the enormous heterogeneity observed in the stretching behavior of identical DNA molecules under identical flow conditions. Not only do molecules in extensional flow unravel via completely different mechanisms, such as folded, vs. dumbbell, etc., but the rates of unfolding vary enormously from one molecule to the next (6,12). Using the simulations, the influence of the molecular starting configuration can be explored systematically and separated from the role of Brownian fluctuations that occur during flow. This can be done by running identical starting configurations repeatedly, each time using a different sequence of pseudo-random numbers to generate Brownian fluctuations. By comparing differences in unraveling behavior observed under these conditions with differences produced by using different random starting configurations subjected to identical Brownian forces during flow, the relative influence of these two sources of heterogeneity can be

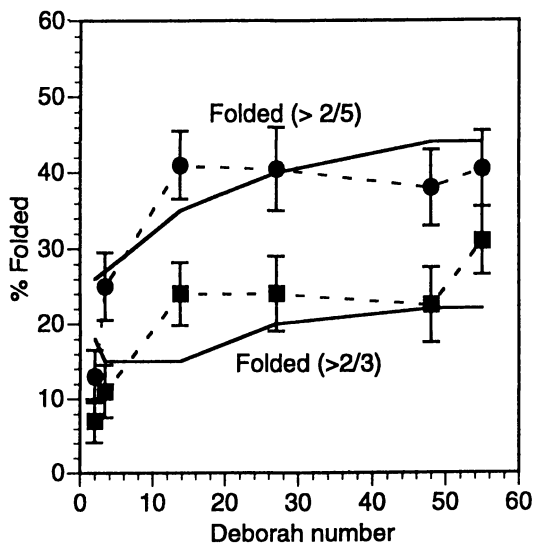


Figure 7. Percentage of folded chains during planar extensional flow as a function of Deborah number. The symbols are the DNA data of Smith and Chu (12). The dashed lines are a guide to the eye through the data. The solid lines are the predictions of Brownian dynamics simulations with  $N = 20$  beads; at each Deborah number an average is taken over 101 Brownian dynamics runs.

assessed (7, 12). The results of this investigation show that under strong stretching conditions, the starting configuration by and large determines the mode of unraveling selected by the molecule. Folded states, in particular, are generated by “hairpin” starting configurations in which both ends of the molecule are closer to each other than either end is to the center of the molecule. When the hairpin is oriented such that the two ends of the molecule move in one direction in the flow and the center moves the other direction, as illustrated in the hairpin configuration in Fig. 4, a folded conformation is produced.

### Literature Cited.

- (1.) Bird, R. B.; Curtiss, C.F.; Armstrong, R.C.; Hassager, O. *Dynamics of Polymer Liquids*, 2nd Ed., Wiley: New York, NY, 1987, Vol. 2.
- (2.) Menasveta, M.J.; Hoagland, D.A.; *Macromolecules* **1991**, *24*, pp. 3427-3433.
- (3.) James, D.F.; Sridhar, T.; *J. Rheol.* **1995**, *39* pp. 713-724.
- (4.) Keunings, R. *J. Non-Newt. Fluid Mech.* **1997**, *68*, pp.85-100.
- (5.) Perkins, T.; Smith, D., Larson, R.G., Chu, S. *Science* **1995**, *268* pp. 83-87.
- (6.) Perkins, T.T.; Smith, D.E.; Chu, S.; *Science* **1997** *268* pp.83-87.
- (7.) Larson, R.G. ; Hu, H., Smith, D.E., Chu, S. *J. Rheol.* **1998** submitted.
- (8.) Doyle P.S.; Shaqfeh, E.S.G. *J. Non-Newt. Fluid Mech.* **1998**, *76* pp.43-78.
- (9.) Larson, R.G.; Perkins, T.; Smith, D.E.; Chu, S. *Phys. Rev. E.* **1997**, *55* pp. 1794-1797.
- (10.) Marko, J.F.; Siggia, E.D., *Macromolecules* **1995**, *28* pp.8759-8770.
- (11.) Smith, D.E.; Perkins, T.T.; Chu, S. *Macromolecules* **1995**, *29* pp. 1372.
- (12.) Smith, D.E., Chu, S. *Science* **1998**, *281* pp.1335-1340.

# Unfolding Forces of Titin and Fibronectin Directly Measured by Single Molecule Force Spectroscopy

Matthias Rief and Hermann E. Gaub

Lehrstuhl für Angewandte Physik, Ludwig-Maximilians Universität  
München, Amalienstrasse 54, 80799 München, Germany

AFM based Single Molecule Force Spectroscopy provides a new tool for probing the mechanical properties of single molecules. In this chapter we show that the unfolding forces of single protein domains can be directly measured. Unfolding forces give new insight into protein stability which cannot be deduced from thermodynamic measurements. A comparison of the unfolding forces measured in Ig domains in the muscle protein titin to those measured in Fibronectin Type III domains reveals an extraordinarily high stability of titin domains.

With the advent of piconewton instrumentation mechanical experiments with single molecules have become possible. Force induced conformational transitions in DNA (1,2) as well as in polysaccharides (3,4) have been revealed, unbinding forces of receptor ligand complexes (5,6) and the unfolding forces of proteins (7-10) have been measured. These experiments have given insight into the forces stabilizing the complicated structure of biomolecules. From conventional calorimetric measurements only information about the energies involved in processes like receptor-ligand binding or protein folding can be obtained. Force, however, is a new structural parameter especially for proteins that are designed to exert or resist forces, like eg. muscle proteins. In this chapter we present a comparison of unfolding forces between immunoglobulin domains (Ig domains) of the muscle protein titin and type III domains of the protein fibronectin (Fn3 domains). The aim of this comparison is to elucidate whether titin which is constantly subject to stretching forces during muscle action exhibits a higher mechanical stability than the structurally similar cell adhesion protein fibronectin. From thermal denaturation experiments such a conclusion is not possible. In these studies both the Fn3 domains of fibronectin and the Ig domains of titin show similar melting temperatures (11,12).

## Titin.

The giant muscle protein titin (also known as connectin) (13) is a modular protein mainly consisting of more than 200 structurally similar Ig and Fn3 domains (see Fig. 1 a)). A single titin molecule spans the whole range between the M-line and the Z-disc ( $>1\mu\text{m}$ ) in striated muscle (14). In the A-band titin is firmly attached to the thick filaments whereas in the I-band part, titin acts as a reversible spring when the sarcomere is passively stretched (reviewed in (13)). The molecular mechanism of this

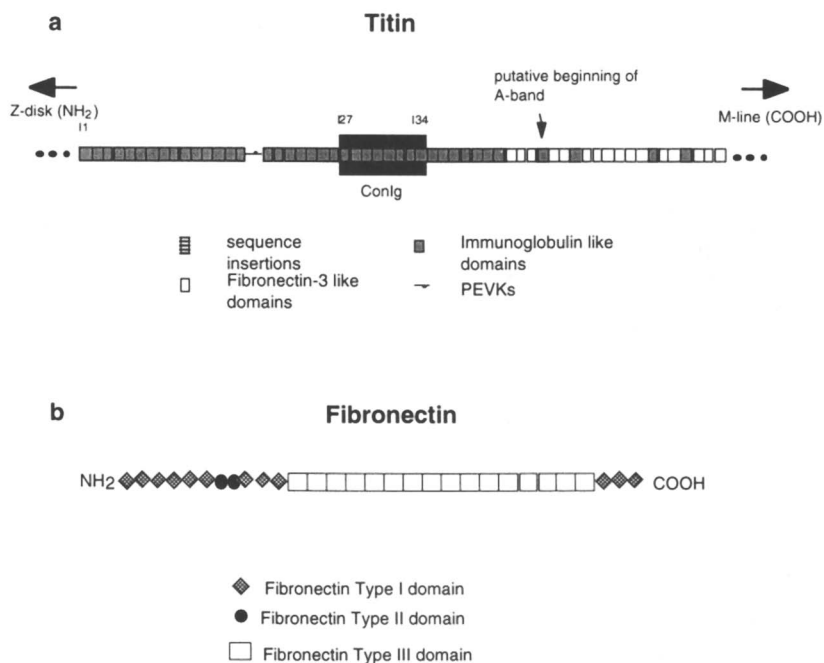


Figure 1. a) Schematics of the arrangement of domains in the I-band part of human cardiac titin. b) Arrangement of domains in bovine Fibronectin.

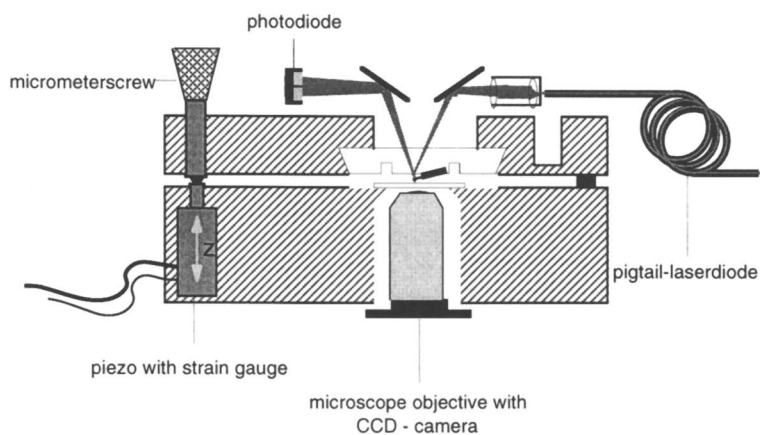


Figure 2. Schematics of a force spectrometer.

elasticity has been elucidated in several recent studies. Even the unfolding of Ig domains has been suggested as a source of elasticity (15). In this study measurements of the unfolding forces of a recombinant construct comprising 8 Ig domains (I27-I34) from the I band are shown (cf.(7) and see Fig. 1 a), black box). In order to improve anchoring to the gold surface two carboxyterminal cysteines were appended to the construct. Each of the 8 Ig domains comprises 89 aminoacids which fold into a compact  $\beta$ -barrel structure. The construct was generously provided by Dr. Mathias Gautel (EMBL Heidelberg, Germany).

### Fibronectin.

Fibronectins are high molecular weight glycoproteins found in many extracellular matrices and in blood plasma (16). They promote cell adhesion and affect cell morphology, migration and differentiation and cytoskeletal organization. Each fibronectin molecule is made up of a series of repeating units, the main part of which consists of 15-17 Fn3 repeats (see Fig. 1 b)). In contrast to Fibronectin type III domains, the type I and type II domains are multiply disulfide bonded. On average each of the Fn3 repeats comprises 93.5 aminoacids folding into a  $\beta$ -barrel structure. In this study bovine plasma fibronectin (Calbiochem, Germany) was used.

### Experimental.

**The Force Spectrometer.** An instrument capable of measuring the mechanical properties of single molecules must combine high force resolution ( $\sim 1$  pN) with high spatial resolution ( $\sim 1$  Å). The Atomic Force Microscope (AFM) fulfills these two prerequisites in an ideal way: commercially available AFM force sensors have low spring constants ( $\sim 10$  mN/m) and very sharp tips (apex curvature  $\sim 20$  nm) allowing to address single biological macromolecules.

A schematic of the custom built force spectrometer used in this study is given in Fig. 2. The spectrometer is based on AFM technology, however, it is optimized for z-resolution. x-y translation occurs manually. The instrument works like a clamp consisting of two massive aluminum bars that are forced together with a strong cantilever spring and opened with a stack piezo with built in strain gauge. Sample and cantilever are mounted on the opposing blocks of the clamp. The deflection sensing optics is mounted on the upper block and moved together with the cantilever. To avoid pointing instabilities creating force artefacts, the light is coupled into the optics via a monomode fiber. Tip and sample can be monitored through a microscope objective with a CCD camera. The cantilever holder is made of plexiglass. The liquid drop is kept between holder and sample by surface tension without an additional O-ring. Actuation and data acquisition is performed with 16 bit resolution. Typically 4096 datapoints are taken per scan at 140 kHz. The desired pulling rate was achieved by oversampling.

**Sample Preparation.** Proteins were allowed to adsorb onto a freshly evaporated gold surface from a 50  $\mu$ l drop of a 50  $\mu$ g/ml solution in PBS (phosphate buffered saline, pH 7.4, 150 mM NaCl). After the incubation process (10 minutes) the sample was rinsed with PBS. Force measurements were carried out in PBS as well.

**Force Measurements.** Spring constants were determined for each cantilever by measuring the amplitude of its thermal noise (17,18). All force curves for which pulling speeds are not explicitly given, were recorded at a piezo extension velocity of 0.5  $\mu$ m/s.

Fig. 2 shows a force spectroscopic experiment performed on a recombinant construct of a modular protein. For simplicity a construct comprising only 4 Ig domains is sketched. The construct is anchored to the gold surface via two carboxy terminal

cysteines. The AFM tip is carefully brought into contact with the protein coated surface and the proteins are picked up by the tip via adsorption. It has been shown in various studies that adsorption can lead to very high connecting forces ( $> 700$  pN) (3,4,7). The pickup can occur at any domain along the construct. Subsequently, the mechanical stability of the domains spanning the gap between tip and gold surface can be probed. Sequential unfolding of the domains results in a sawtooth pattern as is depicted in Fig. 3. In a previous study (7) it could be shown that the slope leading up to each peak is mainly determined by the elasticity of the already unfolded polypeptide. At the peak force the weakest of the folded domains in the chain unfolds in an all or none event adding an additional stretch of unravelled polypeptide to the chain. Hence, the absolute value of the peak force marks the unfolding force of a domain and the spacing to the following peak reflects the gain in length during a transition from the folded configuration to the fully unravelled polypeptide strand and can be correlated to the number of aminoacids folded in this domain.

**Worm Like Chain (WLC) Fits.** In order to model the force vs. extension characteristics of the unfolded polypeptide the interpolation formula introduced in (19) was used:

$$F(x) = \frac{k_B \cdot T}{p} \left( \frac{1}{4 \cdot (1 - x/L)^2} - \frac{1}{4} + \frac{x}{L} \right) \quad (1)$$

The persistence length  $p$  describes the polymer stiffness,  $k_B$  is Boltzmann's constant,  $L$  the contour length and  $T$  the temperature. Fig. 3 shows a release trace of a previously unfolded stretch of the TenFn construct. The two black lines are WLC force vs. extension curves with two different persistence lengths and contour lengths. The solid line uses a persistence length of  $p=0.4$  nm as in (7). This value describes the elasticity of the unfolded polypeptide strand best in a force range of 50-200 pN. Nevertheless, there are deviations, especially in the low force regime. This reflects the problems in describing by a single parameter  $p$  the complicated elasticity of a real polymer which is dominated by entropic as well as enthalpic contributions due to bond angle deformations. For the purpose of the current study where a model is needed to obtain values for changes in contour length and correlate these to the number of aminoacids in a domain the WLC model with a persistence length of 0.4 nm is satisfying.

### Unfolding Forces in Titin and Fibronectin.

The unfolding traces of the titin Ig construct exhibit a clear sawtooth pattern as can be seen from Fig. 4 a). Each of the sawteeth reflects the unfolding of an Ig domain. Peak forces rise from 190-250 pN. The forces are not identical because the individual domains in the construct are not identical either. In fact, measurements on the thermodynamic stability resulted in folding free energies that differed by up to a factor of three among the titin Ig domains (12). The last peak in the unfolding pattern which is distinctly higher than all the preceding peaks does not reflect the unfolding of a domain but just shows the detachment of the protein from the AFM tip. Using Eq. (1) the left hand slopes of the unfolding pattern could be fitted (black solid lines in Fig. 4). The change in contour length  $\Delta L=28.2$  nm from one peak to the next correlates well with the gain in length expected if the 89 aminoacids folded in a domain are completely elongated after the unfolding process. The maximum force exerted on a single titin molecule at physiological conditions has been estimated to be 20-30 pN. Consequently domain unfolding should not take place during normal muscle action. It has been shown, however, that the unfolding force of domains also depends on the rate at which the force is applied (7). Thus if a constant force of around 20 pN is applied to a titin molecule domain unfolding will occur after several minutes. At the typical time scale of

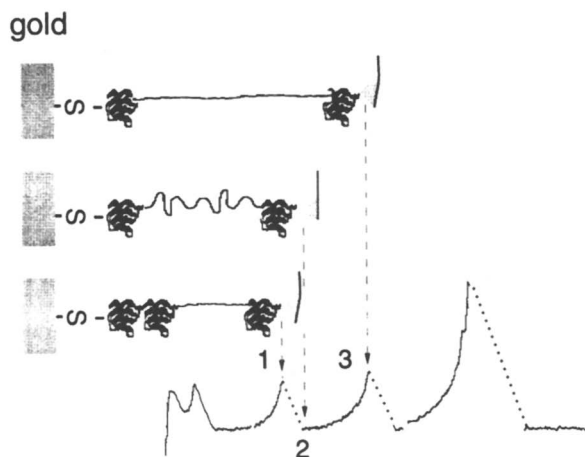


Figure 3. Schematics of a force spectroscopic experiment performed on a recombinant construct comprising 4 Ig domains in series.

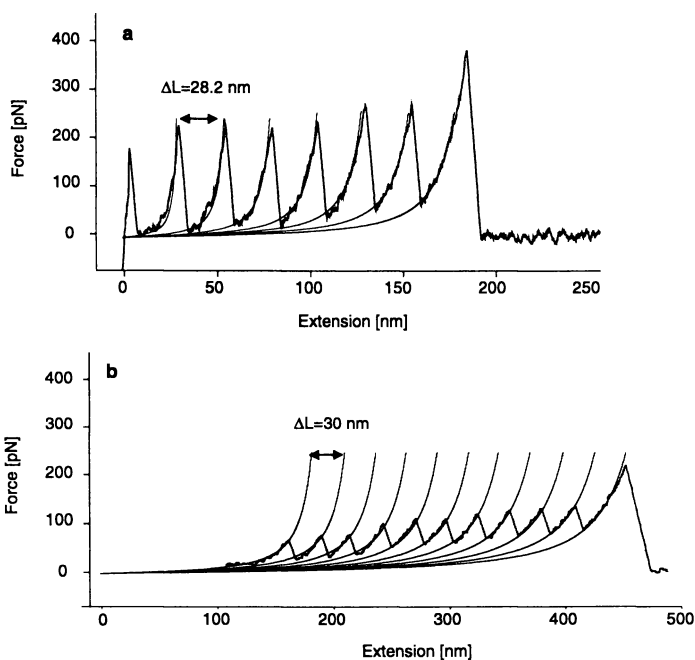


Figure 4. a) Force vs. extension curve reflecting the unfolding of 6 Ig domains of the muscle protein titin. The superimposed black lines are WLC fits according to Eq. (1). b) Force vs. extension curves taken on native Fibronectin.



muscle cycles (~seconds) which is comparable to the time of the pulling cycle in Fig. 4 unfolding is not to be expected.

The unfolding of 10 Fibronectin Fn3 domains is shown in Fig. 4 b). A similar sawtooth pattern as with the titin construct can be observed. Again the last high peak reflects the detachment of the molecule from the AFM tip. Nevertheless, there are distinct differences from the titin trace. The most obvious difference are the much lower unfolding forces. Once again due to the variation in stability of the individual Fn3 domains peak forces rising from 60-130 pN can be observed. This is 2 to 3 times lower than the forces in the titin construct. As already pointed out in the introductory paragraph this difference in stability cannot be deduced from thermal denaturation experiments (11,12).

Another, more subtle, difference shows up in the spacing of the peaks. The WLC-fits according to Eq. (1) yield an average peak spacing of  $\Delta L=30$  nm. This is due to the slightly higher number of aminoacids (93.5 on average) folded in the Fn3 domains. This demonstrates the high spatial resolution of our technique.

The difference in forces between titin Ig and Fibronectin Fn3 domains supports the conclusion that titin, which has to keep its structural integrity during muscle action, is especially designed to resist mechanical unfolding. For Fibronectin, although a cell adhesion protein, the physiologically relevant forces are much lower.

Single molecule force spectroscopy has proven to provide new information about protein stability that has not been accessible before. Generally, as more and more data on different kinds of protein domains will be available, a collection of characteristic molecular "fingerprints" with well defined unfolding forces and peak spacing similar to the traces in Fig. 4 a) and Fig. 4 b) may even allow for simple structural predictions of proteins.

## References

- (1) Smith, S. B.; Cui, Y.; Bustamante, C. *Science* **1996**, *271*, 795-798.
- (2) Cluzel, P.; Lebrun, A.; Heller, C.; Lavery, R.; Viovy, J.-L.; Chateny, D.; Caron, F. *Science* **1996**, *271*, 792-794.
- (3) Rief, M.; Oesterhelt, F.; Heymann, B.; Gaub, H. E. *Science* **1997**, *275*, 1295-1297.
- (4) Li, H.; Rief, M.; Oesterhelt, F.; Gaub, H. E. *Advanced Materials* **1998**, *10*, 316-319.
- (5) Florin, E.-L.; Moy, V. T.; Gaub, H. E. *Science* **1994**, *264*, 415-417.
- (6) Hinterdorfer, P.; Baumgartner, W.; Gruber, H. J.; Schilcher, K.; Schindler, H. *Proc. Natl. Acad. Sci. USA* **1996**, *93*, 3477-3481.
- (7) Rief, M.; M. Gautel; F. Oesterhelt; Fernandez, J. M.; Gaub, H. E. *Science* **1997**, *276*, 1109-1112.
- (8) Tskhovrebova, L.; Trinick, J.; Sleep, J. A.; Simmons, R. M. *Nature* **1997**, *387*, 308-312.
- (9) Kellermayer, M. S.; Smith, S. B.; Granzier, H. L.; Bustamante, C. *Science* **1997**, *276*, 1112-1116.
- (10) Oberhauser, A. F.; Marszalek, P. E.; Erickson, H. P.; Fernandez, J. M. *Nature* **1998**, *393*, 181-185.
- (11) Plaxco, K. W.; Spitzfaden, C.; Campbell, I. D.; Dobson, C. M. *Proc. Natl. Acad. Sci.* **1996**, *93*, 10703-10706.
- (12) Politou, A. S.; Thomas, D. J.; Pastore, A. *Biophys. J.* **1995**, *69*, 2601-2610.
- (13) Maruyama, K. *FASEB J.* **1997**, *11*, 341-345.
- (14) Fürst, D. O.; Osborn, M.; Nave, R.; Weber, K. *J. Cell Biol.* **1988**, *106*, 1563-1572.
- (15) Erickson, H. P. *PNAS* **1994**, *91*, 10114-10118.

- (16) Hynes, R. O. *Book Fibronectins*; Springer-Verlag: New York, State, 1990.
- (17) Butt, H.-J.; Jaschke, M. *Nanotechnology* **1995**, *6*, 1-7.
- (18) Florin, E. L.; Rief, M.; Lehmann, H.; Ludwig, M.; Dornmair, C.; Moy, V. T.; Gaub, H. E. *Biosensors and Bioelectronics* **1995**, *10*, 895 - 901.
- (19) Bustamante, C.; Marko, J. F.; Siggia, E. D.; Smith, S. *Science* **1994**, *265*, 1599-1600.

## Study of the Fusion Process between Solid- and Soft-Supported Phospholipid Bilayers with the Surface Forces Apparatus

Markus Seitz, Chad K. Park, Joyce Y. Wong<sup>1</sup>, and Jacob N. Israelachvili

Department of Chemical Engineering, University of California,  
Santa Barbara, CA 93106

### Introduction.

Lipid vesicles and planar bilayers have been used extensively to model living cells in the biophysical study of molecular mechanisms and fundamental interaction forces. In this context, the investigation of adhesion and fusion of vesicles with each other as well as with planar biomembranes (1,2) is of particular interest. For structural investigations, biomembranes generally have to be 'held in place', such as by transfer onto solid substrates (3-5). Various preparation techniques have been suggested for mono- and multilayer systems, such as the Langmuir-Blodgett technique (4) as well as self assembly processes on planar surfaces (3,6,7) or on small glass beads (8).

Several methods have been developed that allow the measurement of interaction profiles with a resolution on the sub-nanometer scale (9). One of them is the osmotic pressure (or osmotic stress) technique (10), by which the first quantitative data for the short-range repulsive interaction of lipid bilayers in aqueous solution could be obtained (11,12). However, it is restricted to the repulsive contributions of the interaction profile. Another important method by which mechanical properties as well as the adhesion of vesicles in contact can be investigated is the "pipette aspiration technique" (13-15). In recent years, reflection microscopy techniques have been developed to monitor the distance between bilayer vesicles and modified surfaces which could also be used to investigate interaction forces between bilayers and different types of substrates (16-18).

The complete force-distance profile including adhesive interactions can be directly measured with the surface forces apparatus (SFA, 19,20), by which most fundamental interactions between surfaces in aqueous as well as non-aqueous solvents have been identified and quantified such as van der Waals, electrostatic as well as repulsive hydration forces or attractive hydrophobic interactions (19,21-26). In a unique way, the SFA also allows the observation of the membrane fusion process directly (in 'real time') with a resolution on the molecular level, at least in one dimension. In this contribution we will give a brief summary of earlier fundamental results of bilayer fusion studies employing the SFA technique as well as a brief overview of the most recent developments in this area.

<sup>1</sup>Current address: Department of Biomedical Engineering, Boston University, Boston, MA 02215.

## Study of Normal Interbilayer Forces with the Surface Forces Apparatus.

The SFA used in the surface forces measurements has been described extensively (23,27,28). Briefly, the distance of two cylindrically curved, molecularly smooth mica surfaces, of radii  $R_1$  and  $R_2$ , is visualized using the optical interference technique described previously (26,29). Fringes of equal chromatic order (FECO) are produced when white light is passed through the apposing sample surfaces, and reflect the shape of the surface contact region. Thus, the distance of the two mica surfaces from a separation of several micrometers (Figure 1.A) to close contact (Figure 1.B) of the surfaces can be followed to within 1-2 Å, while at the same time the topography of the contact region can be imaged. One of the surfaces is mounted on a spring with spring constant  $K$ . From the measured deflection  $\Delta D$  of the spring, the force  $F$  between the surfaces can be determined. The corresponding energy per unit area  $E$  between two flat surfaces is simply related to the force between the curved surfaces by the so-called Derjaguin approximation,  $E = F/2\pi R$ , where  $R$  is the geometric mean radius  $R = (R_1 \cdot R_2)^{1/2}$  (21). For repulsive forces, the surfaces are simply pushed together and the spring deflection  $\Delta D$  is measured optically, from which the force is obtained as  $F = K \cdot \Delta D$ . In the case of attractive forces, the system becomes unstable if the gradient of the force  $\partial F/\partial D$  exceeds the spring constant  $K$ , and the surfaces jump to the next stable point of the interaction profile (30). Under very large compressive forces the two initially curved surfaces flatten elastically as the glue supporting the mica sheets becomes compressed. This deformation can be directly observed from the shapes of the fringes which represents a cross section of the contact zone. When one observes flattening, the Derjaguin approximation no longer applies. Instead of the energy per surface area, one can now determine the mean pressure from  $P_{\text{mean}} = F/A$ . However, the maximum pressure occurs at the center of the contact area for repulsive interactions. If the surfaces deform elastically and do not mutually adhere, the "Hertz theory" (31,32) predicts that  $P = 0$  at the edges and that it rises to a maximum at the center, where  $P_{\text{max}} = 1.5 P_{\text{mean}}$ . The elastic deformation of adhering surfaces is more complicated, and the resulting stress in the system is generally highest at the edges of the contact region (32,33).

When two lipid bilayer membranes have come into close, flattened contact, there is still one layer of hydration water separating the lipid head groups (Figure 1.C). As a certain energy barrier is overcome (e.g. by applying a certain pressure), either the center or the outer edge, i.e. the regions of the highest effective pressure, of the ellipsoidal contact spot can "break" through, which can be followed by the FECO technique. These regions then slowly spread out towards the side or towards the center of the contact until, eventually, the whole interference pattern is shifted by the same amount to smaller wavelengths, i.e. smaller distances (26). On a molecular level, this relates to the hydration water layer as well as the two outer membrane leaflets being squeezed out (Figure 1.D).

Thus, the total change in the mica-mica separation distance during the break-through corresponds to the removal of one full bilayer including one layer of hydration water after which one bilayer membrane still remains in the contact region (22,24,26). These observations have been related to a so-called "hemifusion" (Figure 1.E) which is assumed to be an intermediate step in the process of full vesicle fusion (Figure 1.F, 1,34).

### Forces and Fusion between Solid-Supported Phospholipid Bilayers.

To date, almost all SFA measurements on interacting lipid bilayer membranes have made use of solid (muscovite) mica substrates. This material provides an atomically flat surface so that the upper (distal) layer of the substrate-supported membrane can exist in an almost undisturbed fluid state, and the adhesion and fusion of model membranes could be followed directly with these systems (22-24). In general, it was found that adhesion between two bilayers can be progressively increased by up to

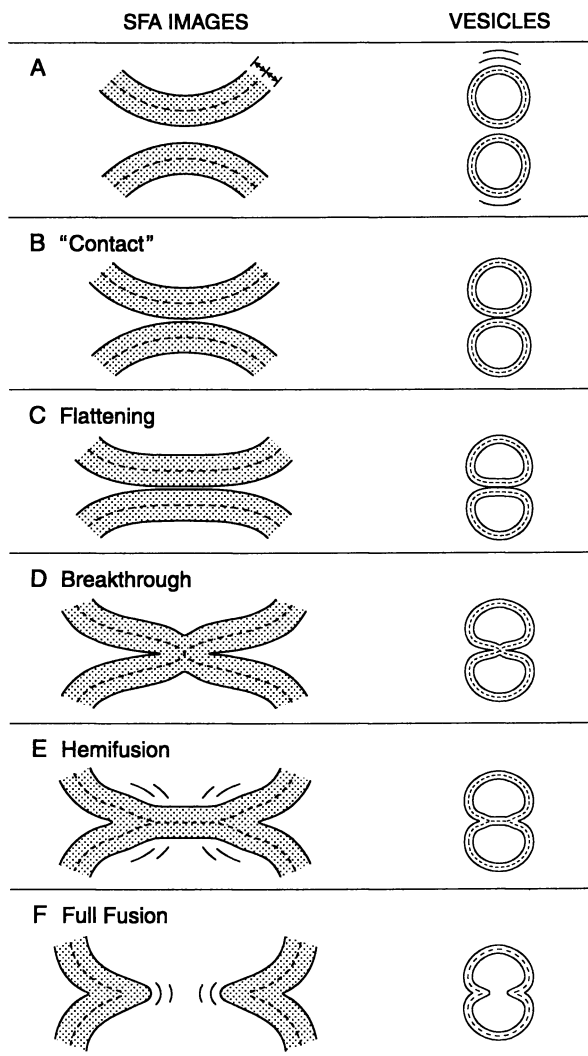


Figure 1. Schematic representation of hemifusion and fusion between bilayer membranes: Two mica-supported membranes in the SFA (left) represent the contact region during approach, contact and fusion of two free lipid vesicles (right).

two orders of magnitude if they are stressed to expose more hydrophobic groups. The most important force leading to direct (hemi-)fusion is the hydrophobic attraction acting between the (exposed) hydrophobic interiors of the solid-supported bilayers (in most cases, the inner layer which is in contact with the mica support consists of a crystalline dipalmitoylphosphatidylethanolamine monolayer, DPPE). However, the occurrence of fusion is not simply related to the strength of the attractive interbilayer forces but also to the internal bilayer stresses (intra-bilayer forces). Fusion can be triggered spontaneously between two repelling bilayers when they are still at a finite distance from each other without their having to first overcome the short-range repulsive forces, e.g. the steric hydration barrier. Localized molecular rearrangements allow this to happen by a process of locally bypassing these forces via a simple breakthrough mechanism. Hereby, fusion starts locally at the weakest point or most highly stressed point of two apposing bilayers (26). With 'fully developed' bilayers no fusion is observed up to applied pressures of 150 atm. Fusion takes place between 'depleted bilayers', that is, when the solution is diluted below the CMC. Depletion also changes the force law between bilayers (26,34). In addition, hemifusion could be in systems with packing defects, e.g. after cooling below the fluid-gel phase transition temperature, or for natural lipid mixtures such as "eggPC" (22). Nevertheless, high pressures of up to  $P = 50 - 100$  atm were needed to achieve hemifusion (22,26).

The second stage of the process depicted in Figure 1.F, from hemifusion to full (or complete) fusion, involves the total removal of the central bilayer. This would be characterized in SFA measurements by a second critical breakthrough step. On mica-supported systems it could be only observed so far between hydrophilic monolayers in humid air or in water-wet organic solvents, when the monolayer binding to the mica surfaces becomes weak (34,35).

The hydrophobic interaction between the inner layers of apposing lipid membranes could also be established as the ultimate driving force during the calcium-induced bilayer fusion of mixed bilayers systems. Dimyristoyl-phosphatidylcholine/dimyristoyl-phosphatidylglycerol (DMPC/DMPG) or dilauroyl-phosphatidylcholine/dilauroyl-phosphatidylglycerol (DLPC/DLPG), i.e. mixtures of zwitterionic PC and anionic PG lipids were investigated (25). It was found that the critical role of calcium is in the induction of phase-separated domains of different lateral stresses followed by 'contraction' of the calcium/PG-rich domains and 'expansion' of the PC-rich domains, with subsequent attraction and fusion of apposed layers. This model was confirmed by the finding that pure PG (or PC) bilayers do not fuse in the presence of calcium as the entire lipid layers become uniformly stressed upon calcium binding and no additional area is exposed to the aqueous phase.

In continuation of this earlier work, recently, the hemifusion of zwitterionic bilayers on solid mica substrates was further studied (Park, C. K.; Israelachvili, J. N., to be published). The following parameters were found to have an effect on the fusion event: deposition density, the lipid shape, and the phase state of the lipids within the supported membrane.

When lipids are deposited at sufficiently low densities, there is not enough coverage of the innermost DPPE layer. The exposure of these hydrophobic regions results in a larger adhesion than is accountable by van der Waals forces alone and frequently leads to hemifusion. Another way of reducing coverage can be accomplished with conically-shaped lipids. These are molecules where the headgroup area is smaller than that of the side groups. When such a lipid, Dilinoleoyl-phosphatidylethanolamine, DLinPE, was deposited at reasonable coverages, an increased adhesion and propensity for fusion was observed. This may be due to the outermost layers' inefficient packing which exposes its own tail groups to the aqueous environment. Finally, by depositing near a liquid-expanded (LE) to liquid-condensed (LC) phase transition we again see a large increase adhesion and frequent fusion events.

In this case, it is believed that the solid-like nature of the substrate induces the outer lipids to pack in a more solid fashion. In doing so, the LE-LC phase boundaries may provide defects which facilitate hemifusion.

To determine the effect of lateral phase separation on the adhesion and fusion of DLPE bilayers was investigated (Park, C. K.; Israelachvili, J. N., to be published). Deposition densities corresponding to fluid phases and solid phases (42 and 55 Å<sup>2</sup> per molecule respectively) gave rise to stable systems. Forces measured here were comparable to that expected from DLVO theory. Further, the FECO fringes did not show any deformations indicating hemifusion. If the lipid was deposited at very low densities, the resulting hemifusion was attributed to insufficient coverage of the proximal DPPE layer. This effect was slightly larger for the inverted phase forming lipid DLinPE. When the deposition of the DLPE was done at temperatures near the fluidlike-solidlike phase transition, the layers were highly susceptible to hemifusion. Interestingly, fluorescence microscopy on this system showed the presence of domains. It is likely that the domains observed are providing defects or exposed edges which lowers the hemifusion energetic barrier. Essentially these effects are methods of (slightly) exposing the proximal DPPE layer to the bulk water. The resulting hemifusion is thought to be driven by strong attraction these hydrophobic groups have for each other.

### **Soft-supported bilayers for the investigation of normal interaction forces.**

In recent years, the SFA was also used for the investigation of the interactions in more complex biological assemblies, such as the ligand-receptor system biotin-streptavidin (36-39). Whereas in most of the cases discussed so far, the fluidity of the outer lipid layer was sufficient for the study of the interaction between simple as well as functionalized lipid membranes, the direct contact between the proximal lipid monolayer with the substrate poses a serious constraint in many desired systems.

The restriction of membrane mobility by the supporting mica substrate provides a significant difference compared to studies on bilayer vesicles or liquid-crystalline multilamellar lipid structures. Bilayer systems which are allowed to fluctuate freely around an average distance exhibit repulsive undulation forces. This effect could not be studied with the SFA technique so far. Although in general there is good agreement in the measured forces between lecithin bilayers using the SFA and the osmotic pressure technique, the interaction forces measured by the latter are usually of longer range (40,41). With respect to probing the fusion process of supported biomembranes, the major drawback resulting from the direct proximity of the solid substrate is the change in the viscoelastic properties of the overall bilayer which are important in governing the initial breakthrough. Also, full fusion is hindered by the substrate which does not allow the study of all aspects of the fusion process. For the investigation of such dynamic processes involving membrane deformations and rearrangements of lipids or membrane-incorporated proteins within lipid bilayers, the realization of substrate-supported, but fluid model membranes is desired. One promising approach is the use of a water-swallowable cationic polyelectrolyte, branched polyethyleneimine (PEI), which electrostatically binds onto the negatively charged surface of the mica substrate (Figure 2.A). This polymer gel can act as a deformable and mobile substrate and can build up an aqueous compartment between the membrane and the mica substrate. Recently, such "soft-supported membranes" have been used for the investigation of biomembrane structure and function (42). It is feasible that alternating polyelectrolyte multilayers can be formed stepwise by the use of a polyanion "counterlayer" which would allow control of the thickness of the polymeric cushion between the membrane and the solid support (43-45). Apart from their use in the study of fundamental principles governing biomembrane interactions, technical and medical interest arises from their potential use in biosensor systems (5,42,46).

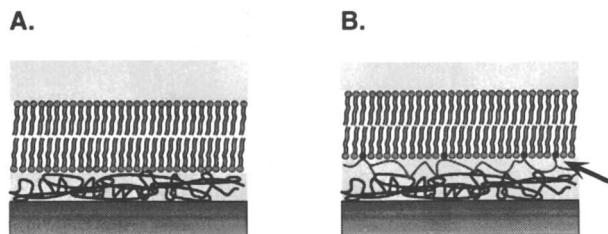


Figure 2. Polymer-supported bilayers; A. physisorbed lipid membrane on supporting water swollen polyelectrolyte; B. partial covalent attachment of lower (proximal) lipid monolayer to the supporting polymer as indicated by the arrow.



The chemical nature of the supporting polyethyleneimine layer also allows for the binding of the lipid headgroups onto the gel support by electrostatic interactions or via the formation of chemical bonds between amino reactive membrane inserting lipids ("tethered supported membranes", Figure 2.B). The covalent fixation can provide an additional stabilization factor which aids in slowing down the membrane desorption from the polymeric substrate. In recent years, this approach has been discussed frequently in the literature as a concept of modelling the effect of the cytoskeleton in living cells (42,47-53).

### Formation of soft-supported DMPC bilayers on mica.

**Physisorbed Bilayers.** The most straightforward method to build up a soft-supported, physisorbed DMPC bilayer membrane on polyethyleneimine would be the unrolling of small unilamellar lipid vesicles onto the polyelectrolyte layer, which was shown to result in polymer-supported bilayers for negatively charged lipid vesicles on negatively charged polymer surfaces in the presence of  $\text{Ca}^{2+}$  ions (45). However, SFA measurements on zwitterionic vesicles adsorbed onto cationic polyethyleneimine indicated a rather undefined multilayer structure which was confirmed in neutron scattering investigations on quartz supports (Majewski, J.; et al. *Biophys. J.*, in press).

A stepwise preparation was thus chosen for this particular system, in which the inner, polymer-supported DMPC monolayer was transferred onto the mica substrate by the Langmuir-Blodgett method from a subphase containing the polyelectrolyte. As reported in the literature for the formation of other bilayer systems supported on solid substrates (6,7,48,54), the second layer was created by spreading unilamellar vesicles onto these preformed polymer-supported monolayers (Wong, J. Y.; et al. *Biophys. J.*, submitted). This approach provides two advantages: first, the sample preparation can easily be done within the SFA on preinstalled surfaces. Second, this method would allow the incorporation of membrane proteins directly from proteoliposomes. Structural investigations by neutron scattering confirmed the successful formation of the desired structures (the detailed results will be published elsewhere). The preservation of lateral lipid mobility within the fluid membrane was studied by fluorescence microscopy in similar fashion as it will be discussed below in the context of partially attached membranes.

**Covalently attached membranes.** Most recently, reactive membrane-inserting amphiphiles have been used for the formation of tethered lipid bilayers on glass substrates (55). Adopting this approach for the purpose of studying membrane interactions employing the SFA technique, a new isothiocyanate-functionalized lipid DMPC-NCS was synthesized from dimyristoylphosphatidylethanolamine (DMPE) and carbon disulfide. Its reactive isothiocyanate head group can selectively react with amino groups to form a N-N'-disubstituted thiourea structure in the presence of water which allows the partial attachment of an interfacial reactive lipid monolayer to the amino functions of branched polyethyleneimine (PEI) dissolved in the water subphase (compare Figure 3). The details of the lipid synthesis, as well as the monolayer characterization at the air-water interface have been described recently (Seitz, M.; et al. *Thin Solid Films*, in press).

The covalent fixation of the lipid monolayer onto the polymeric substrate was shown by IR measurements. Also, their increased stability against water could be observed in studies of the contact angle of a water droplet in contact with the monolayer surface. The results are summarized in Table I.

It can be seen that the observed contact angles of water droplets on pure DMPC monolayers as well as on mixed monolayers of DMPC containing approximately 10 mol% DMPE-NCS on polyethyleneimine were rather low. The advancing angle for the mixture was  $\Theta_A = 43^\circ$  and the receding angle was  $\Theta_R < 15^\circ$ . Moreover, the

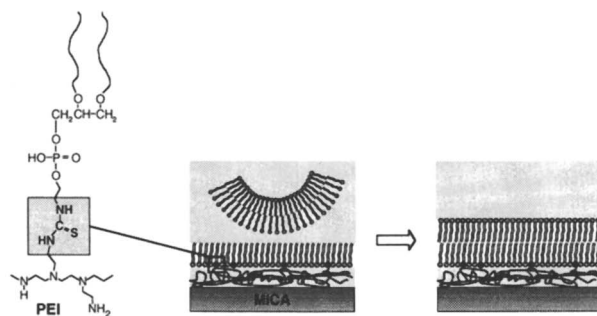


Figure 3. Formation of tethered DMPC monolayer and bilayers partially attached to supporting polyethylenimine (PEI). Bilayers are formed by adsorption of small unilamellar vesicles on the monolayers.

static contact angle of a water drop left on the monolayer decreased with time in both cases, starting at a value of approximately  $20^\circ$ , until within a few minutes the water spread on the surface and wetted the support such that the contact angle was no longer measurable ( $\Theta \approx 0$ ). Obviously, as long as the monolayers consist mainly of physisorbed DMPC they are not stable against water and are being “washed off” the substrate or rearrange, presumably into bilayer patches. In contrast, the monolayers of pure reactive lipid on PEI/mica was much more hydrophobic and stable with their quality depending on the transfer conditions: the measured dynamic values on a monolayer transferred at room temperature from the liquid-expanded (“fluid”) state were  $\Theta_A = 79^\circ$  and  $\Theta_R = 16^\circ$ . Despite this rather high hysteresis, the static contact angle of initially  $64^\circ$  dropped to only  $47^\circ$  after one hour. While these observations point to an increased stability of the PEI-supported monolayers at higher covalent binding densities of the lipid headgroups, the high hysteresis observed between the advancing and receding angles points to a rather heterogeneous surface structure. The quality of the layers can be improved when the films are transferred in a more condensed state in which the monolayer exists at lower temperature (note that isotherm measurements on the reactive lipid DMPE-NCS on pure water as well as on polyethyleneimine subphase have been described recently, Seitz, M.; et al. *Thin Solid Films*, in press).

**Table I: Contact angle measurements on PEI-supported monolayers**

<i>Lipids</i>	<i>Transfer Conditions</i>	$\Theta_A$	$\Theta_R$	$\Theta_{stat.}$	<i>Quality and Stability</i>
DMPC	21°C, 30 mN/m, “fluid” phase	31°	<5°	17° (-> 0°)	not stable against water
DMPE-NCS/ DMPC = 10:1	21°C, 35 mN/m, “fluid” phase	43°	<15°	20° (-> 0°)	not stable against water
DMPE-NCS	21°C, 35 mN/m, “fluid” phase	79°	16°	64° (-> 47°)	more hydrophobic and more stable under water, heterogeneous surface
	13°C, 40 mN/m, “solid” phase	92°	52°	73° (stable)	further improvement of monolayer quality

However, at the same time as the stability of polymer-supported monolayers increases when a higher amount of the lipid head groups is attached to the polymer substrate, the lateral lipid mobility within the monolayers is slowed down significantly. Fluctuations along the surface normal should still be allowed in such tethered systems, and although this provides interesting perspectives with respect to studying the coupling of viscoelastic properties of the underlying polymer layer with the bound lipid layer, a complete fixation of the bilayer is not desired for SFA studies of membrane fusion processes. Thus, in the following a tethered supported membrane with only partial fixation of the proximal lipid layer will be discussed.

In a similar way as physisorbed membranes, tethered supported bilayers can be formed, *e.g.*, by adsorption of DMPC vesicles onto polymer-supported mixed monolayers of DMPC and the synthetic reactive lipid DMPE-NCS (Figure 3). This process was followed by fluorescence microscopy. Figure 4.A shows a mixed lipid monolayer of DMPC containing 10 mol% DMPE-NCS and 0.5 mol% TR-DHPE (Texas Red-labelled Dihexadecanoylphosphatidylethanolamine) on polyethyleneimine/mica in air which was prepared by LB transfer as described above.

Note that two octagonal spots of the homogeneous fluorescing monolayer were bleached with the fluorescent light beam of the microscope, neither of which changed its shape during an hour after exposure of the sample proving that the fluorescent-labelled lipid is rather immobile within the polymer-supported monolayer in air.

After the addition of a DMPC vesicle solution at 28 °C, the fluorescent-dye stayed on the substrate and the fluorescence of the sample remained homogenous. Moreover, the fluorescence of the sample recovered with time as TR-DHPE, now laterally mobile, diffused into a previously bleached spot. Figures 4.B and 4.C show the micrographs taken of the same spot 10 seconds and 10 minutes, respectively, after the initial bleaching with the fluorescent beam. Note that the radius of the darker region decreased with time as a result of the diffusion of the fluorescent lipid. After one hour, the dark spot had almost completely disappeared. Note that these observations are only qualitatively comparable with FRAP experiments (fluorescence recovery after photobleaching, 56,57). However, the observed time-dependent fluorescence recovery agrees well with an increased fluidity of the soft-supported bilayers in aqueous solution as compared to the soft-supported monolayer system in air. As expected, literature reported FRAP measurements for similar tethered bilayer systems show a lowered diffusion constant  $D = 1.5 \mu\text{m}^2\cdot\text{s}^{-1}$  of the dye-labelled lipid, while within a polymer-supported DMPC bilayer  $D = 3 \mu\text{m}^2\cdot\text{s}^{-1}$  (49).

An additional observation that is in agreement with the aforementioned contact angle measurements should be mentioned. After the addition of a pure water droplet to a PEI-supported monolayer of the lipid mixture fluorescence recovery is observed around the wetted region, but where the monolayer is still exposed to air. This points to a swelling of the underlying polymer gel which induces lateral lipid mobility in the supported monolayer. However, once the droplet covers the monolayer a rearrangement in the monolayer takes place resulting in domain formation on the support as well as the detection of a strong fluorescence signal from the water surface. Considering the homogeneous fluorescence in the monolayer systems exposed to a DMPC vesicle solution directly, it appears that a second lipid layer is adsorbed on top of the transferred monolayer on initial contact with the solution which yields a stable, tethered supported bilayer as depicted in Figure 2.B.

It appears that the successful formation of bilayer membranes on polymer supports by the described vesicle adsorption technique depends both on the quality as well as on the lipid mobility in the preformed polymer-supported monolayers, while the long-term stability is improved by the attachment to the membrane support. Whereas a polymer-supported monolayer can be created from a pure layer of reactive lipid on polyethyleneimine which is perfectly stable in water, the bilayer formation by vesicle adsorption is highly critical for these fully attached systems. A high extent of covalent binding between lipid headgroups and polymer support does no longer allow for lateral mobility within the proximal lipid layer which in most cases would be crucial for the system in order to reorganize into a perfectly packed bilayer during the vesicle adsorption process.

### Normal interaction forces of soft-supported DMPC bilayers.

The phase transition temperature between gel and liquid crystalline phase of  $T_C = 24$  °C for DMPC bilayers allows to study the effect of membrane fluidity in SFA measurements close to room temperature. The temperature dependence of the inter-

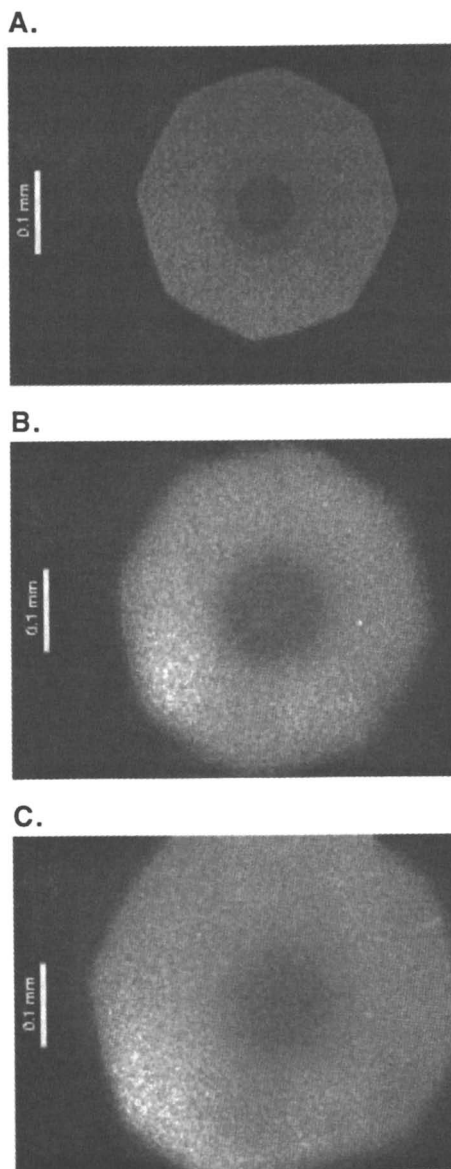


Figure 4. Fluorescence micrographs of a mixed monolayer (DMPC/DMPENCS, 9.6:1 containing 0.5 mol% TR-DHPE on PEI/mica; A. in air; B. mono-layer in DMPC vesicle solution, 10 seconds after bleaching; C. same spot, 10 minutes after bleaching.

action profile of two PEI-supported, pure DMPC membranes is shown in Figure 5. While the details of these experiments have been discussed in a recent publication (Wong, J. Y.; et al. *Biophys. J.*, submitted), a qualitative summary of the force-distance profile at short distances shown in Figure 5 and its implications with respect to the fusion process of biological membranes will be given here.

Above the chain melting temperature of the lipid membrane, at 28 °C, a hemifusion of the apposing bilayers can be observed discontinuity in the force profile from 10.5 to 5.5 nm at  $F/R \approx 20$  mN/m corresponding to pressures ( $P_{\text{mean}} = 7\text{--}10$  atm) which are considerably smaller than for bilayers directly supported on mica (see above). The fluidity of the polymer supported bilayers is also indicated by their recovery after a previous hemifusion event. It was seen that after appropriate healing times ( $< 1\text{--}2$  hrs) an essentially identical force profile was obtained in subsequent measurements on the same contact spot. Also, a complete fusion of two lipid membranes in the liquid crystalline state can now be observed with the SFA as a second discontinuous decrease of the mica-mica separation by  $\Delta D \approx 3.5$  nm at higher pressures (Figure 5). In contrast, this could not be observed with the SFA for lipid bilayers deposited directly onto mica where a full removal of both lipid layers would result in a direct mica-mica contact (22,24,26). Once fully fused and completely removed from the polymer substrate, even the fluid PEI-supported DMPC bilayers do not recover within the time of the experiment (16 hours after fusion). At lower temperatures, when the DMPC bilayers are in the gel state, very high pressures are needed for hemifusion. In measurements at 21 °C, hemifusion was observed at very high  $F/R$  values corresponding to pressures above  $P_{\text{mean}} \approx 50$  atm (Figure 5). In addition, the healing process after hemifusion was very slow, and a second step corresponding to a full fusion of the two apposing membranes could not be achieved under pressures up to 150 atm (within observation times of up to two hours).

The temperature dependence of the systems dimensions can be extracted from the interaction profile between PEI-supported DMPC bilayers at short distances (Figure 5). They correlate well with reported X-ray diffraction data on multilamellar DMPC aggregates in an excess of water; e.g. the observed shift of the steric barrier ("hard wall") by 1.4 nm below the phase transition temperature can be explained by these literature reported numbers (20 °C,  $P_{\beta}$ -phase, bilayer thickness:  $d_{\beta} = 4.45$  nm, thickness of hydration water layer:  $d_w = 2.04$  nm; 37 °C,  $L_{\alpha}$ -phase,  $d_{\beta} = 3.55$  nm,  $d_w = 2.45$  nm (58); thickness of hard wall,  $D_{\text{hw}} = 2d_{\beta} + d_w$ ).

### Conclusions and implications: factors governing the fusion of lipid bilayer membranes.

The fusion barrier of two apposing bilayers (i.e. the pressure and energy required for their hemifusion) is directly related to the measured, temperature-dependent interbilayer forces during the breakthrough process. In comparison with the results obtained for solid-supported lipid bilayers on mica, the observations on soft-supported membranes clearly reflect the influence of the underlying substrate. Bilayers supported on mica alone are restricted in the mobility of their proximal, solid-like DPPE layer which is in direct contact with the solid substrate. This restricted mobility of the lower layer can result in packing stresses and hole formation in the distal DMPC layers when undergoing phase transitions, since the solid and laterally immobile DPPE layers do not accommodate for changes in the mean molecular area of the outer lipid layer. In contrast, polymer supported DMPC membranes can stay intact while undergoing the phase change from the fluid  $L_{\alpha}$  to the  $P_{\beta}$  gel phase. Thus, the data obtained on soft-supported systems more closely relate to the properties of the whole bilayer membrane, whereas measurements on solid-supported bilayers merely probe effects related to structural changes of the outer membrane leaflets.

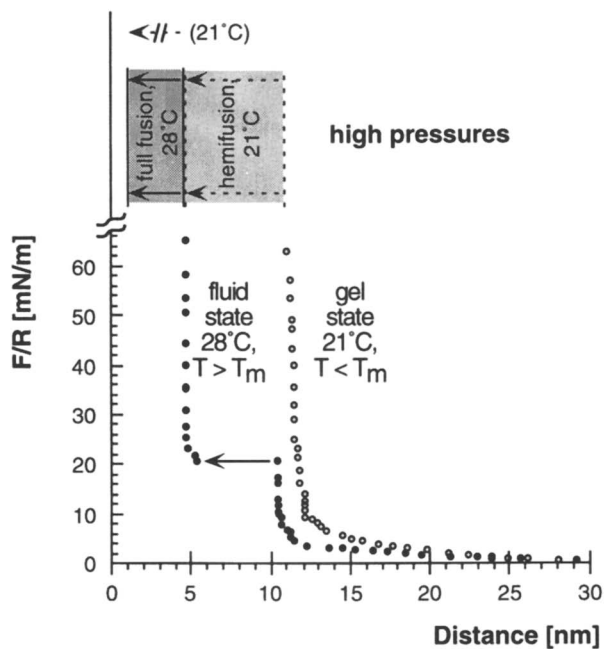


Figure 5. Force distance profile measured during compression of two physisorbed PEI-supported DMPC bilayers in the liquid crystalline state (at  $28^\circ\text{C}$ , full symbols) and in the gel phase (at  $21^\circ\text{C}$ , open symbols; adapted from Wong, J. Y.; et al. *Biophys. J.*, submitted).

It is interesting to compare the SFA results on soft-supported bilayers with fusion studies on spherical bilayer vesicles. As mentioned above, the fusion barrier, i.e. the pressure required to achieve hemifusion of two apposing membranes in the SFA, drastically increases in the gel state. When comparing to unilamellar vesicles of small size ( $R \leq 50$  nm), this observation seems to contradict findings on free unilamellar vesicles in solution for which fusion of the bilayer membranes was found to be favored below the fluid-gel transition,  $T_m$  (21). However, this difference can be explained considering that compared to nearly planar bilayers these small, curved vesicles in the gel state are highly stressed which they can overcome by fusion to larger vesicles (1,2,21). This is supported by the finding that phosphatidylcholine vesicles in contact that have a larger radius of curvature ( $R \approx 2$   $\mu$ m) show a similar trend as the nearly planar bilayer systems ( $R \approx 1$  cm) investigated in SFA studies, as they also fuse more easily with increasing temperature (59,60).

The same general driving force has been discussed both for the hemifusion of solid-supported bilayer membranes in the SFA (24,26) as well as for free vesicles in solution (60). In the first case, it has been argued that the exposure of hydrophobic chains on thinning of the outer membrane layer (which itself can be caused in different ways as described above) has been argued to give rise to an attraction between the inner DPPE layers of the two membranes which ultimately results in the removal of the two outer lipid layers. In the latter case, it was assumed that by increasing the fluidity of the membrane, the freedom of motion of the hydrocarbon chains of lipid molecules can be increased so as to allow the hydrocarbon chains to be exposed at the membrane surface. In both scenarios, the actual fusion process would be governed by an attractive, hydrophobic interaction.

However, in addition to this general hydrophobic driving force several other factors can play a crucial role in the fusion of lipid bilayer membranes, and their relative influence on the process can strongly depend on the particular system under investigation. As discussed before, for solid-supported lipid bilayers, most of these additional factors such as packing defects and phase separation are related to the properties of the outer lipid monolayer which can be considerably different than those of the supporting DPPE layer. In soft-supported bilayers as well as large unilamellar vesicles, the fusion of planar bilayers in contact is facilitated with increasing fluidity of the entire membrane. The additional influence of bilayer curvature is seen in small vesicles for which the fusion of is promoted by their high curvature. Also, it is important to consider how the bilayers are brought into contact. Thus, in studies on free vesicles in solution their enhanced aggregation below  $T_m$  contributes to the overall number of fusion events (21).

### Summary.

Phospholipid bilayers supported by a polymer cushion which can swell and act as a deformable and mobile substrate can preserve their membrane fluidity since their direct interaction with the solid substrate is prevented. For SFA measurements it is convenient to use branched polyethyleneimine as a water-swallowable polymeric substrate, as it can be easily adsorbed electrostatically onto atomically flat mica substrates. A lipid bilayer can be formed by adsorption of small unilamellar vesicles onto polymer-supported monolayers which can be partially covalently attached to the polymer layer using reactive lipids that insert into the membrane in order to provide additional stability to the system. In comparison to lipid bilayer systems deposited on mica directly, the interaction profile - particularly the hemifusion - of two polymer-supported membranes is less affected by the proximity of the supporting substrate and thus more closely resembles the properties of free bilayer vesicles. This also allows the observation of a complete fusion of two apposing lipid membranes with the SFA.

Many molecular processes on the outer membrane surface or within the outer membrane layers can be conveniently studied employing solid-supported bilayers,



such as phase separation, phase changes in the lipid layer, or ligand-receptor-interactions, and the influence of adsorbed polymers on the force profile between biomembranes. In addition to this broad variety of effects that can be investigated and understood with the SFA to date, the described soft-supported bilayers open up new possibilities. They will allow to further study dynamic interactions of more complex, and biologically more relevant model membranes, such as their adhesion and fusion under controllable and near *in-vivo* conditions.

### Acknowledgments.

This work was supported by the National Institutes of Health (NIH) under grant GM 47334, by a NRSA individual postdoctoral fellowship GM17876 (J.Y.W.). M.S. acknowledges partial funding by the Deutsche Forschungsgemeinschaft.

### References

1. Chernomordik, L. V.; Melikyan, G. B.; Chizmadzhev, Y. A., *Biochim. Biophys. Acta* **1987**, *906*, 309-352.
2. *Cell Fusion*; Sowers, A. E., Ed.; Plenum Press: New York, 1987.
3. Brian, A. A.; McConnell, H. M., *Proc. Nat. Acad. Sci. USA* **1984**, *81*, 6159-6163.
4. Tamm, L. K.; McConnell, H. M., *Biophys. J.* **1985**, *47*, 105-113.
5. McConnell, H. M.; Watts, T. H.; Weis, R. M.; Brian, A. A., *Biochim. Biophys. Acta* **1986**, *864*, 95-106.
6. Kalb, E.; Frey, S.; Tamm, L. K., *Biochim. Biophys. Acta* **1992**, *1103*, 307-316.
7. Lang, H.; Duschl, C.; Grätzel, M.; Vogel, H., *Thin Solid Films* **1992**, *210/211*, 818-821.
8. Bayerl, T.; Bloom, M., *Biophys. J.* **1990**, *58*, 357-362.
9. Israelachvili, J. N., *Chemtracts-Analyt. Phys. Chem.* **1989**, *1*, 1-12.
10. Parsegian, V. A.; Rand, P. R.; Fuller, N. L.; Rau, D. C. In *Methods in Enzymology*; L. Packer, Ed.; Academic Press: New York, 1986; Vol. 127; pp 400-416.
11. LeNeveu, D. M.; Rand, R. P.; Parsegian, V. A., *Nature* **1976**, *1976*, 601.
12. Lis, L. J.; McAlister, M.; Fuller, N.; Rand, R. P.; Parsegian, V. A., *Biophys. J.* **1982**, *37*, 657-665.
13. Evans, E. A., *Biophys. J.* **1980**, *31*, 425.
14. Evans, E.; Metcalfe, M., *Biophys. J.* **1984**, *46*, 423-426.
15. Evans, E., *Langmuir* **1991**, *7*, 1900-1908.
16. Prieve, D. C.; Alexander, B. A., *Science* **1986**, *231*, 1269-1270.
17. Prieve, D. C.; Frej, N. A., *Langmuir* **1990**, *6*, 396-403.
18. Rädler, J.; Sackmann, E., *J. Phys. II* **1993**, *3*, 727-748.
19. Israelachvili, J. N.; Adams, G. E., *J. Chem. Soc., Faraday Trans I* **1978**, 975-1001.
20. Israelachvili, J., *Acc. Chem. Res.* **1987**, *20*, 415-421.
21. Israelachvili, J. *Intermolecular and Surface Forces*; Academic Press Ltd.: London, 1991.
22. Horn, R. G., *Biochim. Biophys. Acta* **1984**, *778*, 224-228.
23. Marra, J.; Israelachvili, J., *Biochemistry* **1985**, *24*, 4608-4618.
24. Helm, C. A.; Israelachvili, J. N.; McGuiggan, P. M., *Science* **1989**, *246*, 919-922.
25. Leckband, D. E.; Helm, C. A.; Israelachvili, J., *Biochemistry* **1993**, *32*, 1127-1140.
26. Helm, C. A.; Israelachvili, J. N.; McGuiggan, P. M., *Biochemistry* **1992**, *31*, 1794-1805.

27. Israelachvili, J. N.; Adams, G. E., *Nature* **1976**, *262*, 774-776.
28. Israelachvili, J. N.; McGuiggan, P. M., *J. Mater. Res.* **1990**, *5*, 2223-2231.
29. Israelachvili, J., *J. Colloid Interface Sci.* **1973**, *44*, 259-272.
30. Chan, D. Y. C.; Horn, R. G., *J. Chem. Phys.* **1985**, *83*, 5311.
31. Hertz, H. J., *Reine Angew. Math.* **1881**, *92*, 156.
32. Horn, R. G.; Israelachvili, J. N.; Pribac, F., *J. Colloid Interface Sci.* **1987**, *115*, 480.
33. Johnson, K. L.; Kendall, K.; Roberts, A. D., *Proc. R. Soc. London A* **1971**, *324*, 301.
34. Helm, C. A.; Israelachvili, J. N., *Methods in Enzymology* **1993**, *220*, 130-131.
35. Chen, Y. L. E.; Gee, M. L.; Helm, C. A.; Israelachvili, J. N.; McGuiggan, P. M., *J. Phys. Chem.* **1989**, *93*, 7057-7059.
36. Leckband, D. E.; Schmitt, F. J.; Israelachvili, J. N.; Knoll, W., *Biochemistry* **1994**, *33*, 4611-4624.
37. Helm, C. A.; Knoll, W.; Israelachvili, J. N., *Proc. Natl. Acad. Sci. USA* **1991**, *88*, 8169-8173.
38. Leckband, D. E.; Israelachvili, J. N.; Schmitt, F. J.; Knoll, W., *Science* **1992**, *255*, 1419-1421.
39. Wong, J. Y.; Kuhl, T. L.; Israelachvili, J. N.; Mullah, N.; Zalipsky, S., *Science* **1997**, *275*, 820-822.
40. Horn, R. G.; Israelachvili, J. N.; Marra, J.; Parsegian, V. A.; Rand, R. P., *Biophys. J.* **1988**, *54*, 1185-1187.
41. Pezron, I.; Pezron, E.; Bergenstahl, B. A.; Claesson, P. M., *J. Phys. Chem.* **1990**, *94*, 8255-8261.
42. Sackmann, E., *Science* **1996**, *271*, 43-48.
43. Decher, G.; Hong, J. D., *Ber. Bunsenges. Phys. Chem.* **1991**, *95*, 1430-1434.
44. Decher, G., *Science* **1997**, *277*, 1232-1237.
45. Lindholm-Sethson, B., *Langmuir* **1996**, *12*, 3305-3314.
46. Stelzle, M.; Weissmüller, G.; Sackmann, E., *J. Phys. Chem.* **1993**, *97*, 2974-2981.
47. Häussling, L.; Knoll, W.; Ringsdorf, H.; Schmitt, F. J.; Yang, J. L., *Makromol. Chem., Makromol. Symp.* **1991**, *46*, 145-155.
48. Spinke, J.; Yang, J.; Wolf, H.; Liley, M.; Ringsdorf, H.; Knoll, W., *Biophys. J.* **1992**, *63*, 1667-1671.
49. Beyer, D.; Knoll, W.; Ringsdorf, H.; Elender, G.; Sackmann, E., *Thin Solid Films* **1996**, *285*, 825-828.
50. Jacobson, K.; Sheets, E. D.; Simson, R., *Science* **1995**, *268*, 1441-1442.
51. Janmey, P. In *Handbook of Biological Physics*; R. Lipowsky and E. Sackmann, Ed.; Elsevier: 1995; Vol. 1; pp 805-849.
52. Heysel, S.; Vogel, H.; Sanger, M.; Sigrist, H., *Protein Sci.* **1995**, *4*, 2532-2544.
53. Cornell, B. A.; Braach-Maksvytis, V. L. B.; King, L. B.; Osman, P. D. J.; Raguse, B.; Wiczorek, L.; Pace, R. J., *Nature* **1997**, *387*, 580-583.
54. Kühner, M.; Tampe, R.; Sackmann, E., *Biophys. J.* **1994**, *67*, 217-226.
55. Beyer, D.; Elender, G.; Knoll, W.; Kühner, M.; Maus, S.; Ringsdorf, H.; Sackmann, E., *Angew. Chem. Int. Ed. Engl.* **1996**, *35*, 1682-1685.
56. Axelrod, O.; Kappel, D. E.; Schlessinger, J.; Elson, E.; Webb, W. W., *Biophys. J.* **1976**, *16*, 1055.
57. Merkel, R.; Sackmann, E.; Evans, E., *J. Phys. France* **1989**, *50*, 1535.
58. Janiak, M. J.; Small, D. M.; Shipley, G. G., *Biochemistry* **1976**, *15*, 4575-4580.
59. Breisblatt, W.; Ohki, S., *J. Membr. Biol.* **1975**, *23*, 385-401.
60. Ohki, S. In *Membrane Fusion Techniques, Part A*; N. Düzgünes, Ed.; Academic Press: San Diego, 1993; Vol. 220; pp 79-89.
61. Wong, J.Y., et al. "Interaction Forces and Fusion Between Lipid Bilayers Softly Supported' on Thin Polyelectrolyte Films." *Biophys. J.*, in press.

## Chapter 16

# Protein Transport, Aggregation, and Deposition in Membrane Pores

R. Chan and V. Chen

UNESCO Centre for Membrane Science and Technology, School of Chemical  
Engineering and Industrial Chemistry, University of New South Wales,  
Sydney, New South Wales 2052, Australia

Protein deposition on membrane surfaces and in pores can be probed using constant flux filtration experiments and electron microscopy. Protein precipitation near membrane pores are the result of pre-existing aggregates, shear enhanced multilayer protein adsorption, and aggregate formation and growth. To determine what hydrodynamic conditions and solution conditions are required to create protein aggregates in situ, fluxes were incrementally raised until a critical threshold was reached and membrane permeability suddenly decreased. Addition of electrolytes was also used to change the protein interactions. Filtration below the critical threshold allows only low amount of protein adsorption to be maintained. Above this threshold, multilayer protein growth is rapid and sufficient to reduce the pore size ten fold. Protein aggregates do not appear to occur until after the rapid rise in transmembrane pressure is observed, and the effect of added electrolyte did not appear until a time period for protein rearrangement during filtration.

Membrane ultrafiltration and microfiltration form important separation processes for the separation and purification of proteins and other small colloids. Although membrane filtration has been addressed in the literature for more than 25 years, only recently have the dynamics of protein transport, aggregation, and deposition near the membrane surface and pores have been accessible using new experimental techniques. During filtration through a partially retentive membrane, high concentrations of protein may be confined on the membrane surface and a fraction of the solutes which reaches the surface will undergo both diffusive and convective transport through tortuous pore structures. If adsorption reaches a significant level to prevent solute passage through the membrane yet pass solvent easily, a rapid build up of solute at the membrane surface will occur and fouling will take place. The

conditions leading to the onset of protein adsorption due to concentration polarization, aggregation, and deposition on the surface and within the membrane is not well understood. Furthermore, many previous studies have ignored partially permeable membranes to simplify analysis of the solute transport mechanisms to and from the membrane surface. However, controlling protein transport through ultrafiltration or microfiltration membranes allows optimal protein fractionation to be undertaken. In addition, controlling protein aggregation and deposition allows the maximum flux to be achieved without pore plugging and fouling.

While there has been extensive studies on diffusive transport of protein through membrane pores as well as passive protein adsorption, protein transport through UF and MF membranes is less well understood. Confinement of a high solute concentration to the membrane wall, high local shear, and hindered passage through the membrane structure imposes limitations on solute passage even when the solute is much smaller than the pore size. Thus three potential mechanisms controlling protein transport and deposition in membrane pores should be considered: (a) protein adsorption, (b) protein aggregation (pre-existing and formed *in situ* in membrane pores), and (c) concentration polarization. The dynamics and control of these mechanisms are discussed.

The consequence of the local shear field and small pores is possible denaturation of the protein as they pass through the membrane. This denaturation increases the aggregation of the native protein, possibly to sizes large enough to plug the pores. There have been many studies on possible shear denaturation in processing of biological material, especially enzymes, with regards to pumping and exposure to the air-water interface. Charm and Wong showed that when the product of the shear force and time exceeds 50 Pa s, measurable effect on the activity of enzymes are observed (1). On the other hand, Dunnill and co-workers reported no observable loss in enzymatic activity in their investigations (2). In membrane filtration units, proteins can be exposed to high shear forces (and concentrations) near pore walls for short periods as well as at low shear for long residence times due to pumping and recirculation. Convective deposition of protein aggregates generated by shear forces due to pumping was more extensively studied by Chandavarkar in the context of crossflow microfiltration (3). Using quasi-elastic light scattering and electrophoretic analysis, he showed that protein aggregates consisting of less than 1% of the total protein were detectable on the membrane surface and contributed significantly to pore occlusion. While protein aggregation due to bulk shear may be significant, the forces through small membrane pores are much higher but are of short duration. Several studies have considered the potential for these shear forces to contribute to protein aggregation and fouling in membrane pores.

Truskey et al. first investigated the possibility that membrane filtration may affect the protein conformation using low pressures and no stirring in a dead end cell (4). They did not find any significant protein conformation changes using circular dichroism (CD). Subsequently, Franken et al. investigated fouling of track etched

membranes with bovine serum albumin (BSA) (5). BSA is a prolate ellipsoid with approximate dimensions of  $10 \times 2.7 \times 2.7$  nm. BSA samples were examined by CD and Fourier Transformed Infrared (FTIR) after they have undergone shear, heating, and passage through a microfiltration membrane, and the secondary structures were compared. Using BSA prepared by the manufacturer using heat shock fractionation, rejection was observed with  $0.2 \mu\text{m}$  track etched polycarbonate membranes despite the high pore to protein size ratio. Rejection also increased with stirring rate and higher transmembrane pressures. These results indicated that proteins were able to effectively plug the pore structure, and that aggregation near the pore entrance was a possible mechanism. Franken et al. also observed that rejection did not occur when BSA prepared by Cohn cold ethanol fractionation was used in identical experiments. The FTIR and CD spectra of the BSA before and after filtration only showed small differences compared to the moderate changes shown by prolonged heating (2 hours at  $70^\circ\text{C}$ ) and large changes due to high temperatures (5 min. at  $100^\circ\text{C}$ ). This was not unexpected since BSA is considered a relatively rigid or "hard" globular protein, and the population of shear-denatured protein may be small compared to the bulk solution.

Thus evidence pointed to some population of protein aggregates formed by both shear forces experienced during stirring, by shear experienced through the membrane pores, and by prior history. The effect is particularly magnified by low porosity (9.4%) track etched membranes. The average shear forces through the  $0.2 \mu\text{m}$  track etched membrane at 0.6 bar is calculated to be approximately 460 Pa but the residence time in the pores is less than 0.001 s. In the terminology of Charm and Wong, the shear-time product would be 0.22 Pa s, considerably less than the 50 Pa s they predicted to denature enzymes. This does not account for the possibility of high local shear gradient near the walls to cause protein denaturation.

Hodgson compared multiple filtration of BSA solution through highly porous alumina "Anopore" membranes (with  $0.02$  and  $0.2 \mu\text{m}$  poresize) (6). Hodgson investigated both the possibility of pre-existing protein aggregates and those formed by confinement under shear in membrane pores (6). These membranes have the advantage of the high porosity and uniform capillary pores. Particle sizing of the raw protein solution and protein recovered from the surface of the  $0.02 \mu\text{m}$  membranes were compared in the 200 – 2000 nm range. The aggregates on the surface of the membranes contained a larger proportion of large aggregates than in the raw solution. He found that the reduction of flux and the changes in protein transmission followed neither a simple internal deposition nor an external cake deposition mechanism. Instead he proposed that the following stages of fouling occurred. First, a rapid monolayer adsorption in the pores occurs, with some pre-existing aggregate being deposited from bulk solution. Second, a more substantial aggregate layer formed due to aggregate growth through protein deposition on their surface. Eventually, the growth of the aggregates forms an even cake or "sheet-like" layer which parallels the onset of rejection (6).

Bowen and Gan observed, that unlike normal passive protein adsorption, filtration of dilute BSA proteins in Anopore membranes indicated a continuous protein deposition with a maximum layer thickness of 55 nm on the walls of the 0.2  $\mu\text{m}$  diameter walls (7). This is in contrast with monolayer passive adsorption of 5 – 10 nm observed in the absence of filtration. Thus shear and confinement in membrane pores thus result in both multilayer protein adsorption as well as aggregate initiation or growth. Kelly et al. confirmed that the different types of commercially available BSA showed that the rate of flux decline was most rapid for proteins prepared by the heat shock fractionation and those designated fatty acid free (8). Prefiltration of their protein solutions slowed the flux decline but did not prevent continuous flux decline. Kelly et al added iodoacetic acid which caps the free sulfhydryl group on each BSA molecule in an attempt to limit further aggregation of the protein solution during filtration (9). Their results showed that capping of sulfhydryl group followed by prefiltration to remove the existing aggregates resulted in a solution which exhibited very low flux decline. These results support the preliminary evidence by Franken et al. and Hodgson that both pre-existing aggregates and aggregate formation play a role in the dramatic flux decline observed in protein filtration (5,6).

Attempts to directly observe the protein deposits on membrane surfaces have been conducted using field emission electron microscopy. Small volumes of protein solutions were filtered at various constant pressures, and the initial protein deposits were observed. Kim et al. showed that both pressure and membrane morphology resulted in more evident protein aggregate formation on the surface of the membrane (10). Formation of smooth cake like layers were observed at lower pressure while an increase of from 100 to 200 kPa induced protein aggregates to appear on top of 100 kD molecular weight cut off polysulfone membranes (11). Changes in pH and stirring did not appear to significantly affect the appearance of the initial protein deposit. While the appearance of protein aggregates is important in explaining the apparent rejection of solutes many times smaller than the pore size, the onset of both the irreversible flux decline and rejection was identified as a function of achieving some critical condition near the membrane pore walls.

More recently, additional techniques have been used to probe the critical conditions to initiate irreversible multilayer protein deposition. Anecdotal evidence had often suggested that moderate flux during initial startup of membrane filtration and operation can reduce the severity of fouling. Turker et al. and others controlled the permeate flow rather than use a fixed transmembrane pressure to control deposition to the surface (12-14). Thus much more consistent hydrodynamic conditions can be applied during the filtration process whereas constant pressure filtration resulted in a continuing decreasing convective force on the different layers of deposition.

Since the deposition of the particles depend on the balance between convective drag and axial convection, the concept of “critical flux” has been used to describe the

hydrodynamic conditions to achieve little or no deposition of colloidal particles on the membrane surface. A demonstration of this concept was shown by Field et al. with dodecane emulsion and yeast particles (13,14). Field et al. were able to maintain filtration without flux decline and showed that once a threshold flux was exceeded, deposition rapidly took place (13,14). Using a series of increasing flux steps, Madaeni showed that there was a sharp transition between “nonfouling” or “subcritical” flux and a rapidly fouling regime, even a complex fluid such as activated sludge (15). For smaller particles, Chen et al showed that the transition from concentration polarization to irreversible cake deposition can be detected by the same means using 12 nm silica particles (16). At a fixed, constant flux, the transmembrane pressure is constant when only concentration polarization is present as it is established rapidly; however, at the fouling threshold, a rapidly increasing transmembrane pressure occurs. Reversibility of this deposition depends on the how much excess pressure is applied.

Rather than a “critical flux”, Aimar and co-workers have considered the conditions for irreversible deposition to occur when both the colloidal interactions between particles as well as the convective forces bringing the particles into contact reaches some threshold level (17). This threshold depends on particle size, concentration, and interaction parameters between the colloidal particles such as Van der Waals forces and electrostatic repulsion. The regimes favorable for particle deposition were mapped out by Aimar and co-workers based on the hydrodynamic factors (crossflow and flux) and the potential barrier  $V_B$  which represent the colloidal interactions, using a factor  $W_D = 1 + (V_B/\delta)$  as a criterion for determining if a particle will be retained on a membrane surface (17). High  $W_D$  values indicate low or negligible depositions and the crossover between nonfouling and fouling regimes is delineated by where the  $Sh \approx Pe$ , ie mass is dominated by convection and not by colloidal interaction  $V_B$ .

The Sherwood number is defined as a function of both the Peclet number and the potential barrier  $V_B$ ,

$$Sh = \frac{1}{(W_D - 1)e^{-Pe} + \frac{1}{Pe}(1 - e^{-Pe})}$$

Adsorption is considered as a third region for the case of low Pe number and  $Sh \approx Pe$ . In the case of BSA, Aimar and co-workers predicted a potential barrier  $V_B$  of  $1 \times 10^{-4}$  m for at a 0.001 M ionic strength and  $-6.8$  net charge. Depending on the size and the strength of the colloidal interactions, it is likely that the concepts of “critical flux” and “critical concentration” are both relevant, but the dominance of one factor over another may occur at very high fluxes or very high charge interactions.

To determine the onset of both flux decline and reduction in transmission for BSA, the "stepping" experiments were used for various track etched and polyvinylidene difluoride microfiltration membranes which show partial rejection of BSA (18). For 0.2  $\mu\text{m}$  poresize track etched membranes, the "incipient fouling" region was approximately in the 150  $\text{L}/\text{m}^2\text{h}$  range for 0.4 wt% BSA at pH 7.5. For the module that is used in our laboratory with BSA, Table I shows the values of Peclet number for 150  $\text{L}/\text{m}^2\text{h}$ , using the estimates from Bacchin et al. as  $V_B$  (17,18). The mass transfer coefficient  $k = D/\delta$  was determined by the best fit of the film model from the filtration data.

**Table I.**

Flux ( $\text{L}/\text{m}^2\text{h}$ )	Pe	$W_D$	Sh	Sh/Pe
150	8.89	22.3	8.66	0.97

For the Peclet and Sherwood number evaluated under those conditions, the stability factor for deposition  $W_D$  lies on the transitional area, near the region where Aimar and co-workers define as being favorable for deposition. However, there is no explicit provision for the removal of solute from the interface through a partial permeable membrane.

In addition to looking at the apparent "critical flux", we have used the calculated wall concentrations of BSA where the beginning of the irreversible deposition appear to occur, what we call the "incipient fouling regime". These threshold concentrations appear to be quite low (below 5wt%) (18). This concentration is not sufficient to "gel" or precipitate or flocculate. Thus shear-enhanced adsorption must also play a role in accelerating irreversible deposition at such low concentrations.

In this work, the evidence of protein deposition in the pores of microfiltration membranes, specifically the possible aggregation of protein deposits and the effect of electrolytes on the incipient fouling regime are examined. By applying constant flux below, above, and near the "critical flux" threshold, we can determine the conditions where monolayer protein adsorption undergoes a transition to multilayer adsorption, reflected by a rapid increase in resistance. Electron microscopy of the membrane surface was undertaken to determine whether significant protein aggregation is evident near the critical flux.

The effect of added electrolyte is also examined to determine how the critical flux is affected. Although the electrostatic repulsion will be dampened by the added electrolyte, the effect of added electrolyte will also affect the solubilization as well as the rejection of the protein. In constant pressure experiments, early studies by Suki et al. (19) showed that added electrolytes decreased flux at pH's away from the



isoelectric point and increased them near the isoelectric point. A number of subsequent studies have supported these observations. However, these effects would likely be dominated by cake formation on the membrane surface while our experiments are probing their effects upon the onset of multilayer deposition. If the potential barrier is decreased, the onset of the fouling threshold should be reflected by a shift of the inflection point of the  $\Delta P$  versus flux graph to lower fluxes. We also examine whether or not the kinetics of protein adsorption and multilayer deposition becomes important near the fouling threshold.

## Experimental Methods

Poretic polycarbonate track etched membranes with 0.2  $\mu\text{m}$  pore size were used in the experiments. The bovine serum albumin (Fraction V) was obtained from Calbiochem Australia and made up into 0.1 wt% solution with Milli-Q treated water. The pH of the feed solution was adjusted using NaOH and HCl. The membranes were presoaked in 0.1 wt% BSA solution for 1 hour before filtration experiments were carried out. Concentration was measured for rejection experiments using absorbance at 280 nm via a Cary I spectrophotometer by Varian. The electron micrographs were taken using a Hitachi S900 field emission scanning electron microscope.

The crossflow module provided a channel 2 mm high, 25 mm wide and 210 mm long. The effective area of the membrane was 24.5  $\text{cm}^2$ . A peristaltic pump (Master Flex Model 7529-00) was used to supply the operating pressure and feed circulation. Pressure transducers were used to monitor the permeate pressure as well as the inlet pressure in the membrane module. A small peristaltic pump (Masterflex by Cole Palmer) was used to control the permeate flux. The permeate flow was measured by an electronic balance, and the both the pressures and permeate flow were monitored automatically by a computer. A crossflow velocity of 0.69 m/s was maintained during the experiments.

For "stepping experiments", flux was increased in increments and held for 15 minutes. During that time, the transmembrane pressure remained fairly constant if below the fouling threshold or increased rapidly above the fouling threshold. A range of pH's were used to vary the potential barrier and electrolyte concentrations were also varied. In a number of experiments, only one applied flux was used and the transmembrane pressure was observed to see if there was a time lag due to exposure of the surface before deposition begins to occur.

## Results

The first experiments attempted to change the potential barrier for deposition by using increasing amounts of added NaCl for pH 3, 4.8 (taken to be the isoelectric point of BSA), and 9. In Figure 1, the electrolyte concentration was increased from no added NaCl to 0.15 M added NaCl. Unexpectedly, there was little change in the

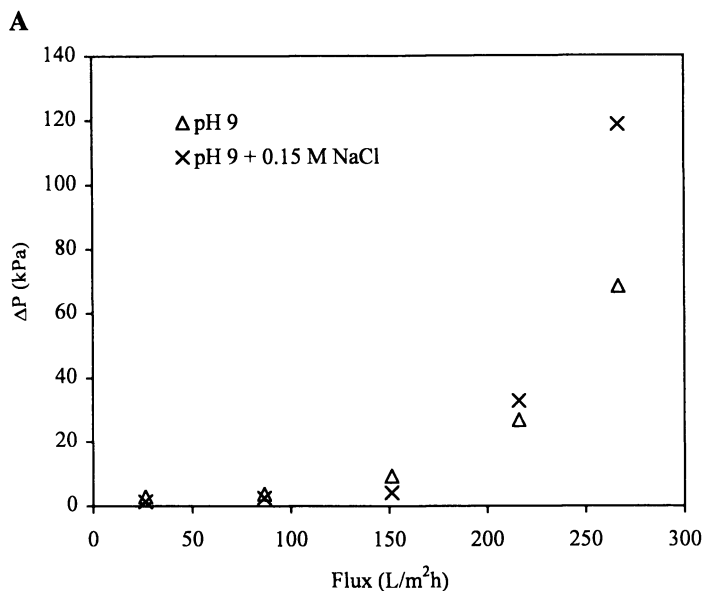


Figure 1a. Effect of added electrolyte on transmembrane pressure versus flux measurements at pH 9.

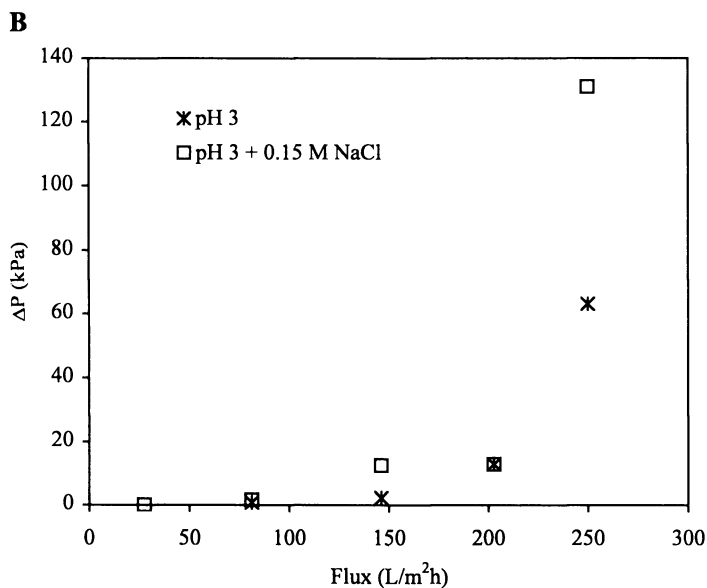


Figure 1b. Effect of added electrolyte on transmembrane pressure versus flux measurements at pH 3.

fouling thresholds. In addition, the rejection of the protein did not change significantly initially when the transmembrane pressure just began to increase but only started to increase after the transmembrane pressure exceeded 100 kPa. At pH 3 and pH 4.8, the rejection remained approximately 10% with and without the addition of electrolyte. For pH 9, the rejection was decreased substantially by the addition of 0.15 M NaCl. To confirm whether the flux increments used in the experiments did not induce an experimental artifact, constant flux experiments were carried out above and below the critical flux without “stepping”. These provided some interesting results in and of themselves.

Below the critical flux, the negligible fouling can be maintained as evidenced by the constant transmembrane pressure in Figure 2. However, at pH 3 when significant 0.15 M NaCl is present, the transmembrane pressure begins to increase after one hour, indicating that possible conformation changes of the protein on the surface allows higher fouling to take place (Figure 3). In order to determine whether this is due to shear denaturation from pumping, the solution was pumped around the system for one hour before the experiment begun. The results were the same as before, fouling only appeared after the filtration had occurred for an hour. This indicates that the fouling was only initiated by the filtration process.

Electron micrographs of the membrane below, near, and just above the critical flux were taken at pH 9 (Figure 4). Even after 30 minutes at 300 L/m<sup>2</sup>h, well above the critical flux, the surface is still relatively clear after they were removed from the membrane module and air-dried. This is also consistent with the rejection data which shows little increase from the initial 10% until the membrane has been held for a time above incipient fouling region. The rapidity of the change in rejection is likely to increase with increasing concentrations of BSA. Earlier experiments with 0.4 wt% BSA showed a much faster increase in rejection after the critical flux has been exceeded. Well above the critical flux for pH 4.8, the multilayer protein deposition and aggregates are clearly evident (Figure 5). Deposition inside the pores appears to occur as well. The presence of electrolytes did not significantly change the appearance of the deposit in this case (Figure 6).

## Discussion

By holding the flux below a threshold value, protein deposition in the form of aggregates and thick layers can be avoided. Near the critical flux, some increase in transmembrane pressure is evident; however, no significant aggregates are immediately detected. Thus it is hypothesized that the multilayer deposition is occurring in the pores and on the surface but may be still not totally irreversible. Previous experiments which increased the flux over the incipient fouling region for short periods and then decreasing them again, show partial dissipation of the resistance. More prolonged filtration substantially above the critical flux shows both aggregates and thick protein layer formation.

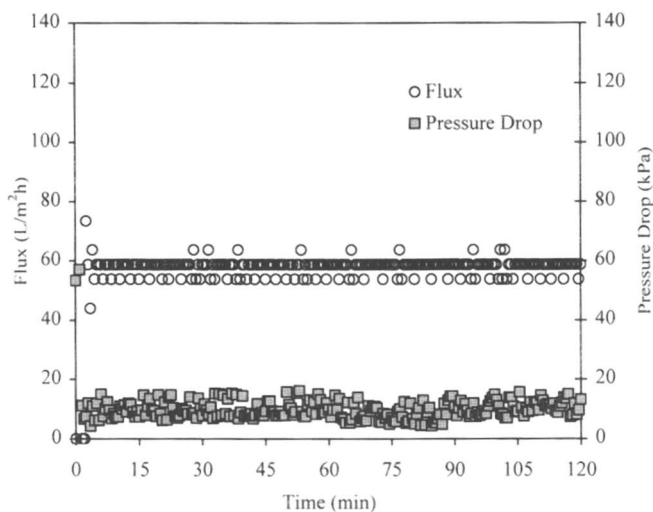


Figure 2. Transmembrane pressure and flux versus time during filtration at constant flux at pH 3 (no added NaCl).

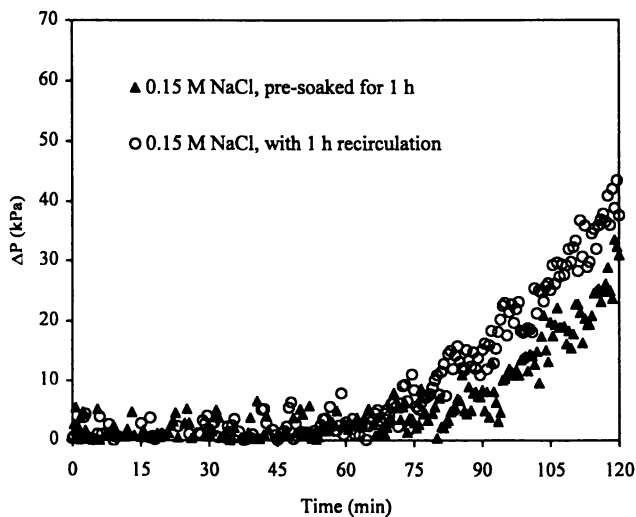


Figure 3. Transmembrane pressure versus time during filtration at  $60 \text{ L/m}^2\text{h}$ , constant flux at pH 3 with  $0.15 \text{ M NaCl}$ . In one case, the protein solution was filtered after being pre-soaked for 1 hour while in the other case the protein solution was circulated for 1 hour in the system prior to the beginning of filtration.

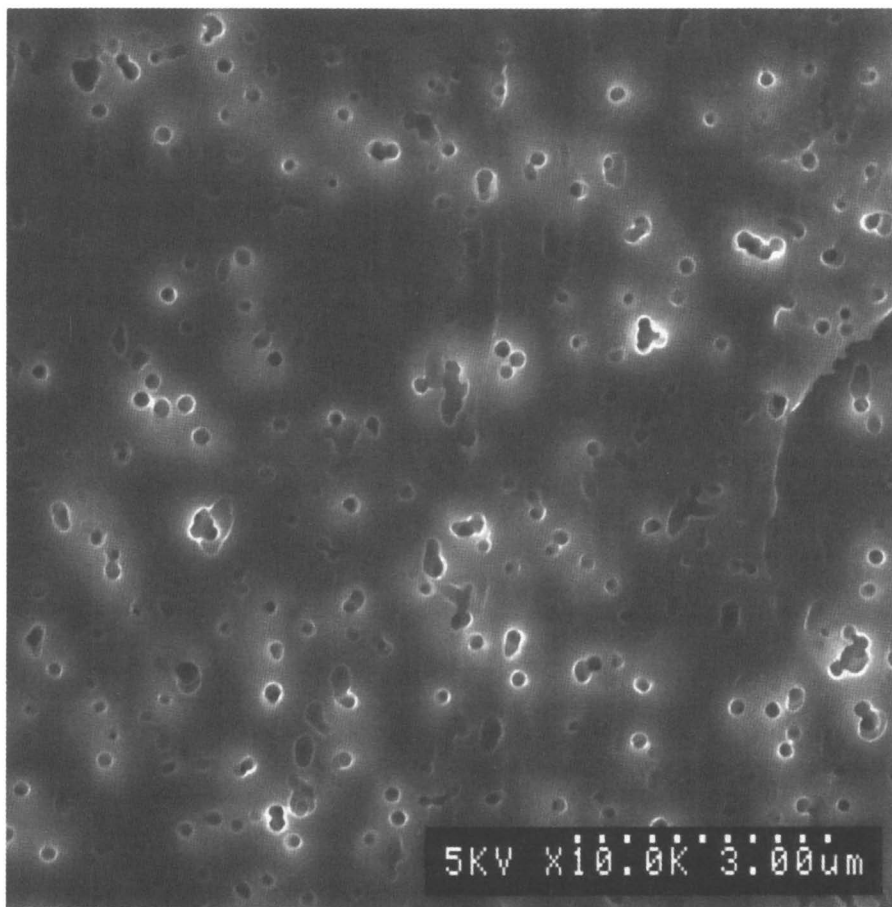


Figure 4. Electron micrograph of 0.2  $\mu\text{m}$  track etched membrane after 30 minutes of filtration at pH 9 at 300 L/m<sup>2</sup>h which is above the critical flux. The distance between the white dots is equivalent to 186 nm.

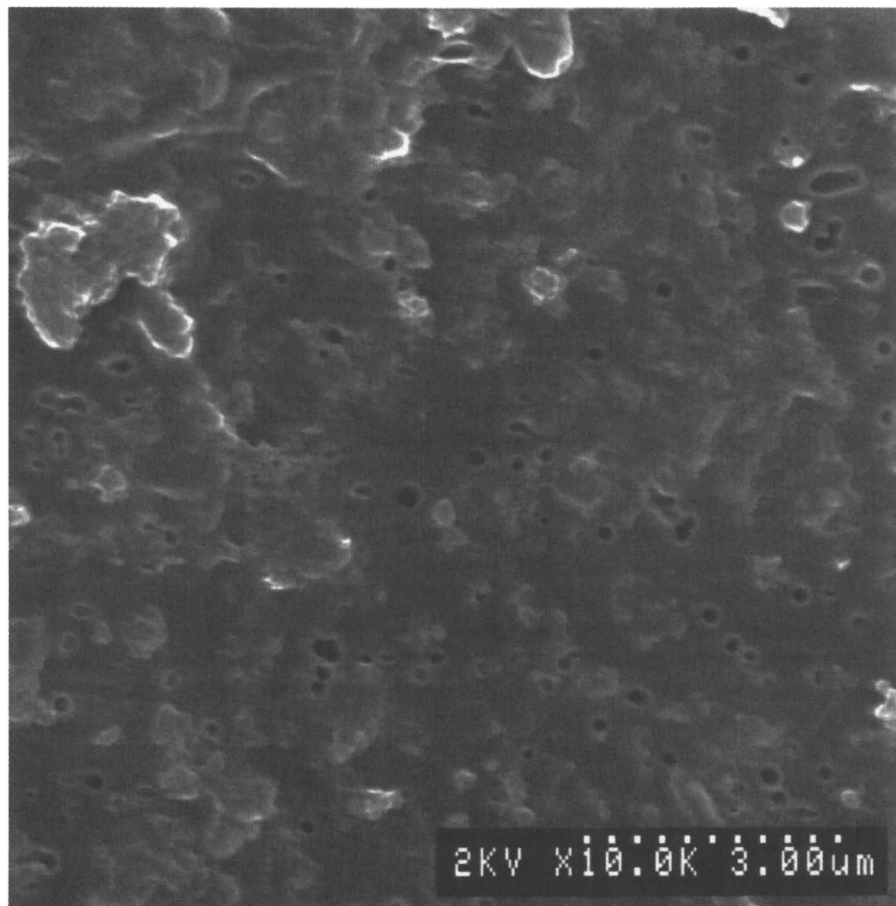


Figure 5. Electron micrograph of 0.2  $\mu\text{m}$  track etched membrane after filtration at 200 L/m<sup>2</sup>h for 1 hour at pH 4.8 with no added salt. The distance between the white dots is equivalent to 186 nm.

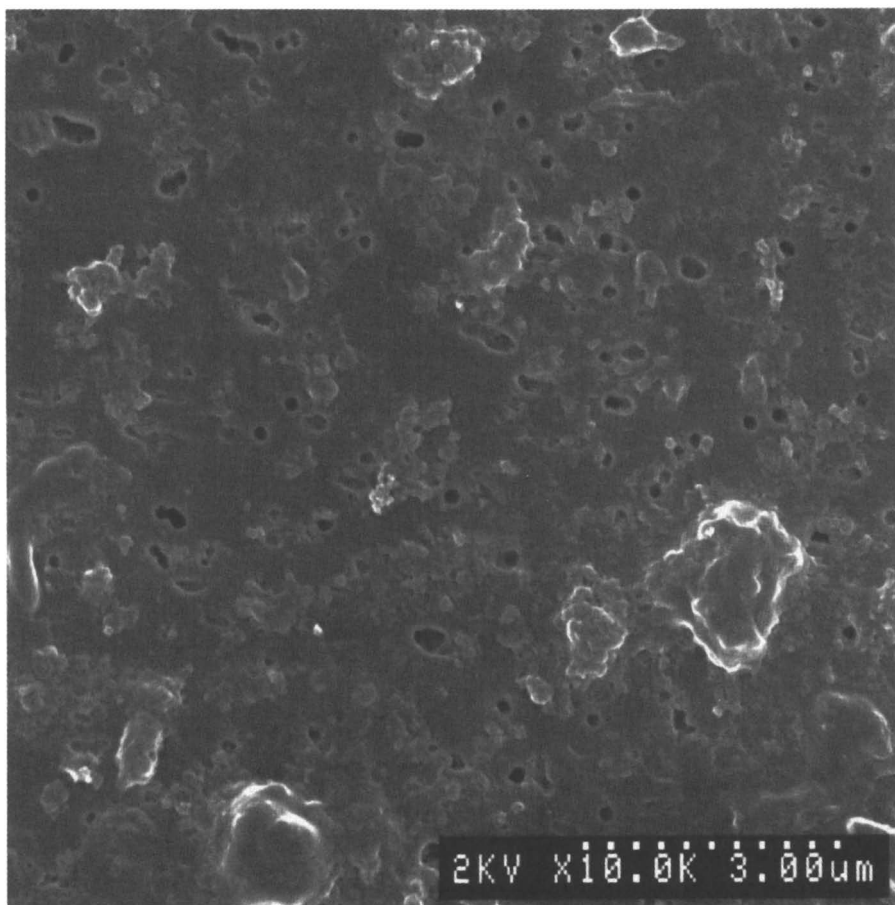


Figure 6. Electron micrograph of 0.2  $\mu\text{m}$  track etched membrane after filtration at 200 L/m<sup>2</sup>h for 1 hour at pH 4.8 in the presence of 0.1 M NaCl. The distance between the white dots is equivalent to 186 nm.

The addition of electrolyte did not produce a dramatic change in the threshold levels for fouling. Theoretically, the potential barrier should decrease due to the dampening of the repulsive interactions, resulting in a shift to lower fluxes and Peclet number for the fouling region. There may be two reasons. First, the "stepping" type experiments slowly increased the flux gradually and the high shear encountered in the initial phase of constant pressure experiments is not present. This may slow the formation of protein-protein linkages and aggregate formation affected by the increased electrolyte concentration. The results at constant flux with 0.15 M NaCl shows that there is a time lag for the onset of rapid deposition when salt was added. Thus the flux increments needed to be taken over longer periods of time to accurately determine the true fouling threshold. Palecek and Zydney observed the addition of electrolytes reduces the electro-osmotic counterflow attributed to the highly charged, protein coated walls on the membranes (20). Measuring saline flux through protein deposits, they observed a net increase in flux was observed at first but then eventually, the flux dropped below those with lower levels of electrolyte. This was attributed by them to slow rearrangement within the protein deposit to accommodate the higher salt concentrations. In our experiments, these rearrangements seem to encourage further deposition of proteins to occur from the bulk solution. The slow kinetics of this multilayer adsorption is pointed out in the early work by Suki et al. (19).

When the electrolyte concentration was increased, the flux-transmembrane pressure relationship during the "stepping" experiments may be attributed to two factors. First, the protein aggregation was sufficiently slow that there was not sufficient time to form and to deposit during the incremental flux step. Since no substantial cake has yet been built up in the incipient fouling regime (as shown by the electron micrographs and rejection data), cake permeability does not dominate the resistance. When the same experiments were done at a constant pressure of 50 kPa, the steady state flux of the solution with added electrolytes were lower than those with no added electrolyte. Secondly, the initial rejection with 0.15 M NaCl was lower than that with no added electrolyte when mutual electrostatic repulsion exists. In the presence of added electrolyte, the electrostatic repulsion is reduced not just between solute molecules but also between the membrane walls and proteins. For pH 9, the wall concentration at the same fluxes would be much higher initially when no added NaCl was present, and the critical wall concentration was encountered at a lower flux. Thus when there is effectively no cake deposition present, the build up of the wall concentration appears to dominate the fouling threshold. Thus despite the smaller potential barrier, the lower rejection can allow an equivalent of an increased mass transfer or enhanced particle removal from the membrane surface. Over time however, the effect of electrolyte does enhance protein adsorption, and the transition to multilayer deposition is observed by the increase in transmembrane pressure after 1 hour.



## Conclusion

By varying the electrolyte concentration and using constant flux experiments, the progression of fouling steps can be better delineated. At low fluxes, monolayer type adsorption is likely. At the incipient fouling region, determined by the pH and solution concentrations, the increase in resistance is due to the beginning of multilayer adsorption within the pores which are not yet irreversible. The narrowing of the pores probably induces more protein deposition, capture of pre-existing aggregates, and growth of protein aggregates on the membrane surface. This culminates into a thick surface layer. By using constant flux experiments, we can slow down the deposition sufficiently to capture the different phases of fouling. By adding electrolyte, the rejection is decreased but the potential barrier for adsorption is decreased. When the kinetics of the latter catches up, fouling can occur even at relatively low fluxes (60 L/m<sup>2</sup> h). At higher protein concentrations, the protein adsorption process is accelerated and the "stepping experiments" will not be affected as much by the adsorption/aggregation kinetics.

## Acknowledgement

The authors acknowledge support from the Australian Research Council.

## References

1. Charm, S. E.; Wong B. L. *Biotechnol. Bioeng.* **1970**, *12*, pp. 1103 - 1109.
2. Thomas, C. R.; Niewnow, A. W.; Dunnill, P. *Biotechnol. Bioeng.* **1981**, *23*, pp. 425 - 429.
3. Chandavarkar A. S. *Dynamics of Fouling of Microporous Membranes by Proteins*, Ph.D. Thesis, Massachusetts Institute of Technology, 1990.
4. Truskey G. A.; Gabler R.; DiLeo, A.; Manter, T. *J. Parenteral Science and Technology* **1987**, *41*, pp. 180-193.
5. Franken A. C. M.; Sluys, J. T. M.; Chen V.; Fane, A. G.; Fell, C. J. D. *Proceedings of the 5<sup>th</sup> World Filtration Congress* **1990**, Vol. 1, pp. 207 - 213.
6. Hodgson, P. H. *Crossflow Microfiltration of Biomass and Biofluids with Inorganic Membranes*, Ph.D. Thesis, University of New South Wales, 1993.
7. Bowen, W. R.; Gan, Q. J. *Coll. Interf. Sci.* **1991**, *144*, pp. 254 - 262.
8. Kelly, S. T.; Opong, W. S.; Zydney, A. L. *J. Membr. Sci.* **1993**, *80*, pp. 175 - 187.
9. Kelly, S. T.; Zydney, A.L. *Biotechnol. Bioeng.* **1994**, *44*, pp. 972 - 982.
10. Kim, K. J.; Fane, A. G.; Fell, C. J. D.; Joy, D. C. *J. Membr. Sci.* **1992**, *68*, pp. 79 - 91.
11. Kim, K. J.; Chen, V.; Fane, A. G. *Biotechnol. Bioeng.* **1993**, *42*, pp. 260 - 265.
12. Turker, M.; Hubble, J. *J. Membr. Sci.* **1987**, *34*, pp. 267 - 281.

13. Field R. W.; Wu, D.; Howell, J. A.; Gupta, B. B. *J. Membr. Sci.* **1993**, *155*, pp. 347 - 359.
14. Howell, J. A. *J. Membr. Sci.* **1995**, *107*, pp. 165 - 171.
15. Madaeni, S. S. *Membrane Filtration of Biological and Non-Biological Solids*, Ph.D. Thesis, University of New South Wales, 1995.
16. Chen, V.; Fane, A. G.; Madaeni, S.; Wenten, I. G. *J. Membr. Sci.* **1997**, *125*, pp. 109 - 122.
17. Bacchin, P.; Aimar, P.; Sanchez, V. *AIChE J.* **1995**, *41*, pp. 368 - 376.
18. Suki, A.; Fane, A. G.; Fell, C. J. D. *J. Membr. Sci.* **1984**, *21*, pp. 269 - 283.
19. Chen, V. *J. Membr. Sci.*, in press.
20. Palecek, S. P.; Mochizuki, S.; Zydney, A. L. *Desalination* **1993**, *90*, pp. 147 - 159.

## Improved Photochemical Selectivity of Vitamin D<sub>3</sub> Isomers via Confinement in Novel Sol–Gel Derived Alumina

Forrest S. Schultz<sup>1</sup> and Marc A. Anderson<sup>2</sup>

<sup>1</sup>Department of Chemistry, University of Wisconsin at Stout,  
Menomonie, WI 54751

<sup>2</sup>Water Chemistry Program, University of Wisconsin at Madison,  
Madison, WI 53706

It has been demonstrated that porous SGD (sol-gel derived)-alumina can function as an effective microorganized medium in which to perform size or shape selective organic transformations. For the photolysis of 7-dehydrocholesterol encapsulated within SGD alumina, it was found that the adsorption characteristics of 7-dehydrocholesterol and the pore size of the SGD-alumina greatly influenced the photoproduct distribution. An increase in the ratio of previtamin D<sub>3</sub> to tachysterol<sub>3</sub> was obtained on photolysis of 7-dehydrocholesterol adsorbed within SGD-alumina with a pore size of <37 Å and activated at 300 °C. This result is attributed to a confinement effect that inhibits the *cis-trans* isomerization of previtamin D<sub>3</sub> to tachysterol<sub>3</sub>.

Significant efforts have been made by many researchers to develop microorganized media to effect the chemical selectivity of a wide variety of chemical reactions. As a result of this research chemical selectivity has been achieved by confining a reactive species within an organized structure which is capable of limiting the conformational flexibility of reactants or transition states leading to different products. Studies of several systems of microorganized media have produced encouraging results, and in many instances it has been demonstrated that the chemoselectivity, regioselectivity and/or stereoselectivity of chemical reactions can be enhanced (1).

Unfortunately many of these systems suffer from shortcomings which limit their ultimate practicality. Our current studies have focused on sol-gel derived alumina (SGD-alumina) as a practical supramolecular host. Thermal stability, chemical stability, mechanical stability, optical transparency, narrow pore size distribution ranging from 3-100 Å (2), controllable pore size and ease of thin film and

monolith preparation are all characteristics of SGD-alumina which distinguish it from other microorganized media systems which, quite often, lack one or more of these desirable features.

In recent years, the synthesis and characterization procedures for SGD-alumina materials have been fairly well established. This work has examined the various aspects of hydrolysis, gel formation, and sintering conditions for the preparation of supported and unsupported alumina materials with controlled pore sizes and pore size distributions (3-5). Although, the results of this work have established many intricacies of SGD-alumina processing, these studies have focused on the application of SGD-alumina for separations and catalysis. Earlier publications have presented the photochemistry and photophysics of adsorbed organic species on alumina and silica; however, the alumina and silica used in these studies are nonporous materials in which any effects are attributed to surface adsorption, rather than confinement within pores (6).

The research presented in this chapter demonstrates the ability of SGD-alumina to function as an effective a microorganized medium. This research also clearly demonstrates that the selectivity achieved in the photochemical production of vitamin D<sub>3</sub> can be greatly altered with the incorporation of a microorganized medium such as SGD-alumina.

### Preparation and Characterization of SGD-Alumina

**Steps in the Sol-Gel Preparation of Porous Alumina.** The preparation of SGD-alumina begins with the controlled hydrolysis of aluminum tri-*sec*-butoxide (see Figure 1). The temperature, pH, ratio of water to metal alkoxide, presence of a secondary solvent, nature of the alkyl substituents on the metal alkoxide, and reaction kinetics are all important factors that collectively control the size distribution of the particles formed during hydrolysis. Subsequent peptization involves the addition of an acid to charge stabilize the particles against aggregation processes, thereby forming a stable colloidal suspension (sol).

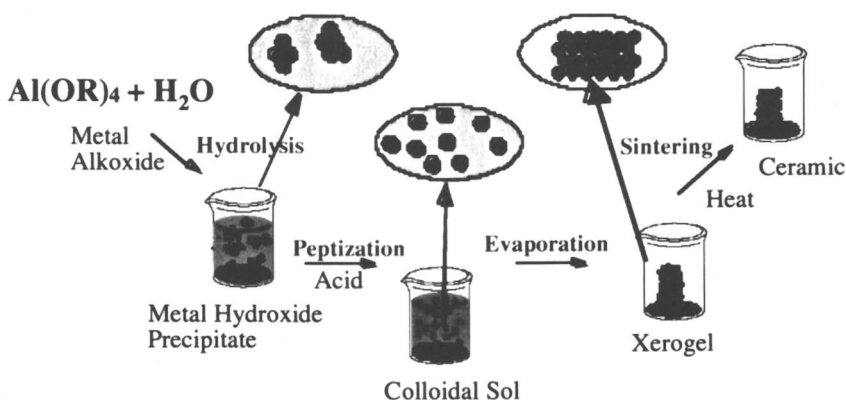


Figure 1. Steps in the preparation of SGD-alumina.

The pH and the nature of the acid are critical concerns in the peptization step. When the solvent of a sol is allowed to evaporate, the particles begin to aggregate until a wet gel is formed. A rigid xerogel is formed when the solvent has completely evaporated. Heating of an amorphous xerogel promotes crystallization and sintering of the particles by diffusion (7). The resulting porous ceramic can be described as a random close-packed arrangement of crystalline particles. The characteristics of the pores are directly dependent on the size, shape, and packing arrangement of the particles. With sol-gel methodology, it is possible in many instances to tailor the processing method to obtain particles of desirable size, shape and packing to produce porous ceramic materials with unique porosity properties.

**Characterization of the Particles and Pores of SGD-Alumina.** The particle size distribution of the boemite ( $\gamma$ -AlOOH) sol was determined by dynamic light scattering to be composed of particles with diameters in the range of 5-8 nm. Atomic force microscopy (AFM) imaging of the surface of a SGD-alumina plate which has been sintered at 400°C is shown in Figure 2. From these images it can be seen that the particles are flat and oblong in shape, with dimensions of 6 x 10 nm across the face of the particle and a thickness of ca. 2 nm.

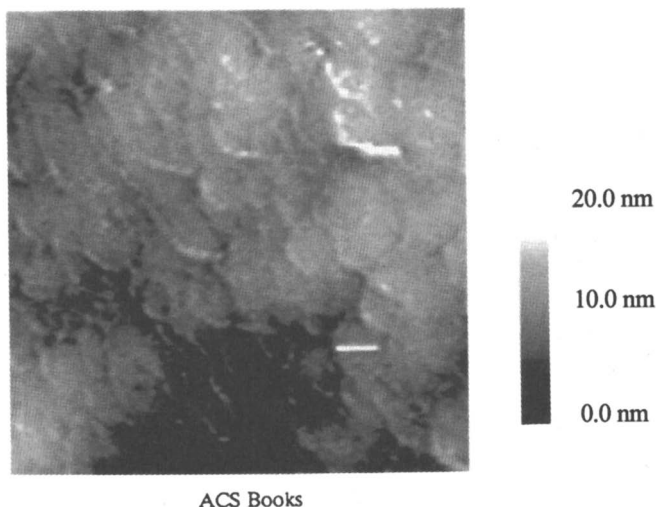


Figure 2. AFM image of SGD-alumina surface sintered at 400°C.

The specific surface areas, as determined by nitrogen adsorption/desorption, for SGD-alumina sintered at 400, 700 and 950°C were 251, 175 and 87 m<sup>2</sup>/g, respectively. The porosities for SGD-alumina sintered at 400, 700 and 950°C were 47.7, 47.7, 41.5%, respectively. The pore sizes were calculated from Brunauer,

Emmett, and Teller (BET) desorption data utilizing the Kelvin equation. These results reveal the relation between sintering temperature and pore size. Figure 3 presents the pore size distribution obtained from the Kelvin equation for SGD-alumina sintered at 400, 700 and 950 °C in which the corresponding average pore diameters are 36, 44, and 69 Å, respectively. The pore size distributions were obtained with the method of Barrett, Joyner, and Halenda (BJH) by utilizing the desorption data of the isotherm (8).

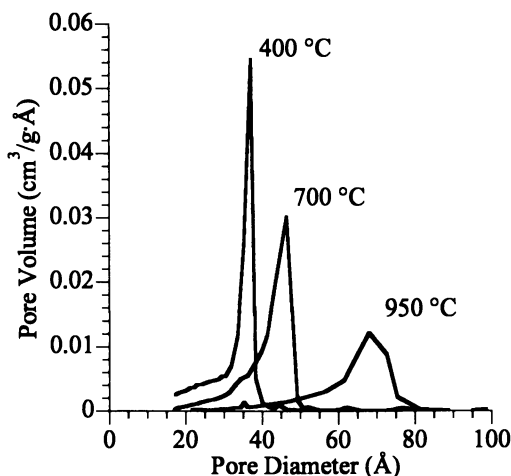


Figure 3. Pore size distribution for SGD-alumina sintered at 400, 700 and 950 °C based on the Kelvin equation and the method of BJH.

An important consideration with the pore widths determined for the SGD-alumina is the validity of the Kelvin equation. Error analyses have been published which demonstrate that the calculated pore size distribution is strongly dependent on the pore size (9). It is highly probable that pores widths of 36 Å may be inflated by more than 50%. Based on the approximate dimensions of the plate-like particles as determined by AFM of  $6 \times 10 \times 2$  nm, a slit-like pore width of ca. 20 Å would be expected. The calculated average pore width for the 700 °C sintered SGD-alumina of 44 Å also falls in the region of uncertainty for the Kelvin equation. Although the uncertainty in this value is not as great as that for the 400 °C sintered SGD-alumina, the average pore width for the 700 °C sintered SGD-alumina would also be expected to be less than 44 Å.

**Optical Characteristics of SGD-Alumina.** Figure 4 shows the transmittance UV-Vis spectra for SGD-alumina sintered at 400°, 700° and 950 °C. From this figure, it can be seen that as the pore size increases with increased sintering temperatures, the low wavelength cut-off exhibits a shift to longer wavelengths. This resulting shift is attributed to increased Rayleigh Scattering from the larger pores and particles within the SGD-alumina structure. Figure 4 also presents the excellent optical properties of

SGD-alumina. The large window of transparency for SGD-alumina allows for a variety of photochemical reactions.

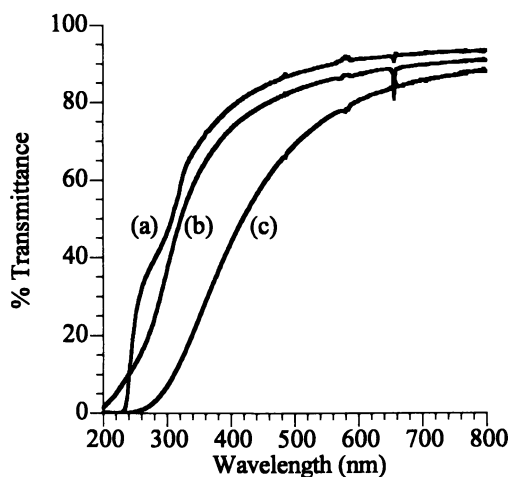


Figure 4. Optical transmission of SGD-alumina plates 0.5 mm thickness sintered at: (a) 400 °C, (b) 700 °C and (c) 950 °C.

### Photochemical Production of Vitamin D<sub>3</sub> within SGD-Alumina

Figure 5 shows the series of isomerizations that occur during the production of vitamin D<sub>3</sub>. The formation of vitamin D<sub>3</sub> begins with a photochemically allowed conrotatory electrocyclic ring opening of 7-dehydrocholesterol yielding previtamin D<sub>3</sub>. Previtamin D<sub>3</sub> is then susceptible to conrotatory electrocyclic ring closure to 7-dehydrocholesterol, conrotatory electrocyclic ring closure to lumisterol<sub>3</sub> or *cis-trans* isomerization to tachysterol<sub>3</sub>. Vitamin D<sub>3</sub> is produced from previtamin D<sub>3</sub> via a thermally allowed [1,7] sigmatropic hydrogen-shift. On photolysis of 7-dehydrocholesterol, a quasi-photostationary equilibrium is established between 7-dehydrocholesterol (7D), previtamin D<sub>3</sub> (P<sub>3</sub>), tachysterol<sub>3</sub> (T<sub>3</sub>), and lumisterol<sub>3</sub> (L<sub>3</sub>). Earlier studies have reported the major product on photolysis of 7-dehydrocholesterol in organic solvents to be tachysterol<sub>3</sub>. The isolated yield of vitamin D<sub>3</sub> from 7-dehydrocholesterol is typically in the range of 10-20% with nearly 100% of the by-product consisting of tachysterol<sub>3</sub> (10).

**Adsorption of 7-Dehydrocholesterol in SGD-Alumina.** For the incorporation 7-dehydrocholesterol, SGD-alumina plates (thickness of 0.5 mm) were placed in a solution containing 7-dehydrocholesterol dissolved in one of several organic solvents. In those experiments in which the plates were activated at 300 °C for 3 hr, the plates were added directly from a heated furnace to the solution. Activation of the SGD-alumina involves removal of surface adsorbed water at elevated temperatures in an atmosphere of air to generate a partially dehydroxylated surface in which Lewis acidic

aluminum sites are exposed. After adsorption equilibrium was reached, the plates were removed from the solution, rinsed with fresh solvent, and evacuated for 4 hours at 1 torr.

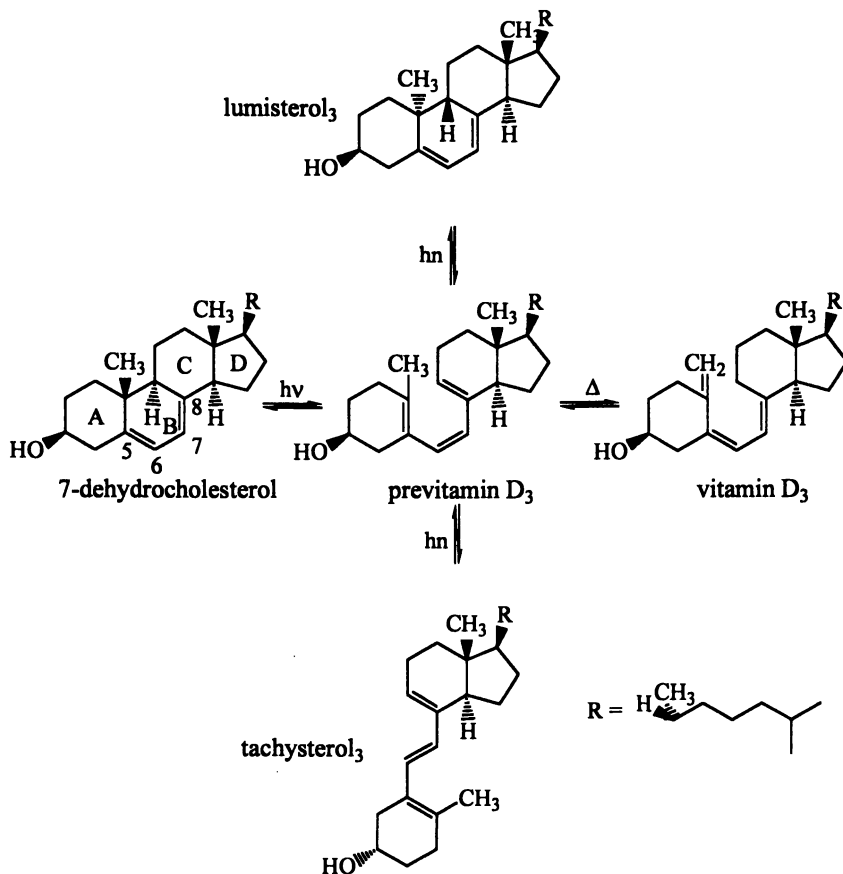


Figure 5. Photochemical and thermal isomerizations of vitamin D<sub>3</sub> related molecules.

Table 1 presents the maximum equilibrium adsorption concentrations for adsorption of 7-dehydrocholesterol within SGD-alumina of different sintering temperatures and activation conditions. The time required to reach these concentration was 4 hours. Based on the surface area of the SGD-alumina and the molecular dimensions of 7-dehydrocholesterol, these adsorption concentrations represent nearly complete occupation of the available surface area.



Table 1. Final adsorption concentrations of 7-dehydrocholesterol adsorbed in activated and non-activated SGD-alumina sintered at 400, 700, and 950°C.

Sintering Temperature	g 7-D/ g SGD-alumina	
	No Activation	Activated at 300°C
400 °C	0.11	0.12
700 °C	0.14	0.15
950 °C	0.08	0.08

**Adsorption Characterization of 7-Dehydrocholesterol with Diffuse Reflectance Infrared.** Figure 6 shows the diffuse-reflectance IR spectra of 7-dehydrocholesterol in the region of 2000-4000  $\text{cm}^{-1}$ . Spectrum (a) results from 7-dehydrocholesterol which has been encapsulated within non-activated SGD-alumina by adsorption from chloroform. The OH stretching frequency occurs at 3471  $\text{cm}^{-1}$ . Spectrum (b) results from a mixture of powdered SGD-alumina which has not been activated and powdered 7-dehydrocholesterol. The OH stretching frequency occurs at 3495  $\text{cm}^{-1}$ . As a comparison spectrum, spectrum (c) is a diffuse reflectance measurement of a KBr pellet of 7-dehydrocholesterol. The OH stretching frequency for this spectrum remains at 3495  $\text{cm}^{-1}$ . Spectrum (d) results from 7-dehydrocholesterol which has been encapsulated from solution into activated SGD-alumina. The OH stretching band has essentially been eliminated. This IR data indicates the hydrogen-bonding of the 3-hydroxyl group to the surface of non-activated SGD-alumina and the chemisorption of the 3-hydroxyl to the surface of activated SGD-alumina (see Figure 8).

**Electronic Interactions of 7-Dehydrocholesterol with Surface of SGD-Alumina as Probed with UV-Vis Spectroscopy.** It has been reported in many instances that the photochemical reactivity of organic molecules adsorbed on alumina or silica surfaces is affected by electronic interactions with the oxide surface (6). Figure 7 shows the UV absorption spectra for 7-dehydrocholesterol dissolved in various organic solvents and encapsulated within activated SGD-alumina. The absorbance maxima are at 262, 272, 282 and 294 nm for all of the systems. The UV-Vis spectra shown in Figure 4 indicate that electronic interactions between the diene moiety of 7-dehydrocholesterol and the surface of the SGD-alumina are not apparent.

**Photolysis of 7-Dehydrocholesterol Within SGD-Alumina.** For the photolysis experiments, SGD-alumina plates containing the adsorbed 7-dehydrocholesterol were placed along the inside of an immersion well photochemical apparatus (Ace Glass, Inc.) which utilizes an Hanovia 400W medium-pressure mercury lamp. A Vycor filter was used to isolate wavelengths greater than 240 nm. The product compositions

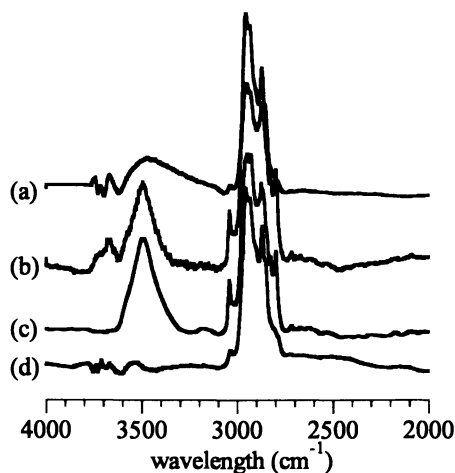


Figure 6. Diffuse-reflectance IR spectra of: (a) 7D adsorbed on non-activated SGD-alumina, (b) 7D mixed with non-activated SGD-alumina, (c) 7D KBr pellet, (d) 7D adsorbed on SGD-alumina activated at 300°C.

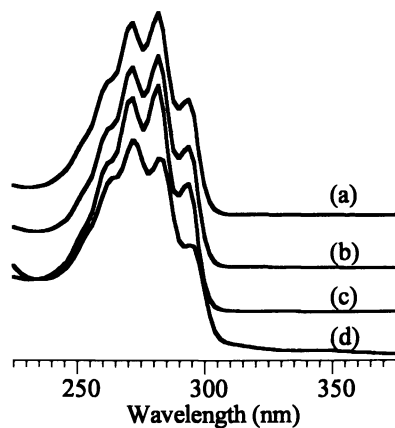


Figure 7. UV-Vis spectra of 7-dehydrocholesterol in various media: (a) ethanol, (b) diethyl ether, (c) hexane and (d) activated SGD-alumina.

were determined by HPLC of the desorbed products obtained from Soxhlet extraction of the photolyzed SGD-alumina plates. Percent recovery of reaction products was typically 99%.

The effect of confinement by the SGD-alumina pore structure is determined by the ratio of previtamin D<sub>3</sub> to tachysterol<sub>3</sub> in relation to the ratio obtained from the photolysis of 7-dehydrocholesterol in a hexane solution. Table 2 summarizes the percent composition of the photostationary-state obtained for the photolysis of 7-dehydrocholesterol encapsulated in SGD-alumina of different pore dimensions, loading percentage and activation condition.

**Table 2.** Percent compositions resulting from the photolysis of 7-dehydrocholesterol encapsulated in SGD-alumina of different pore dimensions and activation conditions.

	Activation	% loading 7D	7D	Percent Composition			
				P <sub>3</sub>	T <sub>3</sub>	L <sub>3</sub>	P <sub>3</sub>
hexane	-	-	6	52	35	7	1.5
400 °C	ambient	9.4	95	2.6	1.9	0.2	1.4
400 °C	ambient	3.5	63	20	15	2	1.4
400 °C	300°C	8.9	96	3.4	0.3	0.2	11
400 °C	300°C	1.3	11	62	24	2.2	2.5
700 °C	ambient	11	85	7.5	4.9	0.9	1.5
700 °C	ambient	3.7	69	18	12	2.2	1.5
700 °C	300°C	1.4	57	26	15	4.2	1.7
700 °C	300°C	6.2	70	18	11	1.1	1.6
700 °C	300°C	12	95	3	1.3	0.3	2.3
950 °C	300°C	0.7	40	36	20	4.3	1.8
950 °C	300°C	6.9	84	10	5.0	0.8	2.0
950 °C	ambient	6.9	76	15	7.8	1.2	1.9
950 °C	ambient	1.9	34	38	23	4.9	1.7

From the results presented in Table 2, it can be seen that the ratio of previtamin D<sub>3</sub> to tachysterol<sub>3</sub> is the greatest for SGD-alumina sintered at 400 °C and activated at 300 °C. Since SGD-alumina sintered at 400 °C contains the smallest pores, this result demonstrates the effect that pore size has on the product distribution.

**Adsorption Geometry of Transition-State.** The relation between molecular dimensions obtained from MM2 (11) for 7-dehydrocholesterol, the surface area of the SGD-alumina, and the adsorption concentration indicates that the adsorption geometry for 7-dehydrocholesterol is quite different in the SGD-alumina materials sintered at different temperatures.

The final adsorption values for 7-dehydrocholesterol indicate that adsorption is not directly related to the specific surface area of the SGD-alumina sample (see Table 1). It is believed that this type of adsorption would arise if the pore dimensions in the 400°C sample are too small to provide access for 7-dehydrocholesterol. It is also possible that the adsorption of 7-dehydrocholesterol in small pores occupies a greater amount of surface area than adsorption in larger pores. In the case of smaller or narrower pores, the adsorption of 7-dehydrocholesterol may be envisioned to occur in such a manner in which the cholesterol ring structure is essentially parallel to the surface of the plate-like particle (see Figure 8). In the case of larger, or wider, pores, the surface adsorption of 7-dehydrocholesterol may occur in a manner in which the cholesterol ring structure is perpendicular to the surface of the plate-like particle (see Figure 9).

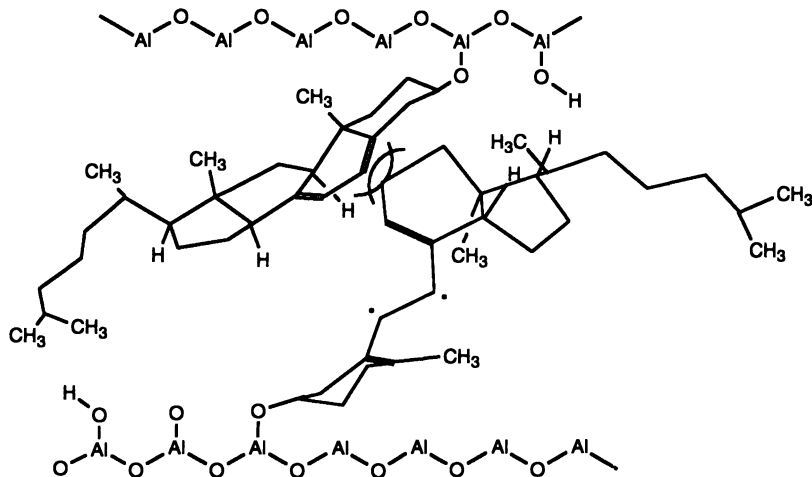


Figure 8. Steric interactions arising from transition-state conformation required for *cis-trans* isomerization of previtamin D<sub>3</sub> to tachysterol<sub>3</sub> in activated SGD-alumina sintered at 400 °C.

It is believed that the confinement effect on the product distribution from the photolysis of 7-dehydrocholesterol is not solely a result of adsorption or chemisorption of 7-dehydrocholesterol to the SGD-alumina surface. In the case of activated SGD-alumina sintered at 400°C, it is believed that the pore dimensions are small enough to inhibit the *cis-trans* isomerization of previtamin D<sub>3</sub> which is chemisorbed to the SGD-alumina surface (Figure 8). Rotation about the C6-C7 bond can

be accomplished by rotation of the A-ring or the C/D ring system or by a combination of rotation of these two ring systems. The anchoring of the A-ring by chemisorption at the 3-hydroxyl of 7-dehydrocholesterol to the surface of the SGD-alumina, as shown by IR analysis, requires rotation about the C6-C7 bond to be performed by the much larger C/D-ring system of the cholesterol molecule. In the case of 7-dehydrocholesterol which is hydrogen-bonded to the surface of the non-activated SGD-alumina sintered at 400 °C, the surface adsorption is not strong enough to prevent rotation about the C6-C7 bond by the smaller A-ring system of previtamin D<sub>3</sub>. From these results it can be concluded that the pore dimensions of the 400°C sample are not small enough to inhibit the rotation of the A-ring system. For the 700°C and 950°C SGD-alumina, the pore dimensions of these materials are not capable of imposing sufficient confinement on previtamin D<sub>3</sub> to prevent the *cis-trans* isomerization to tachysterol<sub>3</sub>. For the 400 and 700°C SGD-alumina which was not activated prior to adsorption, the P<sub>3</sub>/T<sub>3</sub> ratio was essentially unchanged from that obtained with the solution photochemistry. The increase in the ratio with the non-activated 950°C SGD-alumina is attributed to excitation at longer wavelengths which greatly favors the formation of previtamin D<sub>3</sub>. As shown above, the larger pore 950°C SGD-alumina exhibits a lower wavelength cut-off ca. 300nm.

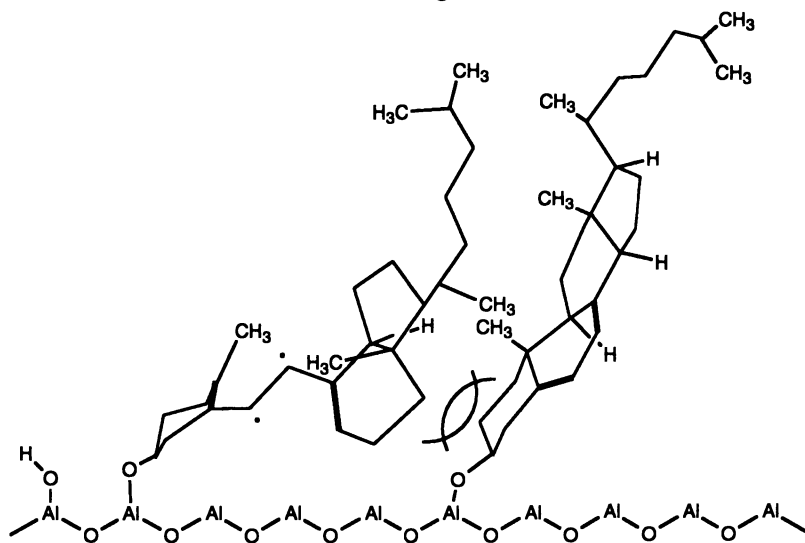


Figure 9. Steric interactions arising between co-adsorbed molecules in SGD-alumina sintered at 700 and 950 °C at the transition-state required for *cis-trans* isomerization of previtamin D<sub>3</sub> to tachysterol<sub>3</sub>.

At higher loading levels it is believed that 7-dehydrocholesterol adsorbs to the surface of activated SGD-alumina in a Langmuir-Blodgett manner. This arrangement at high loading levels provides sufficient confinement to inhibit the *cis-trans* isomerization to tachysterol<sub>3</sub> (Figure 9). The source of confinement results from the

close proximity of surface adsorbed molecules. The chemisorption through the 3-hydroxy group is important since it provides a source of restriction which does not exist in the non-activated systems or the solid-state crystal system. At lower loading levels sufficient distance exists between the adsorbed molecules to allow the *cis-trans* isomerization to tachysterol.

**Solid-State Photolysis of 7-Dehydrocholesterol.** Several studies have demonstrated that the solid-state photochemistry of organic crystals can have a substantial effect on product distributions when compared to the corresponding results of solution photochemistry (12). Since the photolysis of 7-dehydrocholesterol is performed in the absence of solvent, the solid-state photoreactivity of 7-dehydrocholesterol was examined. Films of 7-dehydrocholesterol were prepared by dip-coating a glass tube in a concentrated solution of 7-dehydrocholesterol dissolved in chloroform. The glass tubes were then photolyzed in the same manner as the SGD-alumina containing 7-dehydrocholesterol. The product compositions are shown in Table 3.

Although the results of the photolysis of 7-dehydrocholesterol in the solid-state indicate that different mechanistic concerns may effect the product distribution, it can be concluded that the observed selectivity with the SGD-alumina system is not a consequence of solid-state or condensed phase photochemistry. The SGD-alumina must then provide additional conformational flexibility control on 7-dehydrocholesterol and the isomers derived from it.

Table 3. Percent composition of solid-state photolysis of 7-dehydrocholesterol film.

Photolysis Medium	Percent Composition				
	7D	P <sub>3</sub>	T <sub>3</sub>	L <sub>3</sub>	P <sub>3</sub> /T <sub>3</sub>
hexane	6	52	35	7	1.5
7D thin film	64	17	17	2.4	1.0

**Conclusions.** This research has presented the ability of SGD-alumina to function as a microorganized medium to alter the observed selectivity for the photolysis of 7-dehydrocholesterol. The pore size of SGD-alumina and adsorption concentration of 7-dehydrocholesterol are the two major factors which determine the selectivity. The research also indicates that adsorption of an isolated molecule of 7-dehydrocholesterol via the 3-hydroxyl group does not greatly effect the photochemical product distribution. For adsorption to effect the product distribution, a high loading level of 7-dehydrocholesterol is necessary which then introduces a further degree of confinement. It is recognized that the conversion rates are lower than those observed in organic solvent. However, the lower conversion rate

is a result of confinement in which other decay processes are in effect other than the ring-opening of 7-dehydrocholesterol. Current studies in our laboratories are examining the effect of confinement on conversion rates and the optimization of this conversion rate.

### Literature Cited

1. (a) Thomas, J. K. *Chem. Rev.* **1980**, *80*, 283. (b) Turro, N. J.; Cox, G. S. Paczkowsky, M. A. *Top. Curr. Chem.* **1985**, *129*, 57. (c) de Mayo, P.; Sydnes, L. K. *J. Chem. Soc. Chem. Commun.* **1989**, 994. (d) Takagi, K.; Sawaki, Y.; Crit. Rev. *Biochem Mol. Biol.* **1993**, *28*, 323-367. (e) Suddaby, B. R.; Brown, P. E.; Russell, J. C.; Whitten, D. G. *J. Am. Chem. Soc.* **1985**, *107*, 5609-5617. (f) Spooner, S. P.; Whitten, D. G. In *Photochemistry in Organized and Constrained Media*; Ramamurthy, V. Ed.; VCH: New York, 1991: Chapter 15 and references therein. (g) Hrovat, D.; Lieu, J. H.; Turro, N. J.; Wiess, J. D. G. *J. Am. Chem. Soc.* **1984**, *106*, 7033. (h) Lem, G.; Kaprinidis, N. A.; Schuster, D. I.; Ghatlia, N. D.; Turro, N. J. *J. Am. Chem. Soc.*, **1993**, *115*, 7009. (i) Ramamurthy, V.; In *Photochemistry in Organized and Constrained Media*; Ramamurthy, V. Ed.; VCH: New York, 1991; p 429-493. (j) Ramamurthy, V.; Corbin, D. R.; Turro, N. J.; Zhang, Z.; Garcia-Garibay, M. A. *J. Org. Chem.* **1991**, *56*, 255-261. (k) Turro, N. J.; Cheng, C.C.; Abrams, L. Corbin, D. R. *J. Am. Chem. Soc.* **1987**, *109*, 2449-2456. (l) Ogawa, M.; Kuroda, K. *Chem. Rev.* **1995**, *95*, 399-438. (m) Thomas, J. K. *Acc. Chem. Res.* **1988**, *21*, 275-280. (n) Usami, H.; Takagi, K.; Sawaki, Y. *Chem. Lett.* **1992**, 1405-1408. (o) Ramamurthy Mayo, P.; Ware, W. R. *J. Phys. Chem.* **1993**, *97*, 5995-6001. (p) Lednev, I. K.; Mathivanan, N.; Johnston, L. J. *J. Phys. Chem.* **1994**, *98*, 11444-11451. (q) Thomas, J. K. *Chem. Rev.* **1993**, *93*, 301-320. (r) Ford, W. E.; Kamat, P. V. *J. Phys. Chem.* **1989**, *93*, 6423-6428. (s) Johnston, L. J.; In *Photochemistry in Organized and Constrained Media*; Ramamurthy, V. Ed.; VCH: New York, 1991; Chapter 8. (t) Al-Ekabi, H. In *Photochemistry in Organized and Constrained Media*; Ramamurthy, V. Ed.; VCH: New York, 1991; p 495-534. (u) Fox, M. A. *Acc. Chem. Res.* **1983**, *16*, 314-321.
2. (a) Chu, L.; Tejedor-Tejedor, M. I.; Anderson, M. A. *Mat. Res. Soc. Symp. Proc.* **1994**, *346*, 855-860. (b) Xu, Q.; Anderson, M. A. *J. Am. Ceram. Soc.* **1994**, *77*, 1939-1945. (c) Sheng, G.; Chu, L.; Zeltner, W. A.; Anderson, M. A. *J. Non-Crystalline Solids*, **1992**, *147*, 548-553. (d) Gieselmann, M. J.; Anderson, M. A. *J. Am. Ceram. Soc.* **1989**, *72*, 980-985. (e) Anderson, M. A.; Gieselmann, M. J.; Xu, Q. *J. Membrane Sci.* **1988**, *39*, 243-258.
3. (a) Leenaars, A. F. M.; Burggraaf, A. J. *Journal of Colloid and Interface Science*, **1985**, *105*, 27-40. (b) Leenaars, A. F. M.; Keizer, K.; Burggraaf, A. J. *Journal of Materials Science*, **1984**, *19*, 1077-1088. (c) Hsieh, H.P.; Bhave, R. R.; Fleming, H.L. *Journal of Membrane Science*, **1988**, *39*, 221-241. (d) Okubo, T.; Watanabe, M.; Kusakabe, K.; Morooka, S. *J. Mat. Sci.* **1990**, *25*, 4822-4827. (e) Uhlhorn, R. J.

R.; Huis In't Veld, M. H. B. J.; Keizer, K.; Burggraaf, A. J. *J. Mat. Sci.* **1992**, *27*, 527-537. (f) Vendange, V.; Columban, Ph. *J. Mater. Res.* **1996**, *11*, 518-528. (g) Chane-Ching, J-Y.; Klein, L. C. *J. Am. Ceram. Soc.* **1988**, *71*, 86-90.

4. Gieselmann, M. J. Ph. D. Thesis, University of Wisconsin-Madison, 1991.

5. (a) Yoldas, B. E. *Amer. Ceram. Soc. Bull.* **1975**, *54*, 286-288. (b) Yoldas, B. E. *Amer. Ceram. Soc. Bull.* **1975**, *54*, 289-290. (c) Yoldas, B. E. *J. Mat. Sci.* **1975**, *10*, 1856-1860.

6. (a) Liu, Y. S.; de Mayo, P.; Ware, W. R. *J. Phys. Chem.* **1993**, *97*, 5995-6001. (b) Lednev, I. K.; Mathivanan, N.; Johnston, L. J. *J. Phys. Chem.* **1994**, *98*, 11444-11451. (c) Thomas, J. K. *Chem. Rev.* **1993**, *93*, 301-320. (d) Ford, W. E.; Kamat, P. V. *J. Phys. Chem.* **1989**, *93*, 6423-6428. (e) Johnston, L. J. In *Photochemistry in Organized and Constrained Media*; Ramamurthy, V. Ed.; VCH: New York, 1991; Chapter 8 and references therein.

7. Brinker, C. J.; Scherer, G. W. *Sol-Gel Science*, Academic Press: New York, 1990; Ch. 12.

8. Barrett, E. P.; Joyner, L. G.; Halenda, P. H. *J. Am. Chem. Soc.* **1951**, *73*, 373.

9. Gregg, S. J.; Sing, K. S. W. *Adsorption, Surface Area and Porosity*, 2nd ed.; Academic: New York, 1982; p. 152.

10. (a) Havinga, E.; Sanders, M.; Pot, J. *Fortchr. Chem. Org. Naturstoffen*, **1969**, *29*, 131-157. (b) Verloop, A.; Koevoet, A. L.; Van Moorselaar, R.; Havinga, E. *Recueil*, **1959**, *78*, 1004-1016.

11. Allinger, N. L. *J. Comput. Chem.* **1993**, *14*, 755-68.

12. (a) Scheffer, J. R.; Pokkuluri, P. R. In *Photochemistry in Organized and Constrained Media*; Ramamurthy, V. Ed.; VCH: New York, 1991; Chapter 5. (b) Zimmerman, H. E.; Zuraw, M. J. *J. Am. Chem. Soc.* **1989**, *111*, 2358. (c) Zimmerman, H. E.; Zuraw, M. J. *J. Am. Chem. Soc.* **1989**, *111*, 7974. (d) Ramamurthy, V.; Venkatesan, K. *Chem. Rev.* **1987**, *87*, 433-481. (e) Zimmerman, H. E.; Zhu, Z. *J. Am. Chem. Soc.* **1995**, *117*, 5245-5262.



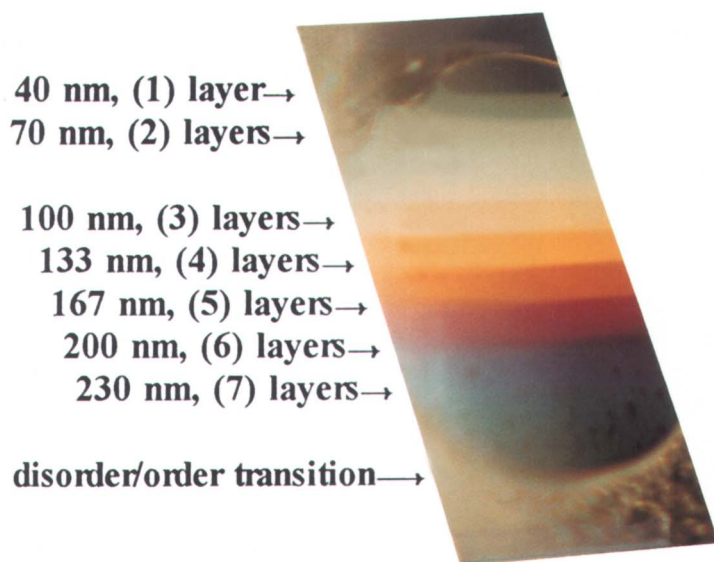


**Figure 3.** Interference strips in a vertical macroscopic stratifying film formed from a 20 v% silica suspension with a particle diameter of 19nm. Each color strips represents a different number of particle layers inside the thinning film. (Reproduced from reference 17. Copyright 1992 American Chemical Society.)

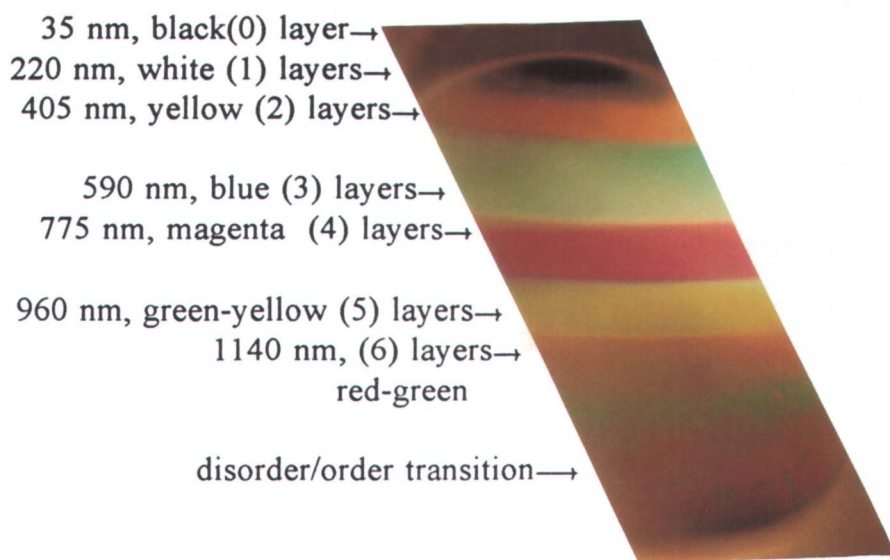


**Figure 4.** Interference stripes in a vertical macroscopic stratifying film formed from a 44 v% latex suspension with a particle diameter of 156nm. Each color stripe represents a different number of particle layers inside the thinning film.

## Author Index

- Anderson, Marc A., 247  
Barois, P., 54  
Braun, Christian, 24  
Butler, Paul D., 73  
Chan, R., 231  
Chen, V., 231  
Chu, S., 196  
Cosgrove, Terence, 153  
Dalnoki-Veress, Kari, 127  
Dedieu, J.-C., 86  
Demé, B., 86  
Dubois, M., 86  
Dutcher, John R., 127  
Findenegg, Gerhard H., 24  
Forrest, James A., 127  
Gaub, Herman E., 208  
Green, Nicholas, 153  
Gulik-Krzywicki, Th., 86  
Harrowell, Peter, 104  
Holland, Nolan B., 180  
Huang, E., 140  
Israelachvilli, Jacob N., 215  
Jack, Kevin S., 153  
Lang, Peter, 24  
Larson, R. G., 196  
Manne, Srinivas, 2  
Marchant, Roger E., 180  
Marques, C. M., 169  
Moreau-Biansan, L., 54  
Nikolov, Alex, 40  
Obey, Timothy M., 153  
Park, Chad K., 215  
Perkins, T. T., 196  
Prud'homme, R., 169  
Qiu, Yongxing, 180  
Richetti, P., 54, 169  
Rief, Matthias, 208  
Rockford, L., 140  
Rueggsegger, Mark, 180  
Russell, T. P., 140  
Schultz, Forrest S., 247  
Seitz, Markus, 215  
Smith, D. E., 196  
Steitz, Roland, 24  
Tsui, O. K. C., 140  
Warr, Gregory G., 2  
Wasan, Darsh, 40  
Wong, Joyce Y., 215  
Wood, Matthew, 153  
Yang, Y., 169  
Zemb, Th., 86

# Subject Index

## A

- Adsorbed aggregates model, neutron reflectometry, 8–9
- Adsorbed cylindrical and spherical micelles, neutron reflectometry model, 8
- Adsorption, solute at interface, 2
- Adsorption isotherms
  - solution depletion methods, 4–5
  - tetradecyltrimethylammonium (TTAB) bromide onto  $\text{Al}_2\text{O}_3$ , 4*f*
- Aggregate morphologies
  - ionic surfactants on oppositely charged hydrophilic surfaces, 14–15
  - mica, 14–15
- Aggregation number, fluorescence or static emission intensities, 10
- Alumina
  - ionic surfactants on, 14
  - specific relaxation rates for PS latex, silica, and alumina in water, 157*f*
  - See also* NMR solvent relaxation studies; Sol-gel derived (SGD) alumina
- Amorphous films, transition to sliding, 122–123
- Amphiphiles
  - adsorption isotherms of  $\text{C}_8\text{E}_4$  on CPG silica glass, 28*f*
  - adsorption of  $\text{C}_8\text{E}_4$  from aqueous solution on CPG porous silica glass, 26, 27*f*
  - oligo-oxyethylene mono-*n*-alkyl ether ( $\text{C}_m\text{E}_n$ ) family, 24–25
  - phase diagrams, 25*f*
  - surface aggregation from dilute solutions, 25–28
- Atomic force microscopy (AFM)
  - basis of single molecule force spectroscopy, 208, 210
  - connection between bulk and interfacial self-assembly structures, 3
  - coupling with other techniques, 13–14
  - dc force resolution, 12
  - image of sol-gel-derived alumina surface sintered at 400°C, 249*f*
  - image of spherical micelles, 13*f*

- imaging sample surface, 12–14
- ionic surfactants on oppositely charged hydrophilic surfaces, 14–15
- limitations of AFM imaging and interpretation, 17–18
- mapping colloidal stabilization forces, 12–13
- micrograph of asymmetric diblock copolymer of P(S-*b*-MMA) containing cylinders of PMMA in PS matrix, 147, 148*f*
- micrograph of P(S-*b*-MMA) symmetric, diblock copolymer on striped Au/SiO<sub>2</sub> substrate, 149, 150*f*
- nonionic and zwitterionic surfactants on hydrophilic surfaces, 15
- schematic of imaging mechanism, 13*f*
- shape changes and kinetics in interfacial aggregates, 17
- surface-induced assembly of surfactant polymers, 184, 186–189
- surfactants on anisotropic hydrophobic surfaces, 15–16
- surfactants on isotropic hydrophobic surfaces, 16–17
- time-dependent adsorption of surfactant polymer with 1:5 ratio dextran to hexanoyl groups (PVAm/Dex-Hex), 186, 187*f*
- topographic images of surfactant polymers with different hydrophobic/hydrophilic ratio adsorbed on graphite, 188*f*
- typical imaging forces, 13
- See also* Single molecule force spectroscopy

## B

- Biomaterial devices
  - existing surface modification methods, 181
  - spontaneous and nonspecific adsorption of plasma proteins, 180
- See also* Oligosaccharide surfactant polymers

Biomimetic surface engineering. *See* Oligosaccharide surfactant polymers

Bovine serum albumin (BSA)

continuous protein deposition, 234

determining onset of flux decline and transmission reduction, 236

evidence of protein aggregates, 233  
fouling of track etched membranes, 232–233

proposed stages of fouling, 233

*See also* Proteins

Bragg peak, specular neutron reflectivity spectra of boundary layer, 29–30, 31*f*

Brillouin light scattering (BLS)

boundary conditions at film interfaces

for film-guided modes, 133

density fluctuations propagating through film and surface, 133

dispersion curves, 133–134

measured and calculated velocity dispersion curves for freely standing PS films, 134*f*

measuring glass transition and associated relaxation dynamics, 128

measuring  $T_g$  for films supported on substrates, 135

reduction in  $T_g$  with decreasing film thickness for freely standing PS films, 135

$T_g$  versus room temperature film thickness for freely standing PS films, 136*f*

using film-guided modes probing temperature dependence of mass density, 134–135

versus photon correlation spectroscopy (PCS), 136

*See also* Glass transition in thin polymer films

## C

Calorimetry, probing energetics of surfactant adsorption, 5–6

Capillary condensation

capillary force by bridging droplet, 61–62

comparison between experimental force profiles and modeling forces above and below bulk phase transition, 65*f*

current phenomenon, 54

Derjaguin-like term, lamellar phase, 60

dislocation loop array model, lamellar phase, 59–61, 62, 64

evolution of force profiles in lamellar phase and symmetrical microemulsion phase, 58*f*

experimental lyotropic system, 56

force profile analysis, 69

force profiles, 56, 59

investigating by surface force apparatus, 55

lamellar droplet capillary condensed from microemulsion phase, modeling, 61–62

lamellar droplet from bicontinuous microemulsion, 55

lamellar phase, force profile analysis, 62, 64

lamellar phase modeling, 59–61

microemulsion phase analysis, 64, 66–70

modeling, 59–62

modeling force profiles between sphere- and plate-confining lamellar phase, 63*f*

previous experimental studies, 69–70

refractive index profiles for lamellar and microemulsion phases, 68*f*

refractive index profiles of microemulsion phase, 66, 69

relaxation mechanism in lamellar phase, 60

scattering experiments choice techniques, 54–55

schematic representation of  $C_{10}E_4$ /octane/ $H_2O$  phase diagram, 57*f*

specific lamellar order, microemulsion phase, 62

sum term, lamellar phase, 60–61

surface force apparatus, 55–56

X-ray scattering, microemulsion phase, 64, 66

X-ray spectra increasing temperature from lamellar to microemulsion phase, 67*f*

Catanionic surfactant aggregates

chain melting temperature dependence on molar ratio of cationic surfactant, 90, 92*f*

comparison with other surfactant microstructures, 98, 100

controlling composition of quasiternary system, 88, 90

electron microscopy after cryofracture, 91, 94*f*, 95*f*, 96*f*, 97*f*

estimated surface potential and osmotic pressure, 89*f*

freeze fracture electron microscopy method, 88

- materials and methods, 87–88  
 osmotic pressure in absence of excess salt, 87  
 pH and electrical conductivity of 2% solution of catanionic system, 89*f*  
 possible uses of nanodiscs, 100  
 rigid platelet characterization, 90  
 sample preparation, 87  
 size control of nanodiscs, 91  
 small-angle neutron scattering method, 87  
 small-angle X-ray scattering spectra above and below chain melting temperature, 93*f*  
 strong electrostatic interactions, 86–87  
 ternary equilibrium phase diagram, 91, 98–100  
 wide-angle and small-angle X-ray scattering method, 87  
 wide-angle X-ray scattering signal at 25°C and 50°C for two sample compositions, 92*f*
- Cetyltrimethylammonium (CTA) surfactants  
 mixed counterion (MC) system, 77, 78*f*, 80*f*  
 NSSANS of worm-like micelles, 77–79  
*See also* Near-surface small-angle neutron scattering (NSSANS)
- Clay. *See* Laponite; Montmorillonite
- Colloidal suspensions in confined films  
 comparing numerical results with experiments, 50, 52  
 diffraction patterns from macroscopic vertical foam film, 45, 46*f*  
 effects of polydispersity in particle size on layering and structural transitions, 52  
 experimental set-up for monitoring particle layers within films, 42*f*  
 experimental techniques, 41–45  
 film thickness estimation from photocurrent intensity, 41, 43  
 hexagonal packing structure inside vertical liquid films containing latex particles, 50  
 inlayer radial distribution function (RDF) of surface layers for different film thickness, 47, 49*f*  
 inlayer RDF for 1.7 $\sigma$  film thickness and particle concentration 46 vol.-%, 50, 51*f*  
 inlayer RDFs for different layers in film of particle concentration 46 vol.-%, 47, 49*f*, 50
- interference stripes in vertical macroscopic stratifying films, 44, 45  
 long-range oscillatory structural forces, 50  
 microinterferometric technique, 43–45  
 Monte Carlo simulation investigating dependence of in-layer particle structuring on film thickness, 45, 47, 50  
 number of film thickness transition steps versus particle concentration, 50, 51*f*  
 particle self-layering phenomenon by vertical macroscopic film-thinning behavior, 44, 45  
 particle structural transition phenomenon using digital videomicrography, 52  
 photocurrent versus time interferogram of film-thinning process, 44*f*  
 radial distribution function (RDF) of particles in layer, 47  
 reflected light microinterferometric method, 45  
 structural disjoining pressure versus film thickness, 47, 48*f*  
 surface plot of inlayer RDF versus inlayer particle distance and concentration, 48*f*  
 typical density distributions of particles across film thickness three times particle diameter, 46*f*
- Comb-like surfactant polymers  
 plots of surface tension versus logarithm of concentration of aqueous surfactant polymer solutions, 185*f*  
 surface-active properties at air–water interface, 182, 184  
 synthesis and characterization, 182, 183*f*  
*See also* Oligosaccharide surfactant polymers
- Confinement  
 effects on ordering in polymers, 143–145  
 influence on relative stability of phases, 24  
 photochemical production of vitamin D<sub>3</sub> within SGD-alumina, 251–258  
*See also* Diblock copolymers; Lyotropic system, ternary; Sol–gel-derived (SGD) alumina; Vitamin D<sub>3</sub>
- Copolymers. *See* Diblock copolymers; Polymer morphology
- Crystallization, appearance of in-plane periodic order in layered liquid, 115–116

## D

## 7-Dehydrocholesterol

- adsorption characterization with diffuse reflectance infrared (IR) spectroscopy, 253
- adsorption in sol-gel-derived (SGD) alumina, 251–253
- diffuse reflectance IR spectra, 254*f*
- electronic interactions with surface of SGD alumina, 253
- photochemical and thermal isomerizations, 252*f*
- photolysis within SGD alumina, 253, 255
- solid-state photolysis, 258
- UV-vis spectra in various media, 254*f*
- See also* Sol-gel-derived (SGD) alumina; Vitamin D<sub>3</sub>

## Denaturation

- possible consequence of local shear field and small pores, 232
- See also* Proteins

## Derjaguin approximation, study of normal interbilayer forces, 216

## Derjaguin-like term, restoring elastic force of confined sample, 60

## Diblock copolymers

- addressing role of interfacial interactions on orientation, 145
- AFM micrograph of asymmetric P(*S-b*-MMA) containing cylinders of PMMA in PS matrix, 148*f*
- AFM micrograph of symmetric P(*S-b*-MMA) on striped Au/SiO<sub>2</sub> substrate, 150*f*
- behavior of asymmetric, P(*d-S-b*-MMA) thin films, 147
- confinement effects on ordering, 143–145
- difference between cylindrical and lamellar structures near polymer-air interface, 147
- intensity of first-order Bragg reflection as function of temperature for P(*d-S-b-n*BMA) films of different thickness, 146*f*
- laterally heterogeneous surfaces, 149
- laterally homogeneous surfaces, 145, 147–149
- log of neutron reflectivity profiles for symmetric P(*d-S-b-n*BMA) film, 146*f*
- manipulating morphology and thermodynamics, 143
- microphase separation into range of morphologies, 141

neutron reflectivity measurements, 144–145

order-disorder transition, 144

removing preferential interactions at polymer-air interface, 145, 147

schematic of lamellar microdomains, 142*f*

*See also* Polymer morphology

## Diffraction patterns

H<sub>1</sub>-phase of surfactant C<sub>12</sub>E<sub>5</sub> in water, 35–36

vertical macroscopic latex film, 45, 46*f*

Diffuse reflectance infrared, adsorption characteristics of 7-dehydrocholesterol, 253, 254*f*

Digital videomicrography, particle structural transition phenomenon, 52

Dimyristoyl-phosphatidylcholine (DMPC) covalently attached membranes, 221–224

formation of soft-supported DMPC bilayers on mica, 221–228

normal interaction forces of soft-supported DMPC bilayers, 224, 226

physisorbed bilayers, 221

*See also* Phospholipid bilayers

Dipalmitoylphosphatidylethanolamine (DPPE)

forces and fusion between solid-supported phospholipid bilayers, 216, 218–219

*See also* Phospholipid bilayers

Dislocation loop array model, lamellar phase, 59–61, 64

## Disordered films

slow relaxation, 116–118

thick and thin *n*-octane films, 117–118

## DNA molecules

analysis of unraveling mechanisms, 205, 207

close agreement between experiment and simulations, 205

comparison of time sequence of experimental images in extensional flow with images from bead-spring simulations, 203*f*, 204*f*

configuration of tethered DNA molecule, 200*f*

crossed-slot device generating extensional flow on freely suspended, 202*f*

Deborah numbers, 205

illustration of bead-spring chain, 198*f*

mass distribution as function of position downstream of tethering point, 201*f*

- micromechanical model of DNA, 197–199
- percentage of folded chains during extensional flow as function of Deborah number, 206*f*
- released, 199, 205
- tethered, 199
- Dodecyl dimethylammoniopropanesulfonate (DDAPS), zwitterionic surfactant, 15
- E**
- Electron microscopy
- freeze-fracture method, 88
- nanodiscs, catanionic surfactant aggregates, 91, 94*f*, 95*f*, 96*f*, 97*f*
- See also* Proteins
- Ellipsometry
- adsorbed nonionic surfactants on silica, 9*t*
- analyzing light specularly reflected from homogeneous film, 128
- commonly used schemes, 131
- first technique measuring  $T_g$  for thin polymer films, 131–132
- investigating adsorbed films of surfactants, 9
- polarizer angle versus temperature for uncapped supported polystyrene film, 132*f*
- sensitive measurement of film properties, 131
- studying glass transition in thin polymer films, 130–132
- See also* Glass transition in thin polymer films
- Elongational flow field, hierarchy of confinement, 3
- F**
- Fibronectin
- arrangement of domains in bovine, 209*f*
- force versus extension curves for native, 212*f*
- high molecular weight glycoproteins, 210
- unfolding forces, 211, 213
- See also* Single molecule force spectroscopy; Titin
- Film thickness
- control parameter for transition between liquid and solid, 106–109
- estimation from intensity of photocurrent, 41, 43
- number of transition steps versus particle concentration, 50, 51*f*
- varying to capture changes in ordering transition, 144–145
- Flow calorimetry, surfactant adsorption, 5–6
- Flow fields
- behavior of long polymer molecules, 196–197
- See also* DNA molecules
- Fluorescence microscopy, adsorption of lipid vesicles onto polymer-supported mixed monolayers, 224
- Fluorescence probe studies
- highly concentrated micelle solutions, 11
- investigating structure of adsorbed surfactant films, 12
- ionic surfactants, 11–12
- key assumptions, 10–11
- micelle classes, 10
- pioneering studies of nonionic surfactant adsorbed films, 11
- static emission method, 10
- surface aggregates, 9–12
- time-resolved quenching experiment, 10
- Fluorescence quenching, adsorbed nonionic surfactants on silica, 9*t*
- Force profile analysis
- difficulty at high temperatures, 59
- evolution in lamellar phase and symmetrical microemulsion phase, 58*f*
- experimental, 56, 59
- lamellar phase, 62, 64
- microemulsion phase, 69
- Fouling
- capturing different phases, 245
- determining true fouling threshold, 239, 244
- incipient fouling regime, 236
- initiation by filtration process, 239
- proposed stages, 233
- See also* Proteins
- Friction
- changes with varying surface topology, 120
- cobblestone model of solid friction, 120–121
- constitutive equation, 119–120
- kinetic, 113–114
- static in rigid films, 111–113
- transformation of mechanical energy into heat, 106

September 7, 2012 | <http://pubs.acs.org>  
 Publication Date: August 20, 1999 | doi: 10.1021/bk-1999-0736.ix002



## G

## Glass transition in thin polymer films

- Brillouin light scattering, 133–136
- diffusely scattered light, 132–138
- ellipsometry, 130–132
- ellipsometry polarizer angle versus temperature for uncapped supported polystyrene (PS) film, 132*f*
- intensity autocorrelation functions for freely standing PS film, 138*f*
- measured and calculated velocity dispersion curves for freely standing PS films, 134
- optical experiments probing glass transition ( $T_g$ ), 128
- photon correlation spectroscopy, 136–138
- schematic diagram of light-scattering mechanisms, 129*f*
- schematic diagrams of cross-sections of different film geometries, 130*f*
- specularly scattered light, 129–132
- $T_g$  versus room temperature film thickness for PS films, 137*f*
- $T_g$  versus room temperature film thickness for freely standing PS films, 136*f*

## Glycocalyx-like surface

- pursuing simple, well-defined practical modification method, 181
- using protruding dextran oligosaccharides mimicking nonadhesive properties of glycocalyx, 189–190

*See also* Oligosaccharide surfactant polymers

## Graphite

- surfactants on, 15–16
- See also* Oligosaccharide surfactant polymers

## H

## Hemicelles, hydrophobic aggregates on surface, 3

## Hertz theory, study of normal interbilayer forces, 216

## Hexagonal packing, interference methods inside vertical liquid films containing latex particles, 50

## Hierarchy of confinement

- shear or elongational flow field, 3
- starting point for building up, 3

Highly oriented pyrolytic graphite (HOPG). *See* Oligosaccharide surfactant polymers

## Hydrocarbon chains, lubrication, 117

Hydrodynamics of single molecule. *See* DNA molecules

## Hydrophilic surfaces

- ionic surfactants, 14–15
- neutron reflectometry, 7
- nonionic and zwitterionic surfactants, 15

## Hydrophobic surfaces

- cleavage plane of MoS<sub>2</sub>, 16
- surfactants on anisotropic, 15–16
- surfactants on isotropic, 16–17

## Hydrophobically modified poly(sodium acrylate) (HMPA)

- phase diagram of HMPA-doped membrane solution, 171, 173*f*, 174
- preparation, 170

*See also* Lyotropic system, ternary

## I

Inlayer radial distribution function, surface layers of different film thickness, 47, 49*f*, 50Interaction forces. *See* Phospholipid bilayers

## Interfaces, area measurement, 4–5

## Interfacial aggregation

- first AFM study, 15
- shape changes and kinetics, 17

## Interfacial interactions

- role in block copolymer on laterally heterogeneous surfaces, 149, 150*f*
- role of orientation of block copolymer on laterally homogeneous surfaces, 145, 147–149

*See also* Diblock copolymers

## Interfacial micelles, evidence for, 5

## Ionic surfactants

- fluorescence probe studies, 11–12
- oppositely charged hydrophilic surfaces, 14–15

## K

## Kinetic friction

- correlation to net normal force, 113
- interaction between surfaces in terms of surface adhesion, 113–114
- lack of correlation between adhesion and, 114
- proportional to applied load, 113
- rigid films, 113–114

## Kinetics, interfacial aggregates, 17

## L

- Lamellar droplet capillary from microemulsion phase  
 capillary condensation, 61–62  
 capillary force by bridging droplet, 61–62  
 modeling, 61–62  
 modeling force for capillary condensation of lamellar droplet, 62  
 modeling force profiles between sphere and plate-confining lamellar phase, 63*f*  
 specific lamellar order, 62
- Lamellar–microemulsion phase transition  
 force profiles on both sides, 70–71  
*See also* Capillary condensation; Lamellar phase; Microemulsion phase
- Lamellar phase  
 analysis, 62, 64  
 coexisting lamellar phases in polymer-doped membrane solutions, 171, 173*f*, 174  
 Derjaguin-like term, 60  
 dislocation loop array model, 59–61, 64  
 force profile analysis, 62, 64  
 modeling, 59–61  
 previous experimental studies, 69–70  
 refractive index profiles, 68*f*  
 relaxation mechanism, 60  
 sum term, 60–61  
*See also* Lyotropic system, ternary
- Laponite  
 phase transitions in clay dispersions, 165, 167  
 specific relaxation rate of water adsorbed onto laponite as function of clay concentration, 166*f*  
 synthetic, hectorite clay, 156  
*See also* NMR solvent relaxation studies
- Light diffraction method, in-layer particle structuring, 45
- Light interference phenomenon, thinning soap film, 40
- Lipid bilayers  
 methods measuring interaction profiles on subnanometer scale, 215  
 modeling living cells in biophysical study of mechanisms and interaction forces, 215  
*See also* Phospholipid bilayers
- Liquid layering  
 behavior of smooth solid surfaces moving laterally, 104–105  
 expulsion of layer from liquid film, 105  
 impurities and surface roughness, 105
- Lubricating films. *See* Stick-slip behavior, microscopic nature
- Lyotropic phases against free interface  
 binding of hexagonal phase to surface and surface relaxation, 34–37  
 image plate of diffraction pattern from H<sub>1</sub>-phase of C<sub>12</sub>E<sub>5</sub> in water, 35*f*  
 position-sensitive detector spectra of peak from H<sub>1</sub> phase of C<sub>12</sub>E<sub>5</sub> in water, 36*f*, 37*f*  
 sketch of scattering geometry in XTERD experiment, 34*f*  
 surface-induced shift of hexagonal-to-isotropic phase transition, 37–38
- X-ray total–external–reflection diffraction (XTERD), 34
- Lyotropic phases against solid surfaces  
 neutron reflectivity at interface of silicon wafer with hydrophobic coating, 32*f*  
 surface effects accompanying L<sub>1</sub>-to-H<sub>1</sub> transition, 31–33  
 surface effects accompanying L<sub>α</sub>-to-L<sub>α+</sub> transition, 29–31  
 technique of neutron reflectivity, 28–29  
 transverse rocking scan of H<sub>1</sub> phase, 33*f*  
 transverse rocking scans of two lamellar states, 30, 31*f*  
 typical neutron reflectivity experiment, 29*f*  
 typical set of specular neutron reflectivity spectra, 31*f*
- Lyotropic system  
 phase diagram, 57*f*  
 solution of tetraethylene glycol decyl ether (C<sub>10</sub>E<sub>4</sub>), water, and octane, 56  
*See also* Capillary condensation
- Lyotropic system, ternary  
 coexisting lamellar phases with polymer inclusion, 171, 174  
 extracting value of  $\delta$  from high-*q* region of neutron scattering spectra, 177*f*  
 factors governing phase behavior and bilayer membrane properties, 176  
 hydrophobe substitution level effect on monophasic L<sub>α</sub> solution at fixed polymer concentration, 172*f*  
 hydrophobically modified poly(sodium acrylate) (HMPA) preparation, 170  
 membrane properties, 174, 176  
 minimum hydrophobic side chains to

- confine polysoap in membrane solution, 171
- normalized neutron scattering data of membrane solutions with different polymer concentrations, 175*f*
- phase diagram determination, 170
- phase diagram of HMPA-doped membrane solution, 173*f*
- phase diagram of reference system (C<sub>12</sub>EO<sub>5</sub>/C<sub>6</sub>OH/brine), 172*f*
- polymer structure and concentration effect on phase behavior of polymer-doped membrane solutions, 174, 175*f*
- relative elastic constant as function of polymer concentration, 177*f*
- small-angle neutron scattering experiments, 170–171
- variation of elastic constant with polymer concentration, 174, 176

## M

### Membrane properties

- confinement of polymers, 174, 176
- See also* Lyotropic system, ternary

### Membrane ultrafiltration and microfiltration

- separation and purification of proteins, 231

*See also* Proteins

### Mica

- forces and fusion between solid-supported phospholipid bilayers, 216, 218–219
- ionic surfactants on, 14–15
- water-swappable cationic polyelectrolyte binding to negatively charged surface, 219, 220*f*
- See also* Phospholipid bilayers

### Micelles, worm-like

- cetyltrimethylammonium surfactants (CTA), 77–79
- nonionic and doped nonionic, 79, 82
- See also* Near-surface small-angle neutron scattering (NSSANS)

### Microemulsion phase

- analysis, 64, 66–70
- force profile analysis, 69
- previous experimental studies, 69–70
- refractive index profiles, 66, 68*f*, 69
- X-ray scattering, 64, 66
- X-ray spectra increasing temperature from lamellar to microemulsion phase, 67*f*

### Microinterferometric technique

- film-thinning interferogram, 44*f*
- particle layering inside films, 43

### Mixed counterion system

- near-surface small-angle neutron scattering (NSSANS), 77, 78*f*
- shear SANS pattern, 79, 80*f*

### Models

- lamellar droplet capillary condensed from microemulsion phase, 61–62
- lamellar phase, 59–61
- nature of stick–slip motion, 119–123
- origins of rigidity in thin film, 115–119
- quasistatic assumption, 121–122
- questions concerning yield event, slip stage, and adhesion recovery, 114
- transition to sliding in amorphous films, 122–123

*See also* Stick–slip behavior, microscopic nature

### Monte Carlo simulation, investigating dependence of in-layer particle structuring phenomenon on film thickness, 45, 47, 50

### Montmorillonite

- determination of T<sub>2b</sub> by extrapolation of measured T<sub>2</sub> data as function of solids content, 163*f*
- effect of end-group structure of poly(ethylene glycol) (PEG) adsorbed onto montmorillonite on bound fraction probability of water, 166*f*
- effect of PEG adsorption on bound fraction probability of water adsorbed onto montmorillonite, 163*f*
- effect of PEG molecular weight on T<sub>2b</sub> of water adsorbed onto montmorillonite, 164*f*
- polymer adsorption onto clay, 162–165
- sample particles, 156
- See also* NMR solvent relaxation studies

### Morphology. *See* Polymer morphology

### Myristic acid–cetyltrimethylammonium hydroxide–water system. *See* Catanionic surfactant aggregates

## N

### Nanodiscs, rigid

- electron microscopy after cryofracture, 91, 94*f*, 95*f*, 96*f*, 97*f*
- main features, 100

- possible uses, 100  
rigid platelet characterization, 90  
size control, 91  
*See also* Catanionic surfactant aggregates
- Near-surface small-angle neutron scattering (NSSANS)  
cetyltrimethylammonium surfactants  
(CTA) worm-like micelles, 77–79  
corrected 2D data sets for mixed counterion (MC) system, 77, 78*f*  
correction for beam flux, 76–77  
corrections for unique geometry of cell, 74, 76  
effective sample volume, 76  
limitations and potential, 82  
nonionic and doped nonionic worm-like micelles, 79, 82  
NSSANS from C<sub>16</sub>E<sub>6</sub> nonionic surfactant with 10% ionic, 79, 81*f*, 82  
refraction correction, 76  
schematic of optics, 75*f*  
schematic of Poiseuille flow cell, 75*f*  
slice (1D) through bulk Couette data set for MC system, 79, 80*f*  
standard Couette SANS experiment of C<sub>16</sub>E<sub>6</sub> nonionic surfactant with 10% ionic, 82, 83*f*  
technique, 74, 76–77
- Neutron reflectivity  
log of neutron reflectivity profiles for symmetric, diblock copolymer film, 144–145, 146*f*  
lyotropic phases against solid surfaces, 28–33  
surface effects accompanying L<sub>1</sub>-to-H<sub>1</sub> transition, 31–33  
surface effects accompanying L<sub>α</sub>-to-L<sub>α</sub>+ transition, 29–31  
technique, 28–29  
thin films of diblock copolymers, 144–145
- Neutron reflectometry  
best fit parameters, 8*t*  
data for tetradecyltrimethylammonium (TTAB) bromide adsorbed onto sapphire crystal, 8*f*  
investigating adsorbed surfactant layers at interfaces, 6  
treating adsorbed layer as laterally unstructured film, 7–9
- NMR solvent relaxation studies  
adsorption of water onto particle surfaces, 156–158  
aspects of polymer adsorption onto inorganic particles, 153–154  
competitive adsorption of polymers onto silica particles, 158–160  
competitive adsorption of poly(vinyl pyrrolidone) (PVP) and poly(ethylene oxide) (PEO) adsorbed on silica, 161*f*  
determination of T<sub>2b</sub> by extrapolation of measured T<sub>2</sub> data as function of solids content, 163*f*  
effect of adsorption of poly(ethylene glycol) (PEG) on montmorillonite, 162, 163*f*, 164*f*  
effect of end-group structure of PEG adsorbed onto montmorillonite on bound fraction probability of water, 165, 166*f*  
effect of PEG adsorption on bound fraction probability of water adsorbed onto montmorillonite, 163*f*  
effect of PEG molecular weight on T<sub>2b</sub> of water adsorbed onto montmorillonite, 164*f*  
experimental particles, 156  
experimental polymers, 155–156  
experimental techniques, 155  
NMR relaxation of water in silica, 154  
NMR samples, 156  
NMR solvent exchange theory, 154  
phase transitions in clay dispersions, 165, 167  
polymer adsorption onto clay, molecular weight and end-group effects, 162–165  
polystyrene latex particle preparation, 156  
R<sub>2sp</sub> (specific relaxation rates) for polystyrene latex, silica, and alumina in water, 157*f*  
R<sub>2sp</sub> for water-laponite solutions as function of particle concentrations, 166*f*  
R<sub>2sp</sub> of silica-polymer-water systems as function of polymer concentration, 159*f*  
sources for observed R<sub>2sp</sub> decreases, 165, 167  
versatility for probing interfacial effects in particulate dispersions, 167
- Nonionic surfactant adsorbed films, fluorescence probe studies, 11
- Nonionic surfactants  
hydrophilic surfaces, 15

September 7, 2012 | <http://pubs.acs.org>  
Publication Date: August 20, 1999 | doi: 10.1021/bk-1999-0736.ix002

- lyotropic phases against free interface, 34–38
- lyotropic phases against solid surfaces, 28–33
- surface aggregation of amphiphiles  
from dilute solutions, 25–28
- tetraethylene glycol decyl ether (C<sub>10</sub>E<sub>4</sub>), 56
- Nonionic worm-like micelles  
doped, 79, 82  
near-surface small-angle neutron scattering (NSSANS) of doped sample, 81*f*  
standard Couette SANS experiment of doped sample, 83*f*
- Nucleation sites, widely spaced alkyl groups, 5
- O**
- Octane  
diversity of behavior, 117  
thick and thin films, 117–118
- Oligo-oxyethylene mono-*n*-alkyl ether (C<sub>m</sub>E<sub>n</sub>) family  
model amphiphiles, 24–25  
phase diagram, 25*f*
- Oligosaccharide surfactant polymers  
absorbance of amide I and II bands  
and absorbance due to adsorbed protein, 190*t*
- AFM topographic images of polymers with different hydrophobic–hydrophilic ratio adsorbed on highly oriented pyrolytic graphite (HOPG), 188*f*
- characterization methods, 182
- comb-like polymers of poly(vinyl amine) (PVAm) backbone with hydrophilic dextran and/or hydrophobic alkanoyl side chains, 181–182
- enthalpic energy gain of adsorption, 189
- epitaxial adsorption pattern varying with alkanoyl concentration, 189
- existing surface modification methods for practical biomaterial devices, 181
- hexagonal angular dependence pattern in 2-D Fourier transform of image, 186, 188*f*
- HOPG modification with surfactant polymer, 189–190
- ideal surface modification, 180–181
- mechanism of epitaxial adsorption of surfactant polymer on HOPG, 186, 189
- plots of surface tension versus logarithm of concentration of aqueous surfactant polymer solutions, 185*f*
- protein adsorption by ATR–FTIR spectra, 190, 191*f*
- protein-resistance of biomimetic, glycolyx-like surface, 189–190
- surface-active properties at air–water interface, 182, 184
- surface-induced assembly on HOPG, 184, 186–189
- synthesis and characterization of comb-like dextran surfactant polymers, 182
- synthetic scheme for comb-like surfactants and molecular model for surfactant polymer, 183*f*
- time-dependent adsorption of polymer with 1:5 ratio dextran to hexanoyl groups, 186, 187*f*
- Optical characteristics, sol–gel-derived alumina, 250–251
- Optical probes. *See* Glass transition in thin polymer films
- Optical reflectometry, thick films, 6
- Order–disorder transition, diblock copolymers, 144
- Ordering, confinement effects, 143–145
- Oscillatory structural forces, low- and high-particle concentrations, 50
- Osmotic pressure (stress) technique  
measuring interaction profiles on subnanometer scale, 215  
*See also* Phospholipid bilayers
- P**
- Particle layering  
experimental set-up, 42*f*  
microinterferometric technique, 43
- Particle self-layering phenomenon, studying vertical macroscopic film thinning behavior, 43, 45
- Particle size  
distribution in sol–gel-derived alumina, 249–250
- effects of polydispersity on layering and structural transitions in thin film, 52
- Particulate dispersions. *See* NMR solvent relaxation studies
- Peclet number, 235
- Phase diagrams  
amphiphiles, 25*f*

- lyotropic system, 57*f*  
 ternary equilibrium in catanionic surfactant aggregates, 91, 98–100  
*See also* Lyotropic system, ternary
- Phospholipid bilayers**  
 adsorption of dimyristoyl phosphatidylcholine (DMPC) vesicles onto polymer-supported mixed monolayers of DMPC and synthetic reactive lipid, 224  
 contact angle measurements on polyethyleneimine (PEI)-supported monolayers, 223*t*  
 convenience of branched PEI as water-swallowable polymeric substrate, 228  
 covalently attached membranes, 221–224  
 factors governing fusion of lipid bilayer membranes, 226, 228  
 fluorescence micrographs of mixed monolayer (DMPC/DMPE–NCS), 225*f*  
 forces and fusion between solid-supported, 216, 218–219  
 formation of soft-supported DMPC bilayers on mica, 221–228  
 formation of tethered DMPC monolayer and bilayers partially attached to supporting PEI, 222*f*  
 hydrophobic attraction between hydrophobic interiors of solid-supported bilayers, 218  
 hydrophobic interaction between inner layers of opposing lipid membranes, 218  
 mixed bilayer systems, 218  
 modeling living cells in biophysical study of mechanisms and interaction forces, 215  
 normal interaction forces of soft-supported DMPC bilayers, 224, 226  
 physisorbed bilayers, 221  
 polymer-supported bilayers, 220*f*  
 schematic of hemifusion and fusion between bilayer membranes, 217*f*  
 soft-supported bilayers for investigating normal interaction forces, 219–221  
 study of normal interbilayer forces with surface force apparatus (SFA), 216  
 temperature dependence of interaction profile of two PEI-supported pure DMPC membranes, 227*f*
- Photon correlation spectroscopy (PCS)**  
 intensity autocorrelation function, 136  
 intensity autocorrelation functions for freely standing PS film, 138*f*  
 measuring glass transition and associated relaxation dynamics, 128  
 motivation for performing measurements of freely standing polystyrene (PS) films, 137–138  
 scattering light by nonpropagating fluctuations, 136–138  
 versus Brillouin light scattering (BLS), 136  
*See also* Glass transition in thin polymer films
- Pipette aspiration technique**  
 measuring interaction profiles on subnanometer scale, 215  
*See also* Phospholipid bilayers
- Polydispersity, particle size, effects on layering and structural transitions in thin film, 52**
- Poly(ethylene glycol) (PEG)**  
 adsorption onto clay, 162–165  
 effect of adsorption on montmorillonite, 162  
 effect of end-group structure of PEG adsorbed onto montmorillonite, 165, 166*f*  
 effect of PEG adsorption on bound fraction probability of water adsorbed onto montmorillonite, 163*f*  
 effect of PEG molecular weight on  $T_{2b}$  of water adsorbed onto montmorillonite, 164*f*  
 materials, 156  
*See also* NMR solvent relaxation studies
- Poly(ethylene oxide) (PEO)**  
 adsorption of PEO-based surfactants on silica, 15  
 competitive adsorption of PVP and PEO adsorbed on silica, 161*f*  
 competitive adsorption onto silica particles, 158–160  
 materials, 155  
 specific relaxation rates for PEO and PVP adsorbed on silica, 159*f*  
*See also* NMR solvent relaxation studies
- Polyethyleneimine (PEI)**  
 contact angle measurements on PEI-supported monolayers, 223*t*  
 covalently attached membranes, 221–224  
 force–distance profile during compression of physisorbed PEI-supported DMPC bilayers, 226, 227*f*

- polymer-supported bilayers, 220*f*  
 water-swellaible cationic polyelectrolyte, 219  
*See also* Phospholipid bilayers
- Polymer films  
 dependence of film relaxation time on molecular weight, 108–109  
 nature of onset of rigidity, 108  
 techniques probing properties, 127–128  
 thickness-dependent slowing down of relaxation, 108  
*See also* Glass transition in thin polymer films
- Polymer morphology  
 confinement effects on ordering, 143–145  
 film thickness constraint to system, 143  
 needing routes to manipulate spatial arrangement, 141  
 schematic of lamellar microdomains of block copolymer, 142*f*  
*See also* Diblock copolymers
- Polymeric materials, morphologies spanning nanoscopic to macroscopic, 140–141
- Polymers  
 behavior of long molecules in flow fields, 196–197  
 interactions with ionic or nonionic membrane, 170  
 interactions with surfactants, 2  
*See also* DNA molecules
- Poly(methyl methacrylate) (PMMA). *See* Diblock copolymers
- Poly(oxyethylene) dodecyl ethers, ellipsometry and fluorescence quenching, 9*t*
- Poly(oxyethylene) octyl phenyl ethers, ellipsometry and fluorescence quenching, 9*t*
- Polypeptides. *See* Fibronectin; Single-molecule force spectroscopy; Titin
- Poly(sodium acrylate). *See* Hydrophobically modified poly(sodium acrylate) (HMPA)
- Polystyrene (PS)  
 adsorption of water onto particle surfaces, 156–158  
 latex particle preparation, 156  
 specific relaxation rates for PS latex, silica, and alumina in water, 157*f*  
*See also* Diblock copolymers; Glass transition in thin polymer films; NMR solvent relaxation studies
- Poly(vinyl pyrrolidone) (PVP)  
 competitive adsorption of PVP and poly(ethylene oxide) (PEO) adsorbed on silica, 161*f*  
 competitive adsorption onto silica particles, 158–160  
 materials, 155  
 specific relaxation rates for PEO and PVP adsorbed on silica, 159*f*  
*See also* NMR solvent relaxation studies
- Pore, confinement expression, 3
- Pore size distribution, sol–gel-derived alumina, 249–250
- Position-sensitive detector (PSD), X-ray total-external-reflection diffraction (XTERD), 35–36
- Pressure, structural disjoining, particles on surface of film for hard-sphere–hard-wall model, 47, 48*f*
- Proteins  
 adsorption, 235  
 attempting to change potential barrier for deposition, 237, 239  
 concept of critical flux, 234–235  
 conditions for irreversible deposition, 235  
 determining onset of flux decline and transmission reduction for bovine serum albumin (BSA), 236  
 determining true fouling threshold, 239, 244  
 dynamics of transport, aggregation, and deposition near membrane surface and pores, 231–232  
 effect of added electrolyte on transmembrane pressure versus flux at pH 3 and pH 9, 238*f*  
 electron micrograph of membrane above critical flux, 241*f*  
 electron micrograph of membrane after filtration with added NaCl, 243*f*  
 electron micrograph of membrane after filtration with no added NaCl, 242*f*  
 electron micrographs of membrane below, near, and above critical flux, 239  
 examining effect of added electrolyte, 236–237  
 experimental methods, 237  
 flux experiments, 239  
 flux-transmembrane pressure relationship during “stepping” experiments, 244  
 fouling of track-etched membranes with BSA, 232–233  
 observing deposits by field emission electron microscopy, 234

possibility of filtration affecting conformation, 232  
 possible denaturation by local shear field and small pores, 232  
 potential mechanisms controlling transport and deposition in membrane pores, 232  
 probing critical conditions to initiate irreversible multilayer protein deposition, 234  
 process scheme for biocatalyst preparation by cell entrapment in epoxy beads, 238*f*  
 Sherwood and Peclet numbers, 235, 236*t*  
 stepping experiments, 237  
 transmembrane pressure and flux versus time during filtration at constant flux at pH 3, 239, 240*f*  
 transmembrane pressure versus time during filtration at pH 3 with added NaCl, 239, 240*f*  
*See also* Bovine serum albumin (BSA); Fibronectin; Single-molecule force spectroscopy; Titin

## Q

Quartz, ionic surfactants on, 14

## R

Radial distribution function, particle structure inside layer parallel to film surface, 47, 50  
 Reflectance techniques  
 ellipsometry, 9  
 investigating thin adsorbed films, 6–7  
 maximum achievable wave vector, 7  
 neutron reflectometry, 7–9  
 optical reflectometry, 6  
 X-ray reflectometry, 6–7  
 Reflected light microinterferometric method, measuring total film thickness and amplitude of transition, 45  
 Refractive index profiles  
 lamellar phase, 68*f*  
 microemulsion phase, 66, 68*f*, 69  
 Relaxation mechanism, lamellar phase, 60  
 Released DNA molecules. *See* DNA molecules  
 Rigid films  
 constitutive equation for friction, 119–120

crystallization, 115–116  
 finite time to re-establish static friction, 112  
 interaction of stick boundary conditions, 118–119  
 kinetic friction, 113–114  
 nature of stick–slip motion, 119–123  
 nonlinear response, 110–114  
 nonlinear response to shear force, 110  
 origins of rigidity in thin film, 115–119  
 properties, 109–110  
 quasistatic assumption, 121–122  
 slow relaxation in disordered films, 116–118  
 static friction, 111–113  
 stick–slip motion as sequential phase transitions, 121–122  
 time dependence of force oscillations on sliding, 112–113  
 time dependence of yield stress, 111–112  
 transition to sliding in amorphous films, 122–123  
 yield stress increasing with increasing pressure, 111

## S

Shape changes, interfacial aggregates, 17  
 Shear flow field, hierarchy of confinement, 3  
 Sherwood number, 235  
 Silica  
 ionic surfactants on, 14  
 specific relaxation rates for PS latex, silica, and alumina in water, 157*f*  
*See also* NMR solvent relaxation studies  
 Single-molecule force spectroscopy  
 arrangement of domains in bovine fibronectin, 209*f*  
 arrangement of domains in I-band part of human cardiac titin, 209*f*  
 experimental, 210  
 fibronectins, 210  
 force measurement method, 210–211  
 force versus extension curve for native fibronectin, 212*f*  
 force versus extension curve reflecting unfolding of titin, 212*f*  
 giant muscle protein titin, 208, 210  
 modeling force versus extension characteristics of unfolded polypeptide, 211  
 sample preparation, 210



- sawtooth pattern of sequential unfolding of domains, 212*f*  
 schematics of force spectrometer, 209*f*  
 unfolding forces in titin and fibronectin, 211, 213  
 worm-like chain (WLC) fits, 211, 212*f*
- Single molecules. *See* DNA molecules
- Slit, confinement expression, 3
- Small-angle neutron scattering (SANS). *See* Near-surface small-angle neutron scattering (NSSANS)
- Small-angle X-ray scattering  
 cationic surfactant spectra above and below chain melting temperature, 90, 93*f*  
 method, 87
- Soap film, thinning, light interference phenomenon, 40
- Sol-gel-derived (SGD) alumina  
 AFM image for surface sintered at 400°C, 249*f*  
 characterization of particles and pores, 249–250  
 optical characteristics, 250–251  
 optical transmission for 0.5-mm plates sintered at 400, 700, and 950°C, 251*f*  
 photochemical production of vitamin D<sub>3</sub>, 251–258  
 pore size distribution for sintering at 400, 700, and 950°C, 250*f*  
 potential selectivity for chemical reactions, 247–248  
 preparation and characterization, 248–251  
 steps in sol-gel preparation of porous alumina, 248–249  
*See also* 7-Dehydrocholesterol; Vitamin D<sub>3</sub>
- Solute, adsorption at interface, 2
- Solution depletion methods, adsorption isotherms, 4–5
- Solvent relaxation studies. *See* NMR solvent relaxation studies
- Spherical micelles, image, 13*f*
- Static emission method, aggregation number, 10
- Stick-slip behavior, microscopic nature characterizing mechanical properties of liquid films, 123  
 constitutive equation for friction, 119–120  
 crystallization, 115–116  
 interaction of stick boundary conditions, 118–119  
 kinetic friction, 113–114  
 liquid layering experiments, 104–105  
 models, 114–123  
 nature of stick-slip motion, 119–123  
 nonlinear response of rigid film, 110–114  
 origins of rigidity in thin film, 115–119  
 properties of rigid film, 109–110  
 rigidity in thin films, 106–110  
 slow relaxation in disordered films, 116–118  
 static friction, 111–113  
 stick-slip motion as sequential phase transitions, 121–122  
 surface topology, 120–121  
 transition to rigidity, 106–109  
 transition to sliding in amorphous films, 122–123
- Structural disjoining pressure, particles on surface of film for hard-sphere-hard-wall model, 47, 48*f*
- Structural transitions. *See* Colloidal suspensions in confined films
- Supramolecular structures  
 adsorption isotherms, 4–5  
 atomic force microscopy (AFM), 12–18  
 calorimetry, 5–6  
 fluorescence probe studies, 9–12  
 interactions between surfactants and polymers, 2  
 reflectance techniques, 6–9  
 surface force measurements, 18–20
- Surface aggregation, amphiphiles from dilute solutions, 25–28
- Surface force apparatus (SFA)  
 force profiles in lamellar and symmetrical microemulsion, 56, 58*f*, 59  
 investigating capillary condensation, 55  
 investigations in surfactant solutions, 19  
 phase transitions for confined complex fluids, 55  
 study of boundary lubrication on microscopic scales, 104  
 study of normal interbilayer forces, 216, 217*f*  
 symmetrical microemulsion approaching lamellar phase, 55–56  
*See also* Capillary condensation; Phospholipid bilayers
- Surface force measurements  
 colloid probe technique, 19  
 drawbacks, 18  
 investigations in surfactant solutions, 19

September 7, 2012 | <http://pubs.acs.org>  
 Publication Date: August 20, 1999 | doi: 10.1021/bk-1999-0736.ix002

theoretical comparisons with models, 19–20

Surface freezing, 24

Surface melting, 24

Surface topology  
changes in friction with varying, 120  
cobblestone model of solid friction, 120–121

Surfactant adsorption  
adsorbed micelles versus classical bilayer, 3*f*  
calorimetry probing energetics, 5–6  
final equilibrium structure, 6  
mechanisms and structure, 6

Surfactant aggregates  
caution interpreting atomic force microscopy (AFM) images, 18  
*See also* Near-surface small-angle neutron scattering (NSSANS)

Surfactant microstructures, comparison to catanionic surfactant nanodiscs, 98, 100

Surfactant polymers. *See* Oligosaccharide surfactant polymers

Surfactants  
anisotropic hydrophobic surfaces, 15–16  
evidence for self-assembly, 3  
interaction with polymers, 2  
isotropic hydrophobic surfaces, 16–17

**T**

Tethered DNA molecules. *See* DNA molecules

Tetradecyltrimethylammonium (TTAB) bromide  
adsorption isotherm, onto Al<sub>2</sub>O<sub>3</sub>, 4*f*  
neutron reflectometry data, 8*f*

Tetraethylene glycol decyl ether (C<sub>10</sub>E<sub>4</sub>)  
lyotropic system, 56  
*See also* Capillary condensation

Thin films  
branched and linear polymers, 107  
crystallization, 115–116  
frequency-thickness superposition of viscoelastic response, 107  
origins of rigidity, 115–119  
rigidity, 106–110  
rigid state resembling soft solid, 109  
thermodynamics of order–disorder transition, 115–116  
transition to rigidity, 106–109

Time-resolved fluorescence, aggregation number, 10

Titin  
arrangement of domains in I-band part of human cardiac titin, 209*f*  
force versus extension curve reflecting unfolding of 6 Ig domains, 212*f*  
giant muscle protein, 208, 210  
unfolding forces, 211, 213  
*See also* Fibronectin; Single-molecule force spectroscopy

## U

Ultraviolet–visible spectroscopy, electronic interactions of 7-dehydrocholesterol with surface of sol–gel-derived alumina, 253, 254*f*

## V

Viscoelastic surfactant solutions  
distinguishing between interfacial and bulk effects, 73–74  
*See also* Near-surface small-angle neutron scattering (NSSANS)

Vitamin D<sub>3</sub>  
adsorption characteristics of 7-dehydrocholesterol with diffuse reflectance infrared spectroscopy, 253  
adsorption geometry of transition state, 256–258  
adsorption of 7-dehydrocholesterol in sol–gel-derived (SGD) alumina, 251–253  
diffuse reflectance IR spectra of 7-dehydrocholesterol, 254*f*  
electronic interactions of 7-dehydrocholesterol with surface of SGD alumina as probed with UV-vis spectroscopy, 253  
final adsorption concentrations of 7-dehydrocholesterol in activated and nonactivated SGD alumina, 253*t*  
percent composition of solid-state photolysis of 7-dehydrocholesterol film, 258*t*  
percent compositions resulting from photolysis of 7-dehydrocholesterol, 255*t*  
photochemical and thermal isomerizations of related molecules, 252*f*  
photochemical production within SGD alumina, 251–258  
photolysis of 7-dehydrocholesterol within SGD alumina, 253, 255

preparation and characterization of SGD alumina, 248–251  
 solid-state photolysis of 7-dehydrocholesterol, 258  
 steric interactions between co-adsorbed molecules in SGD alumina required for *cis*–*trans* isomerization of previtamin D<sub>3</sub> to tachysterol<sub>3</sub>, 257*f*  
 steric interactions for *cis*–*trans* isomerization of previtamin D<sub>3</sub> to tachysterol<sub>3</sub>, 256*f*  
 UV-vis spectra of 7-dehydrocholesterol in various media, 254*f*  
*See also* 7-Dehydrocholesterol; Sol-gel-derived (SGD) alumina

## W

### Water

adsorption onto particles surfaces, 156–158  
 displacement by polymers on montmorillonite clay, 162, 165  
 effect of end-group structure of poly(ethylene glycol) (PEG) adsorbed onto montmorillonite on bound fraction probability of water, 166*f*  
 effect of PEG adsorption on bound fraction probability of water adsorbed onto montmorillonite, 163*f*  
 effect of PEG molecular weight on T<sub>2b</sub> of water adsorbed onto montmorillonite, 164*f*  
 phase transitions in clay dispersions, 165, 167

specific relaxation rate of water adsorbed onto laponite as function of clay concentration, 166*f*  
 specific relaxation rates for polystyrene latex, silica, and alumina in water, 157*f*  
*See also* NMR solvent relaxation studies  
 Wide-angle X-ray scattering catanionic surfactant systems at 25°C and 50°C, 90, 92*f*  
 method, 87  
 Worm-like micelles cetyltrimethylammonium surfactants (CTAs), 77–79  
 nonionic and doped nonionic, 79, 82  
*See also* Near-surface small-angle neutron scattering (NSSANS)

## X

X-ray reflectometry, air–liquid films, 6–7  
 X-ray scattering, microemulsion phase, 64, 66  
 X-ray total-external-reflection diffraction (XTERD)  
 hexagonal diffraction patterns, 35*f*  
 lyotropic phases, 34  
 sketch of scattering geometry, 34*f*

## Z

Zwitterionic surfactants, hydrophilic surfaces, 15